"Heat Transfer and Fuel Transport in the Intake Port of a Spark Ignition Engine"

Michael John Farrelly Colechin BEng CEng MIMechE

Thesis submitted to the University of Nottingham
for the degree of Doctor of Philosophy, October, 1996

Contents

ABSTRACT

"Heat Transfer and Fuel Transport in the Intake Port of a Spark Ignition Engine"

Michael John Farrelly Colechin

Surface-mounted heat flux sensors have been used in the intake port of a fuel injected, spark ignition engine to investigate heat transfer between the surface, the gas flows through the port, and fuel deposited in surface films. This investigation has been carried out with a single-cylinder engine on which the cylinder head is from a production four valve per cylinder engine with a bifurcated intake port. The objective has been to establish how engine operating conditions affect trends in surface heat transfer rates both with and without fuel deposition on the surfaces, and to relate these to the mechanisms involved in the transport of fuel into the engine. The effects on these mechanisms of injector type and fuel characteristics have also been studied.

Fuel transport has been characterised using the τ and X parameters, and experimental studies have been carried out to examine these for fully-warm and warm-up engine operating conditions, with a range of injector types representative of those currently used in service. This data has been compared to the results of a photographic study of the fuel distribution pattern produced by each injector type, and these combined results used to decide upon suitable positions within the inlet port for the heat flux sensors.

The dynamic response characteristics of the surface-mounted heat flux sensors have been determined, and measured heat flux data corrected accordingly to account for these characteristics. Details of the model and data processing technique used, are described. Corrected intra-cycle variations of heat transfer to fuel deposited have been derived for engine operating conditions at 1000 RPM covering a range of manifold pressures, fuel supply rates, port surface temperatures, and fuel injection timings. Both pump-grade

gasoline and isooctane fuel have been used. The influence on heat transfer rates of the deposited fuel and its subsequent behaviour has been examined by comparing fuel-wetted and dry-surface heat transfer measurements. With both fuel types, the heat transfer rate to the fuel reaches peak values up to around 50 kW/m^2 during the engine cycle, and is typically 5 kW/m^2 on average in regions of heavy fuel deposition. The effects of operating conditions on the magnitude and features of the heat flux variations are described.

Integration of this heat flux data has provided values of heat transfer per cycle, allowing direct comparisons of operating condition and injector type effects to be made. For dry-port conditions heat transfer per cycle varies between 0 and 300 J/m^2 depending on location, towards the surface at low temperatures and away from the surface at fully-warm conditions. During warm-ups with fuel deposition, as coolant temperature increases from 0 to 90°C, values of heat transfer to the fuel typically increase from 300 J/m^2 to 1000 J/m^2. For a given coolant temperature, heat transfer values generally increase as manifold absolute pressure (MAP) is lowered or fuel flow rate increases. The effect of fuel deposition on heat transfer has been characterised by a function of MAP, fuel flow rate and coolant temperature.

When running on isooctane fuel the heat transfer measurements were made using a heat flux gauge bonded to the intake port surface in the region where highest rates of fuel deposition occur. Heat transfer changes are consistent with trends predicted by convective mass transfer over much of the range of surface temperatures from 20°C to 100°C. Towards the upper temperature limit, heat transfer reaches a maximum limited by the rate and distribution of fuel deposition. The inferences drawn from the isooctane results are discussed and related to characteristics observed when gasoline is used.

Acknowledgements

My thanks are due to Professor P J Shayler whose guidance has helped me to carry out the research reported here, making the writing of this thesis so much easier, and to Professor B R Clayton for providing the facilities I have used within the Department of Mechanical Engineering at the University of Nottingham. The generous support of the Ford Motor Company must also be acknowledged, particularly that of Mr A Scarisbrick and the staff at their Research and Engineering Centre in Dunton.

In the practical work I have undertaken I have received assistance from the technical staff in the L4 Laboratory and I would like to thank them, especially John McGhee and Brian Webster whose skills and experience have been invaluable.

Other sources of inspiration and support have been Jon Dixon and the other Research Assistants with whom I have worked over the past four years; my family; and friends, particularly David Abbott, David Dadswell and Simon Read. To all of these I offer my appreciation.

Finally, I must thank Clare to whom I owe so much more than just my third name.

a	Thickness of protective layer on heat flux sensor (m)
A	Area over which the heat flux measured through the sensor is assumed to apply (m^2)
B	Convective mass transfer driving force
c_p	Specific heat capacity (J/kg K)
d	Hydraulic diameter of port at specified location (m) or Thickness of thermal barrier in heat flux sensor (m)
g	Adhesive layer thickness (m)
g^*	Mass conductance (kg/m^2 s)
h_{fg}	Latent heat of vaporisation of fuel (J/kg)
k	Thermal conductivity (W/m K)
$\dot{m}_a$	Air flow rate (kg/s)
$\dot{m}_f$	Fuel flow rate (kg/s)
$(\dot{m}'')_{con}$	Mass transferred per cycle under convective conditions (kg/m^2)
$(\dot{m}'')_{dep}$	Mass of fuel deposited per cycle (kg/m^2)
$(\dot{m}'')_{vap}$	Mass of fuel vaporised per cycle (kg/m^2)
Nu	Nusselt number = $\dot{Q}'' d / \theta k$
p	Manifold absolute pressure (bar)
Pr	Prandtl number = $\mu c_p / k$
q''	Integrated heat transfer per cycle (J/m^2)
$\dot{q}''$	Heat flux (W/m^2)
$\dot{Q}''$	Heat transfer rate, q''/t_{cyc} (W/m^2)
$\dot{q}_m$	Heat flux measured through heat flux sensor (W/m^2)
$\dot{q}_s$	Heat flux applied to surface of heat flux sensor (W/m^2)
Re	Reynolds number = $4\dot{m}_a / \mu \pi d$
t	Time (s)
t_{cyc}	Time for one engine cycle (s)
T	Temperature (°C)
x	Distance through heat flux sensor (m)

X	Fuel deposition constant
Y	Proportion of fuel film deposited on heat flux sensor
α	Thermal diffusivity = $k/\rho c$ (m^2/s)
ΔT	Change in fuel temperature (K)
θ	Port gas to surface temperature difference (K)
μ	Viscosity (kg/m s)
ρ	Density (kg/m^3)
τ	Time constant (s)
ω	Frequency (rad/s)

AFR	Air Fuel Ratio
ATDC	After Top Dead Centre of the Firing Stroke
BDC	Bottom Dead Centre
CA	Crank Angle (°ATDC)
CO	Carbon Monoxide
COV	Coefficient of Variance
EEC	Electronic Engine Control
EGR	Exhaust Gas Recirculation
EOI	End of Injection (°ATDC)
EVC	Exhaust Valve Closing (°ATDC)
FFT	Fast Fourier Transform
FID	Flame Ionisation Detector
HC	Hydrocarbon
IMEP	Indicated Mean Effective Pressure (bar)
IVC	Inlet Valve Closing (°ATDC)
IVO	Inlet Valve Opening (°ATDC)
MAP	Manifold Absolute Pressure (bar)
MOSFET	Metal Oxide Semiconductor Field Effect Transistor
MPI	Multi-Point Injection
NO_x	Oxides of Nitrogen
O_2	Oxygen
PC	Personal Computer
PID	Proportional, Integral and Differential
PRBS	Pseudo-Random Binary Sequence
RMS	Root Mean Square
RPM	Revolutions Per Minute
SI	Spark Ignition
SPI	Single-Point Injection
TC	Thermocouple

TDC	Top Dead Centre
UEGO	Universal Exhaust Gas Oxygen [Sensor]

Chapter 1
Introduction

In recent years, some of the most important changes in the design of spark-ignition engines have been concerned with fuel supply and mixture preparation improvements. Manufacturers have now moved from almost exclusive use of carburettors to using fuel injection throughout their product ranges. In most applications these systems are of the multi-point injection (MPI) type, with individual injectors mounted near the intake port entrance of each cylinder and oriented to direct fuel towards the intake valves. These introduce carefully controlled quantities of fuel to the engine close to the point at which it enters the cylinder, helping to ensure that the induced mixture ratio is appropriate to the engine operating conditions.

Although MPI systems are now essentially standard equipment on spark ignition engines, they are indirect injection systems that reduce but still do not eliminate the deposition of fuel on the walls of the intake passages. The injectors deliver fuel as an atomised spray into the intake port of each cylinder, but a significant proportion of the fuel is still deposited on the port and valve surfaces, particularly when the engine is cold. Furthermore, mixture control requirements have become more stringent. Consequently, there is still a need to understand the mechanisms involved in the transport of fuel to the cylinder and the way these influence mixture preparation and control.

MPI systems create an additional problem, in that the proximity of the injectors to the intake valves means that the period during which mixture preparation can take place is short. There is, therefore, a tendency for MPI systems to produce a less homogeneous induced mixture than earlier centrally supplied systems, which increases the engine-out and tailpipe emissions of pollutants. A variety of fuel injector types have been developed for MPI systems, since choice of injector type and targeting of injector spray influence mixture preparation and the dynamics of fuel transport in the intake port. The extent of this influence is rarely clear because of other effects such as fuel control strategy and fuel

quality variations. An aim of the work reported in this thesis has been to compare data obtained from engines tests carried out for a number of injector types at operating conditions which are likely to reveal any significant differences specifically due to these. This was initially achieved through the photographic investigation described in Chapter 4, which established the fuel distribution patterns and spray characteristics created by a selection of four different fuel injectors. Further quantitative comparisons were also made using the heat transfer measurement techniques described later in the thesis. The fuel injectors examined cover the range of types currently used in-service.

Because MPI systems do not totally eliminate fuel deposition, there has been considerable interest in understanding how this deposited fuel is subsequently transported into the cylinder, since this will affect mixture homogeneity, emissions and drivability. Fuel transport and mixture preparation in the intake systems of port-injected spark ignition engines have, therefore, been the subject of numerous investigations. The characteristics of fuel transport in the intake port are principally of interest in connection with the control of induced fuel flow under transient operating conditions. Unless the injected fuel supply is adjusted to provide compensation, the behaviour of deposited fuel can produce significant excursions in induced mixture ratio. Poor control causes mixture ratio excursions which adversely affect the performance of 3-way catalytic converters. The efficiency of NO_x reduction is poor when lean excursions occur, and HC and CO oxidation is poor when rich mixture excursions arise. Minimising the proportion of injected fuel which is deposited on the intake port and valve surfaces reduces the need for compensating fuel supply adjustments to maintain a target induced mixture ratio during transients. For the remaining fuel film a phenomenological modelling approach is often used to describe fuel transfer, and the τ-X model proposed by Hires and Overington **[1.1]** for single-point injection (SPI) systems has been successfully used to define fuel compensation schemes which minimise mixture excursions in MPI systems **[1.2]**. In addition to the photographic work, Chapter 4 of this thesis presents and compares values for the parameters τ and X produced by the different injectors during warm-up conditions. Various attempts have been made at identifying the mechanisms inherent in this fuel transport process, although very little work on firing engine conditions has been reported

in the literature, and the lack of understanding of which factors most influence τ and X remains a limitation on the ability to predict fuel transfer behaviour.

The mechanisms by which fuel leaves the films on the inlet port surfaces not only affect the rate at which it is transferred, but also determine the quality of mixture preparation. The short time available for mixture preparation when MPI systems are used, and the potentially adverse effects this has on the homogeneity of the induced mixture, have already been mentioned. It is well known that raising the surface temperature of the intake port ameliorates these problems, purportedly by raising heat transfer to fuel deposited on the surfaces and thereby promoting evaporation. Most attempts to understand the processes involved have been based on experiments carried out on non-firing engines or bench rigs **[1.3, 1.4, 1.5]**, or on computational model predictions **[1.6, 1.7, 1.8]**, and there is little direct experimental evidence from work on firing engines to support the inferences drawn. The direction and magnitude of heat exchange between fuel, the port surface, and air and any combustion products entering the intake port during periods of reversed flow from the cylinder depend upon a number of factors. The investigation of these processes and their relative importance in a firing engine has been the main aim of the studies described throughout the rest of this thesis. The focus of the experimental work has been the measurement of heat exchange phenomena at the surface of the intake port, using heat flux sensors bonded to this surface.

Heat transfer measurements were made around the inlet port surfaces of a firing, four-valve, port-injected engine, using Rhopoint "Micro-Foil" heat flux sensors. The fuel distribution patterns established by the photographic investigation were used to identify areas where fuel deposition occurred. Heat flux sensors were then fitted inside the port to measure heat transfer through the port walls at points within and around these areas. The surface heat flux sensors used have a response time constant which is too slow to accurately resolve heat transfer variations within an engine cycle. However, using data from dynamic calibration experiments together with a model of the sensor, the raw output signal characteristics can be processed to derive instantaneous heat transfer information. This has enabled details of variations in these instantaneous heat transfer values to be

determined and related to events occurring within an engine cycle. Later in this thesis, the signal processing technique is described and results for intra-cycle heat transfer variations are presented. To separate the effects of fuel deposition and gas flow on heat transfer, complementary tests were carried out with fuel injection into one branch of the bifurcated port, while heat transfer measurements were made in the second. The dry-surface heat transfer rates were subtracted from values measured when the sensors were wetted by fuel to determine the effect of the latter. The effects of both gas flows and fuel deposition depend upon engine operating conditions and fuel injection details, and the importance of the results to improving mixture preparation and fuel transfer processes are described.

Besides the intra-cycle variations, values of heat transfer per cycle to deposited fuel have been derived by integrating intra-cycle heat flux variations around the cycle. Since the heat flux data were essentially periodic with a period of one engine cycle, the integrated values were independent of sensor dynamic response characteristics. These heat transfer measurements were processed for a range of engine operating conditions covering warm-up and fully-warm engine states. During warm-up, increases in coolant temperature led to corresponding increases in heat transfer, and for a given coolant temperature heat transfer values generally increased when manifold absolute pressure (MAP) was lowered or as the supplied fuel flow rate increased. In general, the effect of fuel deposition on heat transfer rate, when running on pump-grade unleaded gasoline, could be characterized as a function of injected fuel flow rate, MAP, and engine coolant temperature or surface temperature. This function reflects the underlying mechanisms of vaporisation and convective mass transfer from the surface film. However, the extent to which these characteristics were dependent on the properties of the fuel used was less clear, and to clarify this further work was undertaken using a single-component fuel, 2-2-4 trimethylpentane (isooctane), for which thermodynamic property values are known.

The heat transfer measurements with pump-grade unleaded gasoline were made using a similar range of injector types to that used in the photographic work, allowing the distribution patterns of these to be compared. The isooctane test work was carried out with a single-spray, single-pintle injector fitted. The photographic work had shown that

this injector type delivered fuel in a cone which impinged on the central bifurcation of the intake port. This deflected the spray partly on to the lower surface of the intake port and partly on to the back of the two intake valves. Of the fuel deflected down on to the port surface, the highest proportion was invariably deposited onto a sensor located close to the intake valves, which is why the single-spray injector was selected for the isooctane tests. In the work with isooctane the analysis has been based on results taken from this sensor.

Chapter 2
Literature Survey

2.1 Introduction

In Chapter 1 it was noted that the introduction of port fuel injection systems, the requirement to reduce emissions of pollutants, and the demand for improved engine drivability have stimulated much research into fuel transport and mixture preparation in the intake port. Much of the research has concentrated on characterising the fuel transport process for mixture control purposes, without looking at the detailed aspects of the physical mechanisms involved. Generally, the more detailed investigations carried out have also used modelling approaches, based on assumptions drawn from observing how an engine responds to changes in operating conditions. Very little of the research has concentrated on measurements of events within the inlet port of a running engine.

This chapter provides some background on the most recent of these developments in the study of fuel injection and mixture preparation in S.I. engines.

2.2 Port Fuel Injection

Aquino **[2.1]**, Hires and Overington **[2.2]** and Boam et al **[2.3]** describe studies of fuel transport in the intake manifold of engines fitted with single-point injection (SPI) systems. Such systems consist of one, centrally located injector to meter fuel into the intake in place of the carburettor, and provide micro-processor control of the fuel supply, which reduces but does not remove engine response delays during throttle transients. Aquino **[2.1]** identified these delays as being due to fuel lag caused by wall wetting, manifold air charging, injector phasing, and sensor and calculation delays. During transient operation these delays cause AFR excursions away from the desired operating conditions. In the worst case, such excursions cause misfires and poor vehicle drivability, but they also have consequences for the use of 3-way catalytic convertors: during an

excursion the catalyst will not operate at its most efficient and may even be damaged. Servati and Herman **[2.4]** identify the deposition of fuel on induction system walls as creating the main contribution to non-steady-state AFR control problems, even when multi-point injection (MPI) systems are used. MPI systems, like those discussed by Boam et al **[2.5]** and Nogi et al **[2.6]**, aim to minimise the size of the deposited fuel films by using a set of injectors, one situated close to the intake valves on each cylinder. Of course, increasing the number of injectors within the system increases its cost, but as noted by Shayler et al **[2.7]** this is offset by the performance and control advantages; besides which, efforts on the part of manufacturers to reduce these costs mean that multi-point injector systems now dominate the market place. MPI systems offered the further advantage identified by Neußer et al **[2.8]**, of allowing design possibilities in the intake system geometry not available with SPI systems; in SPI systems the design of the intake manifold is still constrained by the need to deliver a balanced mixture to every cylinder from a central supply point.

2.3 Detailed Investigations of Mixture Preparation

Rose et al **[2.9]** describe how, under steady-state conditions, a stable fuel film is produced in the inlet port by an MPI system, as a balance is set up between the amount of fuel impinging on the surfaces and the amount leaving. The size of this stable film depends on engine load, with higher loads resulting in thicker films because of the increased fuel flow required to maintain stoichiometric in-cylinder AFR's. Servati and Herman **[2.4]** note that this fuel film acts as a sink during accelerations, as increasing load leads to an increasing film mass, and as a fuel source during decelerations, when the fuel film mass decreases. These film mass variations result in the characteristic lean and rich AFR excursions observed during accelerations and decelerations respectively. Development of effective fuel control strategies, such as that described by Shayler et al **[2.10]**, requires further information on the processes involved in these dynamics.

Boam and Finlay **[2.11]** highlight the complexity of these mixture preparation processes when considering fuel evaporation in the intake system of a carburetted engine. In developing a computer model of this evaporation, they identify the processes involved as simultaneous heat, mass and momentum transfer between highly turbulent pulsating air flows and liquid fuel. They model liquid fuel existing in two states within the system: as droplets entrained in the air flow and as a multicomponent liquid film flowing on the walls. A similar approach was taken by Servati and Yuen **[2.12]** and Maroteaux and Thelliez **[2.13]**, who describe the flows through the inlet port as a mixture of phases: a gaseous phase of air and fuel vapour, a dispersed phase containing the fuel droplet population, and a continuous phase in the flowing fuel film. Chen et al **[2.14]** apply these ideas to mixture preparation with an MPI system, where the AFR excursions are explained by the difference in the response times of the three phases to a change in air flow rate.

2.3.1 Production of a Homogeneous Mixture

Minimisation of fuel films within the inlet manifold is not the only concern for designers of modern fuel supply systems. Other requirements, indicated by several authors **[2.7, 2.15, 2.16, 2.17, 2.18]**, include the need to reduce raw emissions; reduce cyclic variations; improve start-ups and warm-ups; conserve catalyst life; and minimise emission levels prior to catalyst light-off. Realisation of all these aims is aided by the production of a homogeneous air and fuel mixture within the cylinder at the time of combustion. Nogi et al **[2.6]** and Shayler et al **[2.7]** note, however, that the reduced distance between injectors and intake valves in an MPI system means that there is only a short period during which mixture preparation can take place. Often, this leads to fuel entering the cylinder in liquid form and causing non-uniform mixing. Shayler et al **[2.7]** and Takemura et al **[2.19]** characterise this heterogeneity as a combination of well mixed fuel vapour and air, which has an AFR lean of the overall value, with zones of rich mixture around vaporising fuel and liquid droplets. Several different approaches have been adopted in trying to quantify the extent to which this division of the mixture occurs, and to establish how the mixture quality is affected by changes in various engine parameters.

Miller and Nightingale **[2.20]** developed two "air-flow simulation" rigs that allowed measurements to be made of the mixture preparation characteristics of an MPI fuelling system, whilst avoiding some of the problems encountered with engine based measurements. These rigs allowed them to measure the size of suspended fuel droplets in the intake system and the proportion of the injected fuel which entered the cylinder as a wall-film, over a range of conditions. By making comparisons between an MPI system and a carburetted system they found that at high loads comparable fuel droplet sizes were produced by both. As the load was decreased the carburettor produced finer fuel atomization than port-injection and this led to reduced proportions of fuel being induced as a wall-film, leading them to conclude that drastic improvements can be made to the in-cylinder mixture quality by providing good mixture preparation upstream of the valves. Their tests were only carried out at ambient temperatures providing no indication of how the effects vary with temperature, although they argue that this provides useful information about cold-start conditions when the problems associated with mixture inhomogeneity are greatest. Unfortunately, the use of bench-rig rather than engine-based measurements meant that the port thermal environment would not be that of a running engine, where the effects of backflows from the cylinder are significant **[2.15]**.

One of the problems with making engine-based measurements of mixture preparation, identified by Miller and Nightingale **[2.20]**, is that often the instrumentation techniques will disturb flow phenomena important to the process. A solution is offered by taking non-invasive measurements of the engine emissions and inferring the quality of mixture preparation from these **[2.7, 2.17, 2.19]**. Shayler et al **[2.7]** compared the effects on emissions of varying injector type and orientation under fully-warm operating conditions. They found that the effects of these variations on emissions were secondary to the effects of mixture ratio and this made the results difficult to interpret, although they were able to establish a link between emissions levels and mixture inhomogeneity. Similar measurements were undertaken by Takemura et al **[2.19]**, again under fully-warm operating conditions, when looking at the effects of intake port turbulence on fuel/air mixing. They developed two theoretical models to help explain their results in terms of mixture preparation quality: a "Zone Separation Model" and a "Statistical Distribution

Model". In the Zone Separation Model, the above description of in-cylinder heterogeneity was simplified and applied directly by assuming that the mixture could be considered as a series of separated zones of air, fuel and mixture. They set-up combustion equations accordingly to predict the resultant emissions levels and compared these with results from the, perhaps more realistic, Statistical Distribution Model, where varying AFR's throughout the mixture were accounted for by considering the local AFR to be distributed statistically with spatial continuity. They found that both models produced similar results and, therefore, adopted the simpler Zone Separation Model to define an index representing the mixing uniformity, based on measurements of emissions levels.

The test technique used by Daniels and Evers **[2.17]** combined careful control of mixture preparation in the intake system with measurements of the resultant emissions levels and combustion characteristics. They evaluated the individual effects of fuel vapour, droplets and liquid streams on steady-state performance and emissions, finding that IMEP, COV, HC and O_2 were affected most significantly. Generally, engine performance was diminished and HC emissions were increased by increasing the amount of fuel in liquid streams, adding credence to the hypothesis that it is important to maximise in-cylinder homogeneity and minimise the amount of fuel induced as a liquid.

Another unique approach was adopted by Takeda et al **[2.18]**, using the test equipment described by Saito et al **[2.21]**. For this, an engine was specially adapted to have electronically controlled, hydraulically driven intake and exhaust valves, with an additional "intake shutter" valve in the port upstream of the injector. Using these valves, they were able to instantaneously stop the engine and isolate the intake port and combustion chamber at various times during firing operation, hence containing the fuel remaining in these two parts of the system. They then used heated purge air to completely vaporise the trapped fuel and measured the resultant HC concentrations with a Flame Ionisation Detector (FID) to ascertain the quantities of fuel involved. By making these measurements at various points around the engine cycle they were able to build up quantitative data for the proportions of injected fuel involved in the various processes occurring: port-wall wetting, cylinder-wall wetting, combustion and exhausted HC's.

Takeda et al **[2.18]** collected this data at different points throughout a warm-up, but concentrated on the first few cycles after start-up where the problems of mixture inhomogeneity have already been identified as acute **[2.20]**. They found that during a cold-start most of the injected fuel adheres to the intake port and cylinder walls and is carried over to the next cycle, making AFR control difficult and resulting in high engine-out HC emissions. Intake port wall-wetting continued to increase, rising to a peak at around the 300th cycle, after which it decreased gradually as the engine warmed up, whereas cylinder wall-wetting decreased gradually after start-up, engine out HC emissions being more closely related to the latter. Injection timing, fuel quality and injector spray characteristics were all found to influence these observed trends. Adjusting injection timing during the first cycle affected the relative proportions of fuel adhering to the inlet port and cylinder walls. Injecting while the valves were open increased cylinder wall-wetting, while closed-valve injection increased port wall-wetting. They examined the effects of fuel quality by comparing results from fuels with different 50% distillation temperatures. Reducing the fuel's volatility increased the amount required for stable combustion, created greater wetting of all walls, and increased engine-out HC emissions throughout the warm-up. Conversely, increasing the atomization in the injector spray reduced all these parameters.

2.3.2 Formation of Fuel Films & Droplet Behaviour

It is clear from the work reviewed so far that there are two requirements in the design of a fuel injection system: minimisation of inlet port fuel films and vaporisation of injected fuel to create a homogeneous in-cylinder mixture at the time of combustion. At first, these two requirements appear to be mutually exclusive in an MPI system, since, as noted by Shayler et al **[2.7]** and Miller and Nightingale **[2.20]**, complete vaporisation of the fuel requires extended port residence time, which in turn implies increased inlet port fuel films with associated transient response problems. Various strategies have been suggested for avoiding this conflict, but they can be summarised in two basic categories: targeting of the injector spray and increasing injector atomization.

Targeting the spray of fuel from the injectors onto specific areas within the port helps in the realisation of both requirements for a fuel delivery system **[2.20, 2.22, 2.23]**. It helps to minimise the port fuel film by ensuring that the area over which fuel lands is small, particularly avoiding the bifurcation web in a 4-valve engine **[2.5, 2.23]**. Martins and Finlay **[2.22]** and Iwata et al **[2.23]** also found that directing fuel at the hottest part of the port, the back of the valves, improved in-cylinder homogeneity by increasing the rate at which the fuel is vaporised. Iwata et al **[2.23]** describe the development of a twin-spray injector designed to avoid the bifurcation web and produce good targeting of the fuel on the back of the valves, simply by attaching a two-hole adaptor to a "hole-type" injector. Ford Motor Company now use a similar twin-spray injector, constructed by fitting a two-hole adaptor to a single-pintle single-spray injector, in many of their current production instalments of the Zetec engine.

Iwata et al **[2.23]** suggest that minimisation of wall-wetting is the most important consideration in the design of a port fuel injector, since better AFR control means that a three-way catalytic convertor can be used at its most efficient, removing the engine-out emissions and thereby compensating for any loss in mixture preparation quality. Unfortunately, however, this conclusion is based upon evidence from fully-warm tests, whereas it is in the first few seconds before catalyst light-up when the most significant emissions levels occur. Both Neußer et al **[2.8]** and Miller and Nightingale **[2.20]**, therefore, highlight the importance of optimising injector spray atomization in the design of MPI systems. Although MPI systems provide better cylinder-to-cylinder control of mixture strength, they tend to produce a less well mixed charge than their SPI forerunners. SPI systems utilised the high flow velocities and low pressures within the throttle body, where the injector was generally situated, to break the supplied fuel into a very fine spray. This improved in-cylinder homogeneity by providing for fuel that entered the cylinder without being deposited on the port walls to be in a form that was easily vaporised. With an MPI system there is a lower relative velocity between the injection spray and the air flow, and the shorter distances in which atomization can occur mean that the fuel must be broken up through careful injector design. In pursuit of this, four-hole injectors have been developed, such as those described by Zhao et al **[2.24]**, which use a "director-plate"

assembly in the injector tip to break the spray up before passing it through four holes arranged in such a way as to produce two separate sprays. A direct comparison between this and two other types of injector (a single-pintle single-spray and a single-pintle twin-spray) was offered by Shayler et al **[2.25]**. Using the variation of HC and CO during a warm-up as an indicator, they found that of these injector types the four-hole injector gave the best mixture preparation, followed by the twin-spray, the lowest quality being given by the single-spray injector despite apparently producing greater atomization of the fuel than the twin-spray. A similar ranking occurred in the results of transient response tests with the three injector types. By modelling the interaction between fuel droplets and the air flow, Nogi et al **[2.6]** found that improved fuel spray atomization also had some effect on fuel deposition. Small droplets, they inferred, are more likely to be vaporised before deposition, and when deposited will evaporate from the port surface more quickly, a conclusion which they support with experimental data. Further reductions in fuel film deposition can be achieved by injecting during the period when the valves are open **[2.6, 2.26]**, when the injected fuel will be carried straight into the cylinder by the air flow. When using this strategy good atomization is very important; not only do the fuel droplets need to be small to ensure that they can be carried around the valve heads **[2.6]**, but they also need to be vaporised quickly within the cylinder if HC emissions are not to be increased through poor mixture homogeneity. Harada et al **[2.26]** found that this level of atomization could be achieved using an air-assisted twin-spray injector, although their reported tests are for coolant temperatures of 40°C, well above the cold-start temperatures at which problems of in-cylinder heterogeneity are greatest. This type of injector is also less attractive to manufacturers, since it requires an air-supply to the injectors which increases the cost of the fuel supply system.

In addition to the effects of injector design and targeting, fuel film formation and droplet behaviour are likely to be influenced by injector location and engine operating conditions, effects which have been investigated by several authors. When they looked at the effects of injector type, location and orientation on mixture preparation, Shayler et al **[2.7]** found that the influence of improvements in fuel spray atomization were more noticeable when the injector was situated closer to valves. They suggest, however, that the effects of these

parameters were not as important as obtaining the correct calibration for the engine, since calibration changes of 1 AFR had a greater effect on emissions than installation detail changes within the range of options available. In their analysis of fuel sprays, Nogi et al **[2.6]** found that manifold pressure affected the spray pattern from injectors; as pressure was reduced the inferred spray angle decreased until low pressures, around 0.2 bar, when the increased production of vapour around the spray caused it to spread out. They also found that MAP affected the experimentally measured HC levels, which decreased at lower MAP's, and they attributed this to the lower fuel flow rates as well as the lower pressures making vaporisation easier. The inferred effect of increasing speed on mixture preparation was to enhance the atomization of fuel that had adhered to the intake valve surface and could not be completely vaporised. Saito et al **[2.21]** used video and photographic techniques to make inlet port observations of injected fuel behaviour from twin-spray and air-assisted twin-spray injectors in a 4-valve engine. They used two manifold pressures (0.47 bar and 0.95 bar) and two coolant temperatures (30°C and 80°C) to provide comparisons at different operating conditions. At the lower manifold pressure and coolant temperature the twin-spray injector produced a narrow "pencil stream", and fuel spray hitting the walls formed a liquid stream which flowed into combustion chamber as the valves opened. At the higher temperature fuel landing on the walls vaporised and could be seen as "white smoke" (sic) above the valves, again flowing into the combustion chamber when the valves opened. Using valve-open injection at these conditions the fuel apparently flowed directly into the combustion chamber without vaporisation. Running at the higher MAP condition, with a coolant temperature of 30°C and closed-valve injection, fuel droplets in the spray were smaller, which, they suggest, is due to them being crushed by the higher air density. The air-assisted injectors atomised the spray and spread it out. Too much spreading would increase wall-wetting and, therefore, they concluded that it is important to optimise injection timing, spray spread, spray direction and the shape of the intake ports when using such injectors. Iwata et al **[2.23]** and Harada et al **[2.26]** also used photographic techniques to establish the spray characteristics of different injector types. Harada et al **[2.26]**, like Saito et al **[2.21]**, took pictures of the wall-wetting effects of twin-spray and air-assisted twin-spray injectors in situ, while Iwata et al **[2.23]** used an evacuated bench-rig to provide conditions replicating

the lower manifold pressures whilst making it easier to photograph injector spray patterns directly. The work of Iwata et al **[2.23]** included measurements of the droplet diameters within the spray, measurements which were also taken by Miller and Nightingale **[2.20]** who were fairly sceptical about the results being used as anything other than a comparative tool.

2.3.3 Fuel Transfer from the Fuel Film

Acknowledging that it is very difficult to totally eliminate deposited fuel films from the inlet port walls has created a great deal of interest in the mechanisms by which fuel is transferred from these films into the engine cylinder. The views of Martins and Finlay **[2.22]** and Iwata et al **[2.23]** have already been noted on the need to ensure that fuel deposition occurs in hot areas of the port where vaporisation of the fuel will be quicker. Miller and Nightingale **[2.20]** point out, that it is difficult to achieve the sort of vaporisation necessary within the inlet port when the engine is cold. Strategic heating of affected parts of the intake system, as suggested by Neußer et al **[2.8]**, can be used to improve this but may lead to some loss of volumetric efficiency as the engine warms up. Vaporisation is not, however, the only mechanism by which fuel transfer can occur. Aquino **[2.1]** identifies two other possible mechanisms: wall film-flow and re-entrainment of fuel as droplets seeded from the film surface by turbulence in the port gas flows, as described by Takemura et al **[2.19]**. Aquino **[2.1]** concludes that, in an engine fitted with an SPI system, at low temperatures a significant proportion of the deposited fuel will be transferred by wall film-flow, but this proportion decreases as coolant temperature increases. He also highlights the multi-component nature of gasoline fuel and the influence this will have on fuel vaporisation, with events within the intake system being too quick for equilibrium vaporisation to occur. This theme is developed by Servati and Herman **[2.4]** who, when looking at a port-injected engine, further subdivide the vaporisation process into "conductive vaporisation" of the lighter fuel fractions through heat transfer from the higher temperature port walls, and "convective vaporisation" of the heavier fractions as the induced air flows over the film.

Cheng et al **[2.15]** emphasise the importance of the thermal environment within the inlet port on these vaporisation processes, and highlight the need to understand the influence of the flow phenomena which form a large part of this thermal environment: overlap backflow during the valve-overlap period; forward induction flow while the inlet valves are open; and displacement backflow after the piston has passed BDC and before IVC. Their measurements of these phenomena show that they are particularly significant at part load when combustion and emissions issues are critical. Using Fast FID measurements within the inlet port, they found that injection timing influences fuel vaporisation and mixing and used 4 different injection timings to study these effects:

(a) *Injection when the inlet valves are closed, stopping shortly before the valves open*: this gave a short fuel residence time before the overlap backflow broke-up and vaporised the liquid film around the valve seat pushing fuel vapour into the inlet port. The forward induction flow then swept this vaporised fuel into the cylinder, after which the displacement backflow pushed some of the in-cylinder mixture back into the inlet port. While the inlet valves were closed HC levels within the inlet port steadily increased as fuel still in the surface film evaporated and diffused through the port.

(b) *Injection shortly after inlet valve closes*: this gave a relatively long fuel residence time in the port allowing more vaporization to take place before the valves opened, creating a build up of fuel vapour.

(c) *Injection during the inlet valve-open period*: with this injection timing backflows of in-cylinder gas would have minimum impact on fuel behaviour. Correspondingly, less fuel vapour was detected in the port during the valve-closed period.

(d) *Injection during displacement backflow period*: from the results with this injection timing they were able to infer that more fuel was deposited on the walls than in case (c) but less than in case (a).

2.4 Summary and Conclusions

Interest in fuel transport and mixture preparation in port-injected spark ignition engines is reflected in the body of literature published on the subject in recent years. This survey provides a representative picture of contemporary research, the theories that have been developed around the subject, and the hardware developments these have led to. The development of fuel delivery systems can be traced from the original carburetted systems, through single, central-point injection to the modern multi-point, port-injected systems. Some of the detailed investigations of mixture preparation using MPI systems have then been reviewed, looking particularly at the influence of fuel delivery system parameters on transient response and in-cylinder mixture quality. These have included consideration of fuel spray quality, fuel deposition and fuel transfer from these deposited films.

Generally, the main qualities looked for in an MPI system are the ability to minimise wall-wetting, which reduces transient response problems, while creating a homogenous in-cylinder mixture of air and fuel, to create the conditions necessary for good combustion and low engine-out emissions. Most of the literature seems to concur with the idea that this is best achieved by targeting well-atomised fuel sprays at the back of the inlet valves where any fuel that is deposited will be vaporised quickly by the higher temperatures on the valve surfaces. This is the ideal, however, and in reality it is recognised that the design of injection systems requires a compromise between fuel atomization, which tends to create a more diffuse spray, and targeting the spray on the required part of the intake port. This compromise is affected by changes in operating conditions, particularly engine temperature and load, the effects of the latter being through changes in both manifold pressure and fuel flow rate. In addition, the cost of systems and their practicality are issues for manufacturers who are keen to gain competitive advantage by minimising the unit cost of vehicles. The injection system cannot, therefore, be considered in isolation: decisions about injector design must be taken in conjunction with decisions about fuelling strategy, particularly injection timing; intake system design; and the strategies used for removing engine-out emissions such as 3-way catalytic convertors.

Chapter 3
Test Facilities

3.1 Introduction

Investigations of heat transfer and fuel transport in the inlet port of a standard, four-cylinder, spark-ignition engine are fraught with problems: access to the ports for instrumentation is difficult, as are making changes to the engine configuration, while events in the other inlet ports may affect conditions in the port being studied, adding complexity to the results. For these reasons, the work for this thesis, like the similar study of intake port phenomena made by Cheng et al **[3.1]**, has been carried out on a single-cylinder research engine. This chapter describes the single-cylinder rig which has been developed at Nottingham. Based around a Ricardo "Hydra" engine, it is mated to a McClure motor regenerator unit providing power absorption and motoring facilities which allow the engine to be run at a constant speed. It also has facilities for cooling the engine to below ambient temperatures.

Initially instrumented with various general engine monitoring equipment, as the work on the engine progressed, more specific instrumentation was fitted for measuring heat fluxes and temperatures within the inlet port. The set-up of the rig, its monitoring, and the data acquisition systems used reflect the objectives for the rig, both in the work described in this thesis and in future research projects: detailed studies of cycle-by-cycle events and general operating condition trends with different engine configurations.

3.2 The Single-Cylinder Rig

The engine is a Ricardo "Hydra" Research Engine, a single-cylinder engine, "capable of operating at conditions representative of modern automobile and light commercial vehicle engines" **[3.2]**. Like its mythical namesake **[3.3]**, the Hydra has many heads, being designed to accommodate a variety of cylinder head configurations. In this particular case, the piston and cylinder head from a 1.8 litre, high output, Ford Zetec engine were used. Figure 3.1 shows a diagram of the engine and its control systems.

3.2.1 Construction

The main problem with a single-cylinder rig is the high aural noise levels it produces in comparison with a four-cylinder engine. These result from two main sources:

(i) Harmonics set up, particularly within the exhaust system, by the pulsating gas flows. To minimise the noise created within the exhaust system various silencer configurations were tested. The arrangement that was finally adopted, consisted of a spark arrestor and light truck silencer coupled in series and mounted on vibration absorbing rubber mounts. The exhaust gases are passed to atmosphere through a fan assisted extraction system.

(ii) Having only one cylinder makes the engine less balanced when running creating vibrational problems, especially at the engine's resonant frequencies. To minimise the vibrational effects the engine is fitted to an anti-vibration bed; this consists of a seismic mass attached to a base pedestal by rubber mounts, which are designed to absorb the vibrations.

3.2.2 Engine Management

To control the spark and fuel injection timing the standard Ford engine control system is used, with suitable modifications made to the control strategy for single-cylinder

operation. This system does not, however, control the fuelling level successfully. Instead, the injector firing pulses produced by the engine management system trigger a PC-based timer/counter board. This creates an injector firing signal, with its length set by the PC, which fires the injectors through a MOSFET injector driver circuit.

3.2.3 Engine Services and Connections

Temperature control of oil and coolant passing through the engine is obtained using heat exchangers in the respective circuits. The cold sides of both exchangers are connected in parallel either to a total loss cooling system, for warm running, or to a chiller, allowing forced cooling of the engine to temperatures below the ambient temperature. Flow from these cooling sources is controlled by solenoid valves linked to PID (proportional, integral and differential) temperature controllers; these monitor the temperatures of engine oil and coolant through thermocouples fitted in the sump and coolant header tank. One of the benefits realised from the use of a single-cylinder engine is its greater thermal inertia, resulting in a much slower warm up. This is useful when observing changes of inlet port characteristics with engine temperature, but it means that as the Hydra reaches higher temperatures the warm-up becomes very slow, so an oil heater is fitted in the sump to increase the warm-up rate under these conditions. A stepper motor connected to the engine throttle controls air flow into the engine. A calibrated measurement of MAP records the rate of this air flow at a given throttle position and engine speed.

3.3 General Instrumentation

In addition to the instrumentation fitted to the engine as part of its control systems, supplementary instrumentation was provided to give further engine monitoring information and data for experimental work. K-type thermocouples were fitted in the air intake manifold, the fuel rail, the engine coolant passages and the exhaust system. The operating AFR was monitored using a Universal Exhaust Gas Oxygen (UEGO) Sensor fitted in the exhaust pipe and connected to a Horiba Mexa-110λ meter. Cylinder pressure was measured using a piezoelectric pressure transducer connected to a Kistler charge

amplifier. During initial tests with the engine to establish that it was performing correctly through comparison with results produced by a four-cylinder Ford Zetec engine of the same type, data was collected from the sensors using a PC based data acquisition system capable of recording crank-angle resolved data. Later tests required measurements of higher sensitivity than were possible with this PC based system, for which an alternative, self-contained data-logger was used.

3.4 Heat Flux Sensors

Initial tests with the engine used the same methods as Shayler et al **[3.4]** to measure the parameters for the τ and X model of the fuel transport process (this model was introduced in Chapter 1, and is described in more detail in Chapter 4). To study the mechanisms by which this process takes place in more detail, Rhopoint 'Micro-Foil' sensors were used to measure heat flux at various locations around the intake port surfaces. These sensors consist of two arrays of thermocouple junctions either side of a thermal barrier (see Figure 3.2). Heat transfer through the surface to which the sensor is attached sets up a temperature difference across the barrier producing a voltage difference between the two thermocouple arrays. This voltage difference is calibrated for heat flux at the temperature measured by a 'T' type thermocouple also incorporated in the sensor, with positive heat fluxes indicating a flow out of the port walls and vice versa for negative values.

Figure 3.3 shows the positioning of the sensors around the port surfaces. The locations of the sensors were chosen on the evidence of preliminary tests to provide information on the variety of conditions that arise. The number and arrangement of sensors was limited by the space available within the port and the desire to minimise changes to the port surface conditions. Sensors 1, 2 and 3 were positioned at points which remain dry under most conditions; Sensors 4 and 7 were on the floor of the port where most fuel deposition occurs; Sensor 5 detected any fuel deposition on the web; Sensors 6 and 8 were positioned near the valves where the effects of residual gas backflows are greatest. In each case, the leads from the sensors were laid in grooves cut in the port surface and covered in epoxy resin to restore the port profile. The injector was located in the aperture

through the manifold flange shown in Figure 3.3. The position of the injector tip is indicated.

Along with the heat flux sensors, four fast-response, "K" type thermocouples were fitted around the inlet port, to measure cycle-averaged gas and surface temperatures. Figure 3.4(a) shows the positioning of these. Like the heat flux sensor leads, the sheath of each thermocouple was buried beneath the port surface to minimise variations in the port profile. The tips of TC 1 and TC 2 were bent away from the side of the port (see Figure 3.4(b)) to provide the gas temperature measurements. TC 3 and TC 4 were embedded into epoxy resin to provide surface temperature measurements in the same region as Sensors 6 and 7 measured heat fluxes. At all conditions, these two thermocouples recorded higher temperatures than the thermocouples incorporated into Sensors 6 and 7; therefore, they were used for the surface temperature measurements associated with these two sensors. In earlier tests, more thermocouples were arrayed around the port surface but these had shown that for the other sensors the spatial variation of surface temperature was not as great, and the thermocouple incorporated in the sensor was sufficient to measure local surface temperature. Once the heat flux sensors and thermocouples were fitted, repeat tests were carried out to establish τ and X parameters for the port with this new configuration. They showed that the fuel transfer characteristics had not been altered significantly.

A Campbell Scientific 21X Data-Logger was used to record the μV signal levels produced by both the heat flux sensors and the thermocouples at data acquisition rates of up to 1 kHz; this provided crank-angle resolution in the heat flux data. Once recorded, the data was down-loaded to a PC through an RS-232 connection. The measured sensor temperatures remained effectively constant around the cycle and Figures 3.5(a) and (b) show typical traces derived from μV measurements with two of the heat flux sensors, the values quoted being based on the mean of ten consecutive cycles. Each set of traces includes mean, maximum, minimum and standard deviation results. The heat flux data shown in Figure 3.5(a), for Sensor 7, are far more variable than those shown in Figure 3.5(b), for Sensor 5. This has been attributed to the higher concentration of fuel

landing on Sensor 7, a trend repeated throughout measurements from other sensors, greater variability being found in data from those sensors most affected by fuel.

After processing the data to give crank-angle resolved heat fluxes it could be integrated around each cycle to give a value for the total heat transfer per cycle in J/m^2. In this way the data could be presented in a more compact form, allowing comparisons to be made between the heat transfers recorded from the different positions within the port over a range of operating conditions.

The conventions adopted throughout the rest of this thesis are that heat transfer from the surface towards the gas stream is positive, heat flux denotes the heat transfer rate per unit area, and heat transfer per cycle values are also referred to unit area of surface.

Chapter 4

Fuel Spray and Mixture Preparation Characteristics

4.1 Introduction

Stringent regulations on the emission of pollutants **[4.1]** and the demand from consumers for good vehicle drivability and fuel economy have stimulated research into mixture preparation in spark ignition engines. Much of this research has concentrated upon the fuel transfer process and the associated response of the engine during transient operating conditions, although the mixture preparation quality also directly influences engine performance, efficiency and emissions levels. These effects are not only governed by engine operating conditions but also, in engines with port fuel injection, by the fuel distribution pattern that the injector produces, the behaviour of fuel on the inlet port surfaces, and the resultant quality of mixture preparation as the charge is induced. A study of the relative merits of various injector types must be undertaken as part of the design process for an engine, particularly since there are many variables involved in the design of an engine's induction system of which injector selection is only one.

Figure 4.1 shows a typical interpretation of what happens to fuel between injection and its entry into the combustion chamber **[4.2]**. It is generally accepted that to achieve the best engine performance and efficiency, and the lowest emissions levels, a homogeneous in-cylinder fuel and air mixture is needed for good combustion characteristics, with a minimum of fuel deposition in the inlet port to improve transient response. However, it is not easy to satisfy these two requirements in the design of a single injector. To minimise fuel deposition requires an injector with a narrow cone angle (see Figure 4.2) which targets fuel at the inlet valves **[4.3, 4.4, 4.5]**, while production of a homogeneous in-cylinder mixture needs a finely atomised injection spray **[4.6, 4.7, 4.8]**. A solution suggested by many authors **[4.9, 4.10, 4.11]** is to use an air-assisted injector, which combines fine spray atomization for mixture homogeneity with higher forward momentum

to minimise deposition; however, the increased complexity and unit costs of such a system make this expensive and the accruing performance improvements are not always large. This chapter describes some photographic work undertaken to establish the fuel-spray characteristics of four different injector types, when used in conjunction with the cylinder head of the Ford, Zetec engine. The injector types, chosen to give a range of characteristics, were: a pencil beam injector; a single-pintle, single-spray injector; a single-pintle, twin-spray injector; and a four-hole, diffuser-plate injector. The photographs recorded fuel injection into the intake port for each injector type, with the engine running. From these, a series of diagrams of the observed spray patterns was produced.

In addition to the photographic work, measurements were made of the AFR response of the system to fuel perturbations using the same injector types. By processing these data, values can be found for parameters in a well-established model of the fuel transfer process. The model was first proposed by Hires and Overington **[4.12]** and Aquino **[4.13]**, to model fuel transfer in central-point injection systems. This was based on observations **[4.14, 4.15]** that some of the fuel entering the inlet manifold creates a fuel film on the manifold and port surfaces, delaying its induction into the engine. Two parameters, τ and X, are defined in the model; X represents the fraction of injected fuel initially deposited on the surfaces of the intake port and valves creating a first-order lag in the system, and τ is the time constant for fuel transfer from this deposited film. The rate of transfer from the film is assumed to be proportional to the film mass and inversely proportional to τ. In multi-point injection systems, the proximity of the injectors to the inlet valves means that these films are less extensive. For control purposes, though, Hires, Overington and Aquino's model is also widely accepted as a good representation of these systems **[4.16-4.21]** (see Figure 4.3).

Calibration of this parametric model requires a large amount of experimental testing. Much recent work has, therefore, been focused upon defining the best ways of carrying out this testing and building up empirical relationships for τ and X over a range of engine operating conditions. Such work has been carried out at Nottingham University, on a four cylinder engine, by Shayler et al **[4.16]**. The measurements described in this chapter are

an extension to their work, carried out on the single-cylinder rig, in which values for the parameters were established over a range of operating conditions with each injector type. The results of these tests are compared with the visualisation of the injection process produced by the photographic study, and they provide a basis for the heat transfer study described in later chapters.

4.2 Photographic Technique

The photographic work used the flash photography set-up shown in Figure 4.4. The engine was run without the inlet manifold, and therefore effectively at wide-open-throttle conditions, to expose the port area. In most cases it was also run fully-warm, the one exception being a test where the coolant was force cooled to a temperature of 30°C, to allow the effects of colder port walls to be observed. Mixture settings were lean of stoichiometric, to prevent fuel from spraying back out of the ports, and engine speed was maintained nominally at 1000 RPM. The flash trigger point was varied through the engine cycle to produce a sequence of photographic records of injection and deposition conditions covering the main phases of the cycle. Diagrammatic summaries of these records are provided in Figures 4.5-4.9 and the main spray characteristics associated with each of the four injector types investigated are described below.

4.3 Description of Spray Characteristics

4.3.1 Pencil Beam Injector (Figure 4.5)

This injector was originally designed for auxiliary injection into a plenum chamber and produces a poorly atomised, narrow jet of fuel, which is not normally associated with good mixture preparation. However, the jet impinges on the bifurcation web of the port, breaking down into a much finer spray which is deflected onto the port walls. Consequently, the fuel arrives at the valves relatively late in the cycle, when compared to the other injectors. This is evidenced by observations of fuel vapour condensing above

the valves after fuel injection has been completed; for the other injectors this appeared during the injection period.

4.3.2 Single-Pintle, Single-Spray Injector (Figure 4.6)

This injector produced a single spray broken into a conical pattern, with a core of medium sized droplets surrounded by an outer layer of fine droplets. The fine droplets penetrated directly into the ports, while the medium sized droplets hit the bifurcation web, where they were broken into a very fine spray before also travelling on towards the valves.

4.3.3 Single-Pintle, Twin-Spray Injector (Figure 4.7)

A development of the single-spray injector, this injector has a "splitter-cap" fitted to the end, which divides the spray in two. This directed the spray both sides of the intake-port bifurcation. The photographs suggested that it produced the least well atomized spray of the four injector types. The splitter-cap tended to re-coagulate the fuel into larger droplets which it then directed towards the back of the valves. These were not broken up in any way before reaching their destination, producing an accumulation of fuel around the valves as a mixture of droplets, liquid and vapour, a mixture that appears to be far less homogeneous than that created by the other injectors. However, the direction and narrow cone angle of the spray directs fuel deeper into the port.

4.3.4 Four-Hole, Diffuser Plate Injector (Figures 4.8-4.9)

This design, also based on the single-pintle injector, has a four-hole diffuser plate fitted to the end. As for the twin-spray injector, a high proportion of the injected fuel penetrates directly onto the valves, with improved atomization, but also with a wider cone angle which is likely to create greater fuel deposition. Force cooling the engine with this injector fitted (Figure 4.9), resulted in the port filling with condensed vapour. This cleared as the valves went down, although droplets of fuel were seen to break off the valve edges and spray upwards as the valves shut. This phenomenon was not seen under

fully-warm conditions with any injector. It indicates a collection of liquid fuel around the edge of the valve seat, suggesting fuel transfer through a film flow mechanism at lower engine temperatures.

4.4 Measurement of Fuel Transfer Model Parameters

Fuel perturbation and throttle perturbation test procedures are methods of producing AFR measurements from which values of τ and X can be established. Teo **[4.22]** investigated the application of these methods based on the processing of AFR measurements made using a UEGO sensor. He found that the fuel perturbation method was the most effective of the two, so this method was adopted for the work described here. A fuel perturbation is simply a step between two steady state fuelling levels, created by changing the length of time for which each fuel injector is held open during an engine cycle. If these perturbations are carried out whilst keeping all other operating conditions constant, the effect is that of giving a step input to the system. By measuring the response of the engine to such step inputs, it is possible to derive values for the parameters τ and X.

In the tests run for this study, the fuel perturbations used stepped the mixture strength one AFR unit either side of a mean value; at each test point, sufficient repetitions of these steps were made to produce three switches from lean to rich of the mean value, the resultant AFR trace being measured with a UEGO sensor. The data were then processed to give the mean AFR variation produced by the lean-to-rich perturbation. Lean-to-rich fuelling level switches most closely represent the conditions of increasing fuel mass flow rate which occur within the port during an acceleration. They were considered separately from the rich-to-lean perturbations since initial tests indicated that steps in the two directions produced different responses. Accelerations are of greater interest, since suitable fuelling strategies can be developed to add fuel and compensate for the resultant lag in fuel supply; during decelerations the best that can be achieved is to turn off the fuel when the film begins to act as a fuel source. By adjusting the values of τ and X used in the parametric model, modelled AFR traces, which also took account of the UEGO sensor's response characteristics, were fitted to the experimental traces.

The experimental traces were recorded at 10 deg. C steps in coolant temperature during engine warm-ups between 30°C and 80°C, at a speed of 1000 RPM, MAP of 0.79 bar and with a stoichiometric mean AFR. These tests were carried out twice with each of the four injector types used in the photographic study to give an indication of the test repeatability and allow the comparisons between injector types to be made. Figures 4.10-4.12 summarise the results of these tests. Further tests were carried out with the single-spray and twin-spray injectors, over a range of MAP's and mean AFR's. Trends observed in these data have, however, been shown to be inaccurate by recent tests using new techniques for finding values of τ and X **[4.23]**. These inaccuracies are apparently caused by errors in the AFR measurements from the UEGO sensor at extreme operating conditions. At the conditions tested for Figures 4.10-4.12 the effect of these errors is minimal.

Figures 4.10(a)-(d) and 4.11(a)-(d) show the values of τ and X recorded in the initial tests for each of the injectors. Each graph (a)-(d) displays two plots of the mean values from the repeated warm-ups. The mean τ and X values determined for all the injectors are summarised alongside one another in Figures 4.12(a)-(b), where the effects of changing the injector are clearly visible. The low temperature variations in τ and high temperature variations in X with injector type are larger than the variations with most injectors across a warm-up.

4.5 Variations of Fuel Transfer Characteristics with Injector Type

The photographic work and the measurement of the parameters τ and X has shown that there are differences between the fuel transfer characteristics of the four injector types considered. Most of the photographic work could only be carried out under fully warm conditions; direct comparison can, therefore, only be made with the τ and X values derived from data recorded at a coolant temperature of 80°C. Some additional photographs, taken with a force cooled engine, provide possible explanations of the trends apparent in the τ and X values at lower temperatures.

4.5.1 τ Values

Figure 4.12(a) shows that with the engine fully warm, the τ values for most of the injectors are the same. Under these conditions, the main fuel transport mechanism, measured by τ, is normally considered to be evaporation **[4.13, 4.24]**. Accepting this gives an explanation for the convergence of the τ values at higher temperatures, since, if the port surface temperature is uniform, the fuel will evaporate at the same rate regardless of the spray pattern produced by the injector. The slightly higher τ values produced by the pencil beam injector were probably due to the fuel being deflected onto the port walls closer to the injector, which are colder than around the valve seat. Taking this hypothesis further one would expect to find higher τ values from all injectors at lower coolant temperatures, when all of the port surfaces will be colder. Figure 4.12(a) shows this happening, but the values for the different injectors are also seen to diverge. To an extent this will be due to non-uniformity in the port wall surface temperatures interacting with the different spray patterns. This does not, however, give an explanation for the way in which the four hole injector gives by far the highest τ values, or the way the two hole and single pintle values stay so low. To explain this anomaly one needs to look again at the assumptions made about the transfer mechanism.

Monden and Kataoka **[4.25]** found that with a single-point injection system τ consists of two components. These were τ_f, associated with fuel film transfer into the cylinder, and τ_v, due to vaporisation of the fuel film. They are related to τ by the equation:

$$\frac{1}{\tau} = \frac{1}{\tau_v} + \frac{1}{\tau_f} \qquad (4.1)$$

which is analogous to the equation for calculating the total resistance of two electrical resistors connected in parallel. The photographic work indicated that with a force cooled engine some fuel film transfer occurred; this suggested that a similar approach of splitting τ into evaporative and film flow components at lower temperatures might also be adopted with a multi-point injection system. When the engine is fully warm, the discrete nature of the system results in the film flow component of τ being minimised when using closed-valve injection. As observed by Martins and Finlay **[4.5]**, any liquid fuel flowing down to

the valve seat at these conditions evaporates before the induction stage of the engine cycle. At lower coolant temperatures, however, the film flow component becomes far more significant, and acts to reduce the total value of τ recorded, in the same way that connecting one electrical resistor in parallel with another acts to reduce a circuit's total resistance. The extent to which this reduction occurs is dependant upon the injector spray pattern. Indeed, a correlation can be seen between the spray patterns observed in the fully warmed up engine and the τ values recorded at lower temperatures. The two hole injector sprays fuel towards the back of the valves where liquid fuel will collect in a cold engine, making fuel film transfer very quick. All of the other injectors to a greater or lesser extent spray onto the walls, from where fuel film transfer will be slower. The single pintle and pencil beam injectors create sprays that appear to make contact with the walls in quite specific areas, probably leading to a concentrated fuel film. The large cone angle and smaller droplets from the four hole injector, on the other hand, result in the fuel hitting more of the port surfaces. This is likely to create a more wide spread film from which liquid transfer will be much slower.

4.5.2 *X* Values

At a coolant temperature of 80°C, each injector produced a different X value (see Figure 4.12(b)). The pencil beam injector gave the highest values, followed by the four-hole and the single-spray, with the lowest value being produced by the twin-spray injector. There is a correlation between this ranking and the spray patterns deduced from the photographic work. Martins and Finlay **[4.5]** found that fuel landing on the hot backs of the valves evaporates very quickly, leading Martins et al **[4.24]** to conclude that with closed valve injection it will evaporate before the valves open, leading to its exclusion from the deposition fraction measured by the parameter X. Therefore, an injector that directs fuel towards the back of the valves will produce lower X values than one directing fuel onto the walls. The photographs indicated that of the four injector types, it was the twin-spray injector that produced the most coherent targeting of fuel on the backs of the valves, explaining its result as the injector that gave the lowest X value. At the other extreme, the pencil beam injector appeared to direct fuel only onto the port walls, hence

producing the highest X value. At lower coolant temperatures the X values for the four injectors converge (Figure 4.12(b)) to a higher value than those produced with a fully warm engine. This indicates that, despite the apparent differences in their spray patterns, similar levels of deposition are produced by all the injectors at low temperatures, probably as a result of fuel condensing on the cold port walls.

4.5.3 The Effects on Transient Compensation of Differences in τ and X Values Between Injectors

Figure 4.13 shows an example of the transient fuelling compensation which can be expected from a calibrated EEC system. As can be seen, even with this compensation in the system, small excursions in the AFR value can still occur. Possible causes of these excursions include errors in the values of τ and X used. Teo **[4.22]** has developed an equation which predicts the magnitude of such excursions:

$$\frac{\Delta(AFR)}{AFR} = \left[\frac{(k-1)X}{k\left(e^{t/\tau} - X\right) + X}\right]\left(\frac{t}{\tau}\cdot\frac{\Delta\tau}{\tau} + \frac{\Delta X}{X}\right) \qquad (4.2)$$

where $\Delta(AFR)$ is the magnitude of an excursion from the base AFR, k is a constant representing the size of the throttle transient used, t is the time through the transient, $\Delta\tau$ is the error in the τ value and ΔX is the error in the X value.

His work has also shown that values of X affect the primary excursion, having maximum influence when $t = 0$, while values of τ affect the secondary excursion, having maximum influence when $t = \tau$. Thus, by substituting $t = 0$ and $t = \tau$ into Eqn. 4.2, two independent equations can be derived for the effects of errors in τ and X on excursions:

$$\frac{\Delta(AFR)}{AFR} = \left[\frac{(k-1)X}{k(e^1 - X) + X}\right]\frac{\Delta\tau}{\tau} \qquad (4.3)$$

$$\frac{\Delta(AFR)}{AFR} = \left[\frac{(k-1)X}{k(1-X) + X}\right]\frac{\Delta X}{X} \qquad (4.4)$$

These equations were used with the τ and X values obtained for the different injectors, to analyse the effect of changing injector type upon transient compensation quality. For

this comparison it was assumed that the EEC system would initially be calibrated using the two hole injector. The experimental τ and X data was also smoothed to make the results clearer. These results are shown in Figures 4.14(a)-(b), where it can be seen that, without re-calibration, changing the injector can have a significant, detrimental effect on the quality of compensation produced.

4.6 Discussion

The photographic work described in this chapter has produced qualitative descriptions of the injector spray characteristics and their interaction with the inlet port surfaces in a running engine, an improvement on some of the bench rig tests previously carried out **[4.4, 4.5]**. This visualisation work has been complemented by quantitative analysis of the fuel transfer processes resulting from these spray characteristics, using the parametric τ and X model, over a range of operating conditions. Results from both studies have been sufficient to provide a clear indication of the way inlet port mixture preparation varies between the injector types considered, information that has provided a good basis for the subsequent measurements of inlet port heat transfer. It has not, however, produced an exhaustive study of injector spray characteristics of the sort described by Saito et al **[4.26]**, whose technique produced similar observations over a range of operating conditions; nor has it provided accurate measurements of fuel droplet size and distribution within the injector spray established by techniques of the sort described by Kashiwaya et al **[4.7]** and Amer and Lai **[4.27]**. Rather, the photographic technique used in this study has allowed the injectors' spray directionality to be compared, illustrated their relative atomization quality, and shown how each spray interacts with the inlet port surfaces. Apparent heterogeneity in the fuel collection above the valves with the twin-spray injector contrasts with the fine atomization and mixing of droplets and air produced by the four-hole injector. The direction of the sprays from both these injectors, clearly aimed at the back of the valves, is quite different from the interaction of the sprays from the pencil-beam and single-spray injectors with the bifurcation web. These observations indicate that the four-hole injector produces the best mixture preparation, by creating the most homogeneous mixture within the port and would, therefore, be expected to produce the

best combustion characteristics. These conclusions are supported by Shayler et al **[4.28]**, whose measurements of emissions levels from a four-cylinder engine, with a similar range of injector types, indicated that a four-hole injector produced the highest quality in-cylinder mixture preparation. The twin-spray injector, with its spray targeted at the back of the valves, would be expected to produce the fastest engine response characteristics, a conclusion supported by the derived values of τ and X. It might also be expected to produce poor combustion characteristics as it produced the most heterogeneous inlet port mixture of the four injectors considered. However, Shayler et al **[4.28]** rated the combustion resulting from a twin-spray injector only slightly worse than that produced by a four-hole injector, and as an improvement on the results from a single-spray injector. This indicates that despite the apparently poor mixture preparation created by the twin-spray injector in the inlet port, by the time it enters the cylinder the mixture has become more homogeneous. Possible causes of this are vaporisation off the hot valves **[4.5]** or further atomization off the edge of the valve and valve seat **[4.6]**.

The curve fitting technique used to calculate values for the parameters τ and X has been identified as being slow and cumbersome, it does not lend itself to easy automation, and there is some element of subjectivity in the results produced. Alternative approaches are offered by using system identification or parameter estimation techniques **[4.29, 4.30]**. They are a subject of much interest at the moment, with manufacturers looking to obtain engine control calibrations quickly and precisely, to aid the development of engines that produce emissions within the legislated levels. The possibilities of making control systems adaptive are also being considered, so that they can adjust to changing conditions and fuel quality over the life of the engine. The methods used in these approaches are well established and fall into two main categories:

(i) Time based methods
(ii) Frequency response methods

Time based methods, like the curve fitting approach used above, adjust parameters in a model of the system, until its response to a known input is "similar" to that of the system

itself. These methods are more systematic than curve fitting, stepping through values for the parameters until the differences between the model and the system outputs are within some acceptable cost function. Teo **[4.22]** used such a method with a simple least squares algorithm when automating the curve fitting, but found that it was not accurate enough for his purposes. There are alternative algorithms for such identification work, however, including maximum likelihood and the Kalman filter derivatives. While all aim to minimise the squared error, the latter methods are favoured due to their high robustness to noise and application to non-linear systems, although this is gained at the expense of greater computational effort.

Frequency response methods are the classical methods of system identification. In their simplest form a sine wave of varying frequency is used as the input to the system and the output monitored. Assuming a linear system the output will be a sine wave of the same frequency as the input but will be modified in amplitude and phase. Feeding a range of frequencies into the system and plotting out the resultant gain and phase differences in a Bode diagram, defines the frequency response of the system, from which a system model can be derived. While this method can be used effectively in some applications, it is clumsy and time consuming.

A modern alternative uses Fourier transforms. Here an arbitrary input is applied to excite the system. Taking Fourier transforms of the input and measured output of the system it is then trivial to find the frequency response and so determine the transfer function or model for the system. As the engine can be described most simply as a discrete system it is most efficient to use the discrete Fast Fourier Transform (FFT). This method can be used with the fuel perturbation data already collected, the procedure for this being as follows:

(i) Find the FFT of the system's input and output and hence the frequency content of both.

(iii) Calculate the system's frequency response and plot it in a Bode diagram.

(iv) Using methods set out by Dorf **[4.31]** determine estimates for the model parameters.

Figure 4.15 shows the gain plot from the Bode diagram produced in this way from a modelled AFR response to a fuel perturbation. The transfer function ($G(s)$) that describes the τ and X model from which it is produced is given by:

$$G(s) = \frac{(1 - X)\tau s + 1}{(\tau s + 1)} \qquad (4.5)$$

This function has a pole at $\omega = 1/\tau$ and a zero at $\omega = 1/[\tau(1 - X)]$. The τ and X values of 0.53 and 0.42 respectively used for the modelled frequency response, would, therefore, result in a pole at $\omega = 1.89$ and a zero at $\omega = 3.25$, and this is indicated on the magnitude plot by the -20 dB/decade line intersecting the two asymptotes of the plot close to these frequencies. It would be difficult, however, to derive these break frequencies from the magnitude plot without prior knowledge of the system parameters, as they are so close together.

Further problems arise when applying the same technique to experimentally recorded data. It has already been identified that the engine's response to a lean-to-rich step is different from its response to a rich-to-lean step. When taking FFT's of the resultant AFR traces, it is, therefore, necessary to process the data so that the square wave used is made up of one lean-to-rich step followed by its mirror image. Also, the experimentally recorded response of the AFR to fuelling perturbations will contain further poles and zeros due to the response of the UEGO sensor. The response characteristics of the UEGO sensor have been measured independently and shown by Keogh and Shayler **[4.32]** to have a transfer function of the form:

$$G(s) = \frac{a}{(\tau_1 s + 1)} + \frac{b}{(\tau_2 s + 1)} \qquad (4.6)$$

where $a = 0.8$, $b = 0.2$, $\tau_1 = 0.018$ and $\tau_2 = 0.105$ for a lean to rich AFR step.

Figure 4.16 shows the gain plot resulting from a typical fuel perturbation test. It also shows the gain plots of data modelled using a combination of the fuel lag and UEGO response models; parameter values for the fuel lag model are derived from the original curve fitting method, and the three modelled plots include suggested error bands on these values.

The data in Figure 4.16 shows fairly good agreement between the gain plots from the Bode diagrams of the modelled and the experimental data, indicating that the τ and X model is a fair representation of the system being considered. However, it does not offer an alternative approach to establishing values, since attributing system parameters to the Bode diagram produced by the experimental data would be as subjective as using a curve fitting method with the raw AFR data. The problem with using the Bode diagram is a lack of data in the middle of the frequency range being considered. To overcome this the tests would have to be re-designed to provide a wider range of input frequencies to the system. This could be done by providing random white noise as an input to the system, or more practically by providing fuel perturbations in the pseudo-random binary sequence (PRBS) suggested by several authors **[4.20, 4.30, 4.33]**. Such methods would not, however, take account of the differences in response between accelerations and decelerations, and may be difficult to use during a warm up when there is only limited time available to carry out perturbations before the engine conditions change significantly. The solution, therefore, probably lies in the use of improved time based methods for establishing values of τ and X, such as those being developed by Durrant **[4.23]**.

This study has been limited in its scope by the problems encountered with errors in the AFR measurements and the limited temperature range over which it was undertaken. Some of the trends observed in this work are, however, further supported by the later heat transfer work. This heat transfer work has also allowed the mechanisms behind fuel transport to be studied in more detail. The aim of this work is to provide information to allow the mixture preparation and fuel transport for an engine to be optimised through correct injector choice; improved port geometries, providing localised heating to aid fuel vaporisation; and ensuring that the injector open periods are controlled in the most suitable way. From the work described in this chapter it is evident that the selection of the injector in the design of a port-injected, 4-valve engine involves a compromise. An injector that improves combustion by giving good mixture preparation, has important consequences for power output, fuel consumption, emissions levels and cold starting; equally, though, an injector which improves fuel transfer has important consequences for

engine transient response and control, with further benefits to be had for emissions by more efficient operation of the catalytic convertor.

Chapter 5

Heat Flux Sensor Dynamics

5.1 Introduction

The study described in Chapter 4 established that even for port fuel injected engines, a significant proportion of the injected fuel is deposited on the intake port and valve surfaces, with potentially adverse effects on mixture preparation and control, particularly when mixture demand changes. It is also well known that raising the surface temperature of the intake port ameliorates these problems, purportedly by raising heat transfer to fuel deposited on the surfaces and thereby promoting evaporation (see Figure 5.1). These fundamental mechanisms have been investigated either by modelling the flows within the inlet port **[5.1, 5.2, 5.3]**, or through experimentation with bench rigs **[5.4, 5.5, 5.6]**, but there is little direct experimental evidence from work on firing engines to support the inferences drawn. The measurements of inlet port heat transfers described in the next four chapters were designed to produce such evidence from a four-valve, port-injected engine. This chapter describes the construction and mounting of the sensors used and presents an investigation of their dynamic response characteristics. This showed that the response characteristics of the sensors were inadequate to accurately resolve instantaneous heat transfer rates without post-processing the data. A method of reconstructing instantaneous variations from the recorded sensor output has been developed, using Fourier transforms. The method is described in this chapter and the results justified using finite difference analysis techniques.

5.2 Heat Flux Sensor Construction

Figure 5.2 illustrates the construction of the Micro-Foil Heat Flow Sensors manufactured by Rhopoint and used to measure heat transfer through the inlet port walls. Each sensor consists of two arrays of K-type thermocouple junctions either side of a thin polyimide (Kapton) film, which acts as a thermal barrier. Also mounted on the top surface of this

film is a T-type thermocouple junction, used to measure the temperature of the sensor for calibration purposes. Under steady state conditions, the heat flux through the sensor is given by measuring the potential difference between the two thermocouple arrays, which is calibrated for heat flux against the sensor's temperature by applying the calibration factor provided by the manufacturer. To protect the thermocouple junctions two further layers of Kapton (Figure 5.3) are laminated over the top and bottom surfaces of the sensor. The sensors were attached to the port wall surfaces using a high temperature epoxy resin, "Araldite 2014" (see Figure 5.3). Rhopoint quote a response time of 60 ms for the output from the sensors to rise to 62% of a step input **[5.7]**. This is of the same order as the period of an engine cycle, 120 ms at 1000 RPM, and indicates that there will be some attenuation of signals arising from variations in heat fluxes around the cycle. Epstein et al **[5.8]** developed a theoretical approach to assessing the significance of this attenuation, which requires knowledge of the dimensions and thermal characteristics of the various layers highlighted in Figure 5.3.

To establish the adhesive film thickness, a sample sensor was attached to a piece of aluminium plate using the technique developed for fixing the sensors around the inlet port surfaces, and the thickness of the adhesive layer was measured using a dial indicator on a surface table. This measurement was dependent upon finding the relative distance between the sensor's top surface and the surface table at various points before and after applying the layer of adhesive between the sensor and the aluminium plate. It was, therefore, unsuitable for making measurements within the inlet port. To measure the thickness of the two protective laminae and the central lamina between the arrays of thermocouple junctions, an example sensor was first set in a resin block and sections of the block removed with a surface grinder until the visible section passed through the centre of the thermocouple arrays. Magnified images of this section were then captured using a PC in conjunction with a video camera and a microscope (see Figure 5.4), which could then be scaled against the overall thickness of the sensor, previously measured with a micrometer. Values for the dimensions and thermal characteristics of each layer highlighted in Figure 5.3 are listed in Table 5.1. The thermal property values for the port wall material are most uncertain because factors such as casting porosity can have a

significant effect. Variations within the range of values given in the literature are not critical, however, because the port wall still acts as a source or sink of large heat capacity.

Table 5.1 - Thermal Characteristics and Mean Values for Dimensions of Layers Highlighted in Figure 5.3

Layer	k (W/mK)	ρ (kg/m^3)	c (J/kgK)	Thickness (μm)
Upper Protective Lamina	0.12	1420	1090	$a_1 = 15$
Thermal Barrier Lamina	0.12	1420	1090	$d = 80$
Lower Protective Lamina	0.12	1420	1090	$a_2 = 15$
Adhesive	0.36	1600	1050	$g = 75$
Aluminium Port Wall	237	2702	900	5000

5.3 Modelling of Sensor Dynamics

Epstein et al **[5.8]** developed an analytical description of the dynamic characteristics of heat flux gauges with high frequency response for use on metal turbine blades. The construction of the heat flux gauges they used was very similar to that of the sensors used in the study described here, making the theoretical approach transferable. Initially, the five layers of sensor, adhesive and port surface shown in Figure 5.3 are further simplified into two layers: Layer 1, of thickness L, consisting of sensor, protective layers and adhesive all assumed to have the same, uniform thermal properties (those of the sensor's thermal barrier); and Layer 2, the port surface, also with uniform thermal properties and assumed to be semi-infinite. The thermocouple junctions are ignored since they will have a much larger thermal conductivity than the other component materials of the sensor. It is further assumed that there is a spatially uniform heat flux applied to the surface of the sensor; that the two layers make perfect thermal contact; and that Layer 1 is thin in comparison to its lateral dimensions, allowing the flow of heat to be considered as a one dimensional

problem. Making these assumptions, the temperature (T) in each layer will be governed by:

$$\text{Layer 1:} \quad \frac{\partial T_1}{\partial t} = \alpha_1 \frac{\partial^2 T_1}{\partial x^2} \quad \text{for} \quad 0 \le x \le L \tag{5.1}$$

$$\text{Layer 2:} \quad \frac{\partial T_2}{\partial t} = \alpha_2 \frac{\partial^2 T_2}{\partial x^2} \quad \text{for} \quad L \le x \le \infty \tag{5.2}$$

where α is the thermal diffusivity of each layer, given by the following relationship between thermal conductivity (k), density (ρ) and specific heat capacity (c):

$$\alpha = \frac{k}{\rho c} \tag{5.3}$$

At the interface between the two layers in the model the following conditions apply:

$$T_1(L,t) = T_2(L,t) \tag{5.4}$$

$$k_1 \left.\frac{\partial T_1}{\partial x}\right|_{x=L} = k_2 \left.\frac{\partial T_2}{\partial x}\right|_{x=L} \quad \text{for} \quad -\infty < t < +\infty \tag{5.5}$$

and Layer 2 has the following semi-infinite condition:

$$T_2(\infty,t) = T_0 \tag{5.6}$$

where T_0 is the uniform temperature of the sensor and port wall under adiabatic conditions. The response of the system to two forms of driving surface heat flux ($\dot{q}_s$) are considered here:

(i) a step change of the form: $q_s(t) = -k_1 \left.\frac{\partial T_1}{\partial x}\right|_{x=0} = \begin{cases} 0 & -\infty < t < 0 \\ Q_s & 0 \le t < +\infty \end{cases}$

(ii) a sinusoidal variation of the form: $q_s(t) = -k_1 \left.\frac{\partial T_1}{\partial x}\right|_{x=0} = Q_s e^{j\omega t}$

Basic forms of the solution to both of these problems are offered by Epstein et al **[5.8]** using the techniques described by Carslaw and Jaeger **[5.9]**. In both cases to allow easier application of the results to the problem being considered, the results incorporate the thermocouple array separation (d), and L, the thickness of Layer 1 is defined by:

$$L = (1 + 2f_h + f_g)d \tag{5.7}$$

where f_h is the fractional thickness of the protective layers of polyimide film (a/d) and f_g is the fractional thickness of the adhesive layer.

5.3.1 Response to a Step in Surface Heat Flux

When condition (i) is applied to the sensor's surface, the temperature distribution in Layer 1 is given by:

$$T_1(x,t) = T_0 + \frac{Q_s d}{k_1}\sqrt{\frac{t}{\tau}}\sum_{n=0}^{\infty}(-R)^n(\text{ierfc } P_n - R\ \text{ierfc } Q_n) \tag{5.8}$$

where τ is the sensor time constant, given by:

$$\tau = \frac{d^2}{4\alpha_1} \tag{5.9}$$

while P_n, Q_n and R are the following functions:

$$P_n = \frac{x}{d}\sqrt{\frac{\tau}{t}} + 2n\frac{L}{d}\sqrt{\frac{\tau}{t}} \tag{5.10}$$

$$Q_n = -\frac{x}{d}\sqrt{\frac{\tau}{t}} + 2(n+1)\frac{L}{d}\sqrt{\frac{\tau}{t}} \tag{5.11}$$

$$R = \frac{r-1}{r+1} \tag{5.12}$$

and r is given by:

$$r = \frac{\sqrt{(\rho c \alpha)_2}}{\sqrt{(\rho c \alpha)_1}} \tag{5.13}$$

ierfc( ) is the first integral of the complementary error function given by:

$$\text{ierfc}(x) = \frac{1}{\sqrt{\pi}}e^{-x^2} - x\ \text{erfc}(x) \tag{5.14}$$

Values of heat flux measured through the sensor ($\dot{q}_m$), in response to a step change in surface heat flux, can be found by applying suitable values of x to Eqn. 5.8 and using the resultant temperature profiles in Eqn. 5.15:

$$\dot{q}_m(t) = \frac{k_1}{d}\left(T_u(t) - T_l(t)\right) \tag{5.15}$$

where the subscripts u and l represent the upper and lower thermocouple arrays respectively, and, with reference to Figure 5.4, $x_u = a_1$ and $x_l = a_1 + d + a_2$. Figure 5.5

shows typical step responses calculated in this way for three values of adhesive thickness (g) and three values for the thickness of the upper protective lamina defined by x_u. Variations in values of g were considered to provide an indication of the effects of errors introduced by assuming that the adhesive had the same thermal properties as the polyimide film, and to allow for variations introduced during attachment; variations in x_u were apparent in the magnified cross-sectional images of the sensors arising from variations in the thickness of the interstitial glue layers (see Figure 5.4). Both variations have an effect in the time domain, although it is the variations in the thickness of the adhesive layer which are most significant. In Figure 5.5(b), where the time scale is expanded to show the initial response of the sensor, it can be seen that the dimension variations considered give rise to a range of 50-90 ms in values of time for the measured heat flux to rise to 62% of the steady state value. This is in agreement with the "typical" value of 60 ms quoted by Rhopoint [5.7].

5.3.2 Response to a Steady Harmonic Variation in Surface Heat Flux

When condition (ii) is applied at the sensor's surface for all time, the temperature distribution in Layer 1 is given by:

$$T_1(x,t) = T_0 + \frac{Q_s d}{k_1} G\, e^{j(\omega t - \phi)} \tag{5.16}$$

a harmonic function in which G describes the magnitude variation with x:

$$G = \sqrt{\frac{2\omega_c}{\omega}\left(\frac{A^2 + B^2}{C^2 + D^2}\right)} \cdot \exp\left(-\frac{1}{2}\frac{x}{d}\sqrt{\frac{\omega}{\omega_c}}\right) \tag{5.17}$$

and ϕ describes the difference in phase between the temperature variation at x and the applied surface heat flux:

$$\phi = \frac{1}{2}\frac{x}{d}\sqrt{\frac{\omega}{\omega_c}} + \frac{\pi}{4} - \tan^{-1}\left(\frac{BC - AD}{AC + BD}\right) \tag{5.18}$$

where:

$$A = 1 - R.\exp\left(-\sqrt{\frac{\omega}{\omega_c}}\left(\frac{L - x}{d}\right)\right).\cos\left(\sqrt{\frac{\omega}{\omega_c}}\left(\frac{L - x}{d}\right)\right) \tag{5.19a}$$

$$B = R.\exp\left(-\sqrt{\frac{\omega}{\omega_c}}\left(\frac{L-x}{d}\right)\right).\sin\left(\sqrt{\frac{\omega}{\omega_c}}\left(\frac{L-x}{d}\right)\right) \quad \textbf{(5.19b)}$$

$$C = 1 + R.\exp\left(-\sqrt{\frac{\omega}{\omega_c}}\left(\frac{L}{d}\right)\right).\cos\left(\sqrt{\frac{\omega}{\omega_c}}\left(\frac{L}{d}\right)\right) \quad \textbf{(5.19c)}$$

$$D = -R.\exp\left(-\sqrt{\frac{\omega}{\omega_c}}\left(\frac{L}{d}\right)\right).\sin\left(\sqrt{\frac{\omega}{\omega_c}}\left(\frac{L}{d}\right)\right) \quad \textbf{(5.19d)}$$

and R is given by Eqn. 5.12. A sensor characteristic frequency (ω_c) has been introduced in these equations, which is based upon the thermocouple array separation (d):

$$\omega_c = \frac{\alpha_1}{2d^2} \quad \textbf{(5.20)}$$

If the applied surface heat flux has a frequency greater than this, significant attenuation of the signal will occur in the measured heat flux ($\dot{q}_m$). This is indicated by the Bode plots of the system transfer function (Eqn. 5.21) shown in Figure 5.6. The plots shown are for the same variations in g and x_u considered in the analysis of the response to a step in surface heat flux. They show that it is variations in the thickness of the upper protective lamina which have the largest effect in the frequency domain, significantly altering the gain and phase at higher frequencies.

$$\frac{\dot{q}_m(t)}{\dot{q}_s(t)} = G_m e^{-j\phi_m} \quad \textbf{(5.21)}$$

In Eqn. 5.21, the measured heat flux ($\dot{q}_m$) is again given by Eqn. 5.15, where this time:

$$T_u = T_1(x_u, t) = \frac{Q_s d}{k_1} G_u e^{j(\omega t - \phi_u)} \quad \textbf{(5.22a)}$$

$$T_l = T_1(x_l, t) = \frac{Q_s d}{k_1} G_l e^{j(\omega t - \phi_l)} \quad \textbf{(5.22b)}$$

Therefore, Eqn. 5.21 can be re-written as:

$$\frac{\dot{q}_m(t)}{\dot{q}_s(t)} = G_u e^{-j\phi_u} - G_l e^{-j\phi_l} \quad \textbf{(5.23)}$$

and from Eqns. 5.21 and 5.23:

$$G_m = \sqrt{G_u^2 + G_l^2 - 2G_u G_l \cos(\phi_u - \phi_l)} \quad \textbf{(5.24)}$$

$$\phi_m = \tan^{-1}\left(\frac{G_u \sin\phi_u - G_l \sin\phi_l}{G_u \cos\phi_u - G_l \cos\phi_l}\right) \tag{5.25}$$

where G_u, G_l, ϕ_u and ϕ_l are given by the application of values for x_u and x_l to Eqns. 5.17 and 5.18.

5.4 Measurement of Sensor Dynamics

To measure the actual response of the sensors, the beam from an argon ion laser was used as an interruptible heat source. It produced light with a wavelength of approximately 0.5 μm, implying that the frequency of the beam was of the order of 10^{15} Hz, much higher than the frequencies of interest. The sensor that had been mounted up to assess the thickness of the adhesive film was used as the test sensor. The plate on which it was mounted had been milled from a piece of the cylinder head, to provide a substrate with the same thermal properties as the inlet port walls. The laser was used at its highest power setting and the output beam was focussed using a lens. Without the lens, the cross-sectional area of the beam was such that it only covered the thermocouple arrays used to measure the heat flux; with the lens the beam spread out to also cover the surface mounted thermocouple. At these two extremes the relevant recorded values of steady state heat flux were 35 and 6 kW/m^2 respectively. Figure 5.7 shows normalised data recorded from the heat flux sensor when these two beam intensities were applied to its surface as a step input, by moving a shutter out of the path of the beam, along with the modelled response for an adhesive layer thicknesses of 40 μm and an upper protective lamina thickness of 20 μm. Test 1 is data recorded with an applied surface heat flux of 35 kW/m^2 and Test 2 is with an applied heat flux of 6 kW/m^2. There is good repeatability between the two tests, although the data from Test 2 was more variable after reaching steady state conditions. The values of g and x_u applied in the model were chosen to provide the best fit between the modelled and the experimental data. They indicate the level of correction required to take account of variations in these dimensions, in addition to the effects of creating heat fluxes with light of a wavelength comparable to the thickness of the sensor's upper protective lamina.

Figure 5.8 shows a comparison between the magnitude plot from the Bode diagram produced by applying these values of g and x_u to Eqn. 5.21, and those produced from further analysis of the step response data. To transform the step response data from the time domain into the frequency domain, the same technique was used as for the frequency analysis of the fuel perturbation tests in Chapter 4: a pseudo-square wave was produced by inverting the input step and its resultant output and combining the two as a continuous waveform of symmetrical pulses (see Figure 5.9). The magnitude plot produced from the transformed data (Figure 5.8) shows that at frequencies of over 100 rad/s, the resultant frequency response is badly affected by noise. The reason for this is given by considering the frequency content of the input waveform. The Fourier series expansion of an odd function waveform of symmetrical pulses (see Figure 5.9) is given by Waintraub and Brumgnach **[5.10]** as:

$$f(t) = \frac{A}{2} + \frac{2A}{\pi}\left(\sin\omega_0 t + \frac{1}{3}\sin 3\omega_0 t + \frac{1}{5}\sin 5\omega_0 t + \ldots\right) \qquad (5.26)$$

where A is the amplitude of the pulses and ω_0 their frequency. This is made up of an initial component indicating the dc offset of the waveform and then a series of odd harmonics, 1,3...n. The first, fundamental harmonic has the same frequency (ω_0) as the original waveform and an amplitude of $2A/\pi$. Each subsequent harmonic of frequency $n\omega_0$, is attenuated by a factor of $1/n$. In Figure 5.8, the increase in noise for frequencies above ω = 100 rad/s is commensurate with a signal to noise ratio on the heat flux data of 30 dB, since at frequencies higher than ω = 100 rad/s the harmonics in the input signal will be attenuated by more than -30 dB. Figure 5.6 shows that, according to the modelled data, the dynamic response of the sensor is such that significant attenuation (i.e. greater than -30 dB) does not occur until frequencies greater than ω = 1000 rad/s. To provide an experimental comparison for this modelled data, noise free experimental results were required for frequencies in the range 100 to 1000 rad/s. Data could be sampled from the heat flux sensor at 1 kHz, making 3000 rad/s the maximum frequency available from FFT's of this data. It should, therefore, be possible to measure the frequency response of the sensor over the whole range of interest, provided the input waveform contained harmonics of large enough amplitude at the frequencies of interest. To provide this data, further tests were carried out in which a rotating shutter was used to chop the laser beam, producing

an input of symmetrical pulses to the heat flux sensor with nominal frequencies of 2, 5 and 10 Hz, the results of which are shown in Figure 5.10. The tests with an input frequency of 2 Hz were repeated with the two beam intensities used for the step response tests, whilst at the higher frequencies only the more diffuse beam was used. Inaccuracies are apparent in the input frequencies shown in Figure 5.10, which arise from poor rotational speed control of the chopper at low speeds. Figure 5.11 shows the corresponding magnitude plots alongside the modelled plot, which utilises the same values of g and x_u as Figures 5.7 and 5.8 (i.e. $g = 40$ μm and $x_u = 20$ μm). The experimental results give good agreement to the modelled data and show that the frequency response is repeatable when the input magnitude and frequency are varied.

5.5 Compensation for Sensor Dynamics in Measurements from Heat Flux Sensors

In their discussion of the operation of the heat flux gauges Epstein et al **[5.8]** introduce the concepts of direct and semi-infinite modes of operation. In the "direct" mode, for input harmonics of frequency less than ω_c, there will be a uniform temperature gradient across the sensor; the surface heat flux is then proportional to the measured temperature drop across the gauge and can be calculated from the calibration provided by Rhopoint **[5.7]**. For input harmonics with frequencies greater than ω_c, the thermal penetration is comparable to, or smaller than, the sensor thickness and they will be attenuated, creating a non-uniform temperature gradient across the sensor. In this case Epstein et al **[5.8]** suggest that the sensor is operating in a "semi-infinite" mode when the heat flux can be obtained entirely from temperature measurements on the upper surface.

Figure 5.12 shows a typical crank-angle resolved trace recorded with a heat flux sensor in the inlet port of a running engine. Figure 5.13 shows this same data after transformation into the frequency domain using an FFT. In this data, the fundamental frequency occurs at $\omega = 53$ rad/s created by the cycle length of 0.12 s at an engine speed of 1000 RPM. Further harmonics are apparent at frequencies above this, whose amplitudes are attenuated from the amplitude of the fundamental. This attenuation

increases with frequency, reaching -30 dB at ω = 500 rad/s, which has already been identified as the level at which noise becomes significant in the data recorded from the heat flux sensors. No attempt was made to filter out this noise, however, as it became apparent that the signal bandwidth was such that it overlapped the noise bandwidth; removing the noise would, therefore, remove significant elements of the signal, particularly those associated with sudden peaks in the measured heat flux.

Comparison of the data in Figure 5.13 with that in Figure 5.11, shows that the harmonics contained within the heat flux data recorded from the engine have frequencies above the characteristic frequency of the sensor (ω_c = 6.057 rad/s). This means that with the engine running at 1000 RPM, the intra-cycle heat flux variations within the inlet port will have a thermal penetration which is less than the thickness of the sensor, and the sensor will be operating in the semi-infinite mode identified by Epstein et al **[5.8]**. Unfortunately, unlike the sensors used by Epstein et al, the heat flux gauges used in this study do not allow separate measurement of temperature from the upper and lower thermocouple arrays. Therefore, to derive values for the applied surface heat flux, it was necessary to manipulate the data measured from the sensor in the frequency domain and then transform it back into the time domain. The steps involved in this technique entail first decomposing the measured heat flux into a Fourier Series of harmonic components in the frequency domain, using an FFT; each harmonic is then corrected for phase shift and gain in the frequency domain, using the model of the sensor's frequency response characteristics described previously; the inverse transform of these corrected harmonics provides the incident heat flux variation in the time domain. Figure 5.14 shows data resulting from this post-processing, along with the original measured heat flux, for typical crank-angle resolved data recorded from the inlet port. Figure 5.13 shows that the fundamental frequency occurring in data recorded at 1000 RPM is of a higher frequency than that affected by variations in the adhesive film thickness (g) in Figure 5.6. Two values of g were tested in the compensation used to produce Figure 5.14, the measured value of 75 μm and the value of 40 μm found to give the best fit to the experimental response measurements in Figures 5.7 and 5.8; there was found to be no significant difference between the resulting compensated traces. Varying the thicknesses of the upper

protective layer (x_u) in the compensation model did make a difference, however. Figure 5.14 provides a comparison between the compensated data produced when the measured value of 15 μm is used for x_u, and that produced when x_u is given a value of 20 μm, the "best fit" value in Figures 5.7 and 5.8.

5.6 Discussion

The analysis and experimental work described in this chapter has shown that the heat flux sensors have a response time comparable with the period of an engine cycle. Compensation for this dynamic response can be made to infer instantaneous variations in heat transfer using spectral analysis. Limitations are placed on the quality of this compensation by the sensitivity of the sensors, the quality of the signal they produce, and the frequency at which the data can be sampled. The maximum sampling rate is 1 kHz (6380 rad/s) and, therefore, only harmonics of frequency less than 500 Hz (3140 rad/s) can be analysed using the FFT methods applied, any higher frequency harmonics being effectively filtered out of the signal. However, Figure 5.13 shows that at these frequencies the amplitude of the harmonics in typical crank-angle resolved data is attenuated by more than -60 dB from that of the fundamental frequency, suggesting that they are not a significant component of the original signal. The aliasing effects of FFT analysis, discussed by Newland **[5.11]**, must also be considered in such cases. These will lead to distortion of the signal in the frequency domain if there are significant components of the signal at frequencies approaching half the sampling frequency. In this case, the data in Figure 5.13 shows that the components of the original signal are heavily attenuated at frequencies below this and, therefore, the aliasing effects will be minimal. Figure 5.13 also shows that there are noise harmonics in the signal at frequencies above about 500 rad/s (80 Hz), these overlap with significant components of the signal and cannot be filtered out. They arise from a combination of cycle-by-cycle variability in the data, signal noise and the limitations of the data acquisition system, which itself produces a noise level with an RMS value of 3 μV equivalent to a signal to noise ratio of between 40 and 50 dB on typical recorded signals.

Some effort was made to reduce the effects of noise on the measured data by taking the mean of ten consecutive cycles before carrying out the spectral analysis. Figure 5.14 shows that this has been fairly successful. The effects of random noise on the compensated data are limited, being most apparent in the data recorded through Sensor 1 (Figure 5.14(a)), which also displayed the lowest overall values of heat flux. More significant, are the effects of the parameter x_u on the quality of compensation produced. A high frequency component is apparent in each of the compensated traces in Figure 5.14 when x_u is set to 20 μm, the value indicated by results of frequency response measurements using a laser. This is not apparent when a value of 15 μm is used in the compensation model. It leads to a variation of up to 30% in the inferred peak heat flux values and illustrates the level of uncertainty surrounding which value of x_u to use when compensating for the dynamic response of these sensors. The sensor used for the response experiments was purchased at a different time from the sensors used within the inlet port or the one sectioned to provide the measurements in Figure 5.4 and Table 5.1. The calibration factors provided by Rhopoint for the "direct" mode operation of these sensors indicate that significant variations can occur between sensors, particularly when they are purchased from different batches. Also, the conditions for the sensor response tests were somewhat different to those found within the inlet port. It has been excepted, therefore, that the response characteristics of the sensor used in the frequency response tests, when excited by a beam of laser light, are best characterised by a model in which x_u is taken as 20 μm, whereas the response characteristics of the sensors positioned around the inlet port are better characterised by taking x_u as 15 μm.

In Figure 5.14(c) additional high frequency spikes appear in the data at the two ends of the compensated traces. These arise because spectral analysis using FFT's relies upon the assumption that in the time domain the original function is periodic and continuous for $-\infty < t < +\infty$. Figure 5.12 shows a magnified form of the data from which the compensated traces in Figure 5.14(c) are produced, where it can be seen that in this case there is a slight discontinuity between the heat flux values for crank-angles of 0° and 720°, due to cycle-by-cycle variations in the crank-angle resolved data. The effect of these discontinuities

is to produce the high frequency spikes observed at the same points in the compensated data.

To provide further confirmation of the compensated results, a finite difference model of the sensor was developed. Inferred surface heat flux data were applied to this model, and corresponding values of measured heat flux were calculated to see if they matched the uncompensated data recorded from the sensors. In this finite difference model it was assumed that the thermal capacity and conductivity of the aluminium port surface were such that the interface between the adhesive and the port surface remained at a constant temperature, that of the coolant passing through the engine. Above this interface the four layers shown in Figure 5.3 were modelled as two layers with independent thermal properties: the top layer, consisting of the two protective layers and the central thermal barrier of the sensor, was modelled as polyimide film, with the relevant thermal properties from Table 5.1; the bottom layer was modelled using the thermal properties for the adhesive given in Table 5.1. In this finite difference model the thickness of the adhesive layer was taken as the measured value of 75 μm, since it has already been identified that the correction to 40 μm required in the model of the sensor's step response was at least partly due to the error introduced by the assumption of constant thermal properties throughout the sensor and adhesive layers. Figure 5.15 shows that there is good agreement between the measured data from Figure 5.14 and the output from the finite difference model when the compensated traces for $x_u = 15$ μm are applied.

Chapter 6
Heat Transfer for Dry-Port Conditions

6.1 Introduction

In this Chapter, an investigation of heat transfer between the inlet port surfaces and the gas flow in the port is described. Cheng et al **[6.1]** identified four distinct gas flow regimes which occur during various periods of an engine cycle. The timing of these periods is shown in Figure 6.1. When the intake valves are closed, no bulk motion of the gas occurs. During the intake and exhaust valve overlap period, hot combustion products can flow from the cylinder back into the intake port, described as overlap backflow. As induction progresses, a forward induction flow develops. Finally, towards the time of inlet valve closure, a displacement backflow of gas may occur. To differing degrees, each of these stages will affect the heat exchange between the gas mixture and the port walls.

(i) Period of no bulk gas flow:

During this period, although there is no net movement of gas through the port, there is likely to be some movement within the port as a result of eddy currents set up by turbulent flows during previous bulk gas movements. These movements will produce convective heat transfer effects, with heat transfer being further driven by the temperature difference between the port gases and the port walls.

(ii) Overlap backflow:

Valve overlap, between inlet valve opening (IVO) and exhaust valve closing (EVC), improves volumetric efficiency particularly at higher speeds and loads, by increasing the efficiency with which exhaust gas residuals are "scavenged" from the cylinder. At part load conditions it results in a reverse flow blowdown, as the pressure in the cylinder, which is close to atmospheric at the end of the exhaust stroke, equalises with that in the inlet manifold. The resultant *overlap backflow* of hot residual gases from the cylinder will affect inlet port heat transfer both through convection and through the changes such an influx of hot gas will have

on the thermal environment. It is also likely to displace any liquid fuel that has collected around the valve seats during the previous period of valve closure.

(ii) Forward induction flow:

With the inlet valves open there will be a *forward induction flow* of air through the inlet port. This mixes with the burnt gases from the overlap backflow and flows into the cylinder. Like the overlap backflow it will affect heat transfer by increasing convection and changing the thermal environment, this time, however, by inducing colder fresh charge through the port.

(iii) Displacement backflow:

Inlet valve closing (IVC) is timed after bottom dead centre (BDC) of the compression stroke to improve volumetric efficiency at high engine speeds and loads, when the momentum of the air maintains a forward flow into the engine until IVC. However, at lower speeds fresh fuel/air mixture and residual gases from the previous combustion stroke will be displaced back into the inlet port as the piston starts to move back up the compression stroke before IVC. This *displacement backflow* will be warmer than the fresh charge air left in the port and since it will be present for the whole of the valve closed period it may exert an extended influence on the port's thermal environment. Its composition is a mixture of fresh charge and in-cylinder residual gases, which may also affect the vaporisation of fuel from deposited fuel films.

At the present time, there is very little information on the effects of these various gas flow regimes on surface heat transfer. Turin et al **[6.2]** took some account of the effect of displacement backflow on the mass of fuel returned to the port in their model, but otherwise assumed that the flow of gas through the port was steady. The bench rig work of both Martins and Finlay **[6.3, 6.4]** and Ladommatos **[6.5]** simulated unsteady flows using pulsating gas motion to represent periods of forward induction flow between periods of no bulk gas flow; they did not, however, consider the effect of overlap and displacement backflows.

6.2 The Effects of Different Gas Flow Regimes on Measured Heat Fluxes

To establish how each gas flow regime within the port affected heat transfer between the gases and the port walls, tests were carried out with fuel injection restricted to one side of the intake port bifurcation. A twin-spray injector was modified to achieve this, by sealing one hole in the injector splitter cap (see Figure 6.2). By rotating the cap, fuel injection could be directed into either branch of the port leaving either Sensors 3, 4 and 5, or Sensors 6, 7 and 8 dry. Sensors 1 and 2 were outside the region wetted during tests with an unmodified twin-spray injector, the results from which are used as measurements of the dry-port conditions for these two sensors. Engine operating conditions were chosen to cover a range of MAP (0.53, 0.79 and 0.95 bar) with the engine running fully-warm; at a speed of 1000 RPM; a nominally constant, stoichiometric mixture ratio; and with the injection timed to end at 270°ATDC, during the exhaust stroke of the cycle.

Figure 6.3 shows summaries of crank-angle resolved heat flux variations recorded from all the sensors over ten consecutive cycles, with a MAP of 0.79 bar. These results are far less variable than those recorded when fuel deposition occurred, which increased the standard deviation by a factor of up to 10. Figure 6.3 also illustrates the effects on the heat fluxes of variations in gas flow due to overlap backflow, forward induction flow and displacement backflow. As has already been discussed in Chapter 5, the transient response of the heat flux sensors will have reduced the apparent effects of these flows. Inferred data for the actual heat fluxes occurring at the surface of the sensor, after removing the sensor response from the mean results in Figure 6.3, are presented in Figure 6.4 The timings, ATDC of the firing stroke, of the various valve events that produce these inlet port phenomena are: IVO at 350°, EVC at 370° and IVC at 598°. For the two sensors furthest upstream (Sensors 1 and 2), the dominant influence is the forward flow of air during induction, which gives rise to high heat fluxes from the surface to the colder fresh charge passing into the intake port (see Figure 6.4(a)). No obvious discontinuity in heat transfer rate occurs at the end of the induction period. The heat flux continues to decay monotonically to negligible levels at the start of the next induction period, as fresh charge and gases from displacement backflow mix and the mixture motion

decays. The locations of Sensors 3 and 4 are further downstream, in the vicinity of the port bifurcation. Here, the variations of heat flux during the induction period are similar to those for Sensors 1 and 2 (see Figure 6.4(b)), but after inlet valve closing the heat flux drops more rapidly, probably because displacement backflow raises the temperature of the gas within the port to values close to that of the port surface. During the valve overlap period, Sensor 3 records the effects of overlap backflow gases passing back into the port as a large negative spike in heat flux. The variations recorded by Sensors 5 and 7 (Figure 6.4(c)) show a similar response, most obviously in the variation recorded by Sensor 5.

The negative heat flux spikes recorded by Sensors 3 and 5 are substantially larger than that recorded by Sensor 7 and the spike is absent in the variation recorded by Sensor 4. Sensors 3 and 5 were bonded to the side walls of the intake port and Sensors 4 and 7 to the floor. This suggests that the overlap backflow passes up the port as far as these sensors, but is directed into the upper section of the intake port. The heat flux variations for Sensors 6 and 8, which are nearest to the intake valves, are shown in Figure 6.4(d). For these, the overlap backflow produces a negative heat flux spike which is an order of magnitude greater than the positive values during the remainder of the induction period.

Collectively Figures 6.4(a)-(d) show that heat transfer to the gas during the main phase of induction has a similar magnitude at each location in the intake port and that the main difference between locations is the magnitude of the heat flux spike associated with overlap backflow gases. At low manifold pressures, these spikes can more than offset the positive heat transfer to the fresh charge during induction giving a net heat transfer to the surface over the cycle. The effect of manifold absolute pressure is more clear in the data given in Figure 6.5, which shows how crank-angle resolved surface heat fluxes varied with MAP for Sensors 1, 4 and 8. For a MAP of 0.53 bar, the overlap backflow spike in heat flux occurs at all locations including that of Sensor 1, although here the magnitude of the spike is relatively small. At a MAP of 0.79 bar or higher, the spike no longer occurs in the data for Sensors 1 or 4, reflecting the more limited extent of the backflow into the intake port, and at a MAP of 0.95 bar there is no evidence of overlap backflow occurring

even in the data recorded by Sensor 8. At around inlet valve closing, the effects of the displacement backflow can be seen in the data for Sensor 4, and less obviously for Sensor 8, to produce a rapid drop in heat transfer to the gas independent of manifold pressure.

6.3 Spatial Variations in "Dry-Port" Heat Transfers

The crank-angle resolved data described above indicated that the variations in inlet port heat transfer were affected both by engine operating conditions and the spatial positioning of the sensors used to detect the heat fluxes. To provide a clearer representation of these effects, Figure 6.7 shows how integrated results, giving heat transfer per cycle to the port gases, vary with MAP and sensor position. As MAP decreases, the heat transfer decreases from positive to, in some cases, increasingly negative values due to the effect of increasing overlap backflow on gas temperatures in the port. Figure 6.8 shows a simulation of the regions occupied by backflow gas at the two lower MAP values, calculated assuming an adiabatic expansion from the combustion chamber at atmospheric pressure as the valves open. As might be anticipated from this, Figure 6.7 shows that heat transfer at locations near to the valves is most affected by the backflow. Heat transfer from side and bottom surfaces of the port display differing sensitivity to MAP. Only Sensors 3, 5, 6 and 8, which are on the side walls, record large negative values of heat transfer per cycle at low MAP. These sensors appear to be exposed to higher gas temperatures, indicating that the majority of the backflow gases pass through the upper part of the port cross section.

6.4 Variation of "Dry-Port" Heat Transfers During a Warm-Up

To examine the effects of temperature on the "dry-port" heat transfers, each test condition was repeated to cover engine warm-ups from a coolant temperature of 0°C through to fully-warm running conditions. The variation and magnitude of the crank-angle resolved heat fluxes change quite significantly during warm-up as illustrated by the results presented in Figure 6.6 for Sensors 4 and 7. These results were recorded during a warm-

up test following a cold-start from a temperature below 0°C. The air intake temperature was approximately 20°C throughout the warm-up. For both Sensors 4 and 7 the heat flux during induction increases as engine coolant temperature increases, reflecting the growing differential between surface temperature and air charge temperature. During the quiescent part of the cycle, heat fluxes were generally negative at temperatures less than fully-warm, indicating that gas temperatures were generally higher than the surface temperature except for the latter condition. The test data shown is for a manifold pressure of 0.79 bar, for which the effects of overlap backflow are significant. During the early period of engine warm-up the negative heat flux spike peaks at a coolant temperature between 10 and 20°C, beyond which it reduces to a smaller, almost negligible value at fully-warm operating conditions. The observed maximum suggests the temperature of the backflow gases is changing rapidly during the early stages of warm-up. This is probably due to a combination of low cylinder wall and valve temperatures and poor combustion quality. The observation that the spike diminishes at higher temperatures suggests that some restructuring (rather than diminution) of the flow back into the port occurs, since Sensors 3 and 5 continue to record large negative heat flux spikes even at the fully-warm operating conditions, and these two sensors are located at a similar distance from the intake valves as Sensors 4 and 7.

Generally, the temperature of each heat flux sensor, as measured by the T-type thermocouple incorporated in the sensor, varied linearly with coolant temperature during warm-up tests, with a typical spread of 10-15°C at a given coolant temperature. In most cases, the temperature of the sensor followed the coolant temperature so closely that it was assumed that this gave a good indication of the port surface temperature under the sensor. Sensor 1, located upstream of the cylinder head flange face, provided an exception to this. The surface upon which this sensor was mounted was insulated from the cylinder head by a gasket and there were no coolant passages running underneath it. Therefore, the temperature of this sensor was generally lower than the coolant temperature and did not follow a linear variation with coolant temperature. It was still assumed to provide a good indication of the local surface temperature, though. For Sensors 6 and 7, however, the surface temperatures were measured with the additional

K-type thermocouples, TC3 and TC4, to allow for the greater spatial variation in port surface temperatures around these two sensors mentioned in Chapter 3. There was no significant variation with MAP in any of these measured temperatures, and Figure 6.9 shows the surface temperature variation with coolant temperature used in the following for each sensor.

The heat transfer per cycle recorded by the sensors during engine warm-up varied linearly with local surface temperature at the higher MAP conditions (0.95 and 0.79 bar), with different offsets. At the lower MAP setting (0.53 bar) the dependence on surface temperature is more complex, reflecting the influence of high levels of overlap backflow on effective gas temperatures in the port. Illustrative data sets for 1000 RPM and stoichiometric running conditions are given in Figures 6.10(a)-(c). At first sight, the linear relationship between heat transfer values and surface temperature is surprising since the former depends on the surface-to-gas temperature difference rather than surface temperature alone. However, the cycle-averaged gas temperatures measured by thermocouples TC1 and TC2 (see Figure 6.11) varied in a way that indicates the temperature difference is also varying linearly with surface temperature, illustrated in Figure 6.12 by data from Sensors 3 and 5 and thermocouple TC2. Measured gas temperatures generally increased during a warm-up test. The adiabatic surface temperature, at which the heat transfer per cycle was zero, was highest at locations nearer to the intake valves, as can be inferred from the data in Figure 6.10.

6.5 Correlation between Heat Transfer and Gas Flow through the Inlet Port

The convective effects of steady gas flows in various situations have been widely investigated in the past. In most cases, the results have been summarised in the form of a correlation between a series of non-dimensional groups: *Nu* representing the heat transfer from the surface over which the convection is occurring; *Re* representing the flow characteristics; and *Pr* representing the properties of the gas. In the case of turbulent flow of gas at or below 55.5°C through a tube, Burghardt **[6.6]** gives this relationship as:

$$Nu = 0.023\ (Re)^{0.8}\ (Pr)^{n} \qquad (6.1)$$

where n is 0.4 when the gas is being heated and 0.3 when the gas is being cooled. For steady flow through an inlet port, where the gas is being heated and Pr can be considered invariant, Martins and Finlay **[6.3]** deduced the correlation between Nu and Re given in Eqn. 6.2; they showed that this gave good agreement to a similar correlation developed by Ede et al **[6.7]** for a heated tube immediately downstream of a 90° radiused bend.

$$Nu = 0.0675\ Re^{0.713} \qquad (6.2)$$

In the current work, uncertainties in deducing the effective temperature difference between the gas and the port surface have limited the data which can be used to make comparisons with Eqn. 6.2. The data plotted in Figure 6.13, however, has been derived from measurements with thermocouple TC1 and Sensors 1 and 2 with a fully-warm engine. Here the values of Re are calculated using a mean value of air flow rate into the engine. The adjusted correlation line through this data, given by Eqn. 6.3, uses the same Re index as Eqn. 6.2 with the scaling constant increased by a factor of 2:

$$Nu = 0.135\ Re^{0.713} \qquad (6.3)$$

This indicates that heat transfer rates arising upstream of the port bifurcation from the unsteady port gas flows caused by a firing engine are approximately double those predicted from the steady flow result. This is at least partly because the turbulence created by the pulsation of the flow continues to cause convection during the period of no bulk flow.

6.6 Discussion

Principally, these measurements of "dry-port" heat transfer were made for comparison with convective heat transfer data produced by Martins and Finlay **[6.3]** and presented in the form of a correlation between values of Nu and Re. This would provide confirmation of the experimental apparatus and test procedure used here. Comparable data was, however, only produced from Heat Flux Sensors 1 and 2, with a correlation which indicated heat transfer rates from a firing engine are double those produced with steady flow through an inlet port. For the other sensors the effects of backflow gases on the thermal environment made the temperature differences between the gases and the port

surfaces difficult to assess, and where they could be assessed they were often too small to allow for reliable calculation of *Nu* values.

Although it was only Sensors 1 and 2 that produced data comparable with previous convective heat transfer measurements, the data recorded through the other sensors was not without corroboration. The increasing effects of backflow with proximity to the inlet valves, was also observed by Cheng et al **[6.1]** in measurements of HC concentration and gas temperature using a Fast FID and a platinum-iridium hot-wire sensor. Their results indicated similar variations with MAP in the penetration of overlap backflow effects up the inlet port, and the high gas temperatures they found to be associated with overlap backflow are commensurate with the large negative spike observed in the heat flux data. The pressure wave associated with this overlap backflow, particularly at low MAP levels, would be expected to set up oscillations in the flow through the inlet port, similar to those found by Cheng et al **[6.1]** in predictions of mass flow rate through the intake valves. Since these oscillations are of a relatively high frequency, however, their effects on the "dry-port" heat fluxes will be damped out by the response characteristics of the heat flux sensors. Compensation for these response characteristics, as shown in Figures 6.4 and 6.5, will re-amplify these oscillations but amplification of signal noise in the data makes these oscillatory effects difficult to discern.

An indication of the effect the presence of the heat flux sensors has on the heat transfer between the port walls and the gases is given in Figure 6.14. Here, the temperature at the surface of Sensors 2 and 8 is plotted around the cycle, from calculations using the finite difference model of the sensor, glue and port surface described in Chapter 5. For these calculations the port walls are assumed to have a very large thermal mass in comparison with the gas, such that the port surface temperature remains constant. In this case a value of 80°C was used for the port wall temperature below both sensors. Figure 6.14 shows that variations in the temperature difference between the sensor surface and the port wall are insignificant around the cycle in comparison with suggested gas temperature variations. The largest variation occurs across Sensor 8 during overlap backflow, with a peak temperature difference across the sensor of 6 deg. C. However, Cheng et al **[6.1]**

measured port gas temperatures of the order of 300°C during this backflow period. The presence of the heat flux sensors will, therefore, have little effect on the heat transfer between the port walls and the port gases.

Chapter 7

Heat Transfer Under Wetted-Port Conditions

7.1 Introduction

When the surfaces of the inlet port are being "wetted" by fuel, the heat transfer varies significantly from that recorded under "dry-port"conditions. This has been attributed not only to the cooling affects of the fuel, which is generally at a lower temperature than the port surfaces, but also to the processes by which fuel is transferred from the fuel film.

So far in this thesis, a phenomenological modelling approach has been used to describe fuel transfer in the intake port, based on the τ-X model proposed by Hires and Overington [7.1]. This approach is only a macroscopic description, however, of a combination of various mechanisms by which fuel is transferred from the fuel film. Possible mechanisms were identified by Aquino [7.2] as film flow along the port surface, vaporisation, and re-entrainment as droplets back into the air flow. Although liquid film flow might account for some of the transfer, particularly at low temperatures, Aquino suggests that a greater proportion is transferred by the other two methods. Aquino and Plensdorf [7.3] identified the effects of air flow over the fuel as promoting the vaporisation process, in SPI or carburetted engines, through convective mass transfer. They used an analogy between heat and mass transfer to predict the evaporation rates of single component fuels with local heating of the manifold. Sindano [7.4] applied this convective mass transfer approach to port injected systems, considering it to be the only mechanism for evaporation of fuel from the film, even with multi-component fuels. This assumes that the more volatile fuel components vaporise in the air stream, or on contact with the port walls and that the fuel film temperature is well below the boiling temperature of the remaining components. Conversely, predictions made by Chen et al [7.5] suggest the short flight-time of droplets limits vaporisation prior to deposition. They highlight the importance of convective mass transfer from the film on the port walls, and indicate that film vaporisation rates depend on fuel composition and engine speed more than manifold

pressure. The effects of fuel composition identified by both Chen et al **[7.5]** and Turin et al **[7.6]** are that lighter components with boiling points lower than the film temperature will boil off, while heavier components will evaporate through convective mass transfer or, particularly at low temperatures, flow into the cylinder as a film.

The bench-rig studies carried out by Martins and Finlay **[7.7, 7.8]** and Ladommatos **[7.9]** were concerned with heat transfer and fuel vaporisation from the port and valve surfaces. Ladommatos used water as the injected medium, with which he found that vaporisation only accounted for a small fraction of the injected fluid, re-entrainment and film flow being the main transport mechanisms. Martins and Finlay **[7.8]**, injecting gasoline at simulated light load conditions, observed that almost all the injected fluid was vaporised when targeted at the centre of the valve and injected when the valves were closed. At other operating conditions and with different targeting they found that the proportion vaporised decreased. Martins et al **[7.10]** interpreted this as evidence that fuel evaporates more quickly from the back of the valves than from other port surfaces. It is, therefore, fuel transfer from these other port surfaces which they considered to be the main cause of delays in engine transient response. Although Martins and Finlay **[7.7]** made some measurements of heat transfer in a section of the inlet port, their measurements were limited and used methanol and ethanol rather than gasoline as the injected fuel.

All of these models and bench-rig studies have clarified further aspects of the interaction between heat transfer, gas flow and fuel deposition in the intake port. However, the limited amount of work on firing engine conditions reported in the literature creates a lack of understanding of which factors most influence τ and X. This remains a limitation on the ability to predict fuel transfer behaviour. To aid this understanding, this chapter and Chapter 8 present measurements of inlet port heat transfers with the engine running on both pump-grade unleaded and isooctane fuels, along with discussions of the results and a model of the processes that occur.

7.2 The Effects of Fuel Deposition on Inlet Port Heat Transfer

To ascertain the effects of fuel on the heat fluxes, data were recorded with the normal fuel injection arrangement, with fuel delivery split equally between the two intake port branches. Sensor 1, which is upstream of the plane of injection, remained dry. The other sensors were wetted by deposited fuel to an extent which varied with sensor location, injector type and operating conditions. The injector types used were a single-spray, a twin-spray and a four-hole. Initially, heat transfer rates were recorded at the same running conditions used to determine the "dry-port" heat fluxes in Chapter 6. Figure 7.1(a) shows typical results for Sensor 7 from these tests, with the engine fully-warm, using a single-spray injector. Figure 7.1(b) shows "dry-port" heat flux data recorded at the same conditions, while Figure 7.1(c) shows the "net" results obtained by subtracting the "dry-port" data from the raw "wetted-port" data. As with all the following crank-angle resolved data, these data are the mean of ten, consecutive, measured cycles, and have been post-processed to compensate for the dynamic response characteristics of the heat flux sensors. The sign convention described in Chapter 3 has been retained, with positive heat fluxes indicating a flow out of the port walls and vice versa for negative values. If the "dry-port" value is negative and the "wetted-port" value is positive, both contribute to the implied net heat flux to the fuel on the film surface. It is these "net" results which are used in the following discussion of heat transfer to the fuel. Figure 7.1 shows that the heat fluxes recorded when the port is "wetted" are typically much larger than those for a "dry-port". This is particularly the case in regions of the port where fuel deposition is heaviest. With few exceptions, the inferred "net" values for heat transfer to deposited fuel are insensitive to changes at the interface with the gas stream when the surface is "wetted".

Inferred heat flux to the fuel varies substantially from sensor to sensor, primarily because of spatial variations in deposition rate. The prime area of deposition is the floor of the intake port around the locations of Sensors 4 and 7. This is reflected in the data presented in Figure 7.2 for injection with a single-spray injector. With injection timed to end at 270°ATDC, the variation in heat flux recorded by Sensor 7 exhibits a sharp rise at or shortly after the end of fuel injection to an initial peak value near to the time when inlet

valve opening occurs. A second peak occurs at around 360°ATDC, due to the effect of overlap backflow on fuel vaporisation. The fall in heat flux after the valve overlap period is arrested by the influence of the forward induction flow on mass transfer conditions and the lower temperature of the fresh mixture passing through the intake port. Throughout the remaining part of the engine cycle the heat flux falls monotonically but remains measurable, indicating the continued presence of fuel on the sensor. For Sensors 4 and 5, each of which record peak heat flux values of more than 5 kW/m^2, the heat flux is near to 0 for over ¾ of the cycle suggesting that deposited fuel either fully vaporises or reaches an equilibrium condition. The variation of heat flux recorded by Sensor 4 after the end of fuel injection and throughout the period up to the inlet valve closing point has similar features to the variation recorded by Sensor 7, with the exception of a faster decay in the heat flux during the induction stroke. Sensor 3, which is mounted on the side wall of the port, is unlikely to receive fuel by direct deposition and the small heat flux spike which occurs during the valve overlap period tends to support this. Sensors 6 and 8, which are mounted near the intake valve on the side walls of the port, are again only lightly wetted by fuel deposition. This appears to be vaporised by the backflow of gases during the overlap period, which produces a short but large magnitude (50 kW/m^2) spike in heat flux to the fuel. No data is shown for Sensors 1 and 2, since with the single-spray injector fitted there was no difference between the "wetted-port" and "dry-port" heat flux data at these operating conditions.

7.3 Intra-Cycle Variations in Heat Flux to the Fuel

With EOI timed at 270°, the close proximity of fuel injection to the timing of IVO made it difficult to distinguish independent effects of the two events. By varying the injection timing, an insight into the relative importance of these effects on heat flux to the fuel can be obtained. Figure 7.3 shows variations over the cycle for five injection timings with a single-spray injector, as measured through Sensor 7. For EOI at 450°ATDC, fuel is injected when the forward induction flow is fully developed. This appears likely to have modified the deposition pattern within the intake port slightly, reducing the proportion of the injected fuel deposited on Sensor 7. An indication that this has occurred is given by

values for the integrated heat transfer over the cycle (see Figure 7.4): the value for the EOI = 450°ATDC case is lower than for the other injection timings, each of which give similar values. For this reason the following has focused on the remaining four injection timing cases. In general, the variations show similar peaks in heat flux shortly after the end of fuel injection, followed by a decay until the valve overlap period when a spike in heat flux occurs, and then by a more extended hump in the variation associated with the forward induction and displacement backflow periods.

Excluding the inlet-valve-open period and overlaying the crank angle variations such that the positions of peak heat flux after the end of injection are aligned, gives the result shown in Figure 7.5(a). The variations for each injection timing are very similar. In each case there is an underlying heat transfer rate of 3.7 kW/m^2 throughout the cycle, associated with equilibrium diffusive mass transfer from the fuel film under the relatively quiescent conditions which pertain over most of the engine cycle. Departures from this underlying value arise as newly injected fuel is heated to the film temperature and lighter fractions vaporise, again through a diffusive mass transfer mechanism. Realigning and then subtracting the mean variation given by Figure 7.5(a) from the data in Figure 7.3, gives a heat flux "remainder". This has a variation over the cycle which is, to a good approximation, independent of injection timing. Figure 7.5(b) shows the results for EOI at 0, 90, 270 and 630°ATDC. The "remainder" is associated with enhanced heat transfer due to the high temperature of backflow residuals and the convective effects of gas flows generated during the inlet-valve-open period. The first spike in the variation is associated with the overlap backflow, the second period of enhancement is associated with the forward induction flow, and the third extended period is associated with the displacement backflow effects and the decay of the subsequent gas motion. For this particular engine running condition, and Sensor 7 location, the relative importance of the various effects can be estimated by integrating each contribution over the appropriate crank-angle period. To discriminate between the effect of the overlap backflow and the forward induction flow, the boundary is taken arbitrarily to be at the crank angle where the enhanced effect is a minimum (labelled A in Figure 7.5(b)). Likewise, the boundary between the effects of the forward induction flow and the displacement backflow is taken to be at the crank

angle labelled B. Adopting these assumptions, heat transfer associated with fuel warming and diffusion accounts for 76% of the total, the enhancement due to convective mass transfer during the forward induction period accounts for 13%, the effects of displacement backflow and the decay of gas motion account for 10%, and the overlap backflow produces an enhancement accounting for the residual 1%. Of the heat transfer associated with fuel warming and diffusive mass transfer, knowledge of the fuel deposition characteristics indicates that 51% (38% of the total heat transferred) is associated with equilibrium mass transfer of the established fuel film, 25% (19% of the total) with warming the deposited fuel to the film temperature, and 24% (18% of the total) with vaporisation of the lighter fuel fractions within the engine cycle.

7.4 Heat Transfer Variations Caused by Changing Operating Conditions and Injector Type

To investigate in more detail the effects of injector type, MAP, fuel flow rate and coolant temperature on the heat transferred to the fuel per cycle, a further series of tests was undertaken in which each of these parameters was varied independently. The MAP and fuel flow rate variations were undertaken with the engine running fully-warm, at a speed of 1000 RPM and with EOI timed at 270°ATDC of the firing stroke; the range of MAP and AFR values used is shown in Table 7.1, and the results of these tests for each injector type are summarised in Figures 7.6(a)-(c), which show estimated values for the total heat transfer to the fuel film. Values of local heat transfer per unit area vary substantially over the surface of the port, and the total area covered by the sensors is a small fraction of the total port surface area. As a consequence, any estimate of the total heat transfer to the fuel film will be subject to large uncertainties. However, such estimates provide a useful indication of the effects of changes in operating conditions. The values plotted in Figures 7.6(a)-(c) were obtained from the average "wetted-port" heat flux over Sensors 2 to 8 multiplied by an estimate of the total area of the port downstream of the manifold flange face. No surface area weightings have been applied to individual sensors and the "dry-port" heat transfer contributions have been subtracted before plotting the data. From these data it can be seen that at a given MAP increasing fuel flow rate increases the rate

of heat transfer. Conversely, increasing MAP at a given fuel flow rate tends to decrease the rate of heat transfer.

Table 7.1 - Fuel Flow Rate (mg/s) for given AFR and MAP values at 1000 RPM, with EOI at 270°ATDC

AFR / MAP	18.5	14.5	13.0	11.0	10.0
0.95	150	190	220	250	275
0.79	110	145	165	190	205
0.53	75	90	100	115	125

Clarification of the reasons for these trends is given by Figure 7.7, which shows the variation of heat flux around the cycle for different fuel supply rates (Figure 7.7(a)) and manifold absolute pressures (Figure 7.7(b)). Considering first the effect of fuel supply rate at constant MAP conditions, the variation around the cycle for the lowest supply rates show the general features described earlier when injection is timed to end at 270°ATDC. As fuel supply rate is increased, the rate of rise of heat flux after injection reduces because the film temperature at which mass transfer occurs is depressed by the increased mass of fuel to vaporise. This decrease in the fuel film temperature is illustrated in Figure 7.8 by measurements of the temperature of Sensor 7 as the fuel flow rate is varied. At the highest fuel supply rate only one peak in heat flux occurs, during the overlap backflow period. During the forward induction flow, the heat flux is highest for the highest fuel supply rates, and in all cases the heat flux decays monotonically throughout the induction period and over the remainder of the cycle to a similar low level at the time of the next fuel injection event. Although the heat transfer per cycle increases with fuel supply rate, it does not increase in direct proportion to it, and by implication there is less heat transfer per unit mass of fuel at higher rates of supply. This is at least partly because of the reduction in film temperature. In Figure 7.7(b) the results were obtained for stoichiometric mixture conditions and hence as manifold pressure was reduced the fuel

supply rate was also reduced to maintain this ratio. The effect of reducing MAP is to promote an increasing heat flux soon after the end of injection associated with fuel vaporisation at lower temperatures and partial pressures. It is this improved vaporisation at lower MAP's which produces the observed increase in heat transfer with decreasing MAP in Figure 7.6.

To examine the effects of coolant temperature, warm-ups were carried out at each of the MAP levels (0.95, 0.79 and 0.53 bar) using a stoichiometric mixture setting with the engine again running at 1000 RPM and EOI timed at 270°ATDC of the firing stroke. For each warm-up the engine was cold soaked to a uniform temperature below 0°C while the fuel and inlet air were kept at laboratory ambient temperatures. This resulted in a nominal fuel temperature of 20°C at the start of each test, typically increasing to 30°C at fully-warm conditions, as the spill-back flow was returned to the supply tank. Figures 7.9(a)-(c) show the variation in local rates of heat transfer to the fuel during these warm-ups with a twin-spray injector fitted. Although even at the lowest coolant temperatures apparently significant heat transfer rates were recorded, values less than 50 J/m^2 have been deemed to be within levels of measurement uncertainty and neglected. The injected fuel is generally warmer than the port walls at the low end of the coolant temperature range (see Figure 7.10), so the positive heat transfer from the surface must result from fuel evaporation and indicates the importance of convective mass transfer in the vaporisation process at these conditions. Further evidence for this is given in Figure 7.11, which shows the variation with coolant temperature of crank-angle resolved heat fluxes for the single-spray injector. Here, at low coolant temperatures (0-30°C) very little heat transfer occurs outside of the inlet valve open period, when mass transfer is driven by the increased temperature of the overlap backflow and the convective effects of all the gas flows. By the time the coolant temperature reaches 60°C, heat flux peaks are apparent both immediately after fuel injection and during the inlet valve open period. Finally, at fully-warm operating conditions (90°C) the comparative effects of the events around the cycle are as described for Figure 7.5.

The results presented in Figure 7.9 show that fuel distribution varies with MAP. For a MAP of 0.95 bar, most deposition occurs around Sensor 7 and Figure 7.9(a) shows that heat transfer levels measured through Sensors 4, 5, 6 and 8 are relatively low. This was supported by the photographic evidence, recorded at high MAP values, showing that the twin-spray injector produces two sprays of large droplets directed towards the backs of the valves, close to the position of Sensor 7. A redistribution of deposition around Sensor 4 and Sensor 7 occurs when MAP is lowered, as indicated by comparing Figure 7.9(a) and Figure 7.9(c). The heat transfers recorded through Sensor 4 at a MAP of 0.53 bar are the highest recorded for any sensor across the test range, even though the rate of fuel injection is low. This apparent redistribution of fuel was most obvious with the twin-spray injector and could be due to changes in spray characteristics as MAP is lowered, like those observed by Nogi et al **[7.11]**, or fuel redistribution, as suggested by Curtis et al **[7.12]**. The same occurred with the four-hole injectors at the low MAP condition, to a lesser extent, when heat transfer rates recorded by Sensors 6, 7 and 8 had similar magnitudes. With the single-spray injector the fuel appeared to centre around Sensor 7 at all MAPs.

In Figures 7.12(a)-(c) the effects of injector type on the warm-up data are compared. These three figures show how the estimated total heat transfer per cycle in Joules for each injector type varies with coolant temperature, after subtracting the "dry-port" heat transfer contributions, at three different fuel flow rate and MAP levels. The increase in heat transfer with increasing coolant temperature is similar for each injector, despite marked differences between their deposition patterns. This is coincidence and somewhat misleading. The four-hole injector data is the average of results from two, nominally identical injectors, and the individual sets of data diverge from similar values at 0°C to differ by a factor of two at fully-warm conditions. Some explanation of these inter-injector variations was offered by fully-warm tests carried out with the twin-spray injector in which the splitter cap was rotated through a series of known points and the effects on inlet port heat transfer measured. Figure 7.13 shows the results of these tests, where it can be seen that the orientation of the injector sprays is at least as important as the spray characteristics in determining the heat transfer to the fuel.

The effect of increasing fuel flow rate at a given coolant temperature systematically increased heat transfer per cycle, seen in Figure 7.12, for both the single-spray and four-hole injectors. For the twin-spray injector, at the lowest fuel flow rate, the heat transfer showed an increase over values at the higher fuel flow cases due to the changes in spray characteristics and deposition patterns with MAP. Since AFR was maintained nominally constant at stoichiometric settings for all these tests, the higher fuel flow rates correspond to higher MAP settings, which also influence heat transfer due to the relationship between partial pressure and vaporisation rates. The effect of fuel flow rate and MAP are not separated in Figure 7.12; it has already been shown in Figures 7.6(a)-(c), however, that increasing fuel flow rate increases heat transfer and this is the dominant effect, while increasing MAP tends to reduce the heat transferred.

7.5 The Response of Heat Transfer to a Step Change in Fuel Supply

A step change in fuel supply rate at otherwise steady state engine operating conditions represents an important special case in the study of fuel transport. The rate at which the induced fuel flow changes to match the new fuel supply rate has implications for the control of induced mixture ratio to within a narrow target range. The initial and final quantities of fuel stored in surface films in the intake port are different, according to predictions based upon the phenomenological τ-X model **[7.2, 7.13]**, and the rate at which the film mass adjusts to a new equilibrium condition will depend upon heat transfer to the fuel film. By implication, heat transfer during cycles after the fuelling level change should reflect the changes in fuel deposition rate and the rate of mass transfer from the fuel film which occur.

To examine this, a test was carried out whereby the fuel injection rate was increased in a single step and the variation of the heat transfer measured by Sensor 7 was recorded until a new steady-state condition was established. The engine was run fully-warm at 1000 RPM and 0.79 bar MAP. The fuel supply rate was increased from 112 mg/s to 206 mg/s. The variation of induced mixture AFR was monitored using a UEGO sensor in the exhaust gas stream. The results for heat transfer per cycle and AFR variations are

given in Figure 7.14. The repeatability of the heat transfer variation between initial and final conditions is indicated by the upper and lower bounds on experimental data taken over eight repeated tests. The final to initial ratio of heat transfer values is in agreement with the dependence upon fuel supply rate established previously during steady-state tests.

Figure 7.15(a) shows the variation of instantaneous "wetted" heat transfer rate over twelve cycles spanning conditions before and after the change in fuel supply rate, which occurred after cycle zero. Prior to the change, heat flux peaks at around 20 kW/m^2 shortly after the end of fuel injection, and a second peak of between 11 and 15 kW/m^2 occurs during the induction period. After the change in fuel supply rate, the peak heat flux increases to 40 kW/m^2 but declines to less than 30 kW/m^2 over the first six cycles, despite the increasing value for heat transfer rate per cycle. This declining maximum is associated with changes in fuel film composition as well as quantity. Immediately after the change in fuel supply rate the fuel film will contain a higher proportion of lighter fuel fractions. This proportion will diminish, as the new equilibrium film mass and composition is approached.

For the same engine operating condition the dry surface heat transfer rate is relatively small. Subtracting this from the measured "wetted" port heat transfer variation gives the net heat transfer to the fuel shown in Figure 7.15(b) for cycles 0, 1, 5, 10 and 15. An overlay of these cycles on a crank angle base is shown in Figure 7.15(c). The changes in heat transfer variation which occur over these cycles are consistent with the inferences drawn from the steady state results. On the first cycle with the higher fuel injection rate, the early evaporation of higher quantities of light fractions produces the high peak heat flux, but as the cycle progresses the heat flux decays to levels reflecting mass transfer of the residual heavier fractions from a film mass similar to that prior to the change in fuel flow rate. Over the ensuing cycles the film mass builds up and the initial rate of rise and peak heat flux after injection both diminish, whilst heat transfer in the tail of the variation increases.

These characteristics suggest that the initial response of induced fuel flow rate to changes in supply is strongly influenced by the proportion of lighter fuel fractions in the fuel being deposited and the initial fuel film mass. The response is therefore likely to be more rapid if the initial film mass is relatively small. As the new equilibrium condition is approached, the effect of the lighter fuel fractions is diminished by dilution with the more persistent heavier fractions building up in the fuel film. For the tests carried out, this takes more than 15 engine cycles. The effects of a perturbation in the opposite direction, a decrease in fuel supply rate, are shown in Figure 7.16. Here, on the first cycle with the lower fuel injection rate, the early evaporation of light fractions is immediately diminished by dilution with the more persistent heavier fractions in the residual film from the higher fuel flow rate condition. Over the ensuing cycles the film mass diminishes, reducing heat transfer in the tail of the variation, and the initial rate of rise and peak heat flux after injection both increase. The time to establish new equilibrium conditions for perturbations in both directions is a strong function of surface temperature. This is affected by fuel composition, particularly the relative proportions of light to heavy fractions in the fuel, which dictates the temperature at which the lighter fuel components are transferred from the film. The time required will also be influenced by the persistence of the heavier fuel fractions, which dictates the equilibrium film mass.

7.6 Discussion

The changes in surface heat transfer rates associated with fuel deposition exhibit complex characteristics dependent upon engine running conditions. No attempt has been made in this Chapter to model the fundamental processes of convective mass transfer and evaporation which give rise to these characteristics. As a step towards rationalising the data, however, the functional dependence of heat transfer on fuel flow rate, MAP and coolant temperature has been examined using the data obtained from Sensor 7 (see Figure 7.17), which was "wetted" consistently by deposition over the range of running conditions tested. The results are for the single-spray injector and the "dry-port" heat transfer rate has been subtracted from the measured rate. For a given MAP, the sensitivity of heat transfer rate to fuel supply rate can be approximated to:

$$\frac{\partial \dot{Q}''}{\partial \dot{m}_f} = \exp\left(a_1 + b_1 p^2\right) \tag{7.1}$$

where a_1 and b_1 are constants. Integrating Eqn. 7.1 yields:

$$\dot{Q}'' = \dot{m}_f \exp\left(a_1 + b_1 p^2\right) + \left(a_2 + b_2 p\right) \tag{7.2}$$

where the constant of integration is assumed to be a linear function of MAP, with constants a_2 and b_2 consistent with the values of $\dot{Q}''$ for zero fuel mass flow rate inferred by extrapolation of the results given in Figure 7.17.

Data showing how $\dot{Q}''$ varies with coolant temperature is shown in Figure 7.18. To account for this dependence, Eqn. 7.2 was modified to the form:

$$\dot{Q}'' = cp + \left[\dot{m}_f \exp\left(a_1 + b_1 p^2\right) + a_2 + \left(b_2 - c\right)p\right].f(T) \tag{7.3}$$

Although there are alternatives which would give an equally good fit to the data, the function $f(T)$ was chosen as:

$$f(T) = \frac{1}{2}\left[1 + \cos\left(\frac{\pi T}{90} + \pi\right)\right] \tag{7.4}$$

and the constant c determined from the data taken at a coolant temperature of 0°C. Figure 7.19 shows that the variation given by Eqn. 7.3 compares reasonably well with the raw data in Figure 7.18. By inspection this equation is of the form:

$$\dot{Q}'' = f_1(\dot{m}_f, p).f_2(T) + f_3(p) \tag{7.5}$$

The function f_1, deduced from Figure 7.17, accounts for the effects of fuel supply rate and MAP on fuel warming and diffusive mass transfer. Variations in the fuel supply rate affect the heat transfer required to warm newly deposited fuel to the film temperature, but they also particularly affect the heat transfer to those fractions of the fuel for which the mass available is the limiting factor in the vaporisation process. Variations in MAP also have an effect, through f_3, on those fractions for which the limiting factor is the mass vaporised with the aid of convection. Function f_2 relates f_1 to the temperature of the port. At lower temperatures the evaporation of more components will be limited by convective mass transfer than by the film mass available, until at the lowest temperature recorded

convective mass transfer dominates: the heat transfer becomes dependant on MAP alone, f_1 becomes 0 and the heat transfer is given by f_3. A similar description could be attached to data recorded with each of the other injectors as borne out by Figure 7.12 where similar trends are apparent in all the data, although the constants implicit in Eqn. 7.5 will differ. The prospects of producing a general correlation for the total heat transfer to the fuel appear to be poor, however, because such large local variations arise. Nevertheless, the description given by Eqn. 7.5 should be characteristic of the regions of the port near to the valves where deposition rates are high. Combining Eqn. 7.5 and Eqn. 6.2 gives a value for heat flux as measured with the heat flux sensors under "wetted-port" conditions, which includes the surface-to-gas contribution:

$$\dot{Q}'' = Nu.\frac{k\theta}{d} + f_1(\dot{m}_f,p).f_2(T) + f_3(p) \qquad (7.6)$$

Evaluating the surface-to-gas contribution in Eqn. 7.6 requires knowledge of the magnitude and sense (positive or negative) of the surface-to-gas temperature difference from Chapter 6. Figure 6.12 illustrated how temperature differences vary as the engine warms up. For high MAP, low surface temperature conditions, the direction of heat transfer is towards the surface. As the surface temperature increases, the temperature difference becomes progressively less negative and, at most locations, eventually positive by the time fully-warm conditions are established, giving rise to heat transfer from the surface to the gas. The effects of backflow at low MAP values raise the effective gas temperatures and over much of the region downstream of the port bifurcation, heat is transferred from the gas towards the surface throughout the warm-up.

Sensor 7 was located in the region where most fuel deposition occurs. At this position, for fully-warm conditions, the direction of heat transfer was always from the surface towards the gas when the port was dry. Comparing the results shown in Figures 6.10 and 7.9 indicates that at fully-warm conditions, the inferred heat transfer to the fuel film has been reduced by heat transfer to the gas stream. When the surface temperature is below typically 40°C during a warm-up, the heat transfer to the fuel film is increased by heat transfer from the gas stream. It must be emphasised, however, that these inferences are based on the assumption that heat transfer to or from the gas stream is the same for

"dry" and "wetted" surface conditions. More accurately, these changes in heat transfer rate should be described as being *associated* with fuel deposition.

Unlike the "dry-port" conditions discussed in Chapter 6, the temperature of the sensors when "wetted" was lower than the assumed surface temperature, particularly in areas of heavy fuel deposition. As fuel flow rate and hence fuel film mass increased the sensor temperature decreased further (see Figure 7.8), reflecting a drop in the fuel film temperature. This will be at least partly due to the insulating effect of the heat flux sensor creating a temperature drop between the port-wall and the fuel film, because of the relatively high rates of local heat transfer in areas of heavy deposition. Figure 6.14 showed crank-angle resolved sensor surface temperatures calculated using a finite difference model of the sensor from the inferred "dry-port" surface heat fluxes. Using the same finite difference model, crank-angle resolved temperatures were calculated for a "wetted" Sensor 7 at the surface and at the position of the incorporated T-type thermocouple used to measure sensor temperature. Typical results are shown in Figure 7.20. Figure 7.21 shows mean cycle temperatures calculated from these data over a range of fuel flow rates, along with experimentally measured sensor temperatures for the same operating conditions. The experimental data indicates that the sensor is at a lower temperature than can be explained purely by the insulating effects of the sensor. Other factors in this temperature drop will be the contribution the sensible internal energy of the fuel film makes in providing the required heat of vaporisation for the mass transfer which is occurring, and the effect of newly deposited fuel from the colder injection spray.

For "dry-port" conditions heat transfer per cycle varies between 0 and 300 J/m^2 depending on location, towards the surface at low temperatures and away from the surface at fully-warm conditions. The changes in measured heat transfer per cycle associated with fuel deposition are invariably positive (from the surface). These changes vary with location but, in the vicinity of highest deposition, are in the range 1000 to 1500 J/m^2 at fully-warm operating conditions. During the early period of engine running after start-up, when both surface temperatures and the temperature of the fuel supply are around 20°C, the change is typically 300 J/m^2. The effect of fuel supply temperature has not been examined

systematically in the current work, but a supplementary test was carried out with the fuel supply cooled to an initial temperature of 0°C. Figure 7.22 shows results from this test along with results from the equivalent test with fuel at ambient laboratory temperature, while Figure 7.23 shows the difference in fuel temperatures between the two tests. Comparing the results produced by tests at different fuel temperatures, it is clear that lowering the fuel temperature from 20°C to 0°C gives rise to increases of up to 100 J/m^2 in heat transfer per cycle during the early period of engine running, in areas of the port where fuel deposition is most concentrated.

Chapter 8
Heat Transfer to Isooctane

8.1 Introduction

The work described in this chapter extends the study of inlet port heat transfer presented in Chapters 6 and 7 to cases when the engine is running on a single-component fuel, 2-2-4 trimethylpentane (isooctane). The results obtained for isooctane are of particular interest in connection with the development of a model to describe mass transfer from the fuel film produced by deposition. As for the tests with pump-grade unleaded fuel, the dry-surface heat transfer rates found in Chapter 6 were subtracted from values measured when the sensors were wetted by fuel, to determine the effect of the latter. With both fuel types, the heat transfer rate to the fuel reaches peak values up to around 50 kW/m^2 during the engine cycle, and is typically 5 kW/m^2 on average in regions of heavy fuel deposition. The heat transferred per cycle depends upon engine operating conditions: during warm-up, as coolant temperature increased from 0°C to 90°C, this increased from typically 300 J/m^2 to 1000 J/m^2; for a given coolant temperature, heat transfer values generally increased when MAP was lowered or as supplied fuel flow rate was increased. In general, the effect of fuel deposition on heat transfer rate, when running on pump-grade unleaded gasoline, could be characterized as a function of injected fuel flow rate, MAP, and engine coolant temperature or surface temperature. This function reflects the underlying mechanisms of diffusive and convective mass transfer from the surface film. However, the extent to which these characteristics were dependent on the properties of the fuel used was less clear and to clarify this the work described here, using isooctane fuel which has known thermodynamic properties, was undertaken. The characteristics of isooctane are summarised in Table 8.1 **[8.1]**.

Table 8.1 - Summary of the Characteristics of 2-2-4 Trimethylpentane **[8.1]** Utilised in this Chapter

Temperature (°C)	Sat. Vapour Pressure (bar)	h_{fg} (kJ/kg)
20	0.051	309.4
30	0.083	305.4
40	0.130	301.3
50	0.195	296.9
60	0.280	292.2
70	0.408	287.4
80	0.568	282.6
90	0.774	277.5
100	1.035	272.0
c_p (J/kg K)		2

As during the previous investigations, all the work described in this chapter was carried out on the cylinder head of a Ford 1.8L high output Zetec engine fitted to the Ricardo Hydra single-cylinder rig. The test work was carried out with a single-spray, single-pintle injector fitted. This delivered fuel in a cone which impinged on the central bifurcation of the intake port. The photographic observations of Chapter 4 showed that this bifurcation deflected the spray partly on to the lower surface of the intake port and partly on to the back of the two intake valves. Of the proportion of fuel deflected down on to the port surface, the highest proportion was deposited onto the sensor located as shown in Figure 8.1. In this chapter the analysis has been based on results taken from this sensor.

8.2 Variations in Heat Flux Around Engine Cycle

The significant variation recorded in heat flux through the sensors around an engine cycle was as a result of the various events within the inlet port, particularly fuel injection and

forward induction flow. To investigate these measured variations further and establish their underlying phenomenological causes, a warm-up test was undertaken with the engine running on isooctane and EOI timed to occur at TDC of the firing stroke. Tests with pump-grade unleaded fuel showed that injecting at this point in the cycle clearly separated the effects of fuel injection from those of the forward induction flow (see Figure 7.3). The other operating conditions used for the isooctane fuelled warm-up were an engine speed of 1000 RPM, a MAP of 0.53 bar, and a fuel flow rate of 90mg/s, such that the AFR was stoichiometric once the engine was fully-warm. Data were recorded during an engine warm-up between 0°C and 90°C, after cold soaking to a uniform temperature below 0°C with the fuel supply at laboratory ambient temperature. Figure 8.2 shows the resultant crank-angle resolved heat flux variations. These are "net" values obtained, after compensating for heat flux sensor response, by subtracting the values recorded previously in the absence of fuel deposition. Depending on whether these "dry-surface" values indicate heat transfer towards the surface (a negative value) or from the surface, the net heat transfer to the fuel is increased or decreased respectively relative to the raw data values.

Injection timing was phased to end at 0°ATDC, which is earlier than the standard EOI at 270°ATDC but was selected because it separates two distinct features of the heat transfer variation. Generally, shortly after the fuel injection event, heat transfer rates peak; this is associated with the arrival of fuel on the sensor. Heat is transferred to this fuel as its temperature is raised to that of the port wall and as vaporisation occurs raising the partial pressure of fuel vapour above the film. The rate of heat transfer then decreases monotonically until the forward induction period of the engine cycle, when a second peak occurs due to an increased rate of convective mass transfer from the film. At lower temperatures this peak corresponds to the maximum heat flux arising during the cycle. At these low coolant temperatures the difference between the fuel and surface temperatures is small, as is the partial pressure of the fuel vapour, requiring relatively little heat transfer to raise the film temperature to the surface temperature. This temperature difference and the partial pressure above the film both increase as the engine warms-up, giving rise to the increasing magnitude of heat flux shortly after fuel injection has taken

place. When the coolant and surface temperature increase above approximately 50°C, the second peak is reduced to the level of a small perturbation in heat transfer rate, indicating that the initial rate of fuel vaporisation has been sufficient to reduce the film mass or surface area substantially.

8.3 Variations in Integrated Heat Transfer During Engine Warm-Up

Analysis of the results from the tests with multi-component fuels showed that integration of the crank-angle resolved heat flux data around the cycle provided a useful indication of trends in the data across the warm-up. With isooctane as the fuel, this variation in the integrated values of heat transfer per cycle was closely linked to the changes in underlying vaporisation mechanism observed in the crank-angle resolved data. Figure 8.3 shows the integrated heat transfer values derived from the test described above, where it can be seen that a peak occurs at a coolant temperature of around 50°C, the temperature above which the forward induction flow ceases to play an important part in the vaporisation process. To establish how these trends varied with operating conditions, particularly MAP and injected fuel mass, measurements were made during a further series of warm-ups. For this second set of tests data were recorded over the range of MAPs and fuel flow rates given in Table 8.2, during further engine warm-ups between 0°C and 90°C. In these tests the engine was run with EOI timed at the standard 270°ATDC of the firing stroke, at a speed of 1000 RPM. In the following, the heat transfer rates referred to are again net values obtained by subtracting the values recorded previously in the absence of fuel deposition.

Table 8.2 - Range of Operating Conditions used in Warm-Up Tests (Coolant Temperatures 0-90°C) Run at 1000 RPM with Isooctane as the Fuel

Test	MAP (bar)	Fuel Flow Rate (mg/s)	EOI (°ATDC)
Initial Test	0.53	70	0
2nd Set:1	0.53	70	270
2nd Set:2	0.53	90	270
2nd Set:3	0.79	120	270
2nd Set:4	0.95	170	270

Figures 8.3 and 8.4 show that when the crank-angle resolved data is integrated up to give values of heat transfer per cycle, there is relatively little difference between data recorded with the end of injection (EOI) occurring at 0° ATDC and that recorded with the EOI at 270° ATDC. Values of heat transfer per cycle recorded with the latter injection timing over the range of operating conditions tested are shown in Figures 8.5 and 8.6. Figure 8.5 shows the effect of changing load whilst running at stoichiometric mixture settings, indicating that increasing load increases both the peak value of heat transfer per cycle and also the coolant temperature at which this occurs. Although both MAP and fuel flow rate change over the three test conditions, fuel flow rate is the dominant variable; this is evident in the results presented in Figure 8.6, which shows two data sets obtained at a constant MAP with fuel flow rate varying. In both Figures 8.5 and 8.6, for a given coolant temperature below that at which the heat transfer per cycle peaks, the heat transferred is relatively independent of fuel flow rate and, in this case, MAP.

8.4 Modelling of Heat Transfer and the Fuel Film Vaporisation Process

In the previous analysis of the measured heat transfer rates, resulting when isooctane is used as a fuel, it has been inferred that there are three basic processes that give rise to this transfer of heat between the port walls and the injected fuel:

(i) raising the sensible heat of the injected fuel to increase its temperature from injection temperature to the fuel film temperature;

(ii) diffusive mass transfer of the fuel film, requiring latent heat of vaporisation and dependent upon the vapour concentration gradient above the film;

(iii) convective mass transfer of the fuel film, also requiring latent heat of vaporisation, associated with the convective effects of the various gas flows through the port, particularly the forward induction flow.

An energy balance for the fuel film suggests that the net rate of heat transfer to the fuel deposited on the sensor should be equal to the increase in sensible internal energy of the fuel as its temperature is raised from an initial value to some film temperature, plus the latent heat required to vaporise a proportion of the deposited fuel. This is given by Eqn. 8.1:

$$q'' = t_{cyc}\left[(\dot{m}'')_{dep} c_p \Delta T + (\dot{m}'')_{vap} h_{fg}\right] \qquad (8.1)$$

Eqn. 8.1 cannot be evaluated, however, without knowledge of the rate of vaporisation produced by diffusion and convective mass transfer and limitations on this imposed by the availability of fuel.

The relative importance of diffusive and convective contributions to mass transfer rates depends on the timing of fuel injection within the cycle, port surface temperature, and gas flow conditions. For the conditions pertaining to Figure 8.2, when injection occurred during the compression stroke, mixture motion in the port will be relatively quiescent, and the high heat flux, arising soon after fuel is deposited at the higher coolant temperatures, is associated with mass transfer by diffusion. In such cases, diffusion and convection appear to be of similar importance to the total mass transfer occurring over the cycle, with convection dominating at low temperatures and diffusion dominating at high temperatures. Both mechanisms depend on vapour concentration gradients in a similar way. For diffusion of a volatile liquid through stagnant air Stefan's Law can be used. This is quoted by Kay and Nedderman **[8.2]** as:

$$N = \frac{Dp}{LRT} \ln\left(\frac{p}{p - p_{sat}}\right) \qquad (8.2)$$

where N is the molar flux (mol/m^{2}s), D is the diffusivity of vapour from the volatile liquid through the surrounding gas (m^2/s), R is the universal gas constant (J/mol K) and all the other variables are defined in Figure 8.7, a diagram of Stefan's experiment used to establish rates of diffusion. Eqn. 8.2 has been applied in the following way to diffusive

mass transfer of the inlet port fuel film, as signified by $(\dot{m}'')_{dif}$ the diffusive mass flux (kg/m^{2}s):

$$(\dot{m}'')_{dif} = \frac{M_v D p}{(d/2)RT} \ln\left(\frac{p}{p - p_{sat}}\right) \tag{8.3}$$

Here, p represents the value of MAP (Pa) and p_{sat} represents the saturation pressure (Pa) of the fuel vapour at the given film temperature, while M_v is the molar mass (kg/mol) of the fuel vapour, and d is the diameter of the inlet port at the point being considered. The diffusivity of fuel vapour in air was calculated from the equation quoted in Coulson and Richardson **[8.3]**:

$$D = \frac{1.013 \times 10^{-7} T^{1.75} (1/M_a + 1/M_b)^{1/2}}{P\left[\left(\sum_a v_i\right)^{1/3} + \left(\sum_b v_i\right)^{1/3}\right]^2} \tag{8.4}$$

where a and b are the two components for which the diffusivity is being calculated, M_a and M_b are their respective molecular masses, and Σv_i is the summation of special diffusion volume coefficients for components a and b quoted in Table 8.3.

Table 8.3 - Special diffusion volume coefficients for air and isooctane (C_8H_{18}) **[8.3]**

Component	Diffusion Volume
Air	20.1
Isooctane	167.64

Spalding **[8.4]** states that the assumptions underlying Eqn.(8.2) are too complex to allow generalisation to systems where the gas is not stagnant but flowing. Therefore, he outlines in **[8.5]** a description of mass transfer under convective conditions based around the following equation for convective mass flux, $(\dot{m}'')_{con}$:

$$(\dot{m}'')_{con} = gB \tag{8.5}$$

where g is the mass conductance (kg/m^{2}s) between the film and the intake port gases and B represents the mass transfer driving force given by:

$$B = \left(\frac{m_G - m_S}{m_S - m_T} \right) \tag{8.6}$$

In Eqn. 8.6, m_T is the vapour mass fraction within the fuel film, assumed to be 1; m_S is the fraction immediately above the fuel film surface, and is determined from the partial pressures of the vapour and air and their respective molecular weights. The vapour in this area is assumed to be saturated at the fuel film temperature. Finally, the mass fraction m_G of fuel vapour in the main flow is small and assumed to be 0.

The value of mass conductance can be found from knowledge of the Stanton number (*St*):

$$St = \frac{g}{G} = \frac{Sh}{(Re.\,Sc)} \tag{8.7}$$

where G is the bulk gas velocity along the centre line of the port (m/s), and *Sh*, *Re* and *Sc* are the Sherwood, Reynolds and Schmidt numbers respectively. There is, however, insufficient information in the measurements of heat transfer made with the heat flux sensors to allow *Sh* to be calculated directly. Instead, the Reynolds Analogy between momentum, heat and mass transfer can be utilised:

$$St = St^* = \frac{c_f}{2} \tag{8.8}$$

where c_f is the skin friction factor and *St** is a modified form of the Stanton number derived from heat transfer measurements when no mass transfer is occurring. This uses a relationship which is analogous to Eqn. 8.7, but with *Sh* and *Sc* replaced by *Nu* (Nusselt number) and *Pr* (Prandtl number):

$$St^* = \frac{Nu}{(Re.\,Pr)} \tag{8.9}$$

Kay and Nedderman **[8.2]** suggest that an improvement on Reynolds Analogy is offered by the J-Factor Analogy, in which:

$$St = St^* \left(\frac{Pr}{Sc} \right)^{\frac{2}{3}} \tag{8.10}$$

which leads to the definition of mass conductance given by Spalding **[8.5]**:

$$g^* = St^* G \left(\frac{D\rho}{k/(c_p)_{gas}} \right)^{\frac{2}{3}} \tag{8.11}$$

in which the * again indicates values derived from heat transfer measurements when no mass transfer is occurring, ρ is the density (kg/m^3) of the mixture above the film, while k and $(c_p)_{gas}$ are, respectively, the thermal conductivity (W/m K) and specific heat capacity (J/kg K) of the inlet port gases. Spalding **[8.5]** adds that when utilising this derivation of mass conductance Eqn. 8.5 should be modified to:

$$(\dot{m}'')_{con} = g^* \ln(1 + B) \tag{8.12}$$

There are clear similarities between Eqns. 8.3 and 8.12, particularly in the form of the ln function, which in both cases will tend to infinity as p_{sat} approaches MAP. Spalding **[8.4]** reflects this by offering a form of Eqn. 8.12 for a situation in which no convection is occurring and the mass transfer will be purely diffusive:

$$(\dot{m}'')_{dif} = \frac{D\rho}{d/2} \ln(1 + B) \tag{8.13}$$

Although less accurate than Eqn. 8.3, Eqn. 8.13 is useful for making an estimate of the ratio between the values of mass flux given by Eqn. 8.12 and those for diffusive mass transfer when no convection is occurring. For temperatures below those at which the function ln(1 + B) tends to infinity, Eqns. 8.11, 8.12 and 8.13 can be combined to give the proportion of the mass transfer that is diffusive when convection is also occurring:

$$\frac{(\dot{m}'')_{con}}{(\dot{m}'')_{dif}} = \frac{d/2}{D\rho} \cdot St^* G \cdot \left(\frac{D\rho}{k/(c_p)_{gas}} \right)^{2/3} \tag{8.14}$$

This gives values representative of *Sh*, which, being directly analogous to *Nu* **[8.6]**, is the ratio of mass transfer by convection to that by diffusion across a characteristic dimension. Based on this interpretation, the value of *Sh* is unity when there is no convection and the mass transfer is purely by diffusion. Typical values derived from Eqn. 8.14 are between 10 and 20 for temperatures below those at which the ln function tends to infinity. These are of the same order of magnitude as the values of *Nu* derived for gas flows through a "dry-port". At higher temperatures, when the mass transfer driving force becomes infinite, fuel vaporises even during the quiescent period of the cycle (see Figure 8.2). Under these conditions, the dominant mechanism for vaporisation is diffusive mass transfer.

In principle, therefore, over most of the temperature range, values of $(\dot{m}'')_{vap}$ for Eqn. 8.1 can be derived by calculating $(\dot{m}'')_{con}$ from knowledge of flow conditions and the thermodynamic properties of the gas and fuel. However, the complexity of conditions in the port and measurement limitations give rise to large uncertainties in the calculation of g^*, required for the derivation of $(\dot{m}'')_{con}$. In view of this, g^* has been deduced to best fit the experimental data for the heat transfer characteristics, making use of Eqns. 8.1 and 8.12 to obtain:

$$g^* = \frac{\dot{Q}'' - (\dot{m}'')_{dep}\, c_p\, \Delta T}{\ln(1 + B)\ .\ h_{fg}} \qquad \textbf{(8.15)}$$

Here, the value of g^* reflects the influence of both diffusive and convective mass transfer mechanisms. When evaluating this, measured values of heat transfer rate $\dot{q}''$ have been used together with values of $(\dot{m}'')_{dep}$ inferred using Eqn. 8.16, described later. Figure 8.8 shows the derived variation of g^* with surface temperature, for three MAP values. In general, across the range of temperatures from 30°C to 80°C, the mass conductance value is weakly dependent on MAP and effectively constant. Values for g^* at surface temperatures less than 30°C are more variable. It is not clear if this is a real effect or a consequence of uncertainty in the experimental data. In the following the mass conductance has been taken as a constant independent of surface temperature throughout the whole range of surface temperatures examined.

Using the deduced value of mass conductance, the predicted rate of vaporisation is as shown in Figure 8.9, for three operating conditions. As surface temperature increases, the mass flux increases monotonically towards infinity as the equilibrium saturation vapour pressure approaches the manifold absolute pressure. The heat flux measurements indicate, however, that before this condition is reached the rate of mass transfer becomes limited by some other factor associated with the mass of fuel available for vaporisation in the film. In this case, the rate of fuel vaporisation is assumed to be proportional to the rate at which fuel is deposited on the sensor as given by:

$$(\dot{m}'')_{dep} = \frac{Y}{A}\dot{m}_f \qquad (8.16)$$

and the value of Y/A at a given surface temperature is determined to be consistent with the measured rate of heat transfer. At temperatures below the range when this supply-limit exceeds the predicted rate of vaporisation by convective mass transfer, the excess fuel deposited is assumed to be transferred from the sensor surface by film flow. For these lower temperatures, the value of Y/A has been determined by extrapolating the variation with temperature to give the trend shown in Figure 8.10. This variation is independent of engine operating conditions. Using this, together with the constant value of g^* determined earlier, gives good agreement between the model predictions and measured values of heat flux per cycle over the range of engine operating conditions examined, as illustrated in Figure 8.11. The higher fuel flow rates used at higher MAPs lead to a greater mass of fuel being deposited each cycle; this requires greater heat transfer to increase its sensible internal energy, thus obscuring the effects of the mass flux variations with MAP observed in Figure 8.9. A breakdown of the constituent contributions to the total heat transfer per cycle is given in Figure 8.12, for one operating condition.

8.5 Discussion

The measured rates of heat transfer associated with fuel deposition, and its variation with operating conditions and events within the engine cycle, are consistent with the following interpretation. The injected fuel temperature is generally lower than the surface

temperature of the intake port and the sensor and, once deposited, heat transfer raises the sensible internal energy of the fuel. Depending on the surface temperature a portion of the fuel is vaporised, establishing a partial vapour pressure above the film commensurate with the film temperature. The rate of vaporisation varies with operating conditions and with variations in intake port conditions around the cycle. The rate of vaporisation is affected both by the manifold absolute pressure and the flow conditions in the intake port thus giving rise to relatively high rates at low manifold pressures and during the induction interval of the cycle when charge velocities in the intake port are highest. As surface temperature increases so does the rate of heat transfer up to a maximum value that is dependent on engine operating conditions and fuel flow rate. The measured trends in heat transfer rate suggest that at higher temperatures, the rate of heat transfer is limited by the availability of fuel to vaporise.

The trends observed are well characterised using a relatively simple model for mass transfer together with information on how fuel deposition varies with temperature and engine operating condition. Although two parameters in the model have been calibrated empirically, the inferred value of g^* (i.e. 0.012) is of a similar magnitude to the values estimated for convective mass transfer using Eqn. 8.11; similarly the magnitude and variation of Y are in accord with knowledge of deposition rates determined using the fuel perturbation technique described in **[8.7]**. The values of g^* estimated from Eqn. 8.11 varied from 0.014 to 0.022 across the temperature range tested. They were based on the dry-port heat transfer measurements made through Sensor 7 in conjunction with gas temperatures measured by TC 1, all at a MAP of 0.95 bar when the backflow effects would be minimised. At these conditions with this sensor, the calculated values of Nu were closer to the Martins and Finlay correlation in Figure 6.13 than to the correlation for Sensors 1 and 2. Values of Y were compared with the fraction X of isooctane supplied which is deposited overall, rather than locally. By looking at the temperature variation in X (see Figure 8.13) and values of Y determined from Figure 8.10, using a value for A of 1.3×10^{-3} m^2 (chosen arbitrarily to be ten times the sensor area and representing about ½ of the wetted surface area of the port), the inferred proportion of deposited fuel landing on and immediately around the sensor was found to account for typically 40% of the total

fraction deposited. This is not unreasonable and, by implication, indicates that the remaining 60% is distributed around the other parts of the intake port surface and on the back of the valve. To maintain simplicity in the model the temperature of the fuel film was assumed to be the same as the port surface temperature. It was shown in Chapter 7, however, that the fuel film above Sensor 7 was generally at a lower temperature, creating a temperature difference of over 20 deg. C at higher fuel flow rates. This will undoubtedly lead to errors in the modelled data and may explain the mismatch between the modelled and experimental data in Figure 8.11.

At fully warm conditions the data suggests that a high proportion of the fuel deposited on the sensor is vaporised and that the rate of vaporisation is limited by the availability of fuel in the film. During warm up this is not the case and Figure 8.14 shows how the proportion of fuel vaporised varies with port surface temperature at each MAP level. At a port surface temperature of 20°C and a MAP of 0.95 bar only 5% of the deposited fuel is vaporised, indicating that the remainder is re-entrained as liquid droplets into the airstream or is displaced from the sensor by the flow of liquid in the film.

One of the objectives of the current work was to examine the effect of fuel properties by comparing data obtained using single-component and multi-component fuels. In both cases, the trends in the heat transfer data are associated with the variation of saturation pressure with temperature and conditions in the intake port. Generally the results obtained with pump-grade unleaded gasoline show higher heat transfer rates at lower temperatures, and these rise continuously across the temperature range without evidence of a maximum point (see Figure 7.18). The higher heat transfer rates at lower temperatures indicate that a larger proportion of the deposited fuel is vaporised as a consequence of the lighter components in the multi-component fuel. Conversely the heavier fractions do not vaporise to the same extent as isooctane until higher surface temperatures are reached. These heavier fractions persist in the fuel film and hence the heat transfer rate does not become supply-limited. One consequence of this was the reduction in heat transfer rate with increasing MAP at fully-warm conditions, shown in Figure 7.17. Data recorded under the same conditions with isooctane as the fuel (see

Figure 8.15) did not show the same dependence on MAP, but did maintain a general heat transfer increase in proportion to injected fuel flow rate. The modelled data also shown in Figure 8.15 uses the supply-limitation assumption to predict this trend quite accurately.

Chapter 9
Summary and Discussion

9.1 Introduction

The processes of mixture preparation and fuel transport in the intake systems of spark-ignition engines are receiving much attention, as manufacturers strive to meet emissions regulations with vehicles which fulfill the performance and economy requirements of their customers. The widespread adoption of port fuel injection systems has prompted detailed investigations of the mixture preparation quality these produce. Investigations of injector spray characteristics do not provide sufficient information, in isolation, to characterise fuel transport from the injector to the combustion chamber. More commonly, investigations have sought to define parameters in models of these fuel transfer properties, based on exhaust measurements of combusted AFR. This approach has been utilised in the work for the first part of this thesis, where comparisons were made between the mixture preparation properties of different injector types. These involved photographing the spray patterns they produced in a firing engine, and measuring the response of the combusted AFR to fuelling perturbations with each injector type. Although useful in characterising the fuel transfer processes for control purposes, such approaches do not provide in-depth analysis of the mechanisms by which mixture preparation occurs. A better understanding of these mechanisms is required if mixture preparation is to be optimised through hardware design and selection of the most appropriate control strategies. To this end the majority of this thesis concentrated on the measurement of heat transfer in the inlet port of a spark ignition engine, using these measurements to infer detailed information about the vaporisation of fuel deposited on the intake port walls.

9.2 Crank-Angle Resolved Heat Flux Variations

Surface heat fluxes have been measured in the intake port directly, using heat flux sensors, for the first time in a firing engine. Although the response of these sensors was relatively

slow, experiments to determine their response characteristics, together with an analytical model of the sensors, have enabled measured heat flux data to be processed to derive variations within the period of an engine cycle. The likely temperature reduction at the surface of sensors, due to the insulating effects of their construction, has also been analysed. This analysis has shown that the cycle-averaged temperature at the surface of sensor can vary by up to 15 deg. C from the temperature at the port surface when there is a high local cycle-averaged heat transfer rate, generally associated with heavy fuel deposition. This compares with a measured local temperature difference of 20 deg. C for the same operating conditions, which will also be partly due to a reduction in the sensible internal energy of the film as fuel is vaporised.

In the absence of fuel deposition, heat exchange between the surface and gases within the intake port at fully-warm operating conditions takes place predominantly during the inlet-valve-open period. The direction of this heat flow is towards the surface during the valve-overlap interval, due to the influence of hot backflow gases, and from the surface over the major part of the induction period. Valve-overlap backflow results in heat flux spikes of up to 60 kW/m^2 at low manifold pressures, while the forward induction flow gives rise to heat fluxes of up to 6 kW/m^2. After inlet-valve-closing, the heat flux falls monotonically to a small value, generally within ½ a crank angle revolution, as displacement backflow and the subsequent gas motion decay. The influence of overlap backflow varies with manifold pressure. At low pressures, this backflow both extends further upstream in the intake port and gives rise to higher heat transfer rates to the surface. The overlap backflow also appears to be unmixed in the intake port to an extent which can change during engine warm-up, as evidenced by the development and eventual disappearance of the associated heat transfer spike at some locations over the warm-up period.

Deposition of fuel on the port surfaces invariably produced a heat transfer contribution which was positive (from the surface), at all the test conditions examined. Tests with a single-component fuel (isooctane) indicated that the influence of this contribution on intra-cycle heat flux variations was dependent on the thermal properties of the fuel. The multi-component nature of pump-grade gasoline, therefore, makes the results with this fuel most

difficult to interpret, although the following will generally apply. When surface temperature is low, vaporisation of even the lighter fuel fractions is limited and convective mass transfer during the period of gas motion is important. As surface temperature rises, the influence of the gas flows diminishes. At fully-warm engine running conditions, heat transfer to fuel deposited upon the intake port surface is not substantially enhanced by either the overlap backflow, forward induction flow or decaying gas motion effects. Typically these enhancements contribute 1%, 13% and 10%, respectively, to the total over the cycle. More significant is the heat transfer associated with raising the sensible internal energy of the fuel and vaporising, particularly the lighter fuel fractions, through diffusive mass transfer. Consequently, heat transfer rates increase very rapidly after each injection event, more so at low fuel supply and low manifold pressures. Under these conditions, the effect on the total heat transfer per cycle is partially offset by lower heat transfer rates later in the cycle.

9.3 Variations in Cycle-Averaged Heat Transfer Rates

When the surface is dry and backflow effects are minimal, measured rates of cycle-averaged heat exchange between the gas flow and the surface vary linearly with surface temperature at a given location and charge flow rate. Such data that can be processed to relate *Nu* and *Re*, which has been limited by the difficulty of determining the effective gas-to-surface temperature difference, produces a similar correlation to that derived by Martins and Finlay **[9.1]** from steady-flow experiments.

Strong spatial variations occur in both "dry-port" heat transfer and in heat transfer to the fuel under "wetted-port" conditions. Without fuel deposition, these reflect the domain of influence of reversed gas flows back into the manifold, whereas when the port is "wetted" they reflect variations in local rates of fuel deposition. At fully-warm conditions the positive heat transfer contribution created by fuel deposition increased the heat transfer from the surface. At low surface temperatures, it produced a reduction in the heat transfer to the surface. The magnitude of the contribution depended on manifold pressure, fuel injection rate, and coolant temperature. Increasing coolant temperature or fuel injection

rate gives rise to an increase in heat transfer, as does a reduction in MAP. These variations, both spatially within the port and with operating conditions, provide an indication of the deposition pattern for the injector types examined, which can be compared with the results of the photographic study in Chapter 4. Values of heat transfer per cycle to the fuel deposited under fully-warm conditions at 1000 RPM and three manifold pressure settings are presented in Table 9.1. Only sensors which record values greater than 50 kJ/m^2 at one or more operating conditions have been included in the table. The values given were recorded for a mixture AFR of 14.7 and two other settings at the same manifold pressure. Each case gave similar distributions of values across the set of sensors, although magnitudes changed by up to a factor of 3 in some cases. With few exceptions highest heat transfers were recorded by Sensors 7 and 4, which are located on the floor of the intake port. In most cases Sensor 7 records the highest value. For the single-spray injector, significant levels of heat transfer were recorded for all but Sensor 1 at one or more of the manifold pressures examined, suggesting this injector produced the widest distribution of fuel deposition to the port surface. The greatest spread occurred at the lowest manifold pressure when 66% of the total measured across all sensors was recorded by Sensor 7, a decrease from around 80% at the higher manifold pressures. The most dramatic redistribution of fuel deposition appears to occur with the twin-spray injector. Here, when manifold pressure is lowered, the highest heat transfer per cycle recorded is by Sensor 4 rather than Sensor 7. However, only a small movement of the fuel spray in the upstream direction is required to account for this. At the same time it appears that fuel wetting of the central bifurcation is reduced as evidenced by the fall in heat transfer recorded by Sensor 5. The results obtained for the four-hole injector suggest fuel deposition occurs primarily on Sensors 4, 6, 7 and 8. As manifold pressure is lowered the deposition pattern appears to shift downstream towards the intake valves with nearly equal values of heat transfer per cycle recorded by Sensors 6, 7 and 8.

The photographic studies together with the heat transfer measurements indicated that the most significant differences between the injector types are as follows. The single-spray injector appears to deposit fuel over the widest area of the port. This and the pencil beam injector each direct fuel onto the bifurcation web which deflects the spray and produces

Table 9.1 - Variation of Heat Transfer to Fuel with MAP, AFR and Fuel Injector Type

	Inferred Heat Transfer to Fuel per Cycle (kJ/m²)								
	0.95 bar MAP			0.79 bar MAP			0.53 bar MAP		
AFR	18.5	14.7	10.2	18.5	14.7	10.2	18.5	14.7	10.2
Twin-Spray Injector									
Sensor 4	241	236	276	157	156	283	1616	1791	1899
Sensor 5	193	128	188	147	127	129	0	0	0
Sensor 6	0	0	0	150	123	148	58	35	111
Sensor 7	801	984	1196	775	1212	1629	27	190	425
Sensor 8	0	0	0	131	104	176	21	6	130
Single-Spray Injector									
Sensor 2	0	0	0	57	65	71	94	100	97
Sensor 3	0	0	0	0	0	0	0	0	69
Sensor 4	102	117	140	76	100	141	104	135	426
Sensor 5	199	236	416	78	69	234	103	89	141
Sensor 6	0	0	70	0	0	62	0	0	0
Sensor 7	1037	1243	1487	775	1071	1422	413	706	1201
Sensor 8	0	0	168	70	38	130	5	34	44
Four-Hole Injector									
Sensor 4	121	111	257	116	92	217	0	0	0
Sensor 6	128	117	151	91	111	160	269	307	531
Sensor 7	909	956	960	854	1016	1402	243	341	576
Sensor 8	182	176	203	286	315	366	267	345	504

secondary atomization. Sensor 5 records a significant level of heat transfer to the fuel for the single-spray injector, but this value is always relatively small compared to that recorded by Sensor 7 on the port floor. The twin-spray injector also appears to give rise to wetting of the bifurcation surface, but most fuel deposition appears to occur directly on the port floor around Sensors 4 and 7, with the possibility of some small shift of floor deposition upstream at low manifold pressures. The four-hole injector, although producing a wider cone angle than that of the single-pintle twin-spray injector, appears to give the best penetration of fuel into the intake port. This gives a reasonably uniform distribution of heat flux to fuel over Sensors 6, 7 and 8 at low manifold pressures and a more focused pattern around Sensor 7 at higher manifold pressures, but in each case without evidence of appreciable wetting of the side wall or bifurcation web in the vicinity of Sensors 3 and 5.

When fuel supply rate is step-increased, heat transfer per cycle to deposited fuel adjusts at a similar rate as the induced mixture ratio. This is shown in Figure 9.1, where normalised heat transfer data is plotted alongside inverted and normalised AFR data for the same test conditions. The peak instantaneous heat transfer rate is highest for the first cycle after the change. On subsequent cycles the peak diminishes and levels in the tail of the variation increase. If the fuel supply rate is step-decreased, the peak instantaneous heat transfer rate is lowest for the first cycle after the change with higher rates in the tail of the variation. In this case, the peak increases and levels in the tail decrease during subsequent cycles. These features reflect the changing quantity and composition of fuel in the surface film. It is the time taken for these changes to take place and a new steady-state to be established which produce the engine response delay characterised by τ in the parametric τ and X model of fuel transport.

9.4 Theoretical Interpretation of Heat Transfer Variations

When considering a single-component fuel, which avoids the complexities inherent in multi-component pump-grade fuel, the mechanisms by which heat transfer occurs can be modelled. In this way it was found that trends in the heat transfer data, particularly the

changes with port surface temperature, were consistent with the following interpretation of fuel behaviour:

(i) Fuel deposited on the surface is heated to a film temperature with an associated change in sensible internal energy.

(ii) The rate of vaporisation from the fuel film is controlled by the variation of saturation pressure with temperature through both convective and diffusive mass transfer. The rate of vaporisation increases with increasing surface temperature and is promoted by the forward induction flow during the intake stroke.

(iii) At high surface temperatures the rate of vaporisation may be limited by the availability of fuel supplied to the film by deposition. In this case, a maximum heat transfer rate to the fuel is reached at a temperature dependent upon fuel characteristics. The rate of heat transfer can decrease with subsequently increasing surface temperature, due to a decreasing fraction of fuel supply being deposited on the port surfaces.

These effects are also apparent in results taken with multi-component fuels, although the temperature at which the heat transfer rate becomes supply limited is different for each component, and the heavier components never reach such a point under normal engine operating conditions. Therefore, whereas warm-up results with isooctane rise to a maximum value which is dependent on engine operating conditions and fuel flow rate, multi-component results rise continuously across the temperature range without evidence of a maximum. Modelled data for isooctane fuelling sweeps at different temperatures show the effects of this "supply-limiting" as fuel flow rate changes at different manifold pressures (see Figure 9.2). At low temperatures (Figure 9.2(a)), there is no supply-limiting and the heat transfer rates vary with both MAP and fuel flow rate. With the engine fully-warm (Figure 9.2(c)) the heat transfer rates become supply-limited across the range of conditions considered and they are, therefore, only dependent on fuel flow rate. When an intermediate temperature is considered (Figure 9.2(b)), it is only at lower MAP's and fuel flow that the heat transfer becomes supply limited. The trends in the data at this temperature condition begin to replicate the trends in experimental data recorded under

fully-warm conditions with multi-component fuels (Figure 7.17), where a proportion of the components are supply-limited at lower MAP's and fuel flow rates.

Chapter 10
Conclusions

* Measurements of heat transfer in the intake port of a spark-ignition engine, using surface mounted heat flux sensors, provide a good indication of factors affecting the thermal environment of the port. Under "dry-port" conditions it is the port gas flows which create these effects, while under "wetted-port" conditions they are also affected by the mechanisms involved in mixture preparation.

* Using an analytical model of the heat flux sensors together with experimentally measured response characteristics, it is possible to resolve the heat flux data on a crank-angle basis. This allows the significance of events within an engine cycle to be determined.

* When the port is dry the effects of overlap backflow, forward induction flow and displacement backflow are apparent. The relative significance of these effects vary with manifold pressure and engine coolant temperature.

* Deposition of fuel on the port surfaces generally increases the heat transfer rates by an order of magnitude. The effects of the gas flows are still apparent in the crank-angle resolved data, even in inferred "heat flux to fuel" data, since they enhance fuel vaporisation through convection. Particularly at high temperatures, though, this data is dominated by heat transfer associated with increasing the temperature of newly injected fuel and vaporising fuel from the film by diffusive mass transfer, with the lighter fuel fractions evaporating most quickly. Again the relative significance of the different heat transfer mechanisms is dependent upon engine operating conditions.

* Integrated values of heat transfer per cycle provide a useful indication of variations due to the positioning of sensors within the port and changes in operating conditions. When the port is dry, both spatial and operating condition variations arise from differences

in the penetration of the gas flows, particularly the overlap backflow. With a "wetted" port, the inferred values of "heat transfer to the fuel" are associated with the distribution of the fuel around the port surfaces. These provide a relative comparison between the deposition patterns produced by the different injector types and how these vary with operating conditions.

* When running on isooctane fuel a good correlation with the experimental data has been produced using a model of heat transfer to the fuel. In addition to the heat transfer required to raise the sensible internal energy of newly injected fuel, this model accounts for the heat used in the vaporisation of fuel in one of two ways. At high temperatures where the fuel is vaporised very quickly through diffusive mass transfer, it is assumed that the heat transfer is limited by the availability of fuel supplied to the film by deposition. At lower temperatures the mass transfer is dominated by convection and heat transfer is not limited by fuel availability. The temperature at which the vaporisation mechanism switches from convective to purely diffusive mass transfer is dependent upon MAP and fuel supply rate. This interpretation is also consistent with data from multi-component fuel tests although the picture is far more complex, since each component in the fuel has a different vaporisation characteristic.

References

1.1 S D Hires and M T Overington, "Transient Mixture Strength Excursions - An Investigation of Their Causes and the Development of a Constant Mixture Strength Fuelling Strategy", SAE Paper No. 810495, 1981

1.2 P J Shayler, Y C Teo, A Scarisbrick, "Fuel Transport Characteristics of Spark Ignition Engines for Transient Fuel Compensation", SAE Paper No. 950067, 1995

1.3 J J G Martins and I C Finlay, "Heat Transfer to Air-Ethanol and Air Methanol Sprays Flowing in Heated Ducts and Across Heated Intake Valves", SAE Paper No. 900583, 1990

1.4 J J G Martins and I C Finlay, "Fuel Preparation in Port Injected Engines", SAE Paper No. 920518, 1992

1.5 N Ladommatos, "Mechanisms of Heat Transfer to Liquid Films in the Manifold of Port-Injected Petrol Engines", *Proc Instn Mech Engrs*, Vol 207 pgs 211-221, 1993

1.6 H Sindano, "Phenomenological Transient Fuelling Model for Port Injected Engines", I.Mech.E. Seminar on Engine Transient Performance, 7th Nov. 1990

1.7 G Chen, M Vincent and T Gutermuth, "The Behaviour of Multiphase Fuel-Flow in the Intake Port", SAE Paper No. 940445, 1994

1.8 R C Turin, E G B Casartelli and H P Geering, "A New Model for Fuel Supply Dynamics in an SI Engine", SAE Paper No. 940208, 1994

2.1 C F Aquino, "Transient A/F Control of the 5 Litre Central Fuel Injection Engine" SAE Paper No. 810494, 1981

2.2 S D Hires, M T Overington, "Transient Mixture Strength Excursions - An Investigation of Their Causes and the Development of a Constant Mixture Strength Fuelling Strategy" SAE Paper No. 810495, 1981

2.3 D J Boam, I C Finlay and G S Fairhead, "The Optimization of Fuel Enrichment Patterns with Throttle Body Injection", Proc Instn Mech Engrs Vol 202 No D1, 1988

2.4 H B Servati, E W Herman, "Spray/Wall Interactions Simulation" SAE Paper No. 890566, 1989

2.5 D J Boam, I C Finlay and J J G Martins, "A Model for Predicting Engine Torque Response During Rapid Throttle Transients in Port-Injected Spark-Ignition Engines", SAE Paper No. 890565, 1989

2.6 T Nogi, Y Ohyama, T Yamauchi and H Kuroiwa, "Mixture Formation of Fuel Injection Systems in Gasoline Engines", SAE Paper No. 880558, 1988

2.7 P J Shayler, W D P Marshall, J Turner and K Ford, "Exhaust Emissions: the Influence of Fuel Injection System Details", I Mech E Paper No. C394/015, 1990

2.8 H J Neußer, H Endres and M Breuer, "New Variable Intake and Mixture Formation System for Multi-Valve SI Engines", SAE Paper No. 940449, 1994

2.9 D Rose, N Ladommatos, R Stone, "In-Cylinder Mixture Excursions in a Port-Injected During Fast Throttle Opening" SAE Paper No. SP-1029, 1994

2.10 P J Shayler, Y C Teo and A Scarisbrick, "Fuel Transport Characteristics of Spark Ignition Engines for Transient Fuel Compensation", SAE Paper No. 950067, 1995

2.11 D J Boam and I C Finlay, "A Computer Model of Fuel Evaporation in the Intake System of a Carburetted Petrol Engine", I Mech E Paper No. C89/79, 1979

2.12 H B Servati, W W Yuen, "Deposition of Fuel Droplets in Horizontal Intake Manifolds and the Behaivour of Fuel Film Flow on Its Walls", SAE Paper No. 840239, 1984

2.13 F Maroteaux and M Thelliez, "Modeling of Unsteady Multiphase Flow in the Intake Manifold of Spark Igniton Engines", SAE Paper No. 910392, 1991

2.14 G Chen, M T Vincent and T R Gutermuth, "The Behaviour of Multiphase Fuel-Flow in the Intake Port", SAE Paper No. 940445, 1994

2.15 C Cheng, W K Cheng, J B Heywood, D Maroteaux and N Collings, "Intake Port Phenomena in a Spark-Ignition Engine at Part Load", SAE Paper No. 912401, 1991

2.16 M C Bourke and L W Evers, "Fuel Film Dynamics in the Intake Port of a Fuel Injected Engine", SAE Paper No. 940446, 1994

2.17 C H Daniels and L W Evers, "The Influence of Mixture Preparation on a Warm 1.9L Ford Engine", SAE Paper No. 940444, 1994

2.18 K Takeda, T Yaegashi, K Sekiguchi, K Saito and N Imatake, "Mixture Preparation and HC Emissions of a 4-Valve Engine with Port Fuel Injection During Cold Starting and Warm-up", SAE Paper No. 950074, 1995

2.19 J Takemura, D Sabuyashi and H Ando, "Effect of Turbulence in Intake Port of MPI Engine on Fuel Transport Phenomena and Nonuniformity of Fuel/Air Mixing in Cylinder", SAE Paper No. 900162, 1990

2.20 M J Miller and C J E Nightingale, "Measurement of the Changes in Mixture Preparation that Occur During Flow Past the Inlet Valve of a Spark-Ignition Engine", IMechE Paper No. C394/004, 1990

2.21 K Saito, K Sekiguchi, N Imatake (Nippon Soken), K Takeda and T Yaegashi, "A New Method to Analyze Fuel Behaviour in a Spark Ignition Engine", SAE Paper No. 950044, 1995

2.22 J J G Martins and I C Finlay, "Fuel Preparaton in Port Injected Engines", SAE Paper No. 920518, 1992

2.23 M Iwata, M Furuhashi and M Ujihashi, "Two Hole Injector Improves Transient Performance and Exhaust Emissions of 4-valve Engines", SAE Paper No. 870125, 1987

2.24 F Zhao, M Lai and D L Harrington, "The Spray Characteristics of Automotive Port Fuel Injection - A Critical Review", SAE Paper No. 950506, 1995

2.25 P J Shayler, M T Davies, M J F Colechin and A Scarisbrick "Intake Port Fuel Transport and Emissions: the Influence of Injector Type and Fuel Composition", SAE Paper No. 961996, 1996

2.26 K Harada, R Shimizu, K Kurita, M Muramatsu, M Ohashi and T Makimura, "Development of Air-Assisted Injector System", SAE Paper No. 920294, 1992

3.1 C Cheng, W K Cheng, J B Heywood, D Maroteaux and N Collings, "Intake Port Phenomena in a Spark-Ignition Engine at Part Load", SAE Paper No. 912401, 1991

3.2 **Operator's Manual for the Ricardo Hydra Research Engine**, Ricardo Consulting Engineers Ltd., 1985

3.3 **The Oxford English Reference Dictionary**, Edited by J Pearsall and B Trumble, Oxford University Press, Oxford, 1995

3.4 P J Shayler, Y C Teo and A Scarisbrick, "Fuel Transport Characteristics of Spark Ignition Engines for Transient Fuel Compensation", SAE Paper No. 950067, 1995

4.1 O Hadded, J Stokes and D W Grigg, "Low Emission Vehicle Technology for Ultra Low Emissions Vehicle and European Stage 3 Emissions Standards", Proc Instn Mech Engrs, Vol 209, Part D, pgs 159-170, 1995

4.2 C Cheng, W Cheng, J Heywood, D Maroteaux and N Collings, "Intake Port Phenomena in a Spark-Ignition Engine at Part Load", SAE Paper No. 912401, 1991

4.3 M Greiner, P Romann and U Steinbrenner, "BOSCH Fuel Injectors - New Developments", SAE Paper No. 870124, 1987

4.4 M Iwata, M Furuhashi and M Ujihashi, "Two-Hole Injector Improves Transient Performance and Exhaust Emissions of 4-Valve Engines", SAE Paper No. 870125, 1987

4.5 J J G Martins and I C Finlay, "Fuel Preparation in Port Injected Engines", SAE Paper No. 920518, 1992

4.6 T Nogi, Y Ohyama, T Yamauchi and H Kuroiwa, "Mixture Formation of Fuel Injection Systems in Gasoline Engines", SAE Paper No. 880558, 1988

4.7 M Kashiwaya, T Kosuge, K Nakagawa and Y Okamoto, " The Effect of Atomization of Fuel Injectors on Engine Performance", SAE Paper No. 900261, 1990

4.8 K Takeda, T Yaegashi, K Sekiguchi, K Saito and N Imatake, "Mixture Preparation and HC Emissions of a 4-Valve Engine with Port Fuel Injection During Cold Starting and Warm-Up", SAE Paper No. 950074, 1995

4.9 H Manger, "Electronic Fuel Injection", SAE Paper No. 820903, 1982

4.10 K Harada, R Shimizu, K Kurita, M Muramatsu, T Makimura and M Ohashi, "Development of Air-Assisted Injector System", SAE Paper No. 920294, 1992

4.11 F Zhao, M Lai and D L Harrington, "The Spray Characteristics of Automotive Port Fuel Injection - A Critical Review", SAE Paper No. 950506, 1995

4.12 S D Hires and M T Overington, "Transient Mixture Strength Excursions - An Investigation of Their Causes and the Development of a Constant Mixture Strength Fuelling Strategy", SAE Paper No. 810495, 1981

4.13 C F Aquino, "Transient A/F Control of the 5 Litre Central Fuel Injection Engine", SAE Paper No. 810494, 1981

4.14 W S James, H C Dickinson and S W Sparrow, "Intake Manifold Temperatures and Fuel Economy", SAE Transactions V. 15, Part II, 1920

4.15 J O Eisinger, "Engine Acceleration Tests", SAE Transactions V. 22, Part II, 1927

4.16 P J Shayler, Y C Teo, A Scarisbrick, "Fuel Transport Characteristics of Spark Ignition Engines for Transient Fuel Compensation", SAE Paper No. 950067, 1995

4.17 S R Fozo and C F Aquino, "Transient A/F Characteristics for Cold Operation of a 1.6 Litre Engine with Sequential Fuel Injection", SAE Paper No. 880691, 1988

4.18 H B Servati and E W Herman, "Spray/Wall Interactions Simulation", SAE Paper No. 890566, 1989

4.19 D J Boam, I C Finlay and J J G Martins, "A Model for Predicting Engine Torque Response During Rapid Throttle Transients in Port-Injected Spark-Ignition Engines", SAE Paper No. 890565, 1989

4.20 A J Beaumont, A D Noble and A Scarisbrick, "Adaptive Transient Air-Fuel Ratio Control to Minimize Gasoline Engine Emissions", Paper Presented at the FISITA Congress, London, June 1992

4.21 E Hendricks and S C Sorensen, "Mean Value Modelling of Spark Ignition Engines", SAE Paper No. 900616, 1990

4.22 Y C Teo, "Mixture Ratio Control of a Spark Ignition Engine During Transient Operations", Ph.D. Thesis, University of Nottingham, 1994

4.23 A J Durrant, "Closed Loop UEGO Probe Feedback Engine Control", Progress Report 2, University of Nottingham, 1996

4.24 J J G Martins, D J Boam and J F Bingham, "A Computer Model for the Assessment of Engine Control System Parameters", SAE Paper No. 940484, 1994

4.25 H Monden and R Kataoka, "Practical Measuring Method of Deposited Fuel and Evaporated Fuel in the Induction System", SAE Paper No. 905042, 1990

4.26 K Saito, K Sekiguchi, N Imatake, K Takeda and T Yaegashi, "A New Method to Analyze Fuel Behaviour in a Spark Ignition Engine", SAE Paper No. 950044, 1995

4.27 A A Amer and M Lai, "Time-Resolved Measurements in Transient Port Injector Sprays", SAE Paper No. 950509, 1995

4.28 P J Shayler, M T Davies, M J F Colechin and A Scarisbrick "Intake Port Fuel Transport and Emissions: the Influence of Injector Type and Fuel Composition", SAE Paper No. 961996, 1996

4.29 K J Bush, N J Adams, S Dua and C R Markyvech, "Automatic Control of Cylinder by Cylinder Air-Fuel Mixture Using a Proportional Exhaust Gas Sensor", SAE Paper No. 940149, 1994

4.30 G V Stuuart, "A System Identification Approach to the Modelling of Engine Transients", SAE Paper No. 900237, 1990

4.31 R C Dorf, **Modern Control Systems**, Fifth Edition, Addison-Wesley, California, 1989

4.32 P R Keogh, P J Shayler, "Transient Fuel Compensation", Progress Report 3, University of Nottingham, 1994

4.33 H Melgaardt, E Hendricks and H Madsen, "Continuous Identification of a Four-Stroke Engine", 1990 American Control Conference, Paper No. TP-10, 5:30, San Diego CA, 1990

5.1 H Sindano, "Phenomenological Transient Fuelling Model for Port Injected Engines", I.Mech.E. Seminar on Engine Transient Performance, 7th Nov. 1990

5.2 G Chen, M Vincent and T Gutermuth, "The Behaviour of Multiphase Fuel-Flow in the Intake Port", SAE Paper No. 940445, 1994

5.3 R C Turin, E G B Casartelli and H P Geering, "A New Model for Fuel Supply Dynamics in an SI Engine", SAE Paper No. 940208, 1994

5.4 J J G Martins and I C Finlay, "Heat Transfer to Air-Ethanol and Air Methanol Sprays Flowing in Heated Ducts and Across Heated Intake Valves", SAE Paper No. 900583, 1990

5.5 J J G Martins and I C Finlay, "Fuel Preparation in Port Injected Engines", SAE Paper No. 920518, 1992

5.6 N Ladommatos, "Mechanisms of Heat Transfer to Liquid Films in the Manifold of Port-Injected Petrol Engines", *Proc Instn Mech Engrs*, Vol 207 pgs 211-221, 1993

5.7 RdF Corporation, "Micro-Foil Heat Flow Sensor Calibration Sheet", Hudson, 1994

5.8 A H Epstein, G R Guenette, R J G Norton and C Yuzhang, "High Frequency Response Heat Flux Gauge for Metal Blades", *AGARD Conference Proceedings No. 390* - Heat Transfer and Cooling in Gas Turbines, pgs 30-1 to 30-16, May 1985

5.9 H S Carslaw and J C Jaeger, **Conduction of Heat in Solids**, 2nd Edition, Oxford University Press, Oxford, 1959

5.10 J L Waintraub and E Brumgnach, "Electric Circuits for Technologists", West Publishing Company, St Paul, 1989

5.11 D E Newland. **An Introduction to Random Vibrations, Spectral Analysis and Wavelet Analysis**, 3rd Edition, Longman, Harlow, 1993

6.1 C Cheng, W Cheng, J Heywood, D Maroteaux and N Collings, "Intake Port Phenomena in a Spark-Ignition Engine at Part Load", SAE Paper No. 912401, 1991

6.2 R C Turin, E G B Casartelli and H P Geering, "A New Model for Fuel Supply Dynamics in an SI Engine", SAE Paper No. 940208, 1994

6.3 J J G Martins and I C Finlay, "Heat Transfer to Air-Ethanol and Air Methanol Sprays Flowing in Heated Ducts and Across Heated Intake Valves", SAE Paper No. 900583, 1990

6.4 J J G Martins and I C Finlay, "Fuel Preparation in Port Injected Engines", SAE Paper No. 920518, 1992

6.5 N Ladommatos, "Mechanisms of Heat Transfer to Liquid Films in the Manifold of Port-Injected Petrol Engines", *Proc Instn Mech Engrs*, Vol 207 pgs 211-221, 1993

6.6 M D Burghardt, **Engineering Thermodynamics with Applications**, 3rd Edition, Harper and Row, New York, 1986

6.7 A J Ede and E J Febre, "The Effect on the Heat Transfer from a Pipe to a Fluid Flowing Through it of a Bend in the Pipe", *Prog. 9th Int. Congress on Refrigeration*, 1955, Vol. 1, pp 2127-2132

7.1 S D Hires and M T Overington, "Transient Mixture Strength Excursions - An Investigation of Their Causes and the Development of a Constant Mixture Strength Fuelling Strategy", SAE Paper No. 810495, 1981

7.2 C F Aquino, "Transient A/F Control of the 5 Litre Central Fuel Injection Engine", SAE Paper No. 810494, 1981

7.3 C Aquino and W D Plensdorf, "An Evaluation of Local Heating as a Means of Fuel Evaporation for Gasoline Engines", SAE Paper No. 860246, 1986

7.4 H Sindano, "Phenomenological Transient Fuelling Model for Port Injected Engines", I.Mech.E. Seminar on Engine Transient Performance, 7th Nov. 1990

7.5 G Chen, M Vincent and T Gutermuth, "The Behaviour of Multiphase Fuel-Flow in the Intake Port", SAE Paper No. 940445, 1994

7.6 R C Turin, E G B Casartelli and H P Geering, "A New Model for Fuel Supply Dynamics in an SI Engine", SAE Paper No. 940208, 1994

7.7 J J G Martins and I C Finlay, "Heat Transfer to Air-Ethanol and Air Methanol Sprays Flowing in Heated Ducts and Across Heated Intake Valves", SAE Paper No. 900583, 1990

7.8 J J G Martins and I C Finlay, "Fuel Preparation in Port Injected Engines", SAE Paper No. 920518, 1992

7.9 N Ladommatos, "Mechanisms of Heat Transfer to Liquid Films in the Manifold of Port-Injected Petrol Engines", *Proc Instn Mech Engrs*, Vol 207 pgs 211-221, 1993

7.10 J J G Martins, D J Boam and J F Bingham, "A Computer Model for the Assessment of Engine Control System Parameters", SAE Paper No. 940484, 1994

7.11 T Nogi, Y Ohyama, T Yamauchi and H Kuroiwa, "Mixture Formation of Fuel Injection Systems in Gasoline Engines", SAE Paper No. 880558, 1988

7.12 E W Curtis, C F Aquino, D K Trumpy and G C Davis, "A New Port and Cylinder Wall Wetting Model to Predict Transient Air/Fuel Excursions in a Port Fuel Injected Engine", SAE Paper No. 961186, 1996

7.13 P J Shayler, Y C Teo and A Scarisbrick, "Fuel Transport Characteristics of Spark Ignition Engines for Transient Fuel Compensation", SAE Paper No. 950067, 1995

8.1 N B Vargaftik, **Tables on the Thermophysical Properties of Liquids and Gases**, Second Edition, Hemisphere Publishing Corp., London, 1975

8.2 J M Kay and R M Nedderman, **Fluid Mechanics and Transfer Processes**, Cambridge University Press, Cambridge, 1985

8.3 J M Coulson and J F Richardson, **Chemical Engineering Vol. 6: An Introduction to Chemical Engineering Design by R K Sinnott**, 2nd Edition, Pergamon, Oxford, 1993.

8.4 D B Spalding, **Some Fundamentals of Combustion**, Butterworths Scientific Publications, London, 1955

8.5 D B Spalding, **Convective Mass Transfer, An Introducion**, Edward Arnold Ltd, London, 1963

8.6 M N Özişik, **Heat Transfer, A Basic Approach**, McGraw-Hill, Singapore, 1985

8.7 P J Shayler, Y C Teo and A Scarisbrick, "Fuel Transport Characteristics of Spark Ignition Engines for Transient Fuel Compensation", SAE Paper No. 950067, 1995

9.1 J J G Martins and I C Finlay, "Heat Transfer to Air-Ethanol and Air-Methanol Sprays Flowing in Heated Ducts and Across Heated Intake Valves", SAE Paper No. 900583, 1990

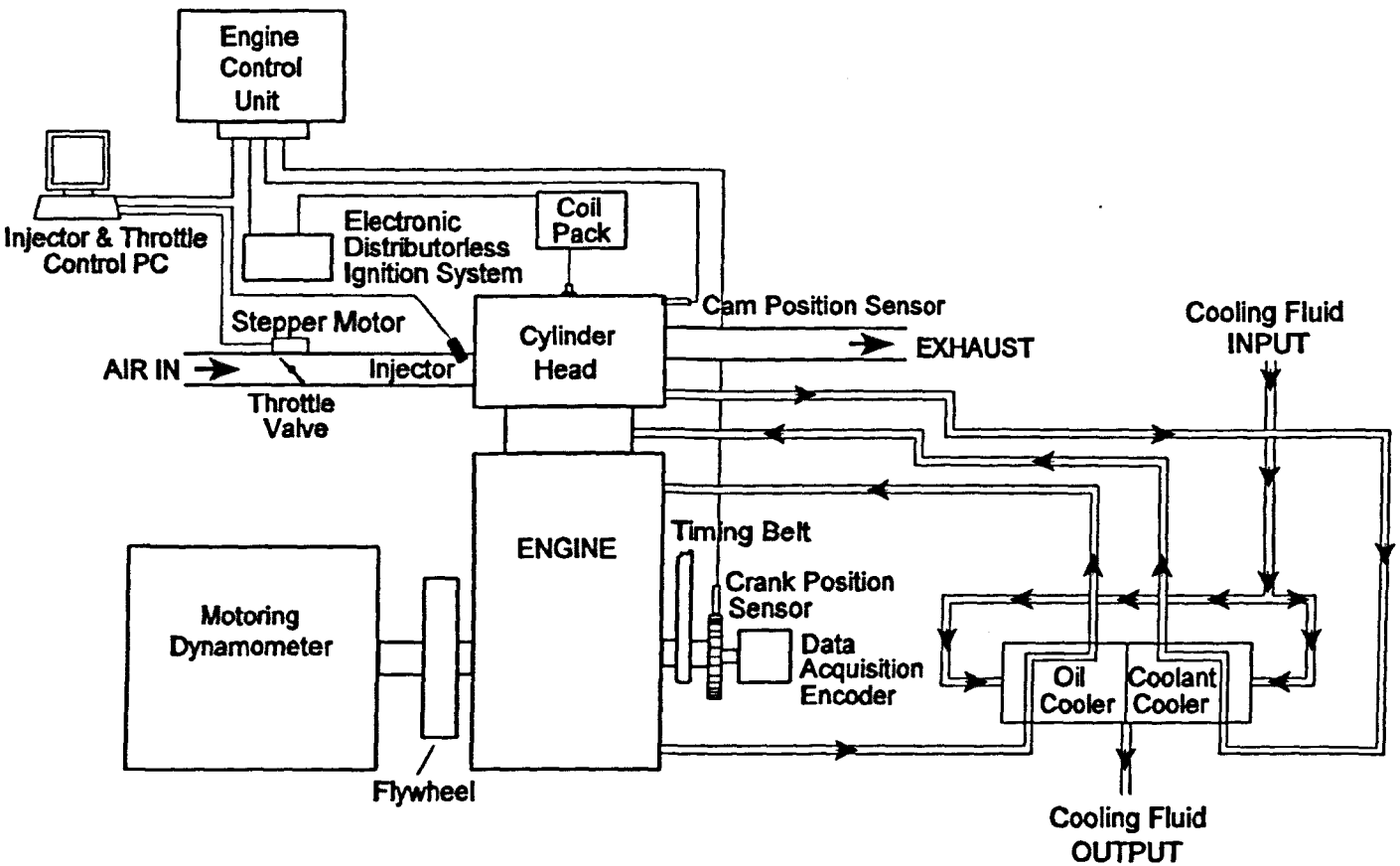

Figure 3.1 - Block Diagram of Engine and Control System

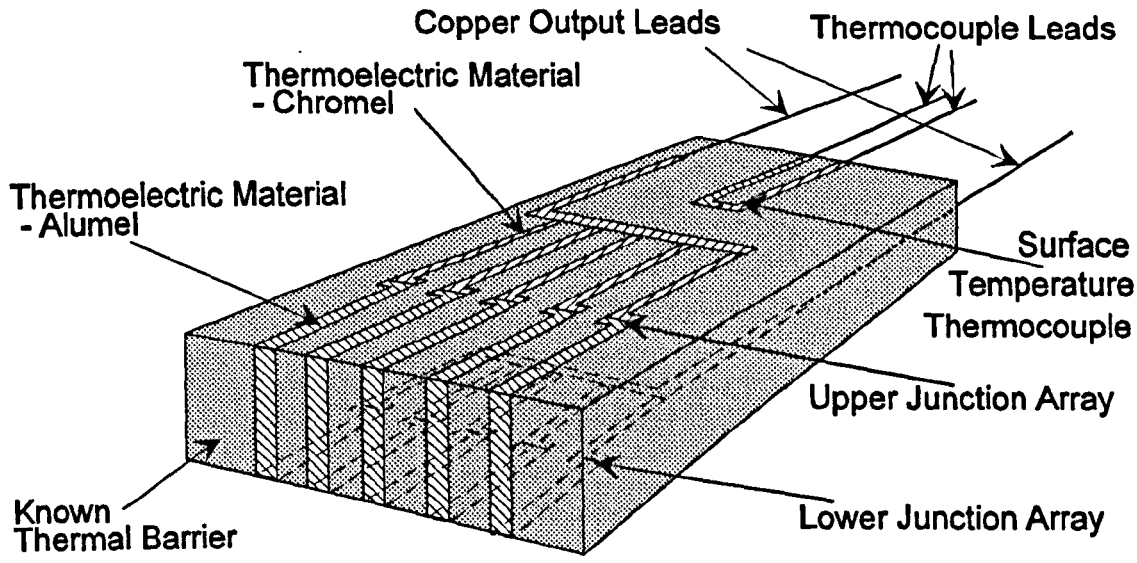

Figure 3.2 - Heat Flux Sensor Construction

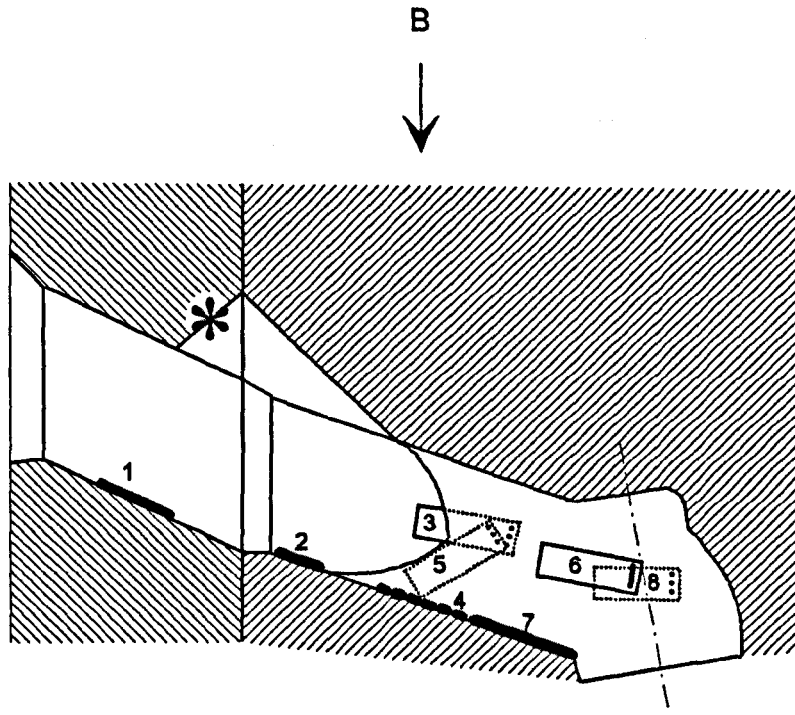

Figure 3.3 - Positioning of Heat Flux Sensors within Inlet Port (Injector Tip Position - '*')

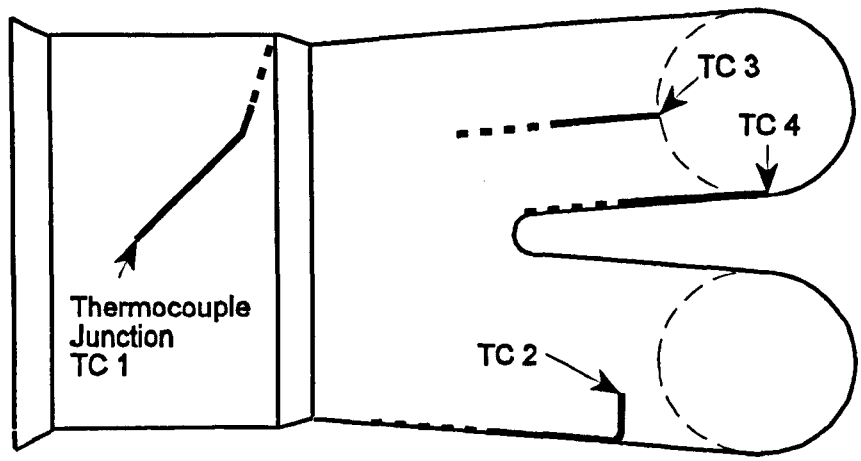

(a) Plan View of Thermocouple Positions

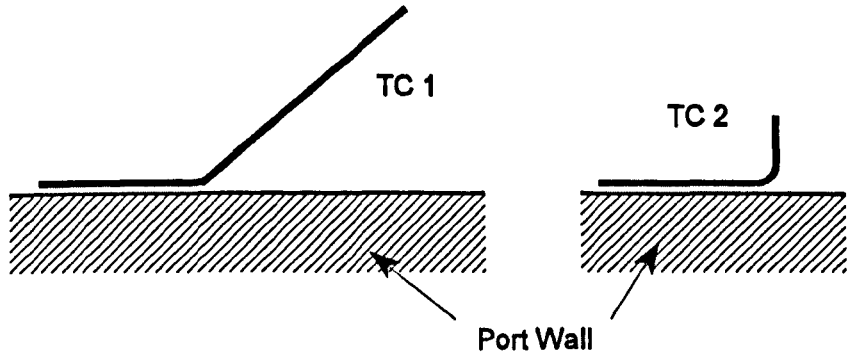

(b) Detail of Tip Positions for TC 1 & TC 2

Figure 3.4 - Thermocouple Positions

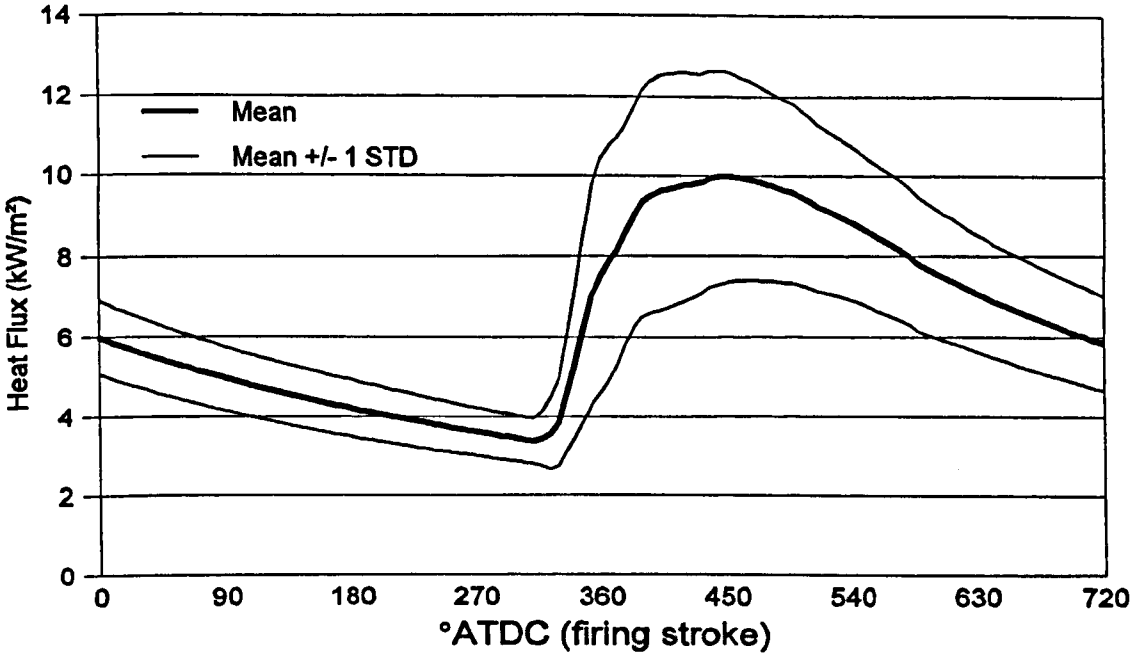

(a) Sensor 7

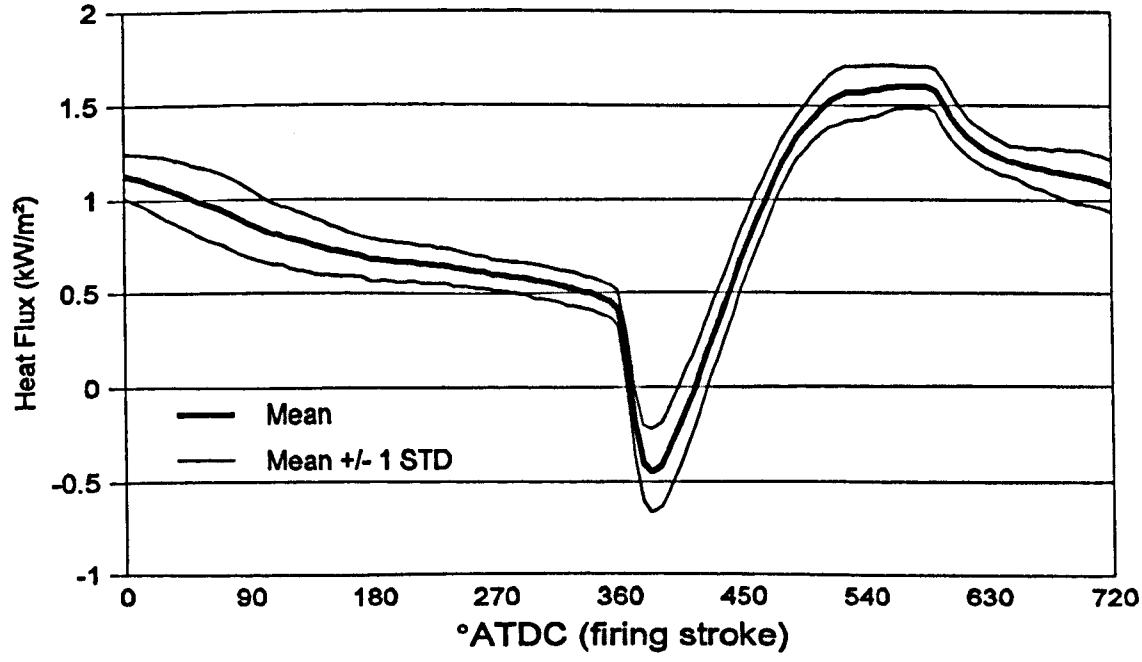

(b) Sensor 5

Figure 3.5 - Typical Traces Recorded from Heat Flux Sensors

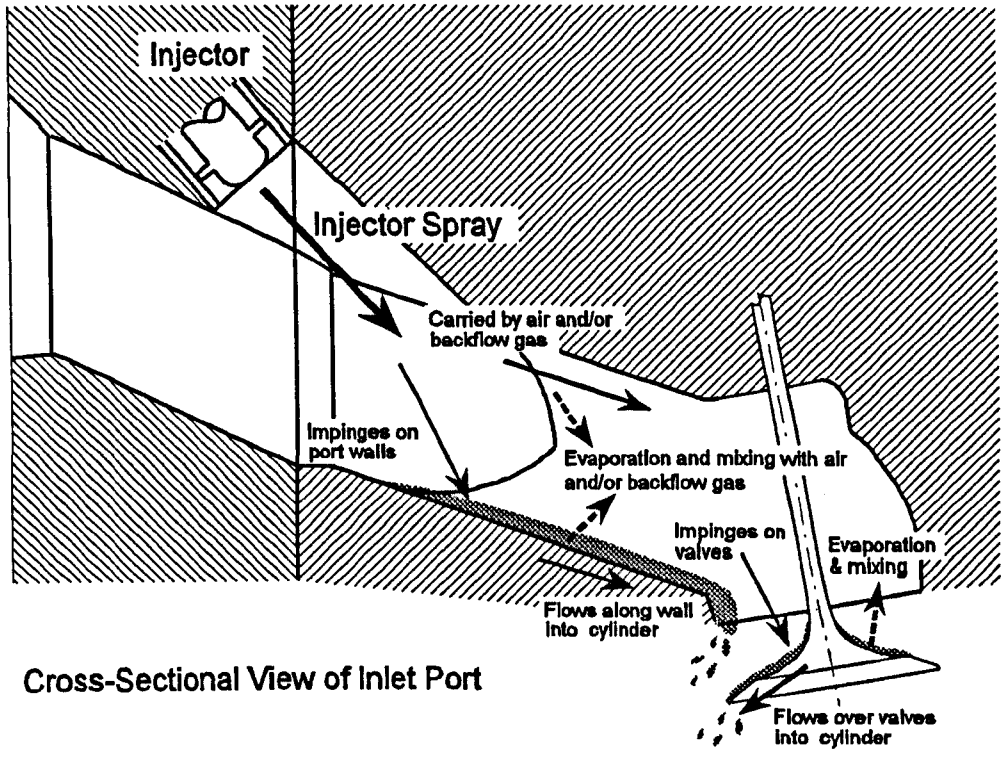

Figure 4.1 - Typical Interpretation of the Fuel Transfer Process **[4.2]**

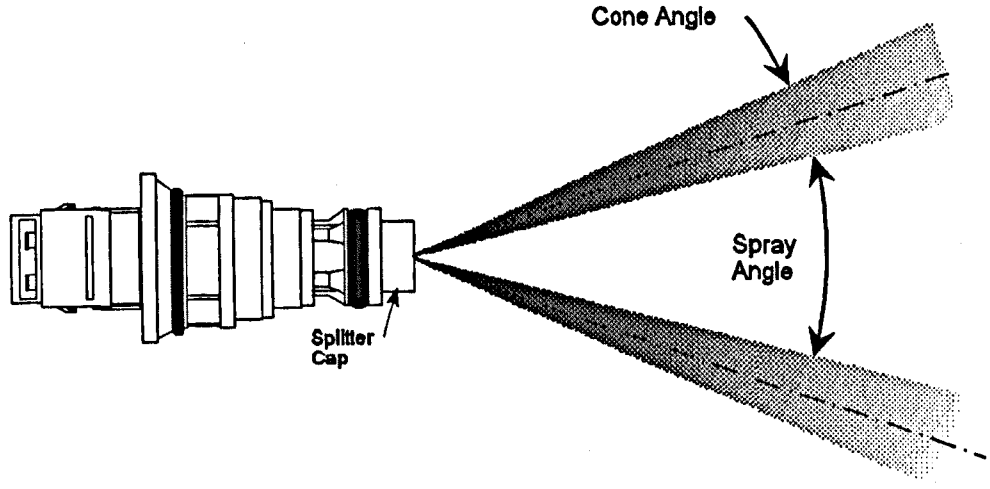

Figure 4.2 - Diagram of Fuel Injection with Single-Pintle, Twin-Spray Injector, Showing Spray Angle and Cone Angle

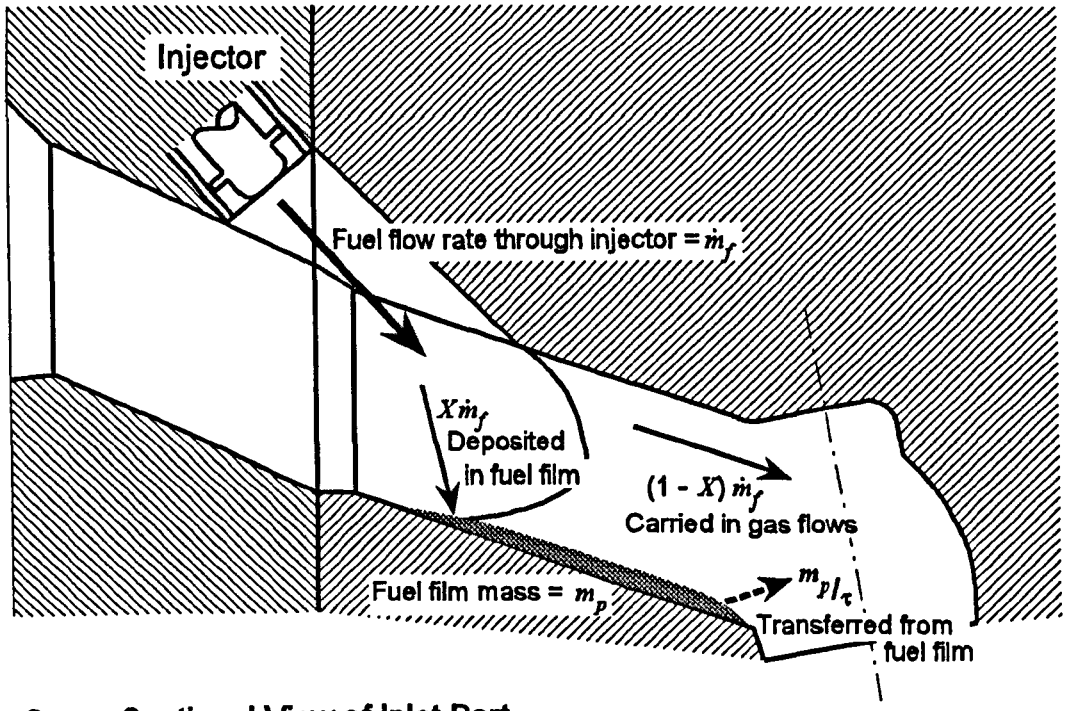

Figure 4.3 - Application of the τ and X Model to a Port-Injected System

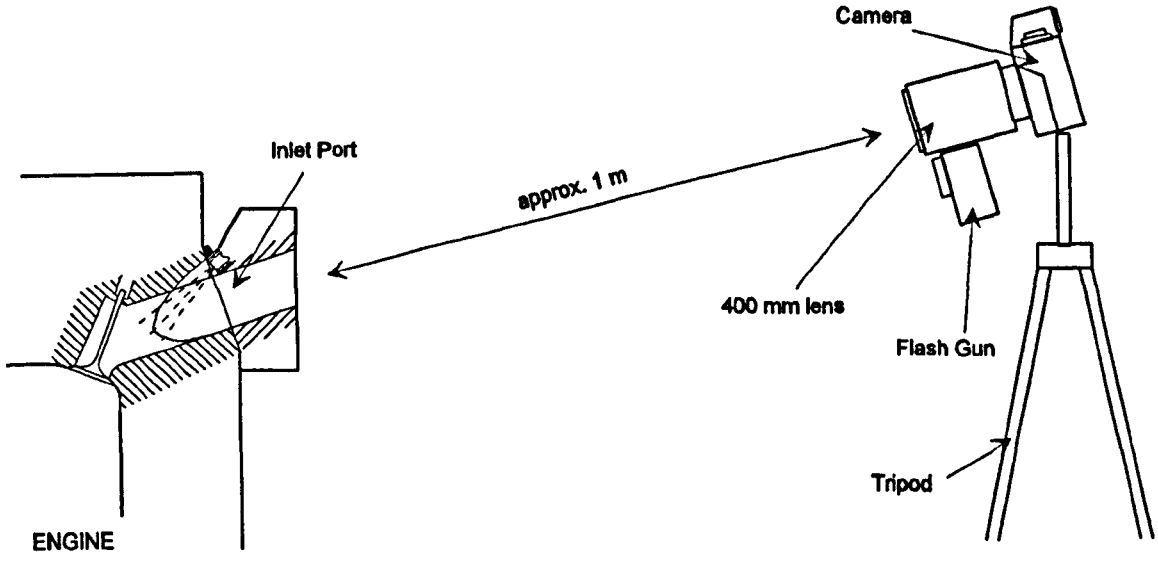

Figure 4.4 - Equipment for Photographic Work

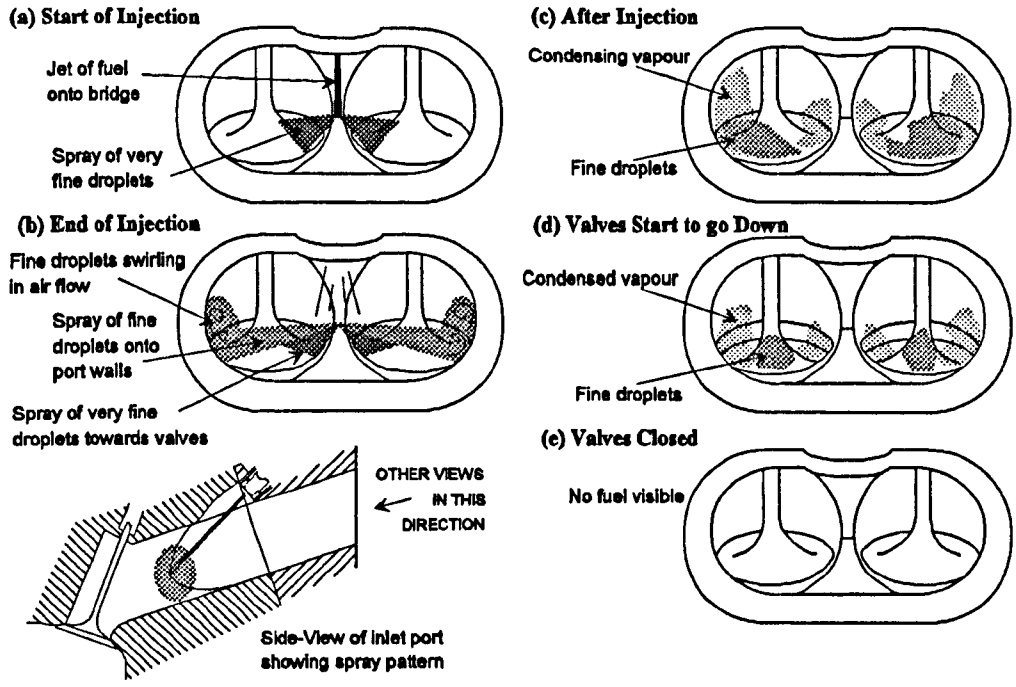

Figure 4.5 - Diagrams Produced from Photographs Taken of Fuel Transfer Characteristics for the Pencil Beam Injector

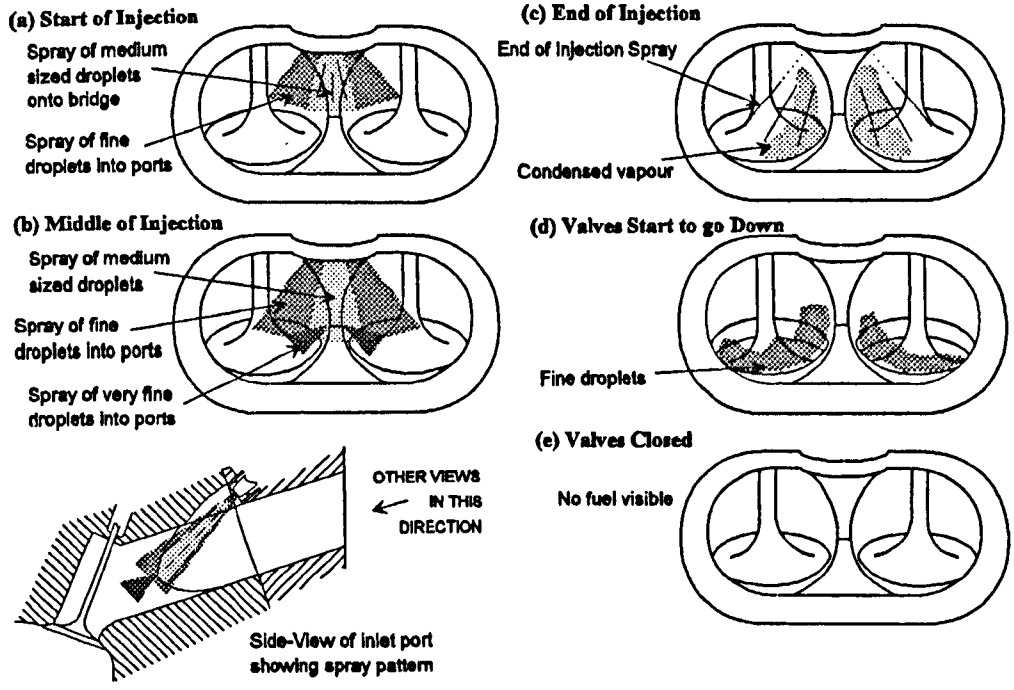

Figure 4.6 - Diagrams Produced from Photographs Taken of Fuel Transfer Characteristics for the Single-Pintle, Single-Spray Injector

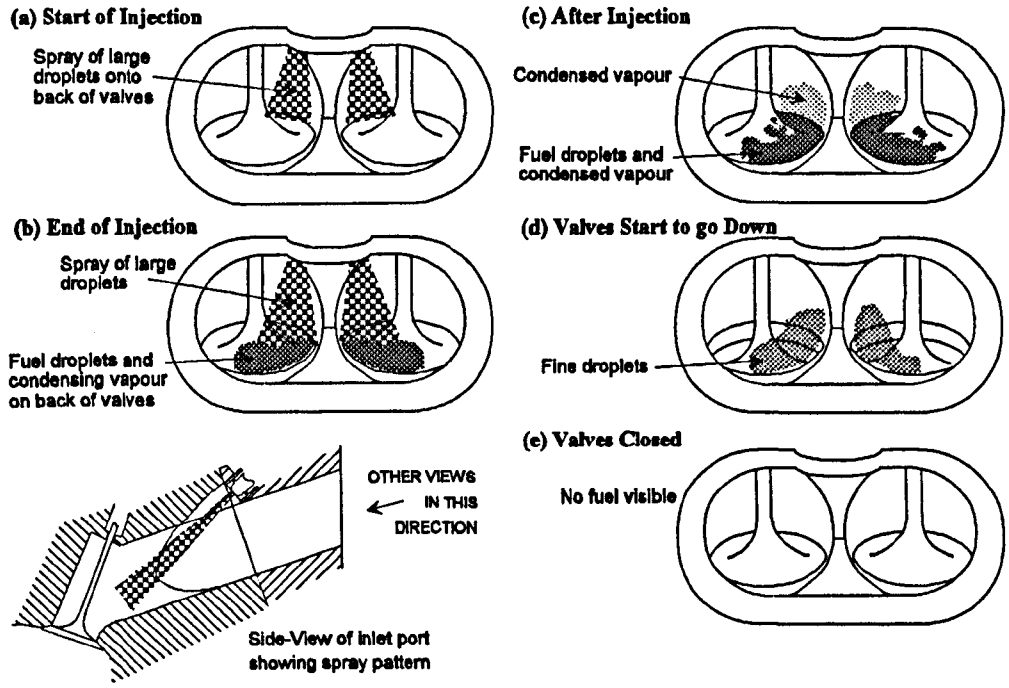

Figure 4.7 - Diagrams Produced from Photographs Taken of Fuel Transfer Characteristics for the Single-Pintle, Twin-Spray Injector

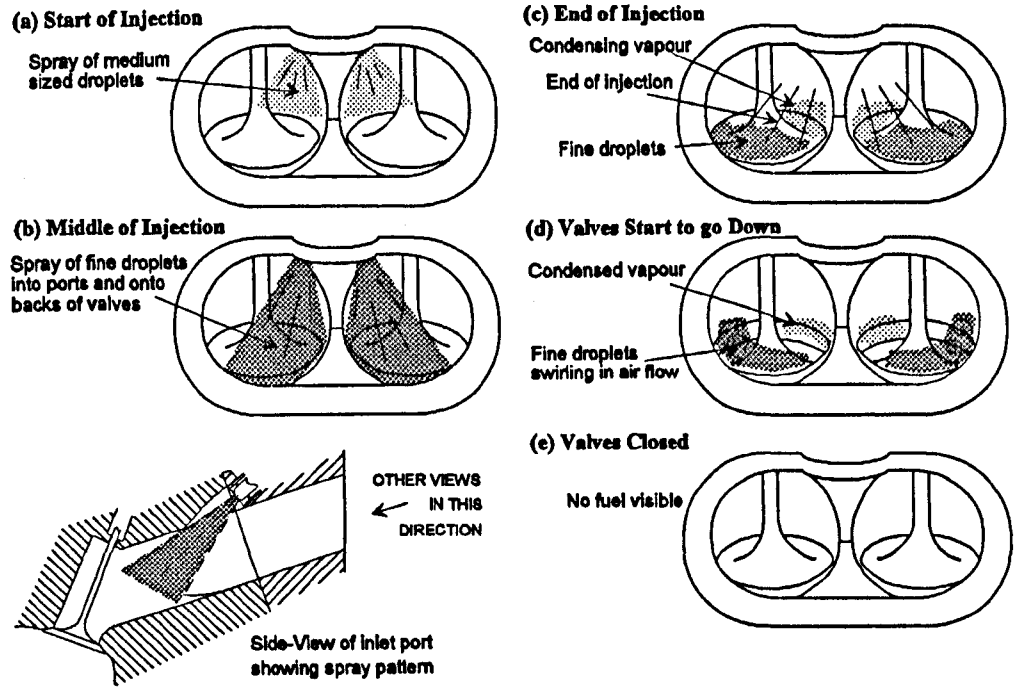

Figure 4.8 - Diagrams Produced from Photographs Taken of Fuel Transfer Characteristics for the Four-Hole Injector

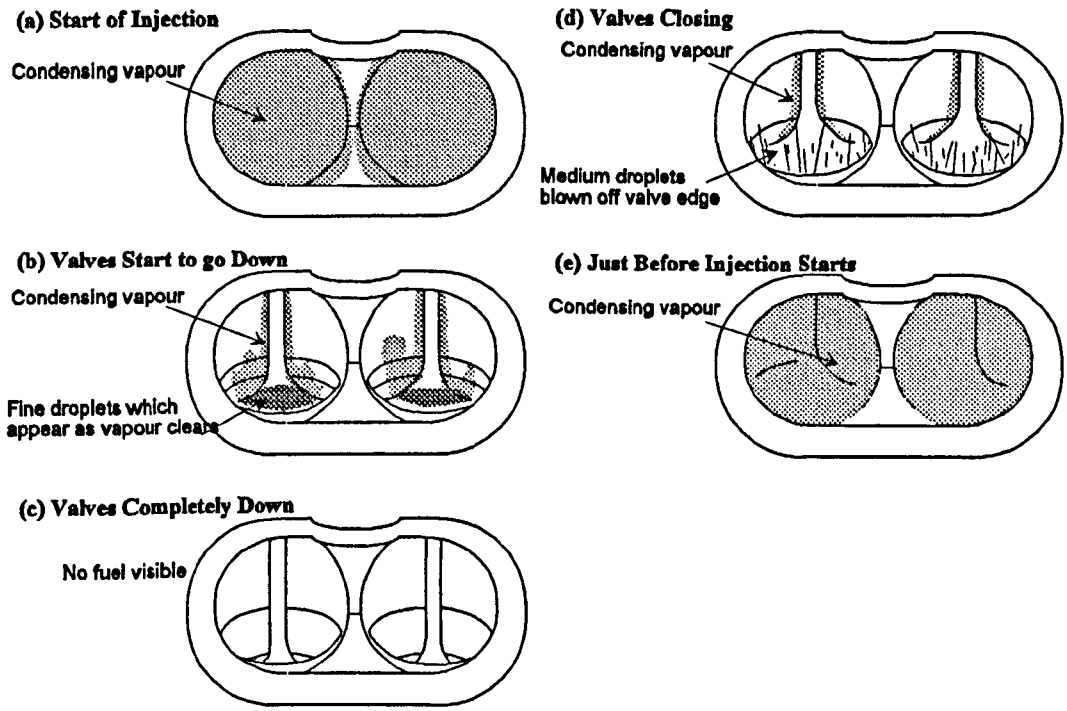

Figure 4.9 - Diagrams Produced from Photographs Taken of Fuel Transfer Characteristics for the Four-Hole Injector when the Engine is Being Force Cooled

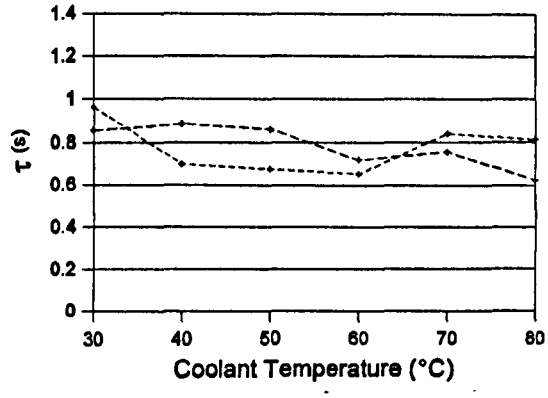

(a) Pencil-Beam Injector

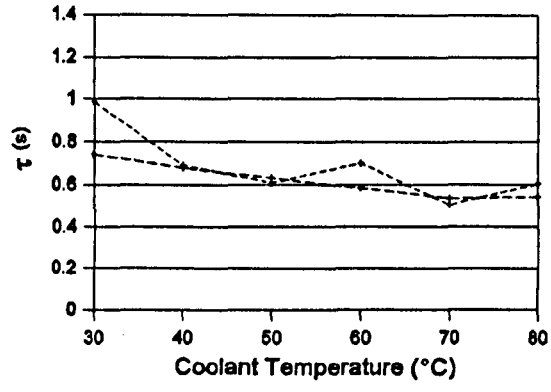

(b) Single-Spray Injector

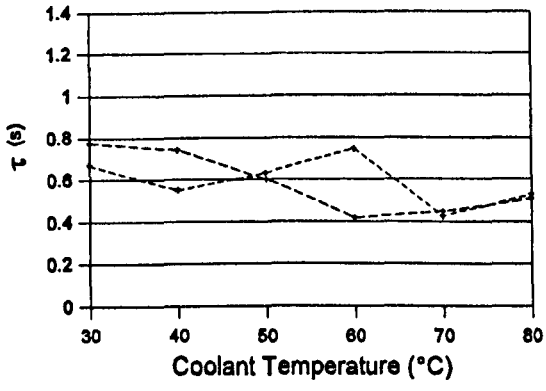

(c) Twin-Spray Injector

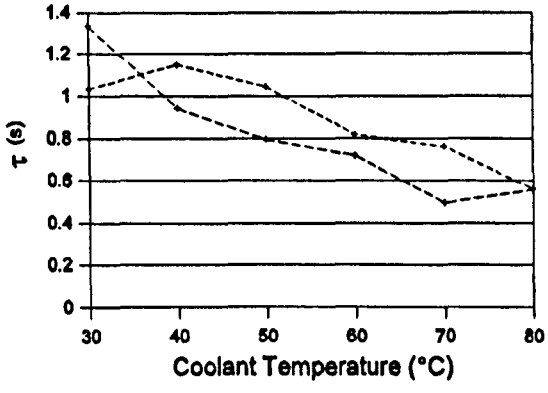

(d) 4-Hole Injector

Figure 4.10 - Variations in τ Produced by Each Injector During Repeated Warm-Up Tests at an Engine Speed of 1000 RPM, MAP of 0.79 bar and with a Stoichiometric Mean AFR

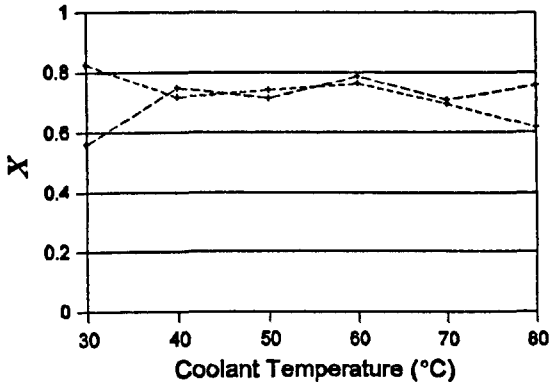

(a) Pencil-Beam Injector

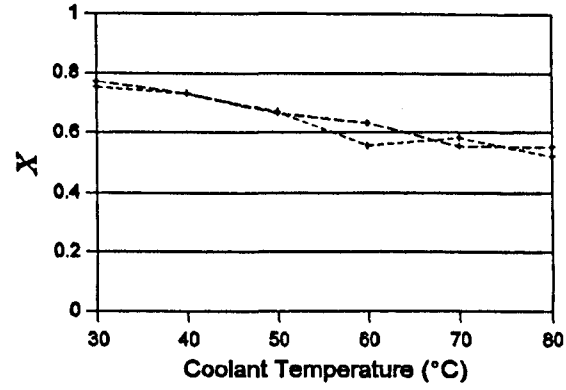

(b) Single-Spray Injector

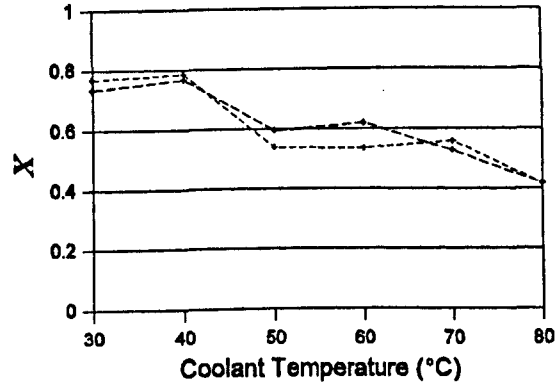

(c) Twin-Spray Injector

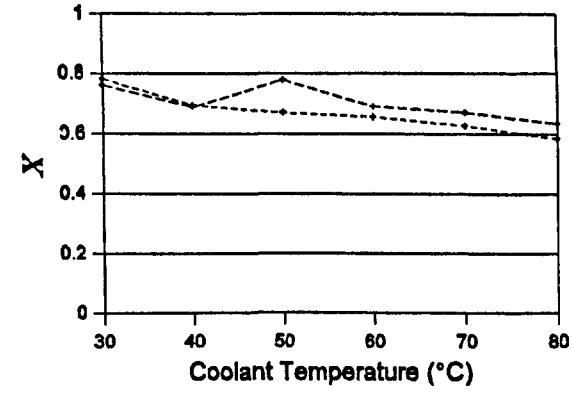

(d) 4-Hole Injector

Figure 4.11 - Variations in X Produced by Each Injector During Repeated Warm-Up Tests at an Engine Speed of 1000 RPM, MAP of 0.79 bar and with a Stoichiometric Mean AFR

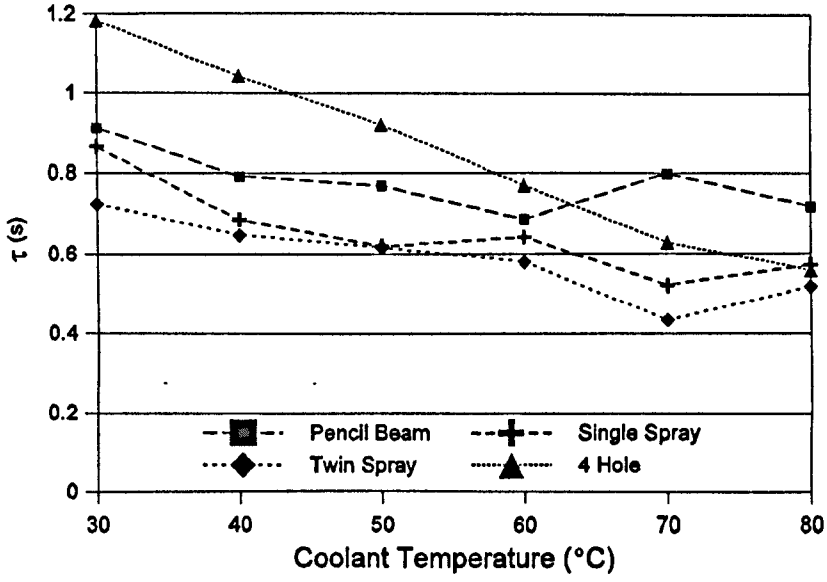

(a) τ Variations

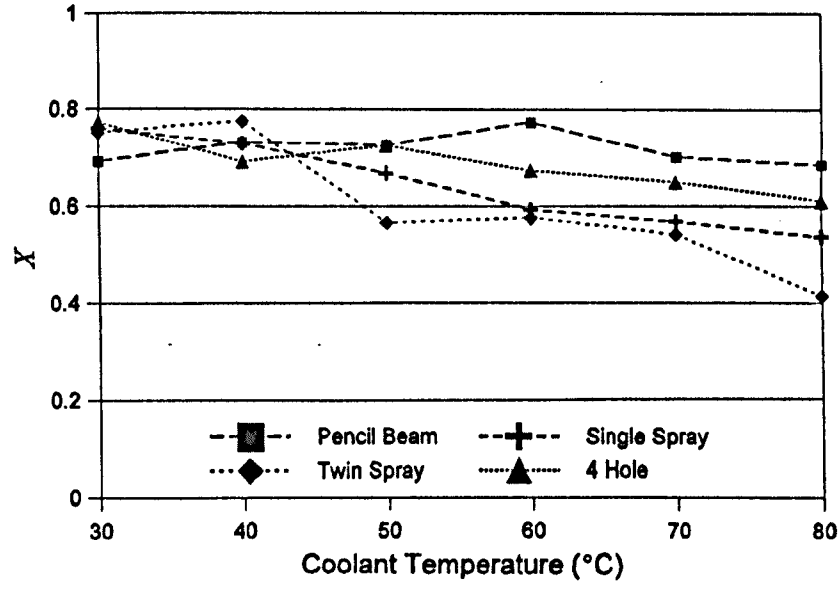

(b) *X* Variations

Figure 4.12 - Summary of Mean τ and *X* Variations Produced by Each Injector During Repeated Warm-Up Tests at an Engine Speed of 1000 RPM, MAP of 0.79 bar and with a Stoichiometric Mean AFR

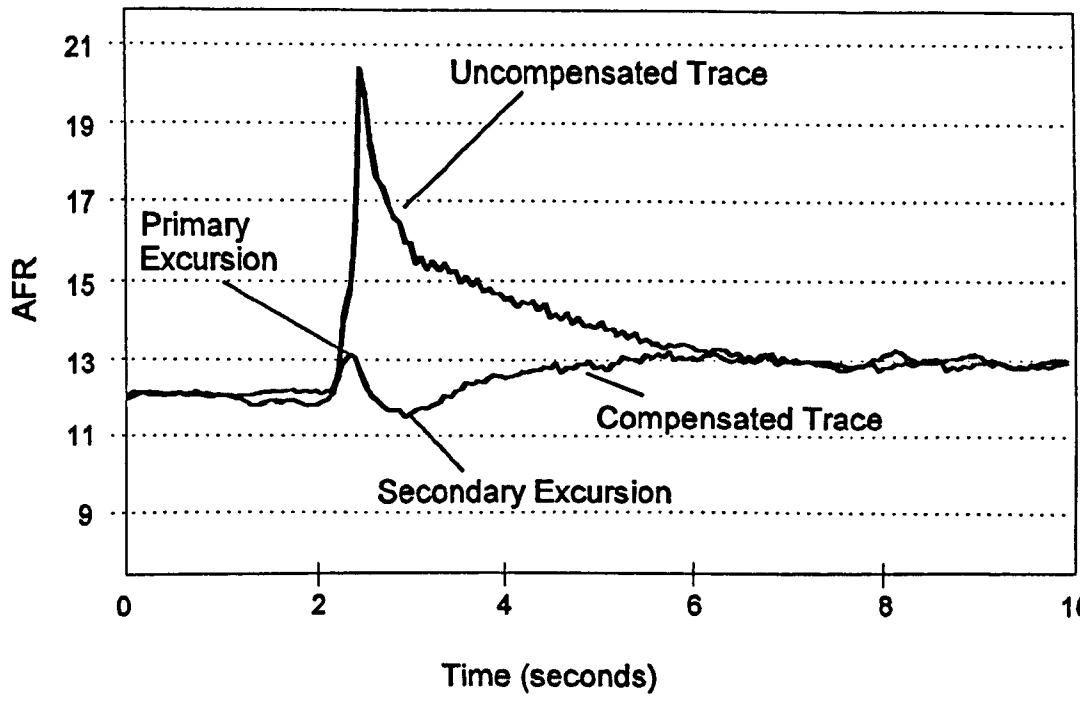

Figure 4.13 - Examples of Recorded AFR Values for Compensated and Uncompensated Throttle Transient Tests at -7°C **[4.22]**

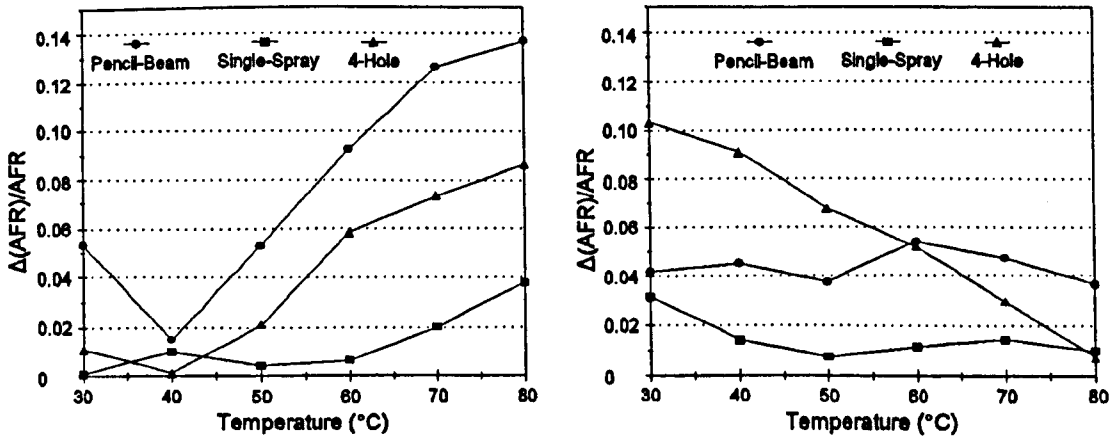

(a) Effect of Varying X on Expected Primary Excursion

(b) Effect of Varying τ on Expected Secondary Excursion

Figure 4.14 - Effects of Changing Injector Type on Primary and Secondary Excursions in Compensated Throttle Transients, Assuming System Calibrated with Twin-Spray Injector, During Warm-Up at 1000 RPM, 0.79 bar MAP and with Stoichiometric Mean AFR

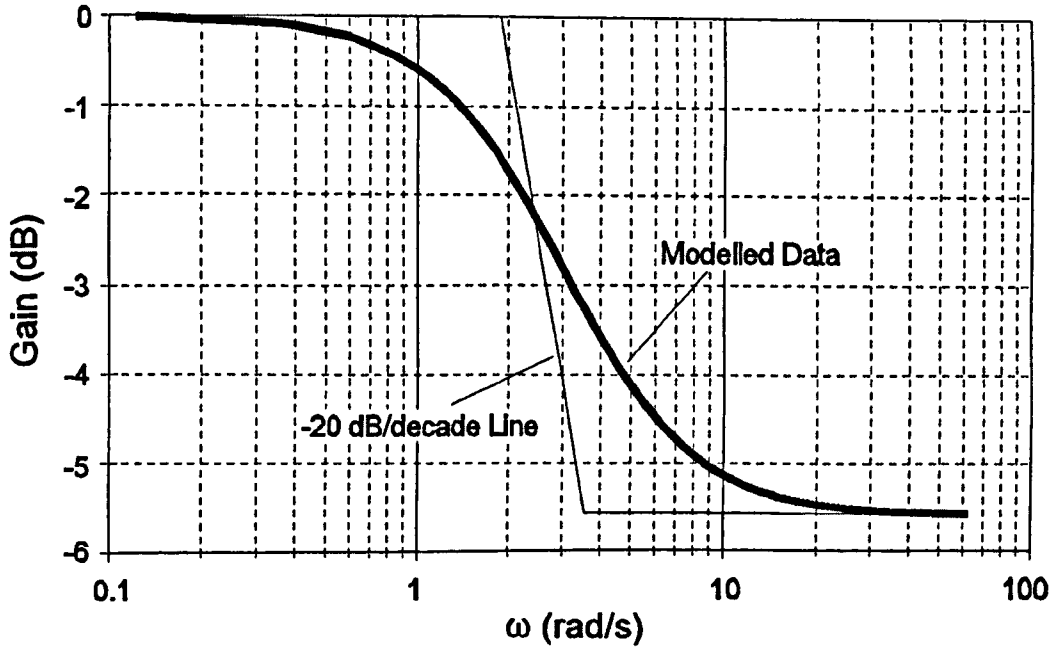

Figure 4.15 - Gain Plot from Modelled Frequency Response of AFR (excluding UEGO response) to a Fuel Perturbation with a Twin-Spray Injector, for an Engine Running at 1000 RPM, 0.79 bar MAP and with a Stoichiometric Mean AFR

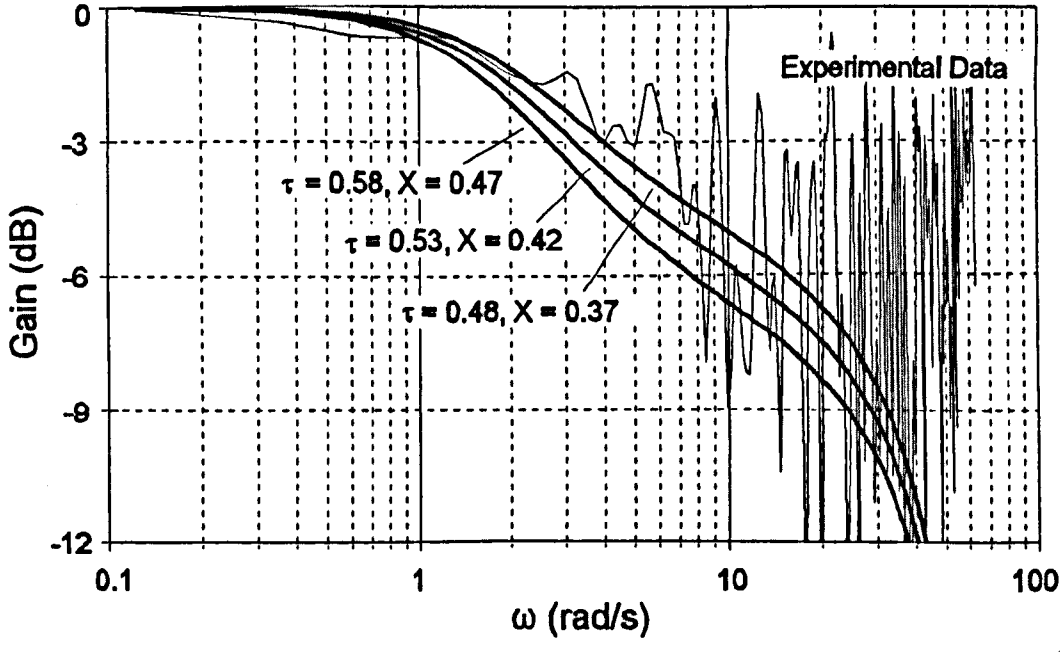

Figure 4.16 - Gain Plots for Modelled and Experimental Frequency Responses of AFR (including UEGO response) to Fuel Perturbations with a Twin-Spray Injector, for an Engine Running at 1000 RPM, 0.79 bar MAP and with a Stoichiometric Mean AFR

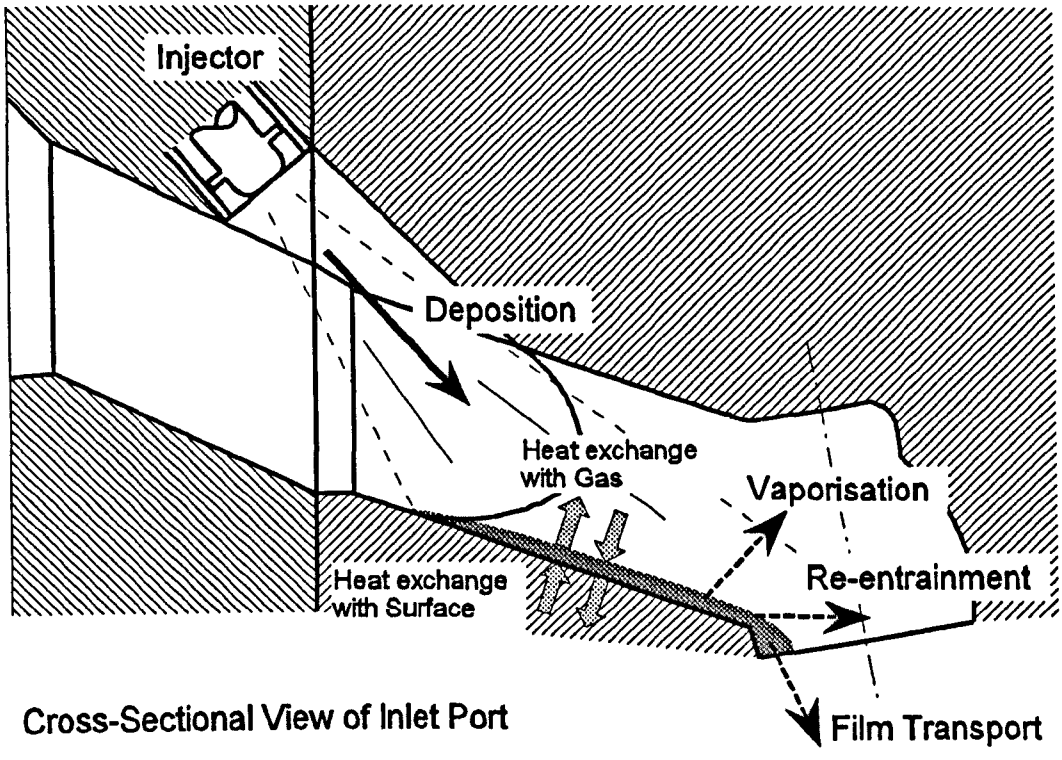

Figure 5.1 - Heat Transfer and Mixture Preparation Processes in the Inlet Port

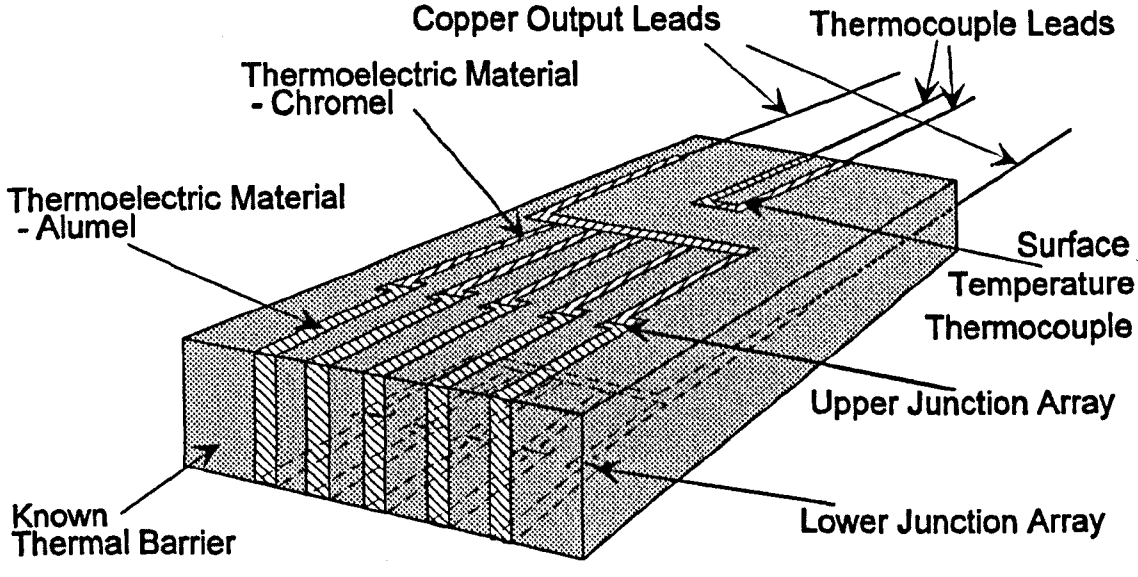

Figure 5.2 - Diagram Showing Heat Flux Sensor Construction

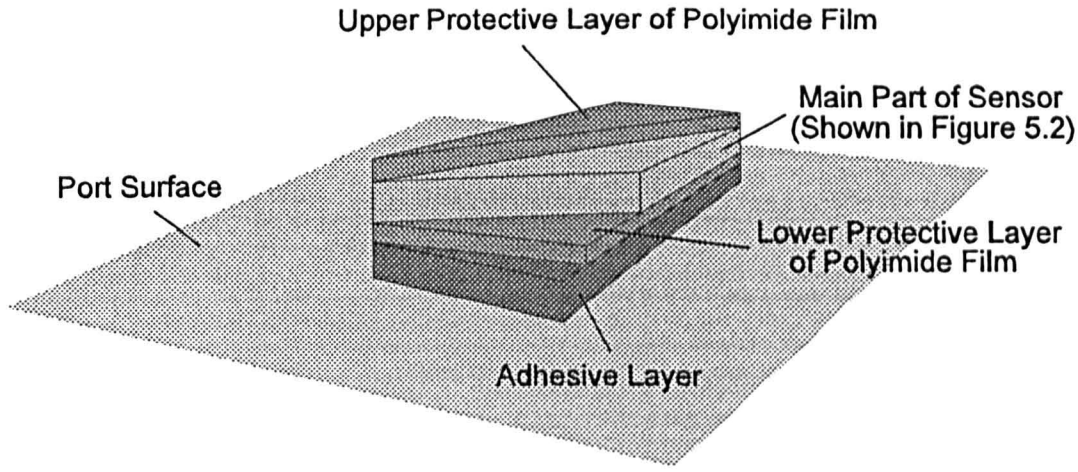

Figure 5.3 - Simplified Diagram of Sensor/Adhesive/Port-Wall Interface. Vertical Dimensions Exagerated for Clarity.

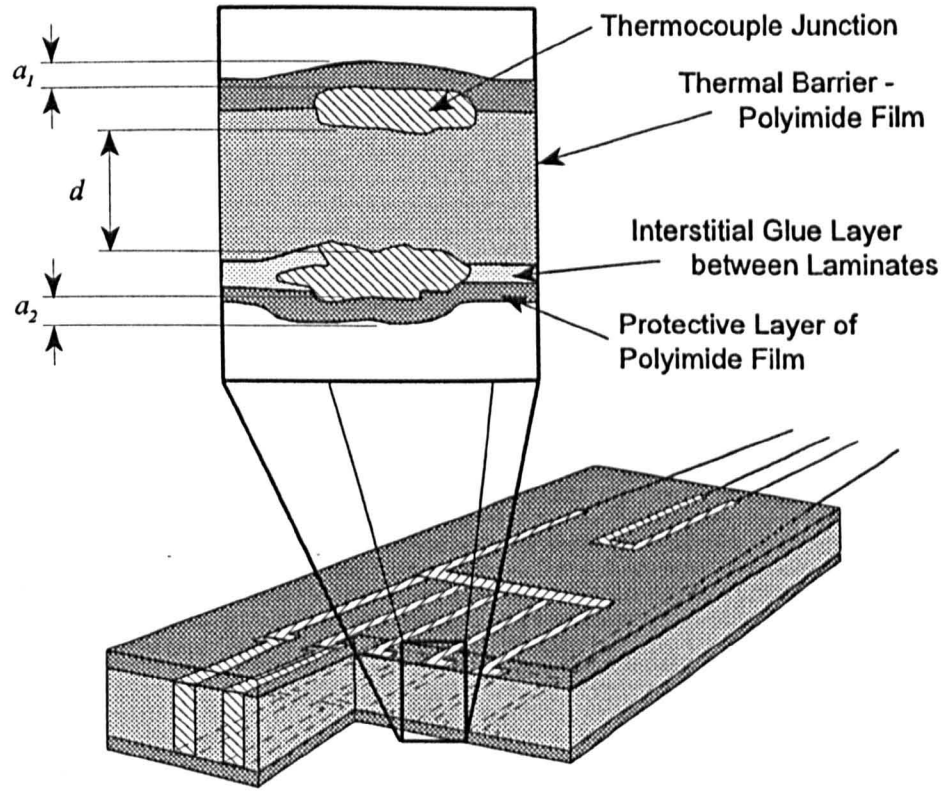

Figure 5.4 - Diagram of Heat Flux Sensor with Graphically Enhanced Enlargement of Section Through Thermocouple Junctions

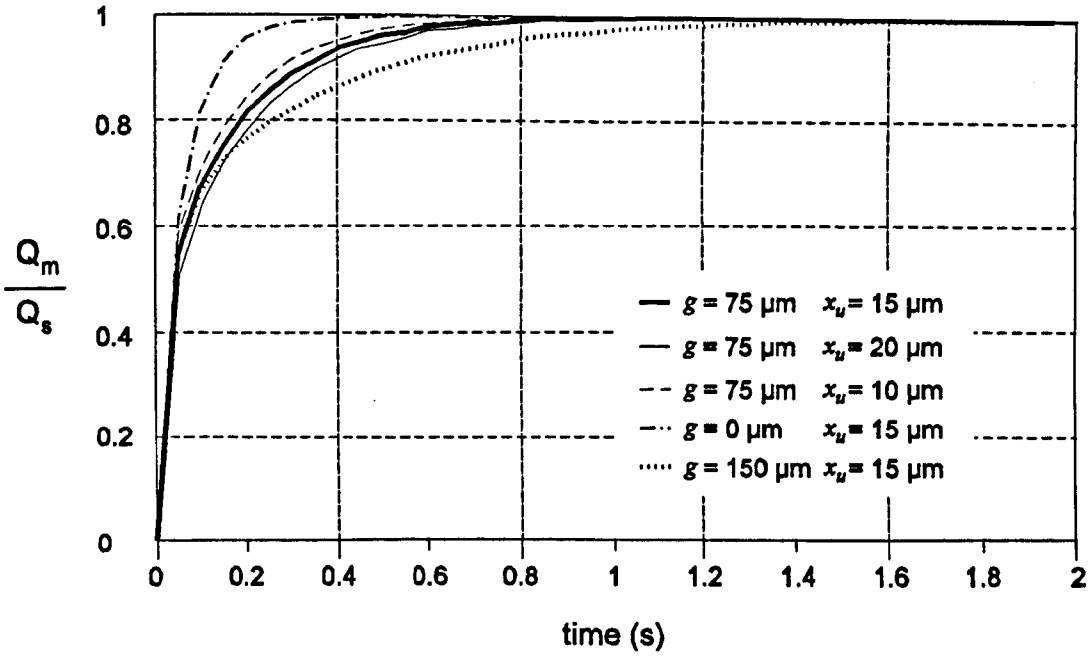

(a) Full Response to Steady State Conditions

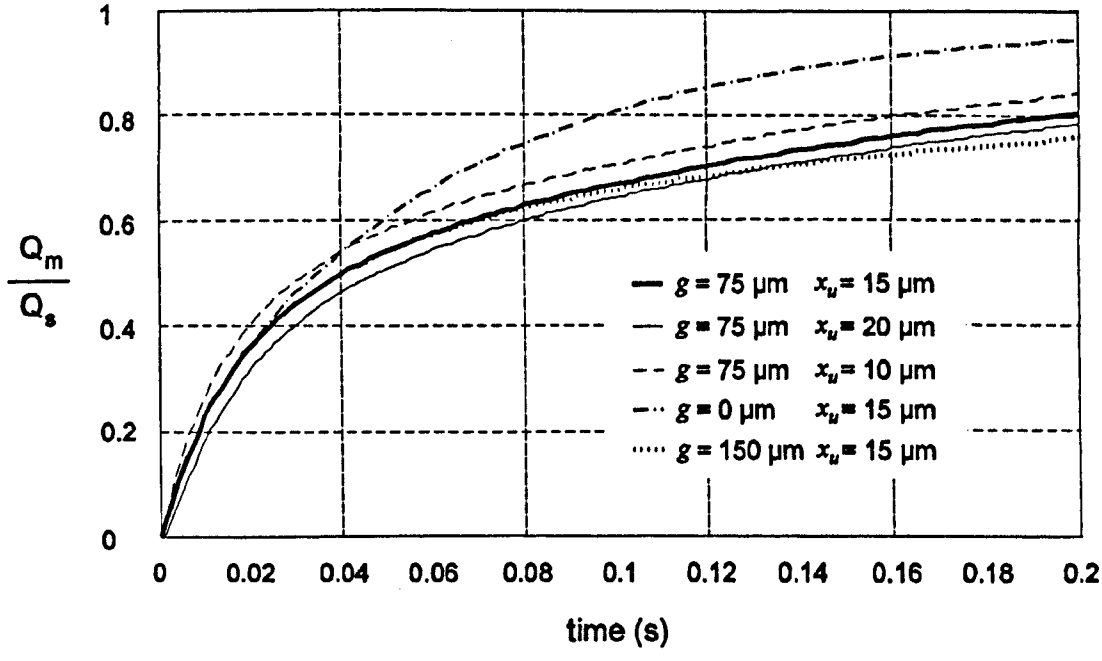

(b) Magnified Time-Scale, Showing Rise to 62% of Steady State Value

Figure 5.5 - Variation with Adhesive Film Thickness in Modelled Response of Heat Flux Sensor to a Step Change in Surface Heat Flux

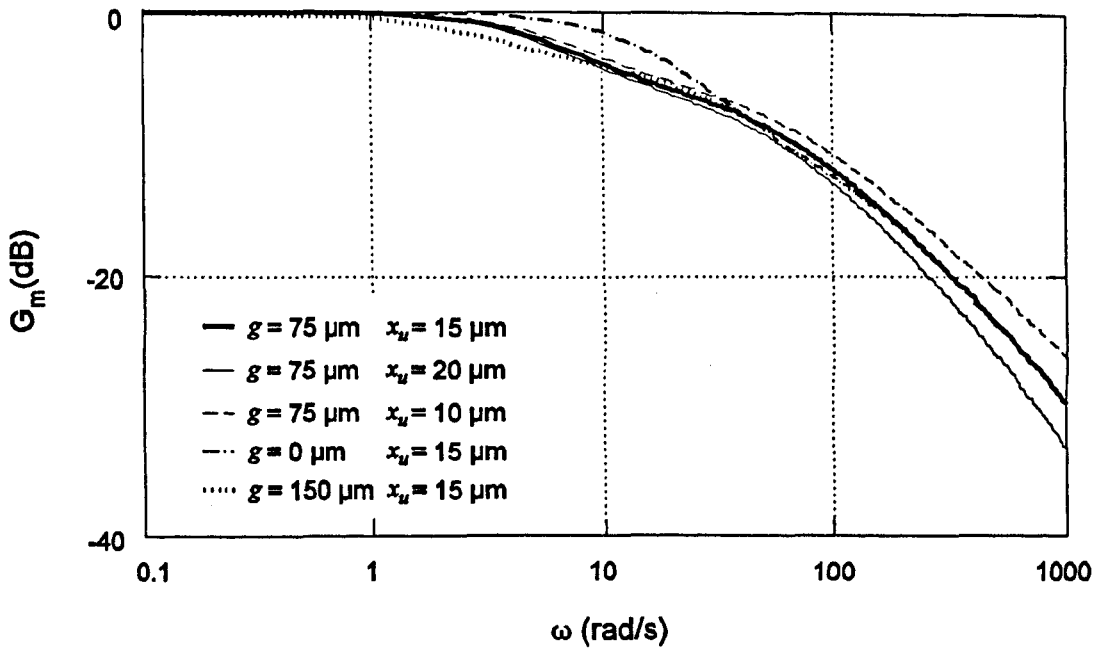

(a) Magnitude Plot

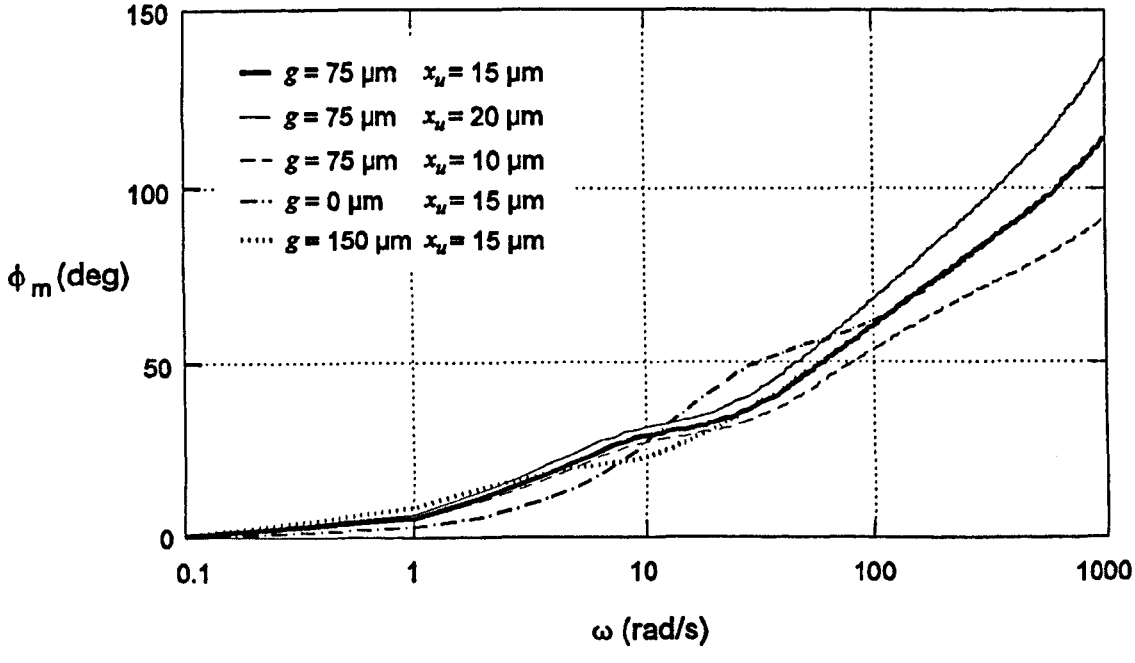

(b) Phase Plot

Figure 5.6 - Bode Diagram of Data Calculated from Modelled Transfer Function for Heat Flux Sensors

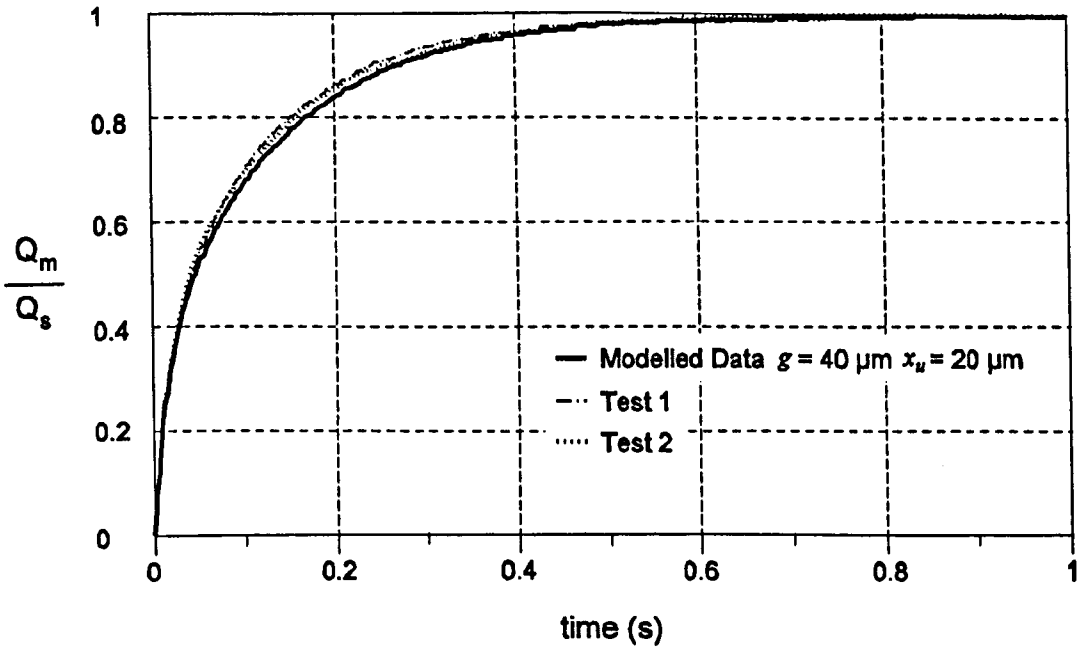

Figure 5.7 - Experimentally Recorded and Modelled Step Response Data for Heat Flux Sensor

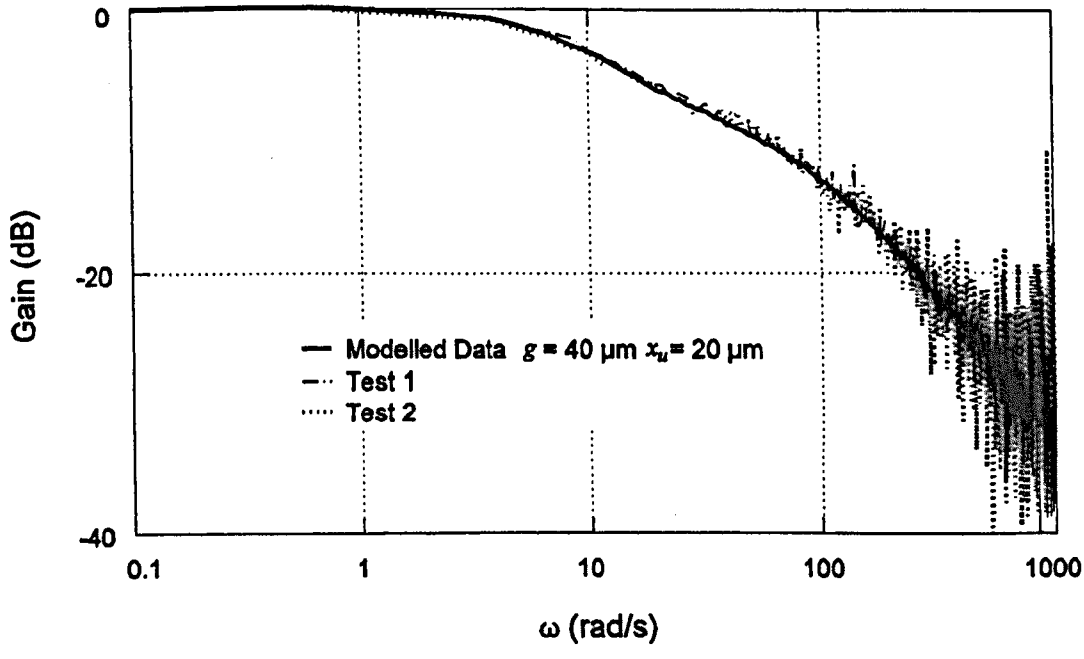

Figure 5.8 - Magnitude Plots from Bode Diagrams of Heat Flux Sensor Response Dynamics Derived from Modelled and Experimentally Recorded Data

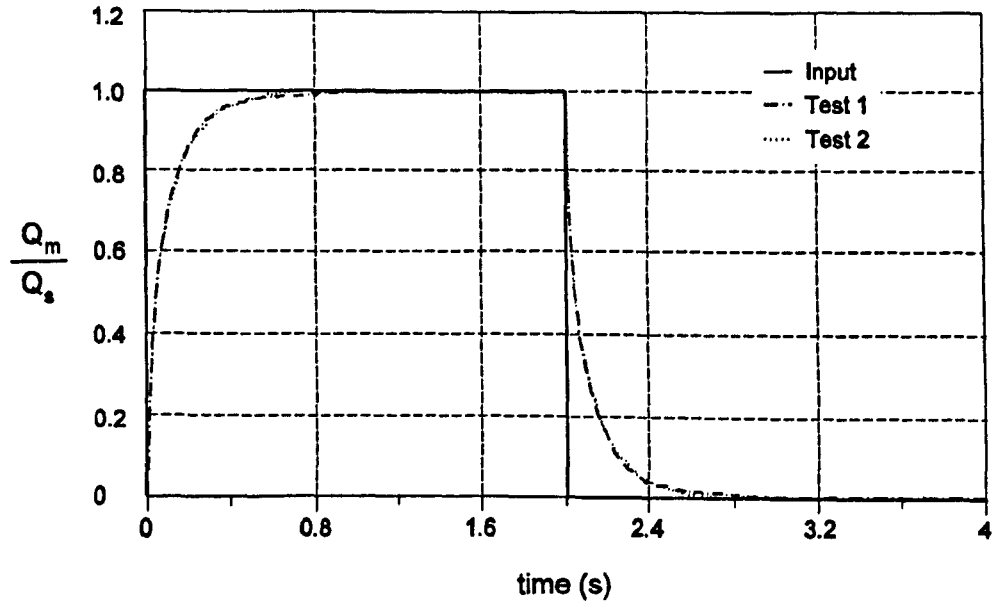

Figure 5.9 - Input and Output Pulse Waveform Data
Synthesised from Normalised Results of Step Response Tests

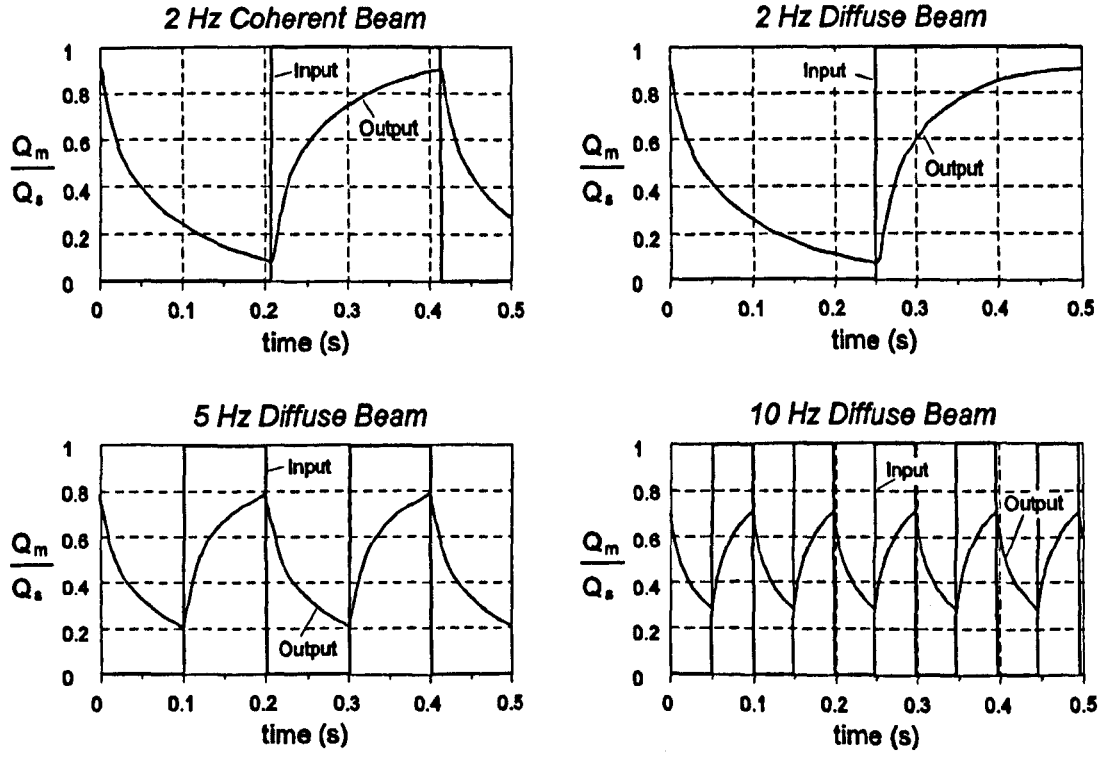

Figure 5.10 - Normalised Input and Output Pulse Waveform Data
Produced Using Rotating Shutter with Laser Beam

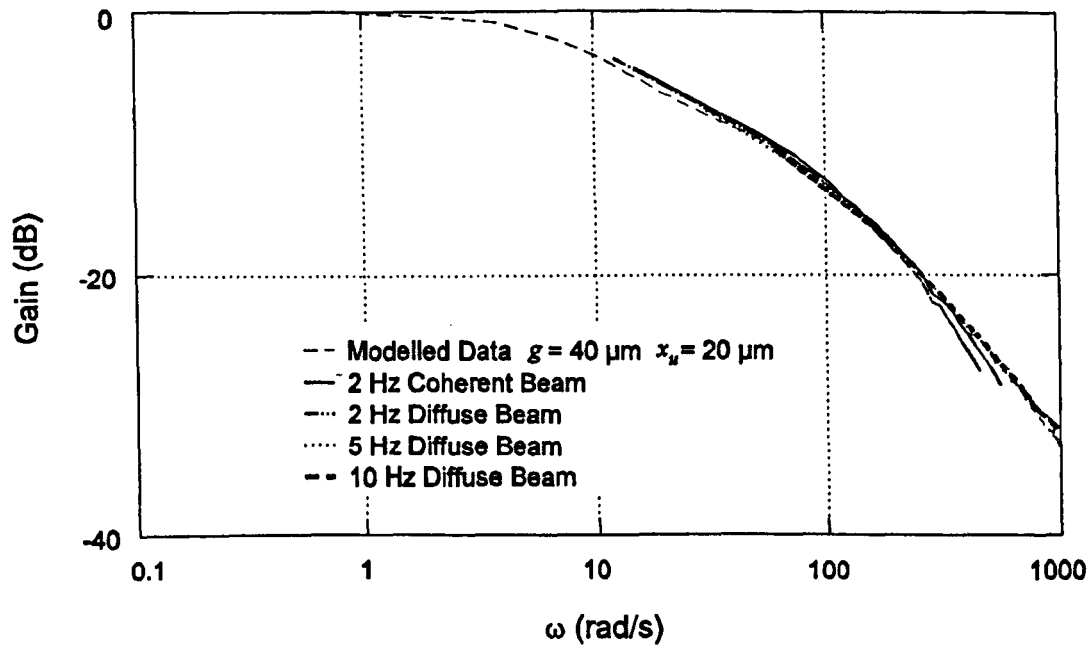

Figure 5.11 - Magnitude Bode Plots of Heat Flux Sensor Response Dynamics Derived from Modelled Data and Experimentally Recorded Pulse Waveform Results

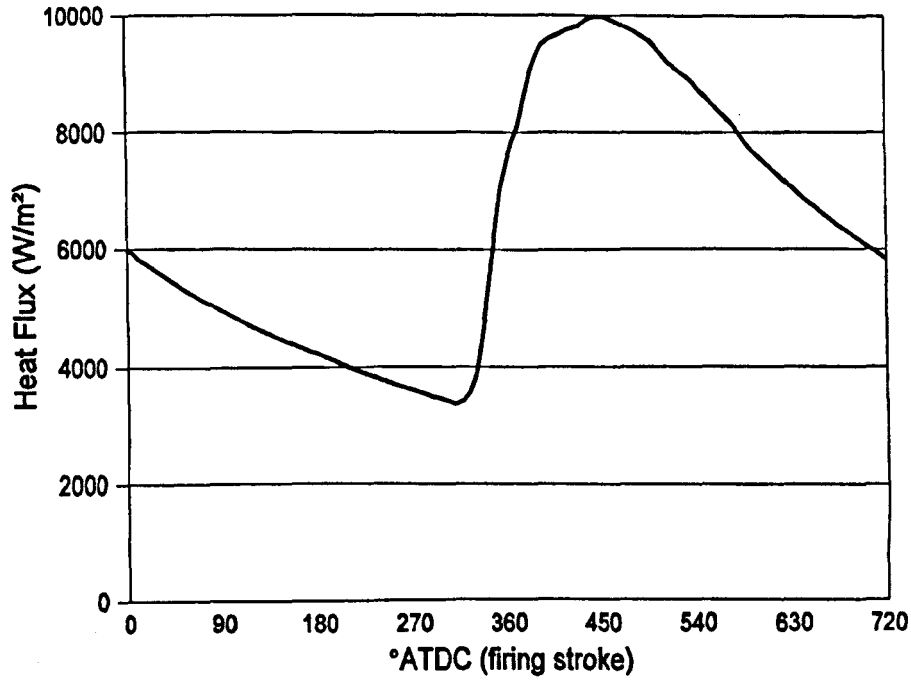

Figure 5.12 - Typical Crank-Angle Resolved Heat Flux Data Measured through Sensor 7 with Engine Running at 1000 RPM, 0.79 bar MAP and with a Stoichiometric AFR

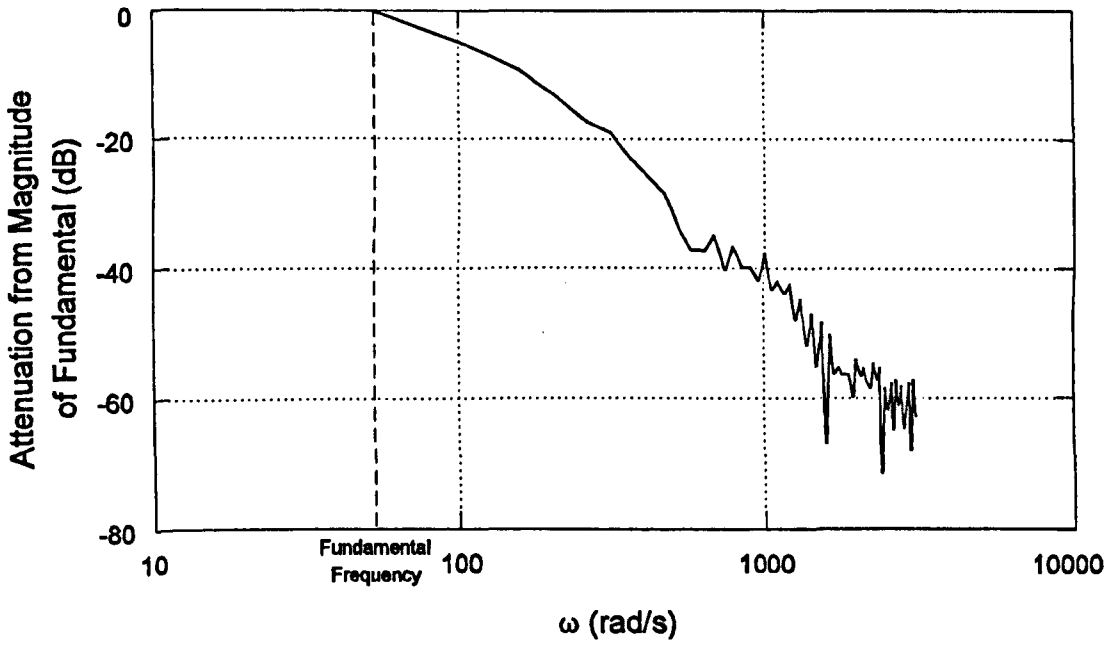

Figure 5.13 - Frequency Content of Crank-Angle Resolved Data Shown in Figure 5.12

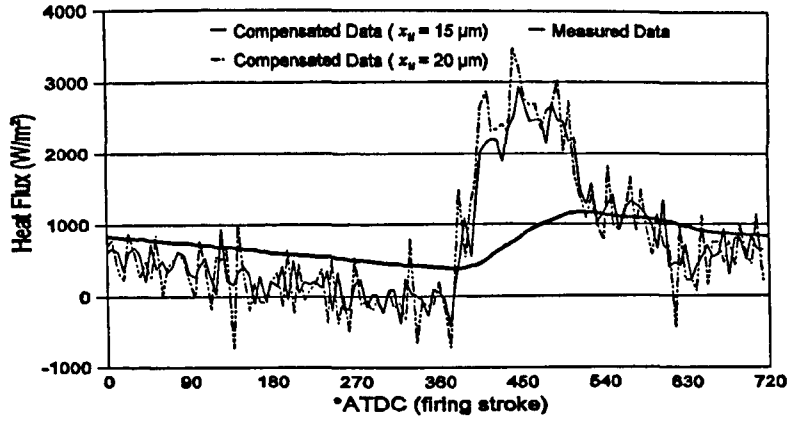

(a) Data Recorded from Sensor 1 when No Fuel Landing

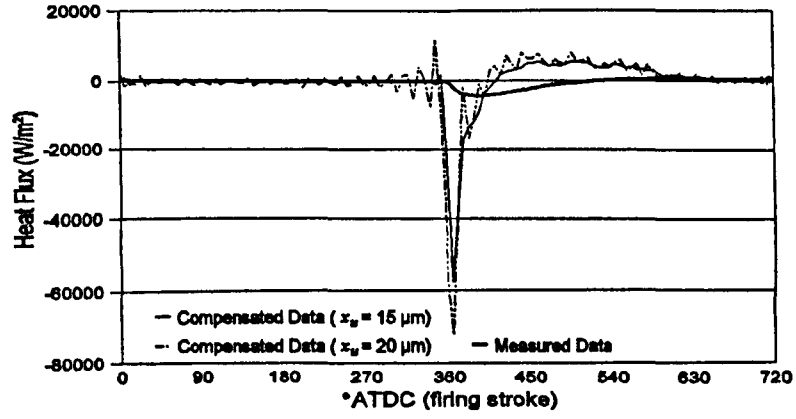

(b) Data Recorded from Sensor 6 when No Fuel Landing

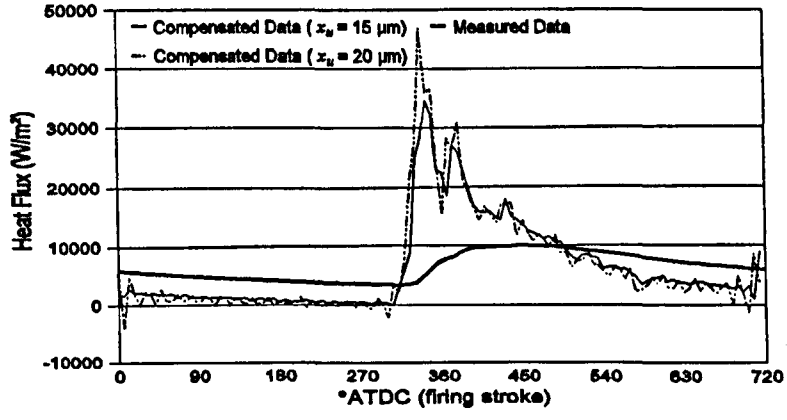

(c) Data Recorded from Sensor 7 when Wetted by Fuel

Figure 5.14 - Crank-Angle Resolved Heat Flux Data from Engine Running at 1000 RPM, 0.79 bar MAP and with a Stoichiometric AFR, Before and After Compensation for Sensor Dynamic Response Characteristics

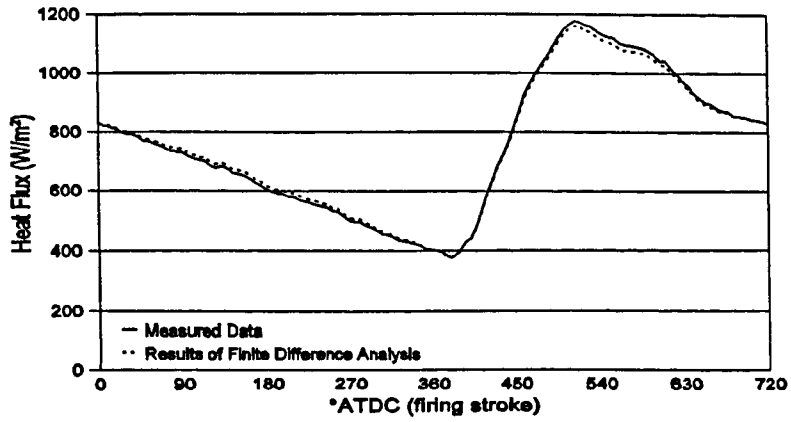

(a) Data Recorded from Sensor 1 when No Fuel Landing

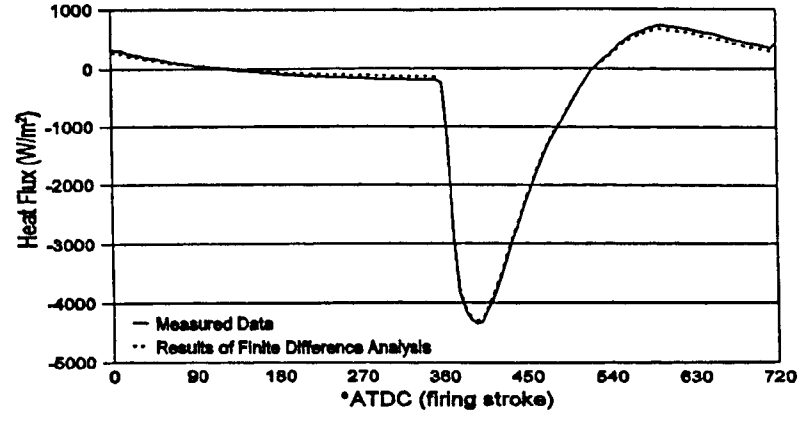

(b) Data Recorded from Sensor 6 when No Fuel Landing

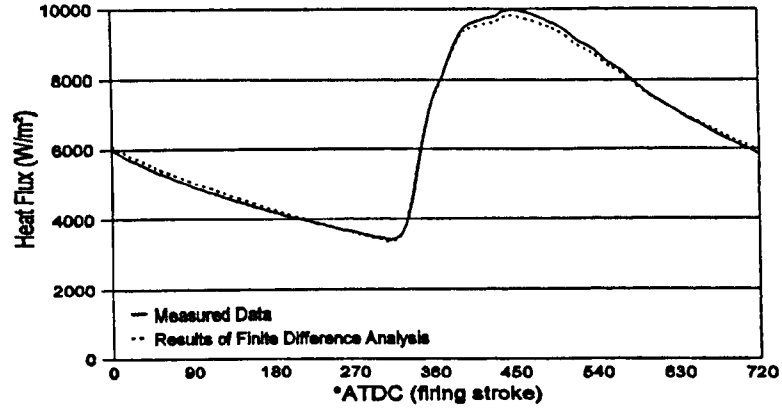

(c) Data Recorded from Sensor 7 when Wetted by Fuel

Figure 5.15 - Comparison Between Measured Crank-Angle Resolved Heat Flux Data and the Results of Finite Difference Analysis on Inferred Surface Heat Fluxes

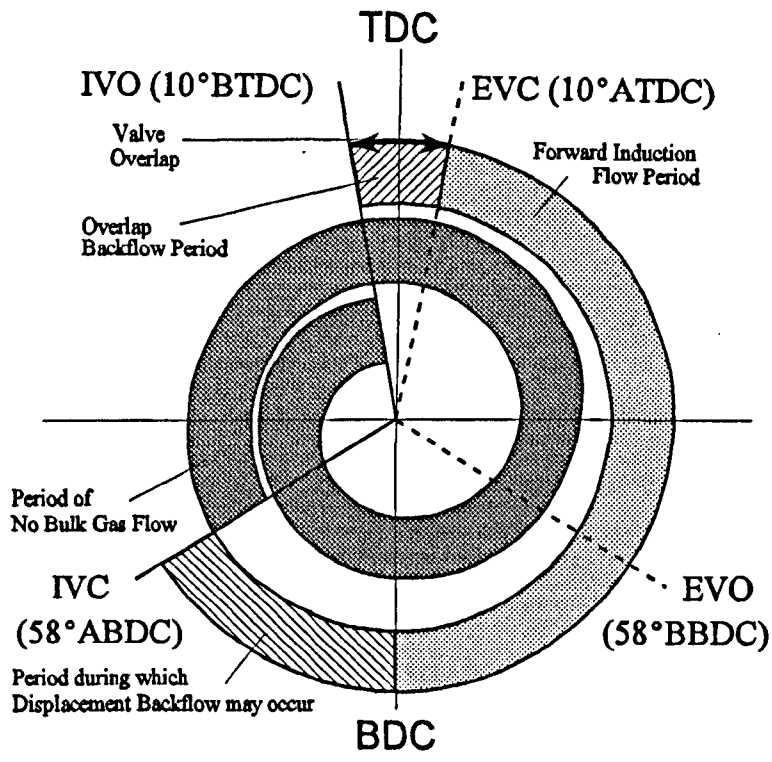

Figure 6.1 - Diagram Showing Timing of Inlet Port Events for a Ford Zetec High Output Engine

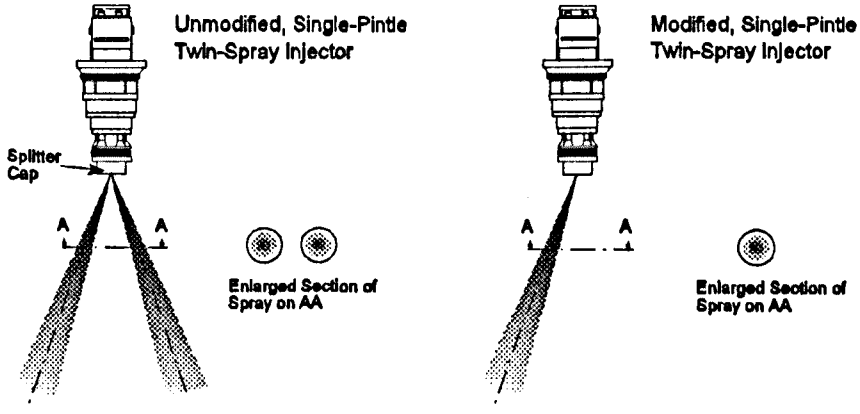

Figure 6.2 - Injector Spray Patterns for Modified and Unmodified Twin-Spray Injectors

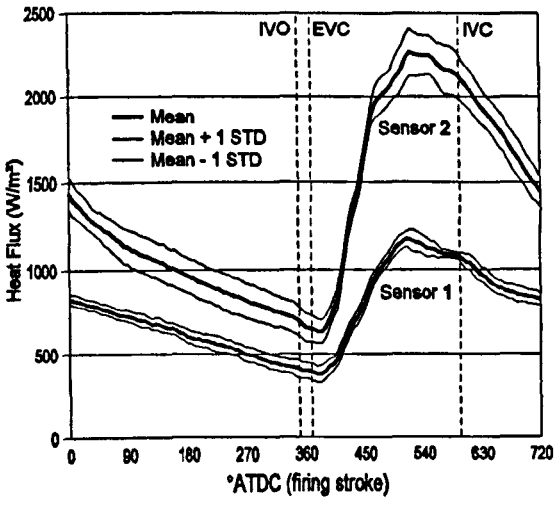

(a) Sensors 1 and 2

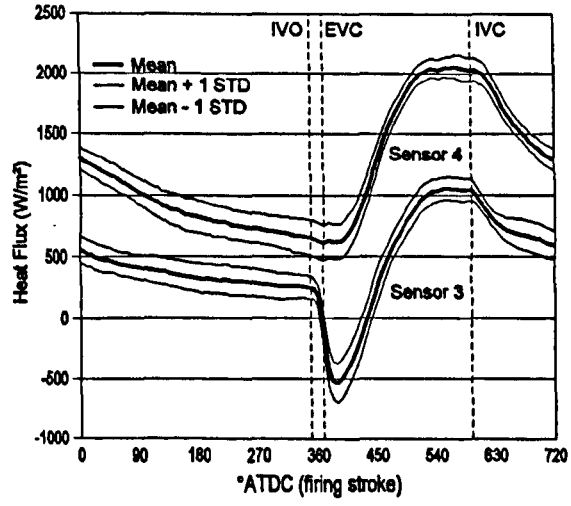

(b) Sensors 3 and 4

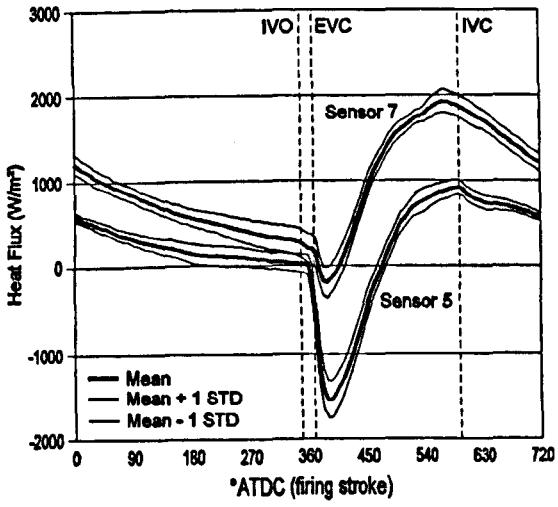

(c) Sensors 5 and 7

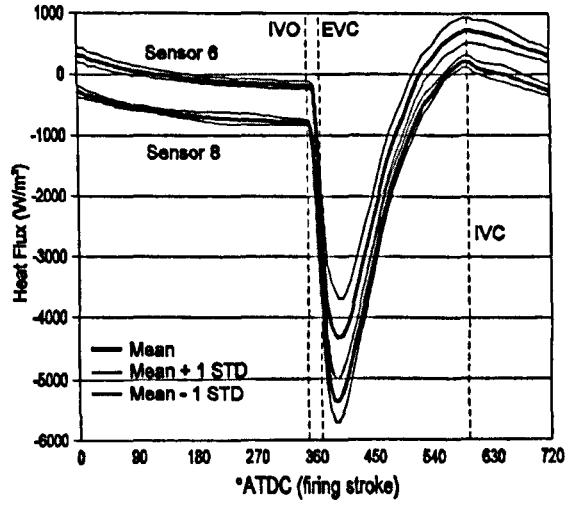

(d) Sensors 6 and 8

Figure 6.3 - "Dry-Port" Crank-Angle Resolved Heat Fluxes with a Fully-Warm Engine Running at 1000 RPM, 0.79 bar MAP and a Stoichiometric AFR

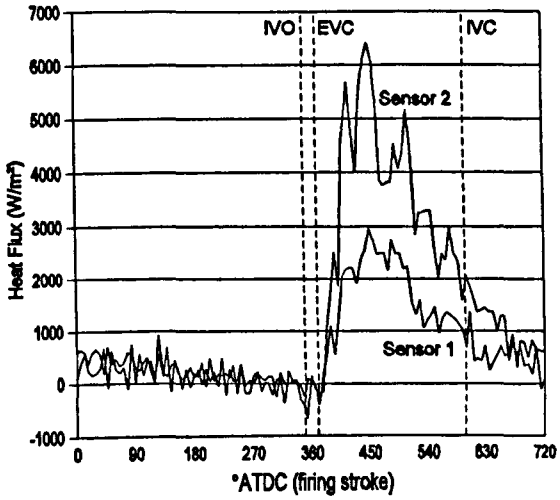

(a) Sensors 1 and 2

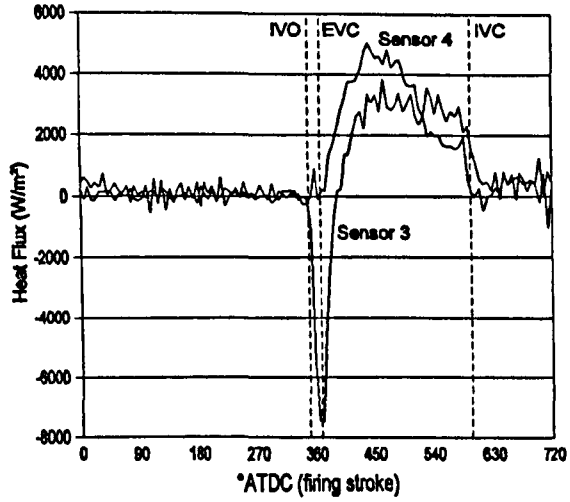

(b) Sensors 3 and 4

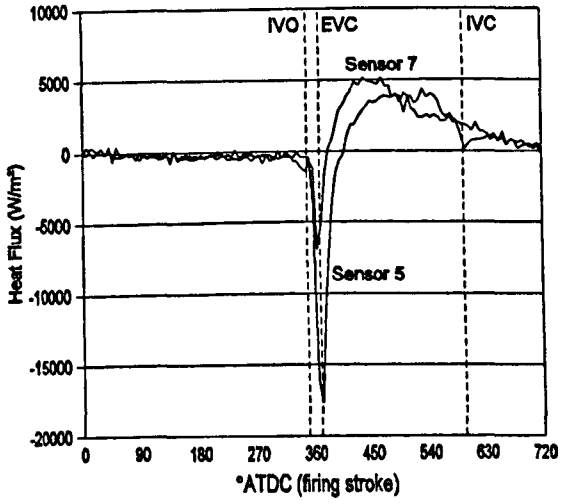

(c) Sensors 5 and 7

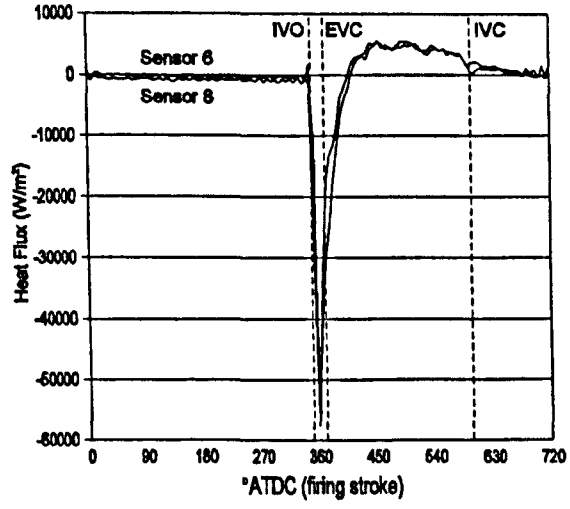

(d) Sensors 6 and 8

Figure 6.4 - "Dry-Port" Crank-Angle Resolved Heat Fluxes with a Fully-Warm Engine Running at 1000 RPM, 0.79 bar MAP and a Stoichiometric AFR, After Compensating for the Effects of Sensor Response

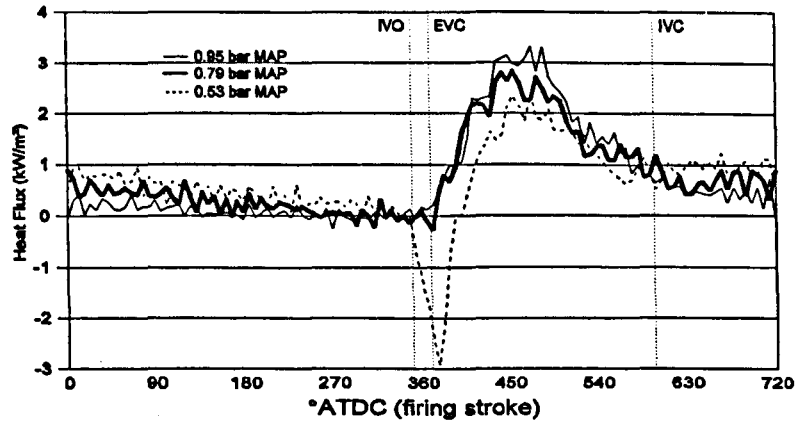

(a) Sensor 1

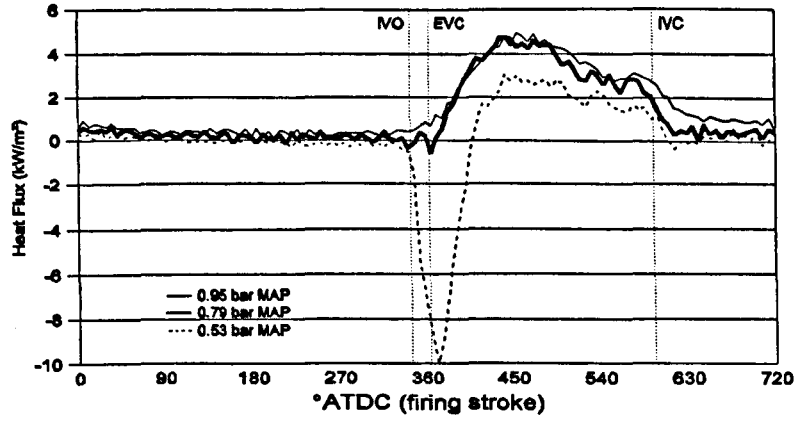

(b) Sensor 4

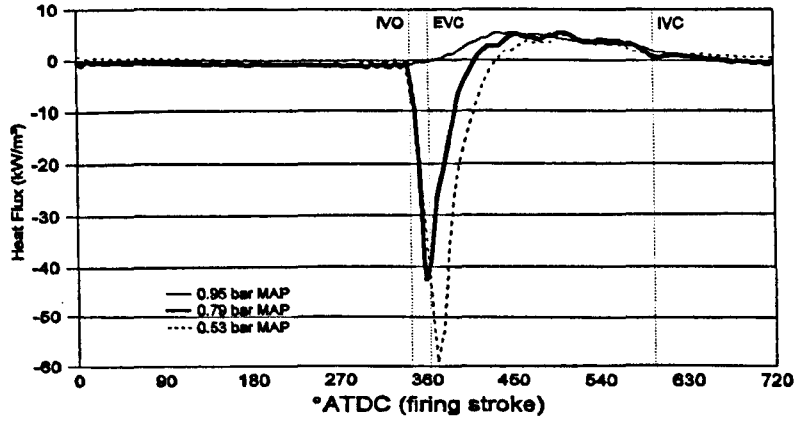

(c) Sensor 8

Figure 6.5 - Variation with MAP of Crank-Angle Resolved "Dry-Port" Heat Fluxes through Sensors 1, 4 and 8 with a Fully-Warm Engine Operating at 1000 RPM and Stoichiometric AFR, After Compensating for the Effects of Sensor Response

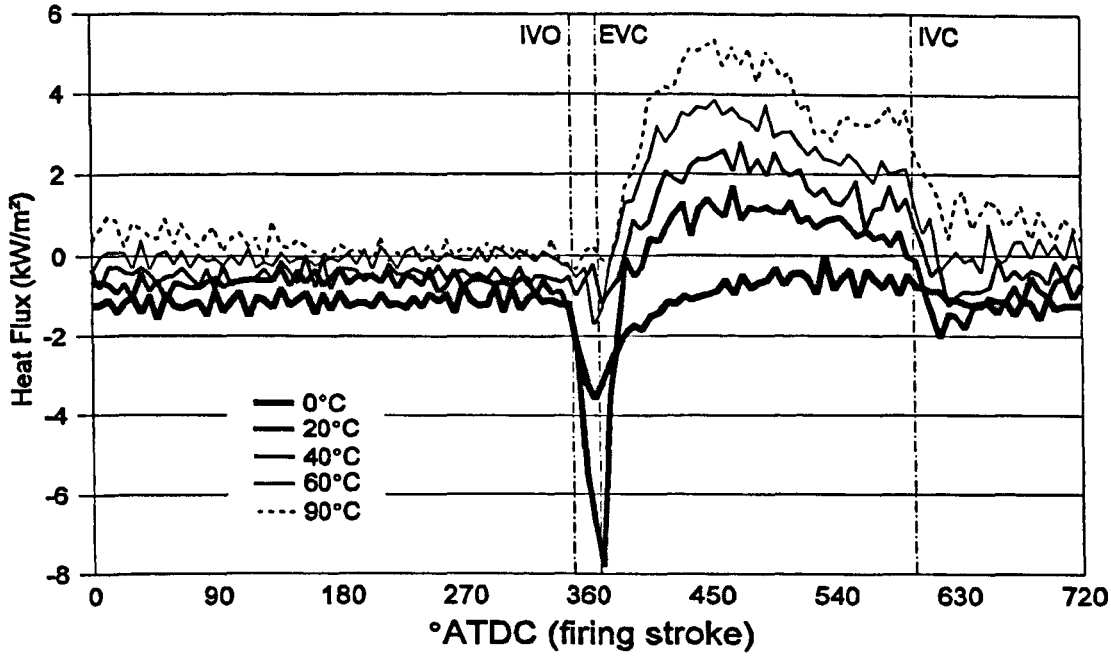

(a) Sensor 4

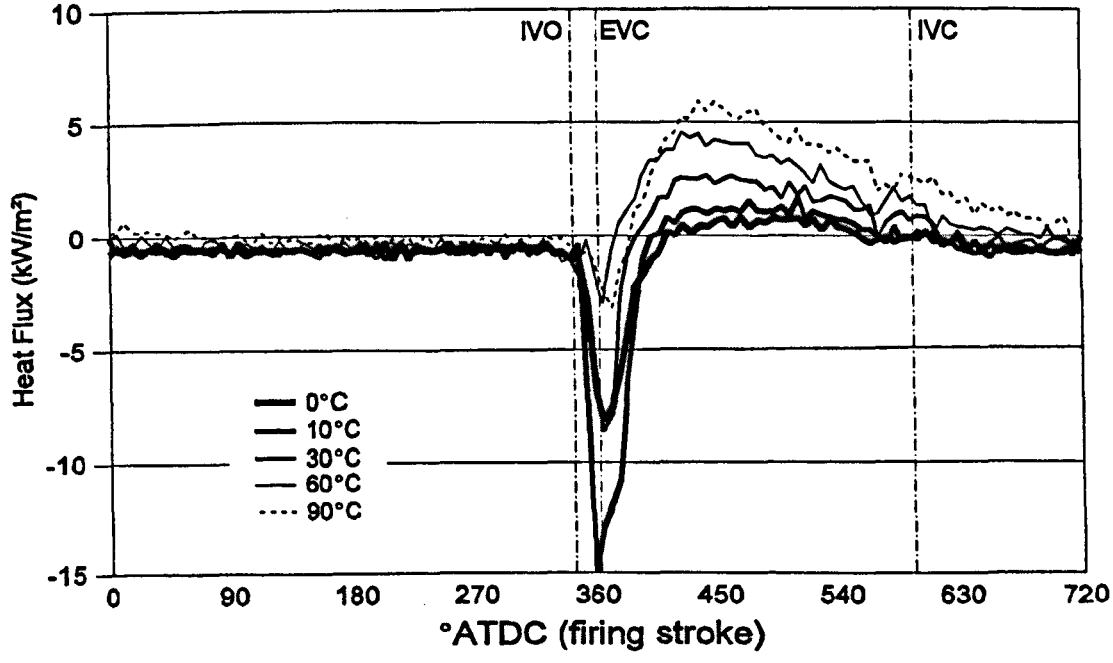

(b) Sensor 7

Figure 6.6 - Variation with Coolant Temperature of Compensated, Crank-Angle Resolved "Dry-Port" Heat Fluxes through Sensors 4 and 7, with the Engine Operating at 1000 RPM, 0.79 bar MAP and Stoichiometric AFR

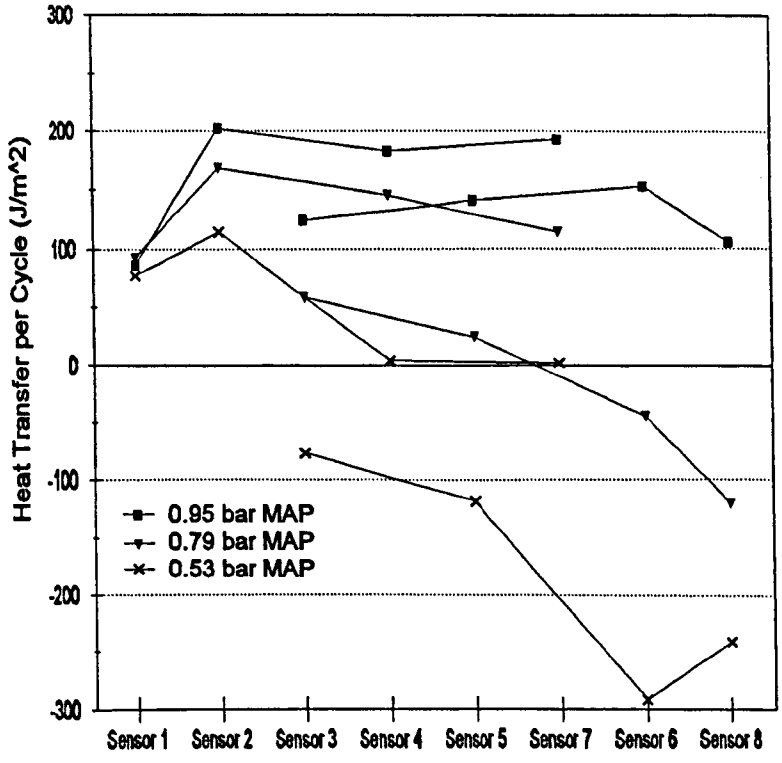

Figure 6.7 - Variations in Cycle-Averaged "Dry-Port" Heat Transfer Rates with Sensor Position and MAP. Engine Running Fully-Warm at 1000 RPM & 14.7 AFR

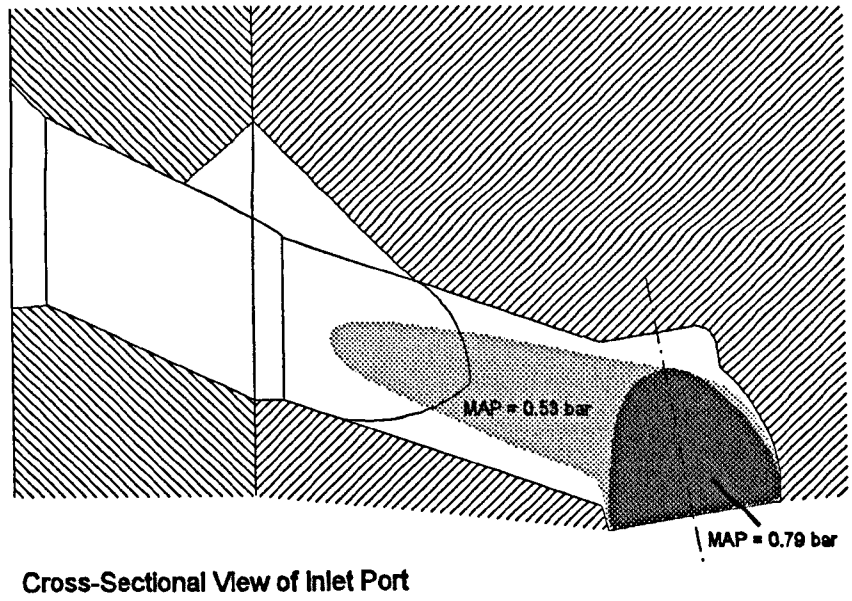

Figure 6.8 - Representation of Volumes of Backflow Gas in Inlet Port at 1000 RPM, Stoichiometric AFR and 2 Different MAP Conditions

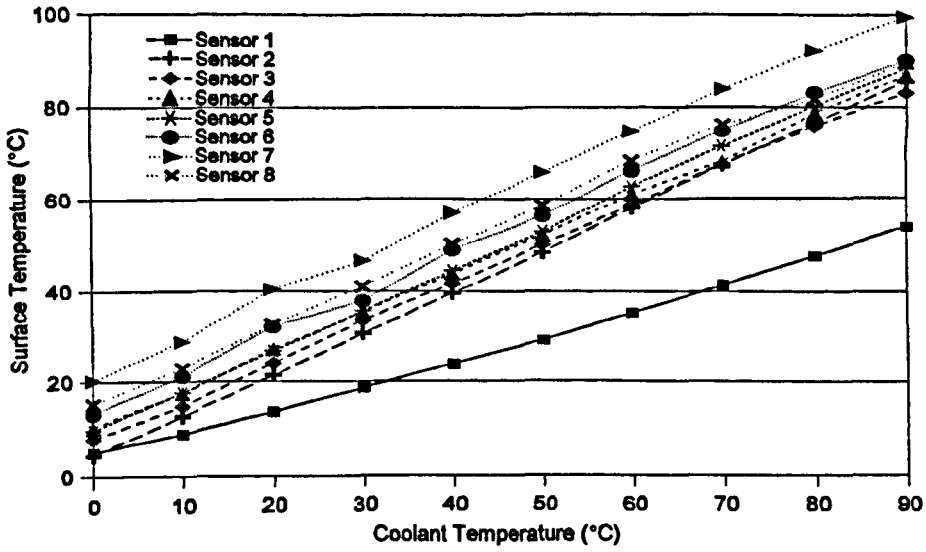

Figure 6.9 - Mean Variation of "Dry" Port Surface Temperatures with Coolant Temperature Over All Conditions Tested

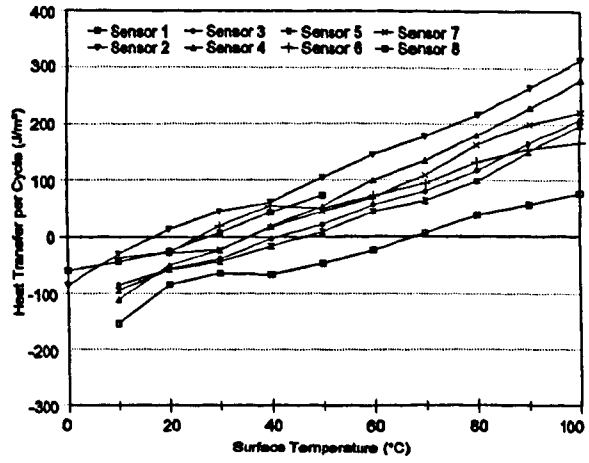

(a) 0.95 bar MAP

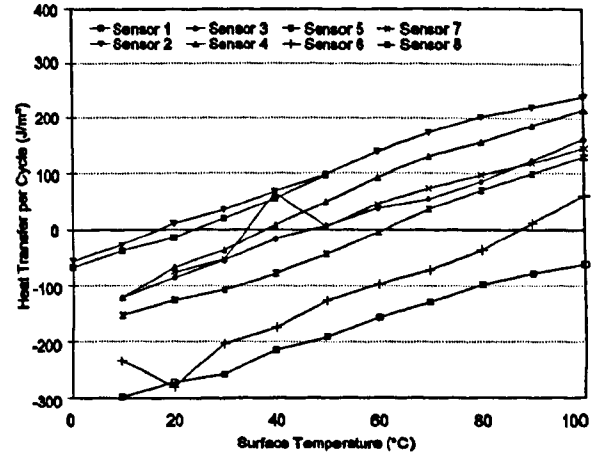

(b) 0.79 bar MAP

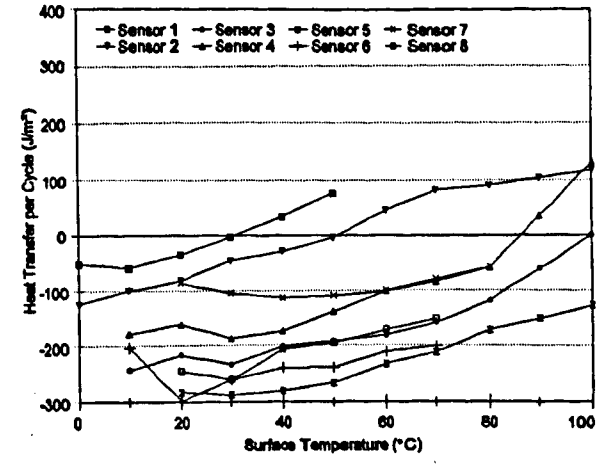

(c) 0.53 bar MAP

Figure 6.10 - Spatial Variations in "Dry" Surface Heat Transfer Rates with MAP, at 1000 RPM, with Fuel Flow Rate set to give Stoichiometric AFR

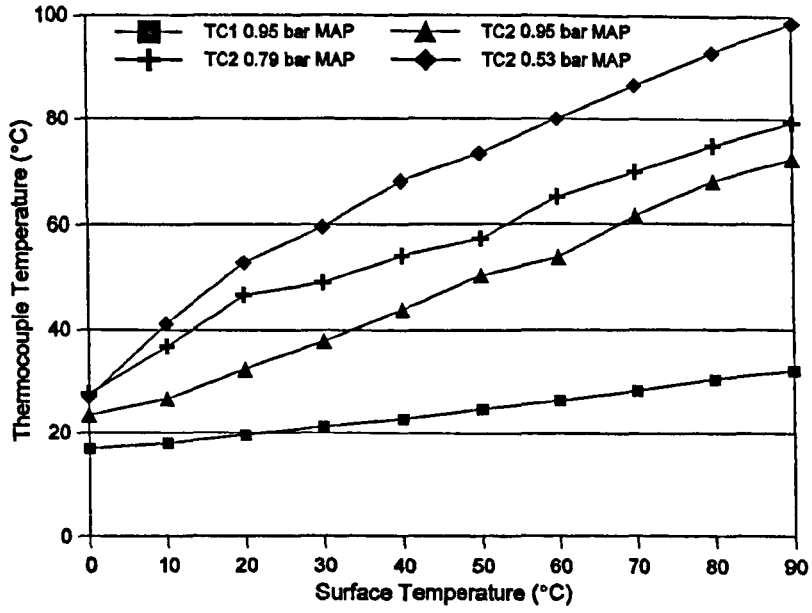

Figure 6.11 - Variation in Gas Temperature Measured by TC1 with Surface Temperature and for TC2 with Surface Temperature and MAP; Engine Operating at 1000 RPM and Stoichiometric AFR

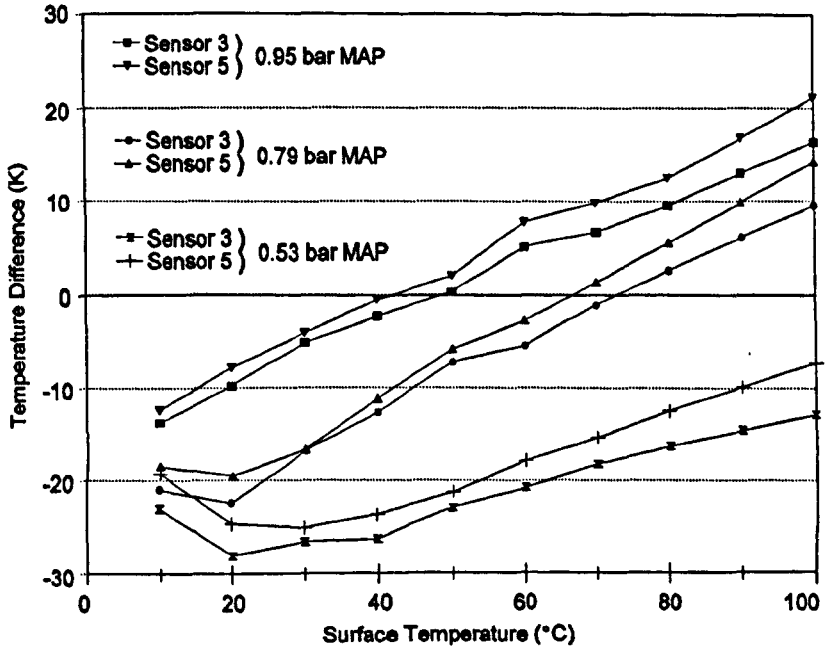

Figure 6.12 - Surface to Gas Temperature Difference Variation with MAP and Surface Temperature for Sensors 3 and 5 when "Dry"; Engine Operating at 1000 RPM and Stoichiometric AFR (Gas Temperature Measured with Thermocouple TC2)

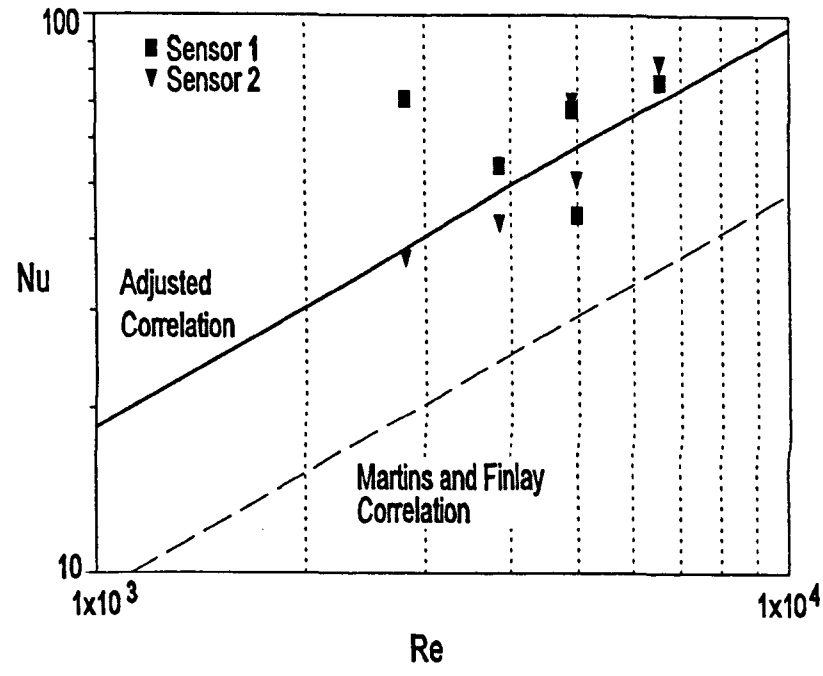

Figure 6.13 - *Nu* and *Re* Data from "Dry-Port" Operating Conditions, Plotted Alongside Martins and Finlay Correlation **[6.3]**

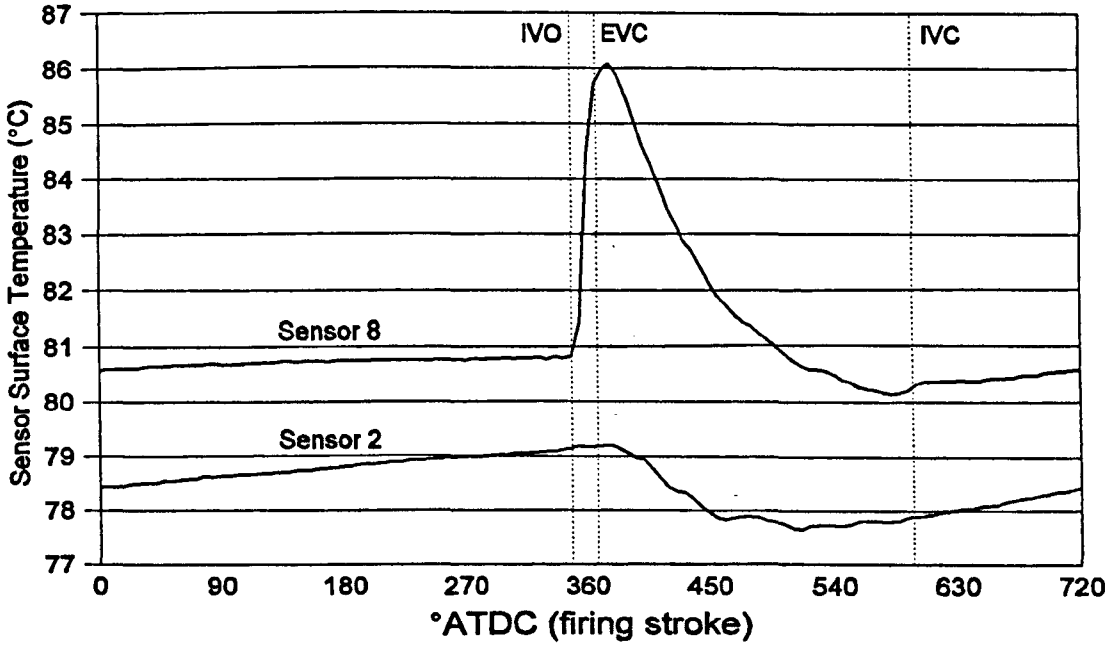

Figure 6.14 - Variation of Heat Flux Sensor Surface Temperatures, Calculated Using Finite Difference Model with Data from Figure 6.4

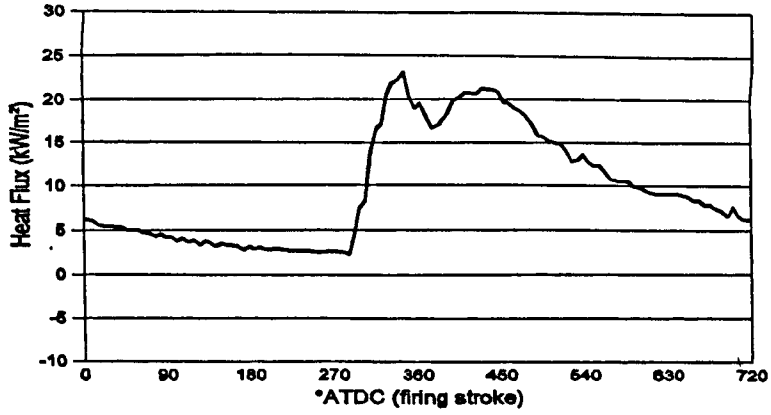

(a) Total Heat Flux with Deposition

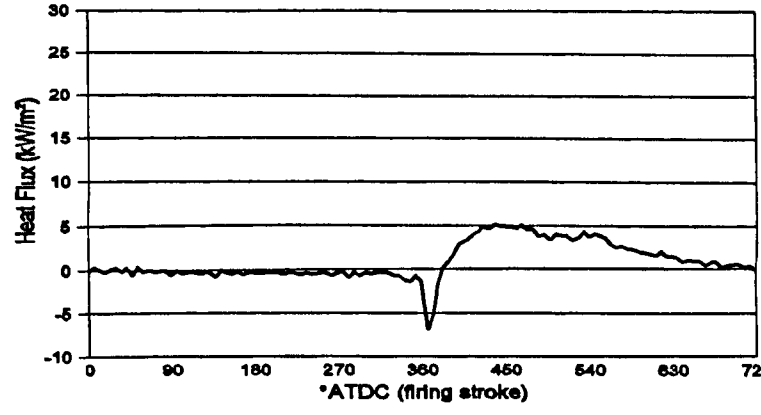

(b) "Dry-Port" Heat Flux Data

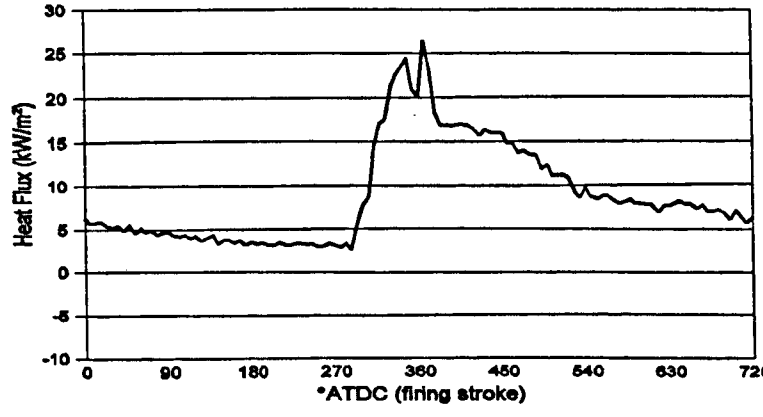

(c) Net "Heat Flux to Fuel"

Figure 7.1 - Crank-Angle Resolved Heat Flux Data from Sensor 7; Fully-Warm Engine Running at 1000 RPM and 0.79 bar MAP, Injection Timed at 270°ATDC, with a Stoichiometric AFR, and using a Single-Spray Injector

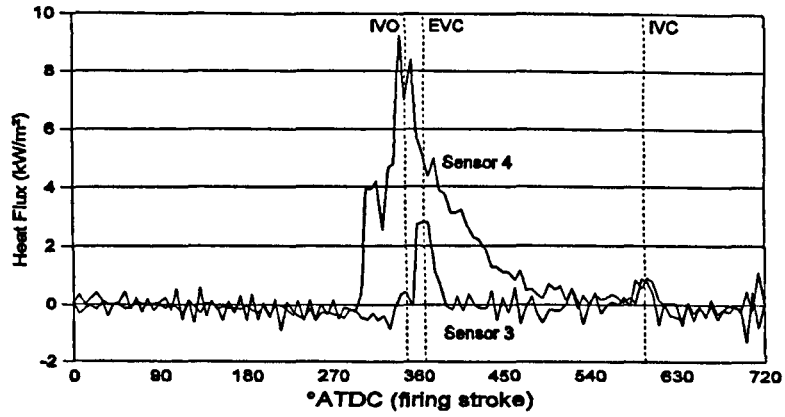

(a) Sensors 3 and 4

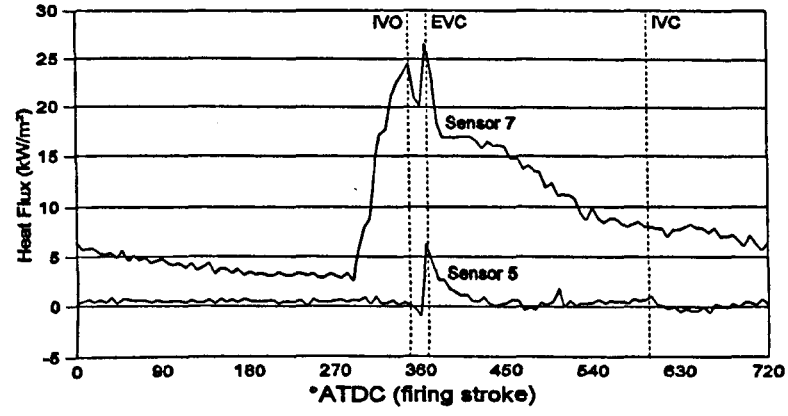

(b) Sensors 5 and 7

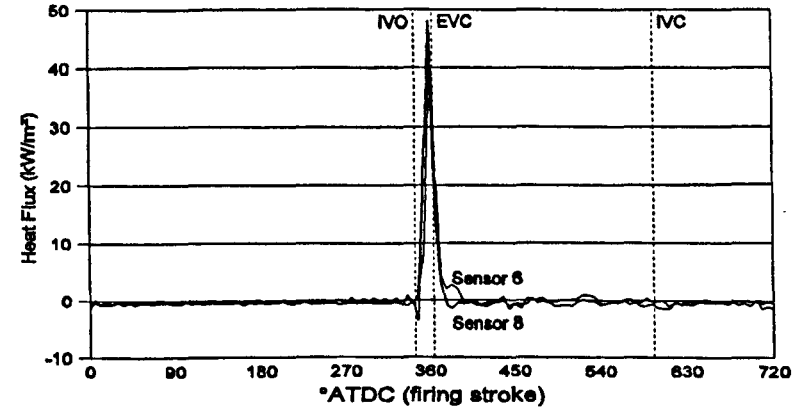

(c) Sensors 6 and 8

Figure 7.2 - Crank-Angle Resolved "Heat Flux to Fuel" with a Fully-Warm Engine Running at 1000 RPM, 0.79 bar MAP, with a Stoichiometric AFR and using a Single-Spray Injector

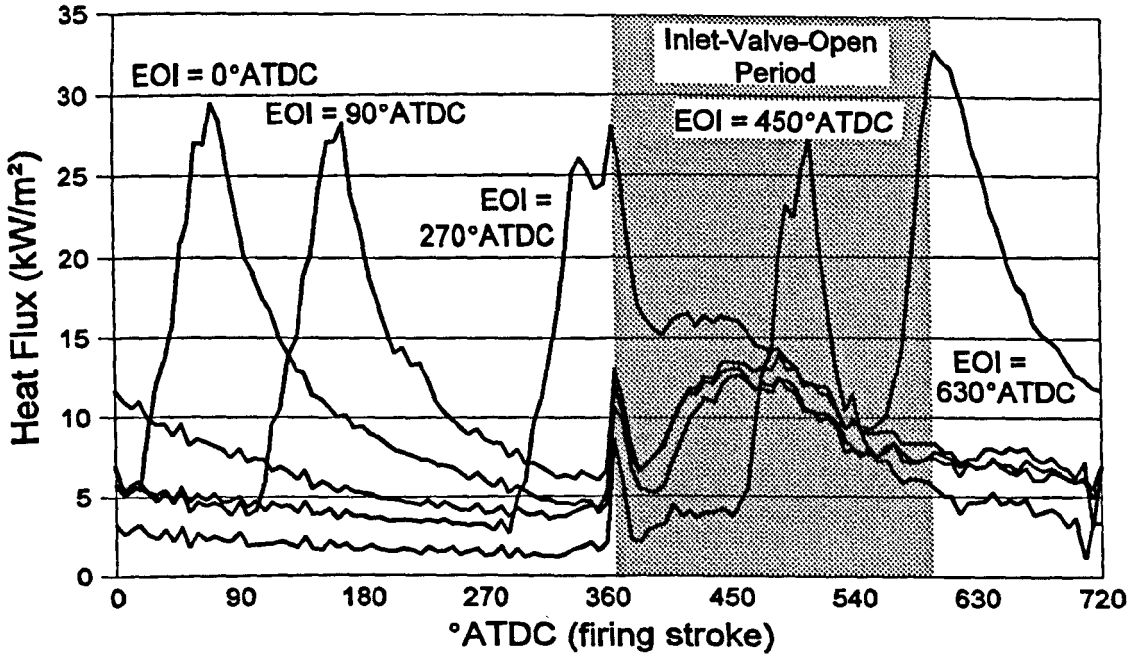

Figure 7.3 - Variation of Crank-Angle Resolved "Inferred Heat Flux to Fuel" with Injection Timing. Data Recorded from Sensor 7 with a Fully-Warm Engine Running at 1000 RPM, 0.79 bar MAP and a Stoichiometric AFR, using a Single-Spray Injector

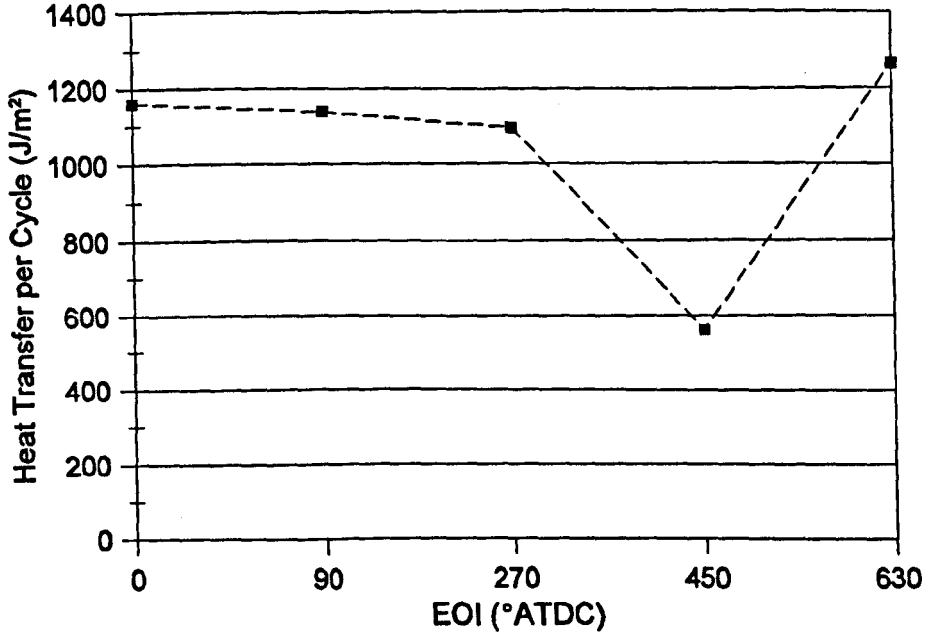

Figure 7.4 - Variation of Heat Transfer Rates through Sensor 7 with Injection Timing using Single-Spray Injector, at 1000 RPM, Stoichiometric AFR and 0.79 bar MAP

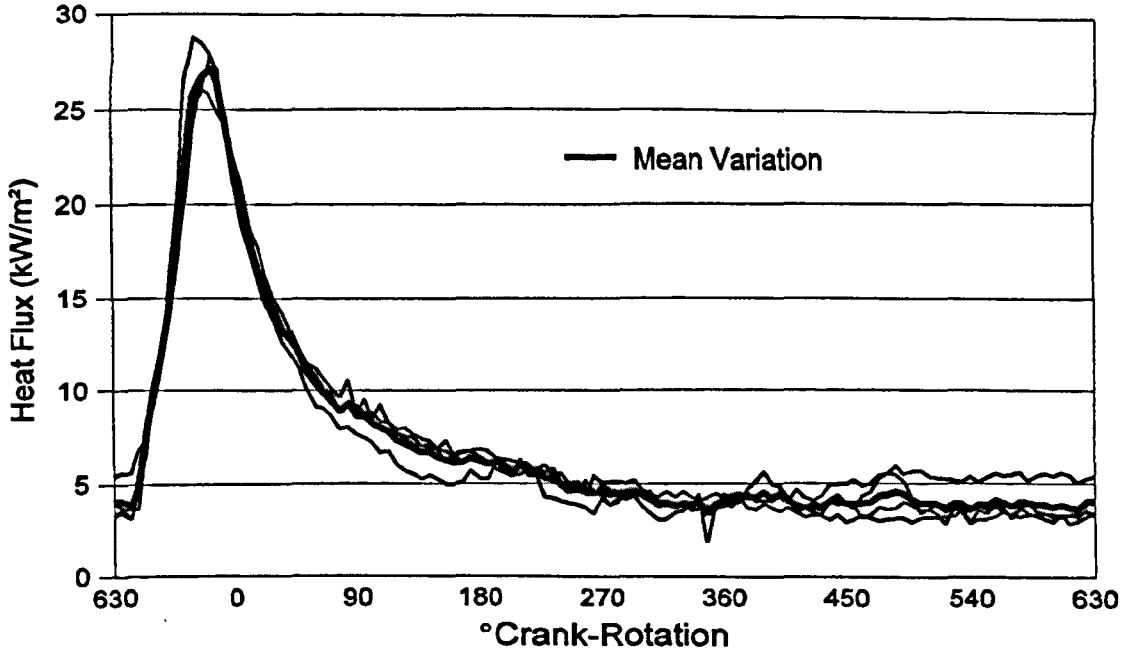

Figure 7.5(a) - Aligned Variations of Heat Flux given in Figure 7.3, Excluding Data for the Inlet-Valve-Open Period, for Injection Timings (EOI) of 0, 90, 270 and 630°ATDC

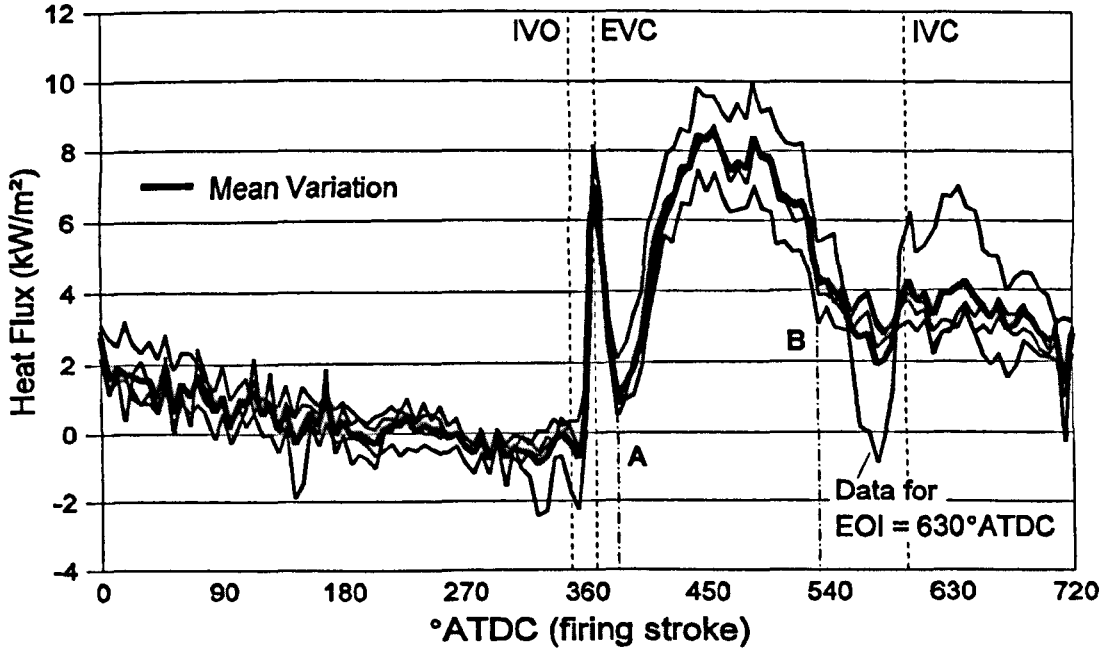

Figure 7.5(b) - Heat Flux "Remainder" After Subtracting the Mean Variation given in Figure 7.5(a) from the data given in Figure 7.3, for Injection Timings (EOI) of 0, 90, 270 and 630°ATDC

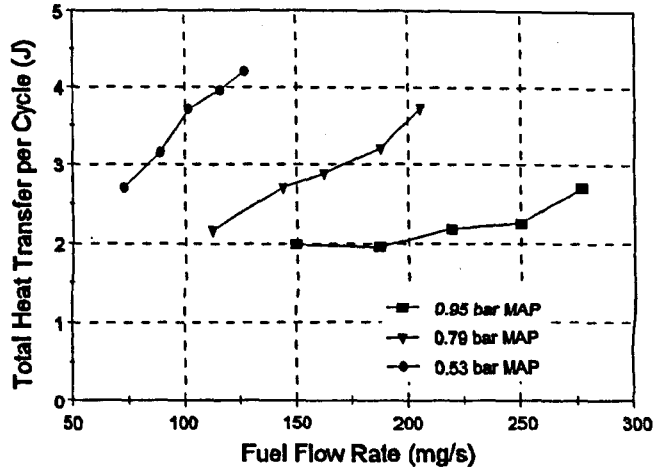

(a) Twin-Spray Injector

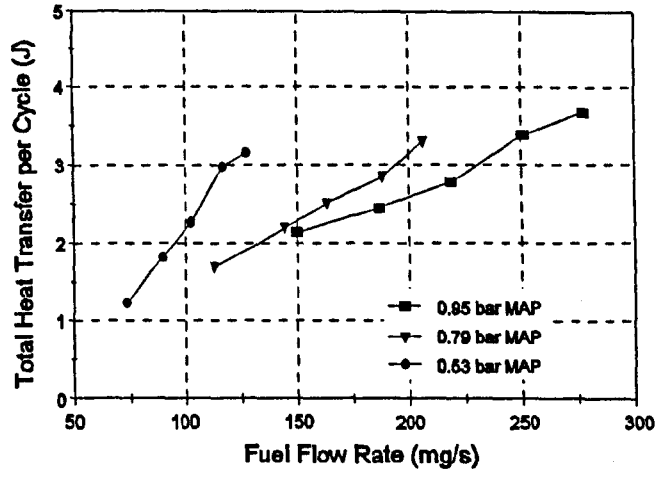

(b) Single-Spray Injector

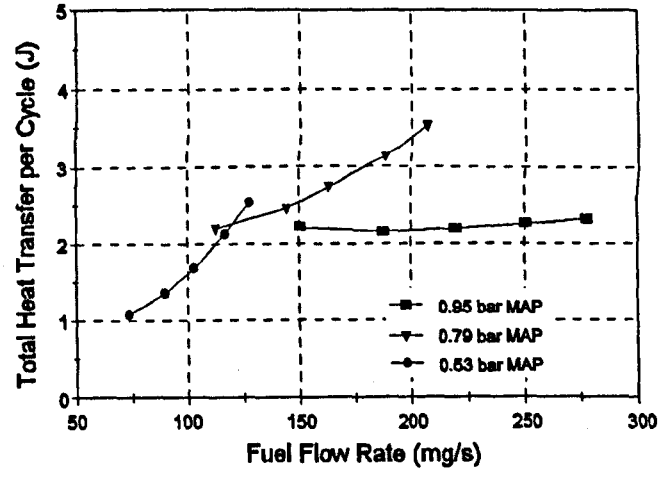

(c) Four-Hole Injector

Figure 7.6 - Variation in Estimated Total Heat Transfer Rates with Injector Type, MAP and Fuel Flow Rate with the Engine Fully-Warm and Running at 1000 RPM

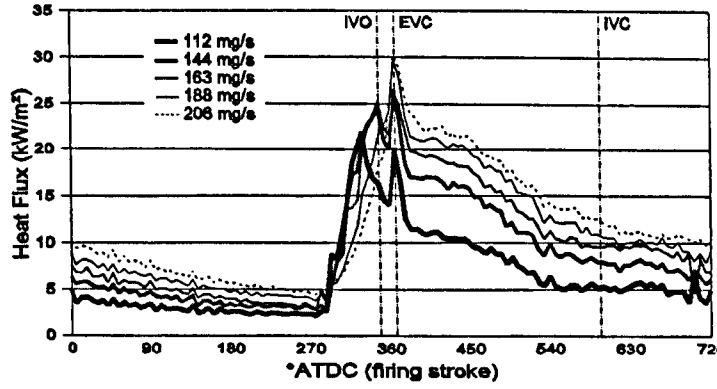

(a) Fully-Warm Variation with Fuel Flow at 0.79 bar MAP

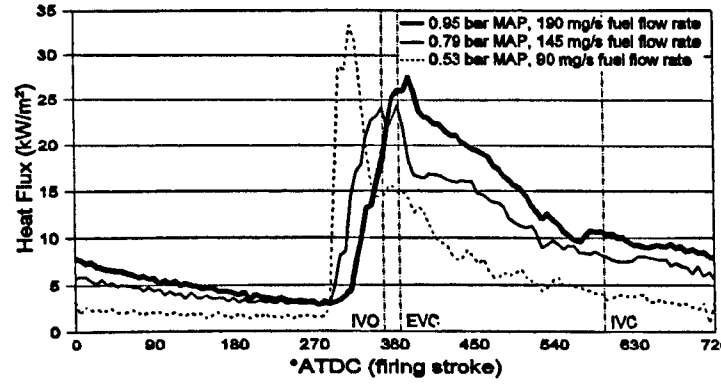

(b) Fully-Warm Variation with MAP at Stoichiometric AFR

Figure 7.7 - Comparison of Crank-Angle Resolved "Heat Flux to Fuel" at Different Operating Conditions. Engine Running at 1000 RPM using a Single-Spray Injector

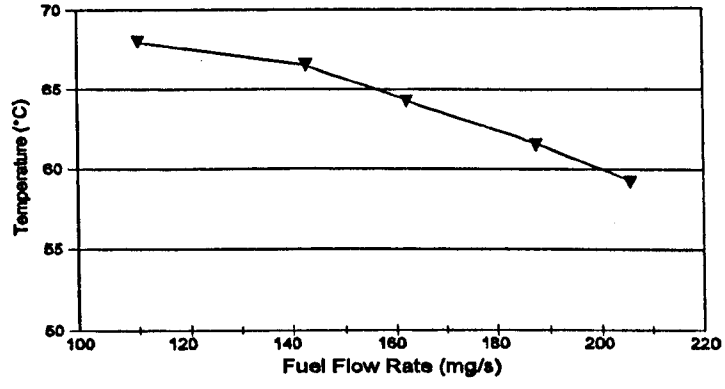

Figure 7.8 - Variation in Measured Sensor Temperatures for Sensor 7 with Fuel Flow Rate. Engine Operating at 1000 RPM and 0.79 bar MAP

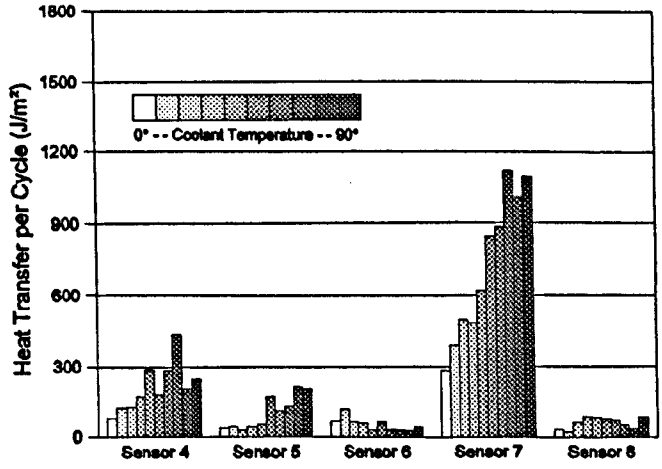

(a) 0.95 bar MAP, 190 mg/s Fuel Flow Rate

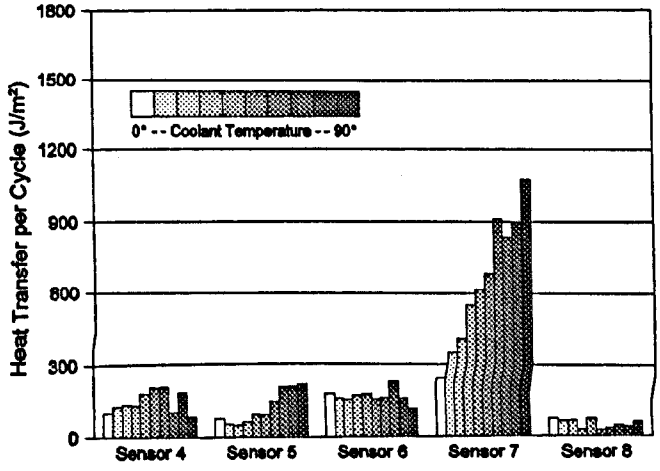

(b) 0.79 bar MAP, 145 mg/s Fuel Flow Rate

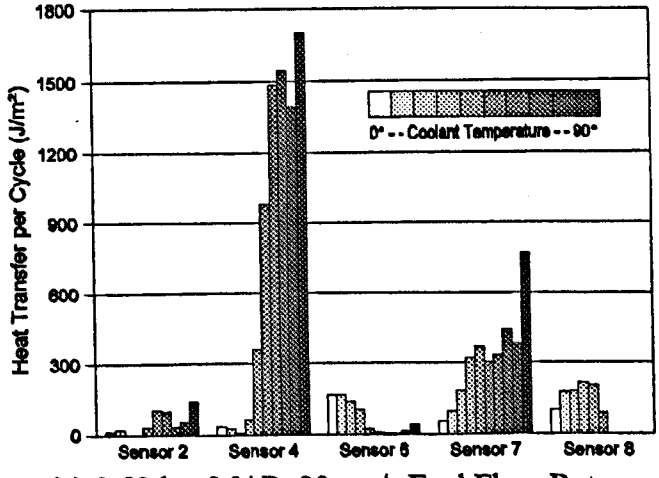

(c) 0.53 bar MAP, 90 mg/s Fuel Flow Rate

Figure 7.9 - Spatial Variations in Heat Transfer Rates with MAP using a Twin-Spray Injector at 1000 RPM, with Fuel Flow Rate set to give Stoichiometric AFR

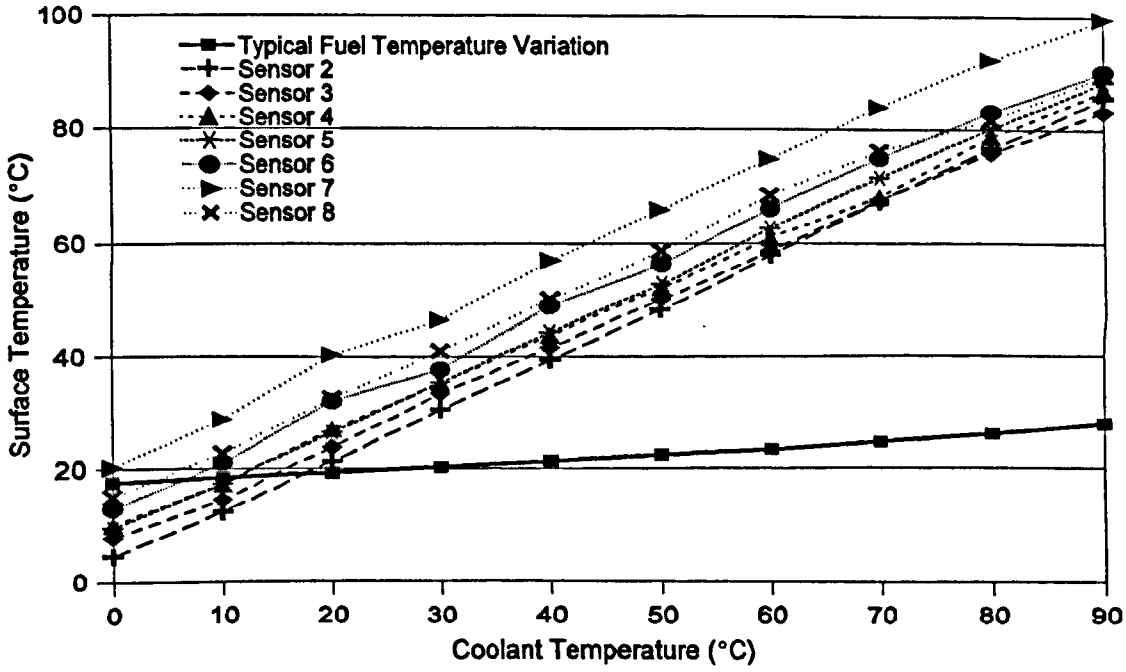

Figure 7.10 - Variation with Coolant Temperature of Mean Port Surface Temperatures (from Figure 6.9) and Typical Fuel Temperature

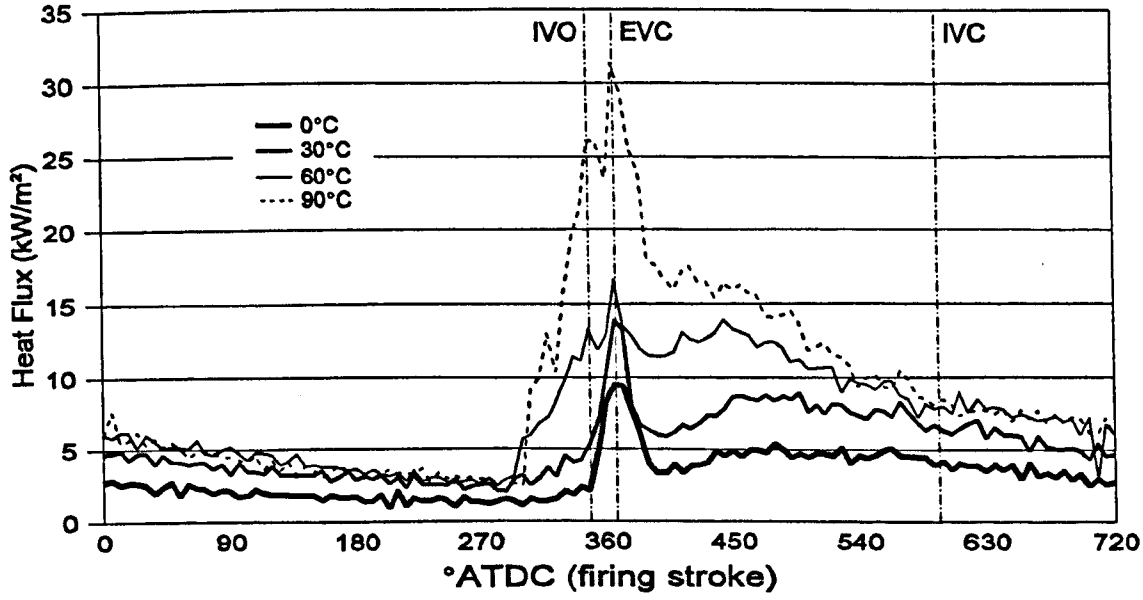

Figure 7.11 - Variation of Crank-Angle Resolved "Heat Flux to Fuel" Data with Coolant Temperature, when Injecting with an EOI of 270° ATDC and with the Engine Operating at 1000 RPM, 0.79 bar MAP and a Stoichiometric AFR, using a Single-Spray Injector

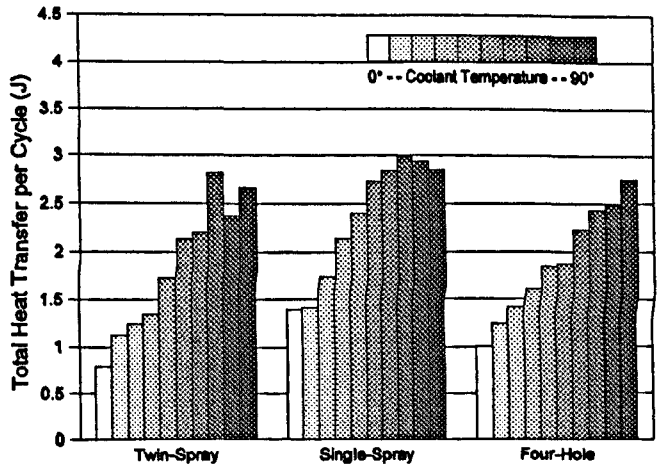

(a) 190 mg/s Fuel Flow Rate, 0.95 bar MAP

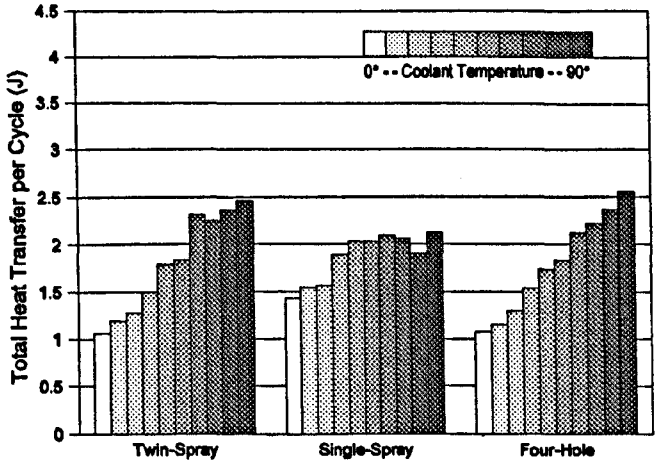

(b) 145 mg/s Fuel Flow Rate, 0.79 bar MAP

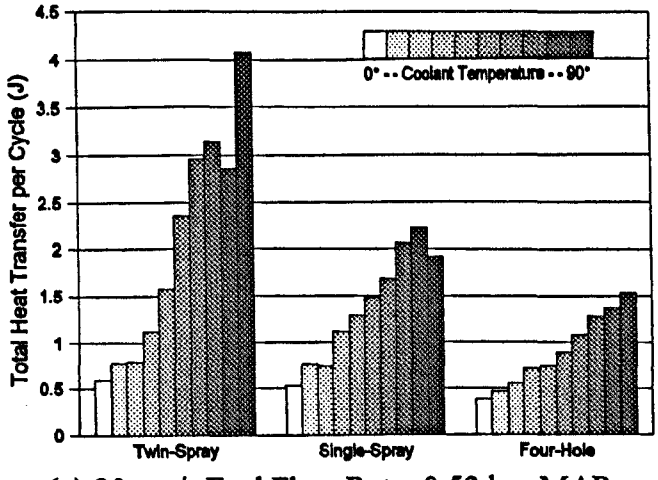

(c) 90 mg/s Fuel Flow Rate, 0.53 bar MAP

Figure 7.12 - Variations in Estimated Total Heat Transfer per Cycle with Injector Type, Coolant Temperature and Fuel Flow Rate at 1000 RPM. MAP set to give Stoichiometric AFR

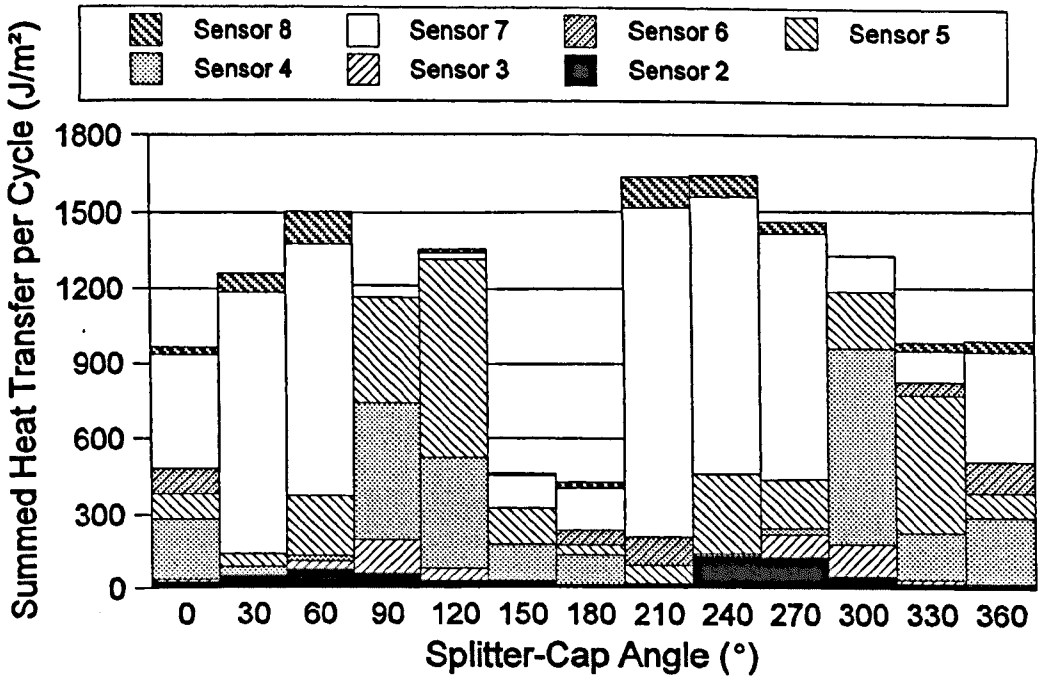

Figure 7.13 - Variation in Summed Heat Transfer Rates through Sensors 2-8 with Twin-Spray Injector Splitter-Cap Rotation, with a Fully-Warm Engine Running at 1000 RPM, 0.79 bar MAP and Stoichiometric AFR

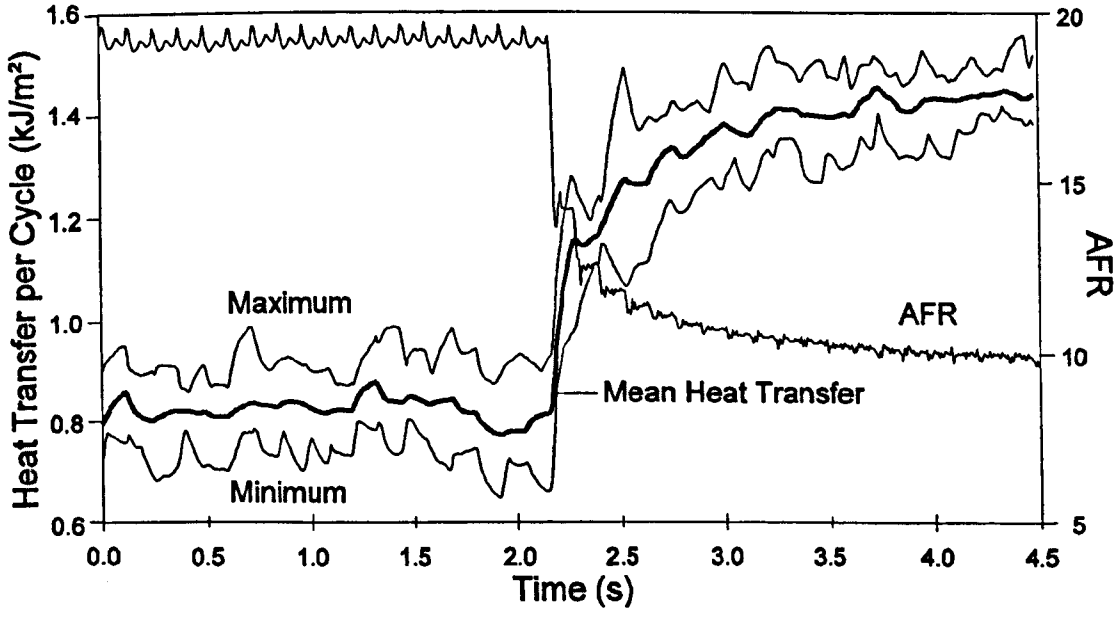

Figure 7.14 - Variation of Heat Transfer per Cycle Recorded from Sensor 7 when Fuel Flow Rate is Increased from 112 mg/s to 206 mg/s with a Fully-Warm Engine Running at *1000 RPM* and 0.79 bar MAP

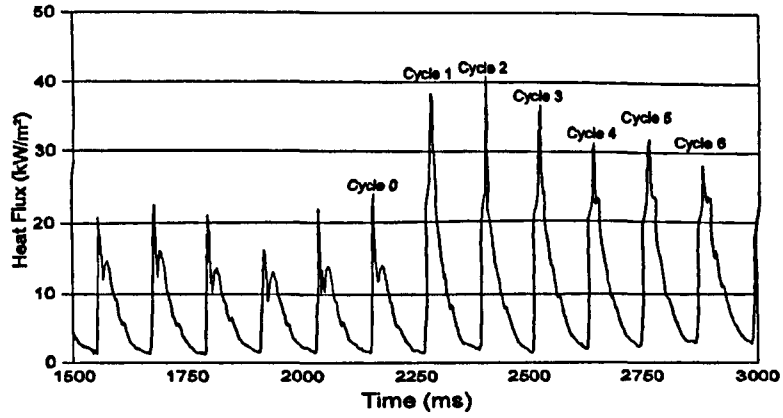

(a) Recorded Cycles of "Wetted" Data

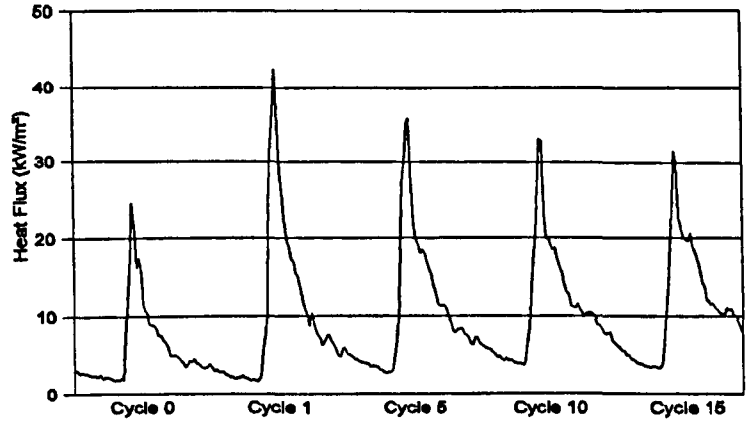

(b) Progressive Cycles of "Heat Flux to Fuel" Data

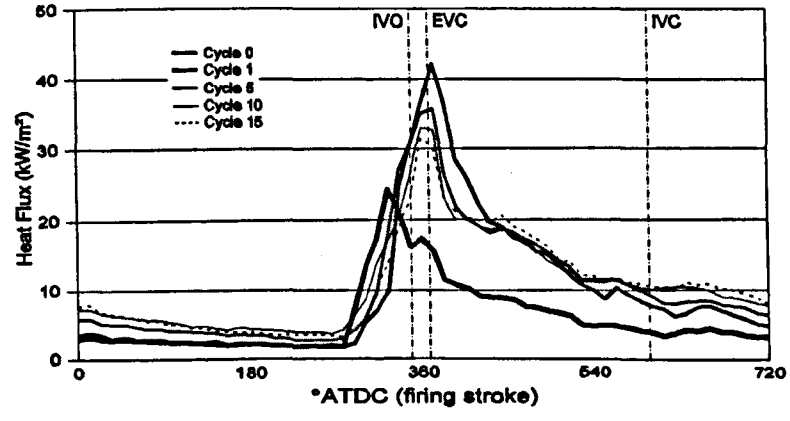

(c) Overlayed Cycles of "Heat Flux to Fuel" Data

Figure 7.15 - Variation of Crank-Angle Resolved Heat Flux Data when Fuel Flow is Increased from 112mg/s to 206 mg/s between Cycles 0 and 1. Data Recorded from Sensor 7 with a Fully-Warm Engine Running at 1000 RPM and 0.79 bar MAP, using a Single-Spray Injector

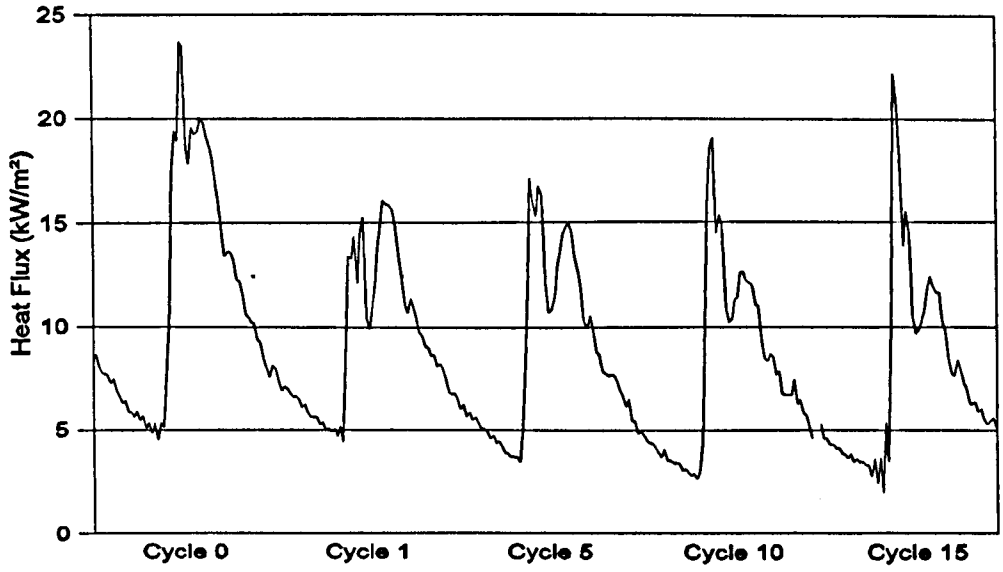

Figure 7.16 - Progressive Cycles of Heat Flux to Fuel Data when Fuel Flow Rate is Decreased from 206mg/s to 112 mg/s between Cycles 0 and 1. Data Recorded from Sensor 7 with a Fully-Warm Engine Running at 1000 RPM and 0.79 bar MAP, using a Single-Spray Injector

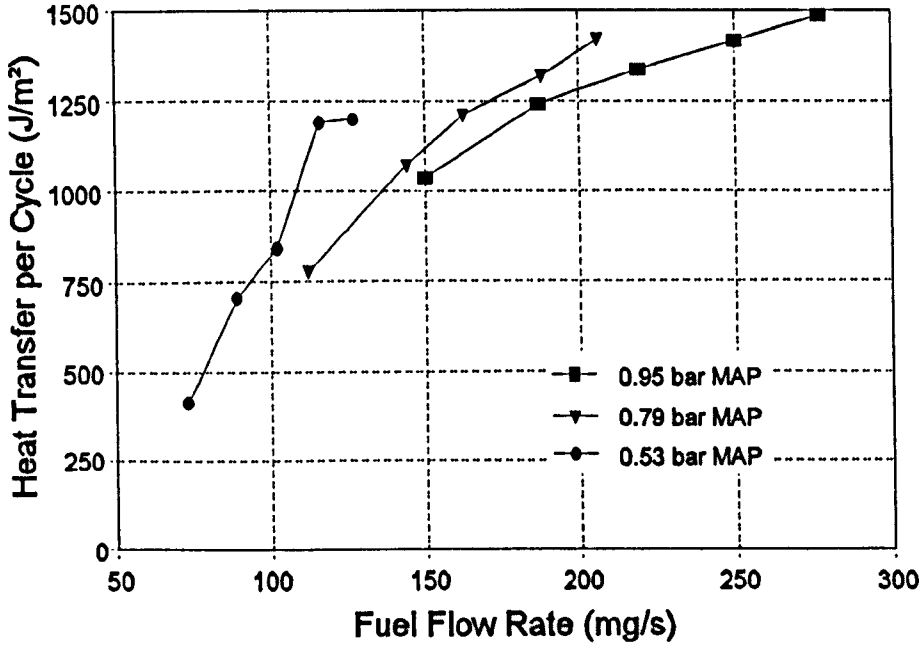

Figure 7.17 - Variation in Heat Transfer Rates through Sensor 7 with Fuel Flow Rate and MAP using a Single-Spray Injector with the Engine Fully-Warm and Running at 1000 RPM

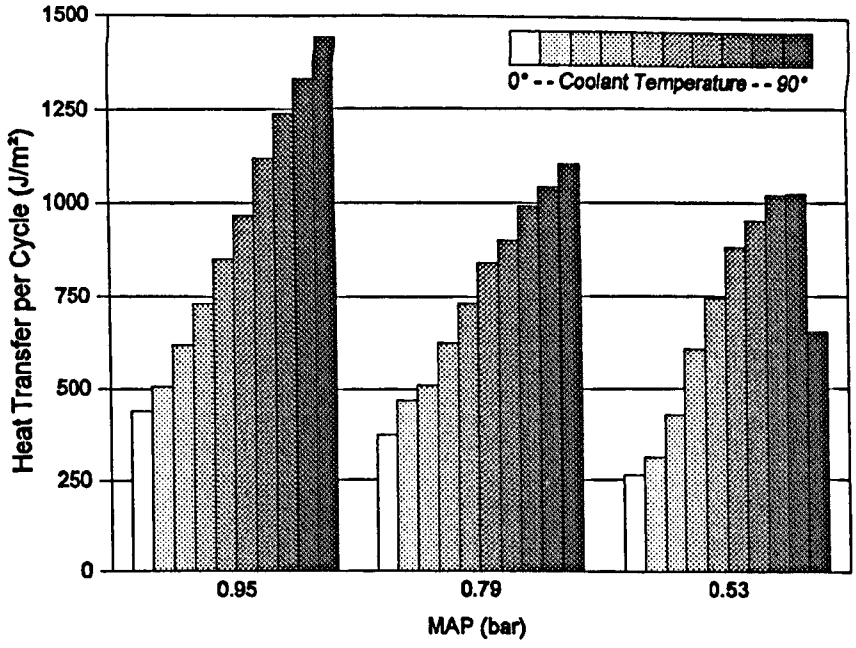

Figure 7.18 - Variation in Heat Transfer Rates Recorded through Sensor 7 with MAP and Coolant Temperature using a Single-Spray Injector at 1000 RPM and with Fuel Flow Rate set to maintain Stoichiometric AFR

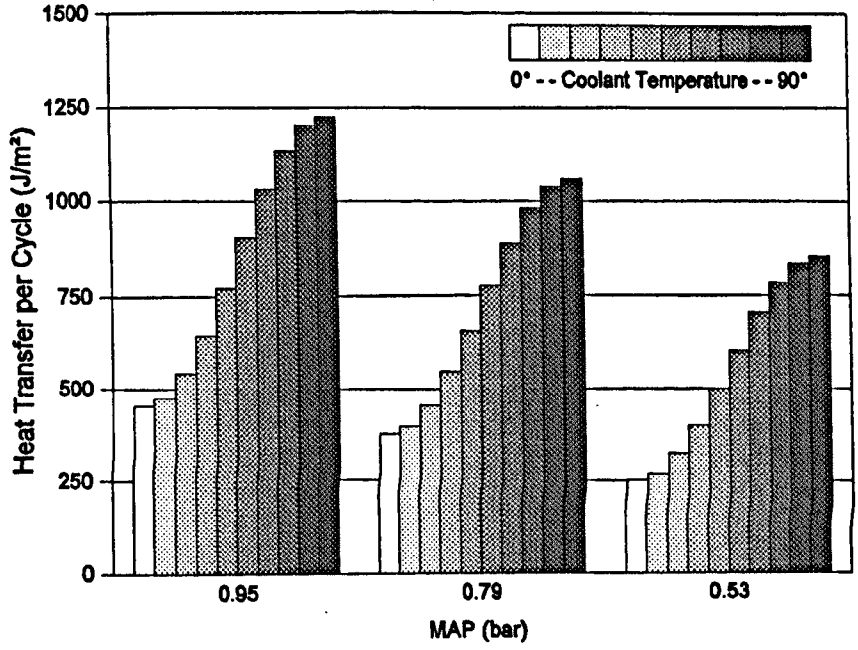

Figure 7.19 - Variation in Heat Transfer Rates with MAP and Coolant Temperature derived from Eqn. 7.3 using Fuel Flow Rates required for Stoichiometric AFR

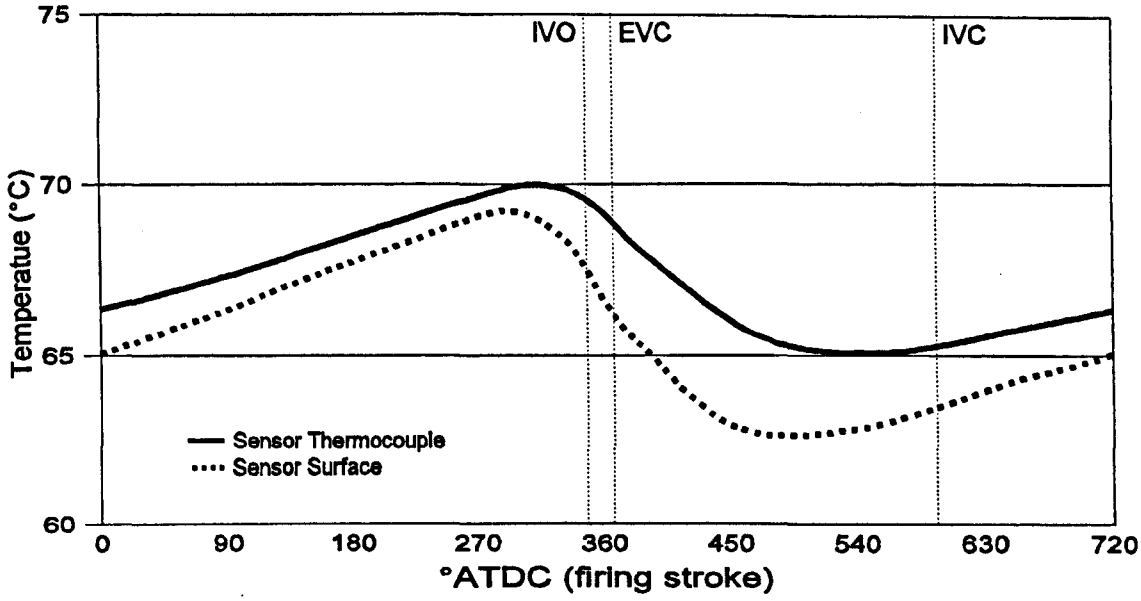

Figure 7.20 - Calculated, Crank-Angle Resolved Temperatures for Sensor 7, with the Engine Operating at 1000 RPM, 0.79 bar MAP and a Fuel Flow Rate of 206 mg/s

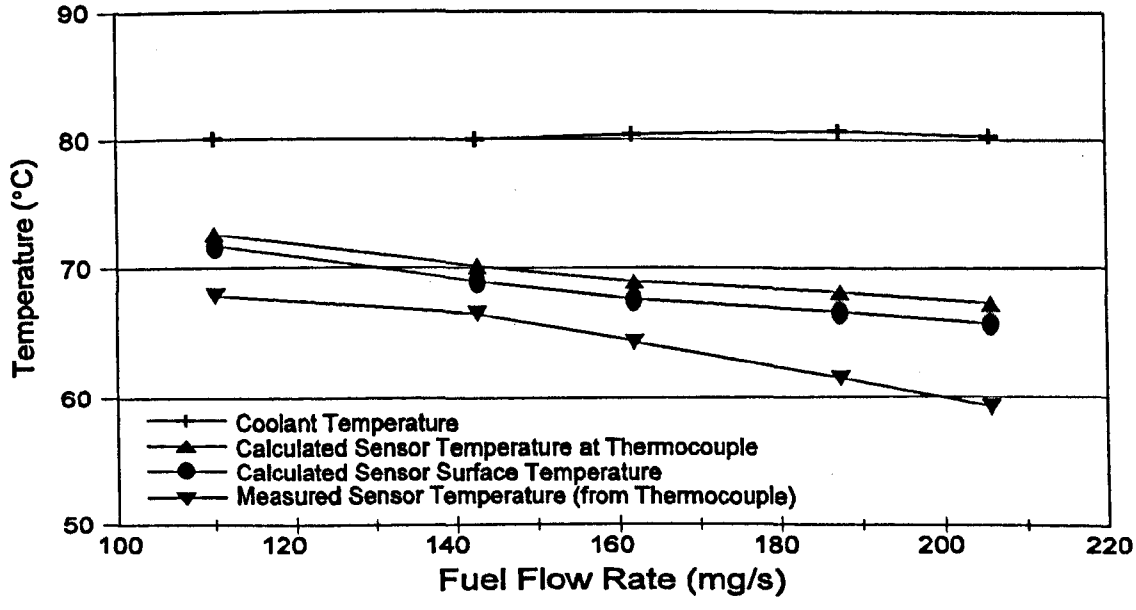

Figure 7.21 - Variation of Measured and Calculated Temperatures Across Sensor 7 with Fuel Flow Rate; Engine Operating at 1000 RPM and 0.79 bar MAP

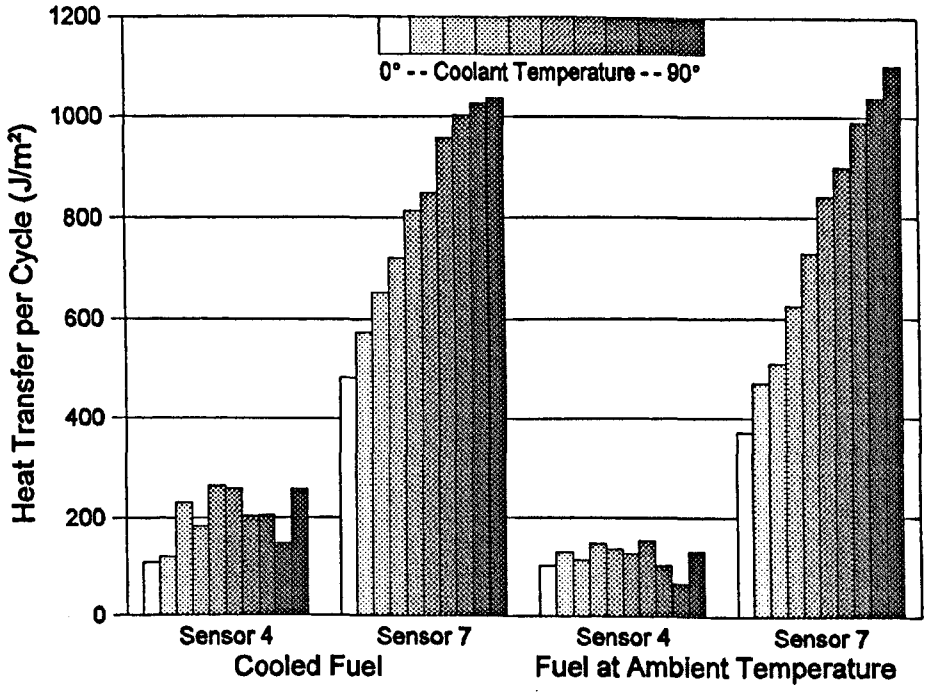

Figure 7.22 - Effect of Fuel Temperature on Variation in Heat Transfer Rates Recorded through Sensors 4 and 7 with Coolant Temperature, using a Single-Spray Injector at 1000 RPM, 0.79 bar *MAP and* with Fuel Flow Rate set to maintain Stoichiometric AFR

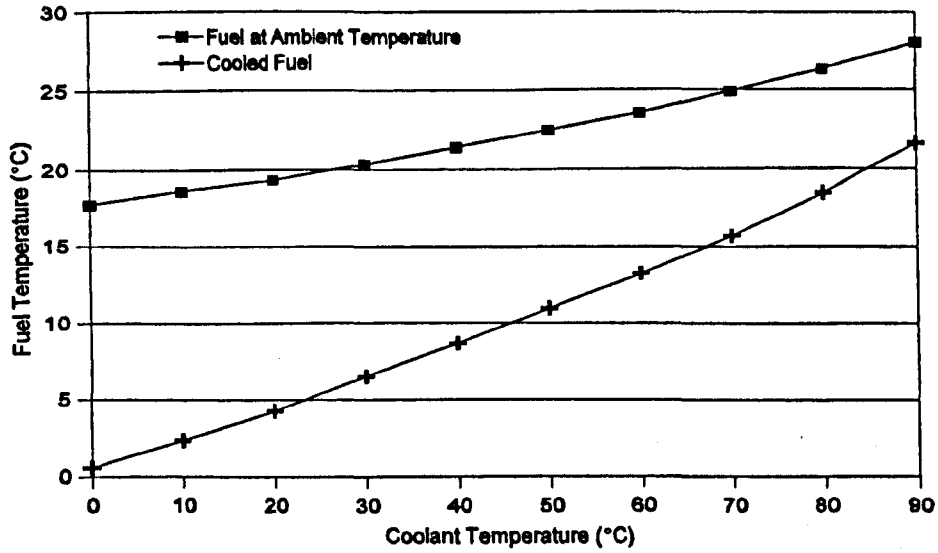

Figure 7.23 - Difference in Fuel Temperatures for Tests Shown in Figure 7.22

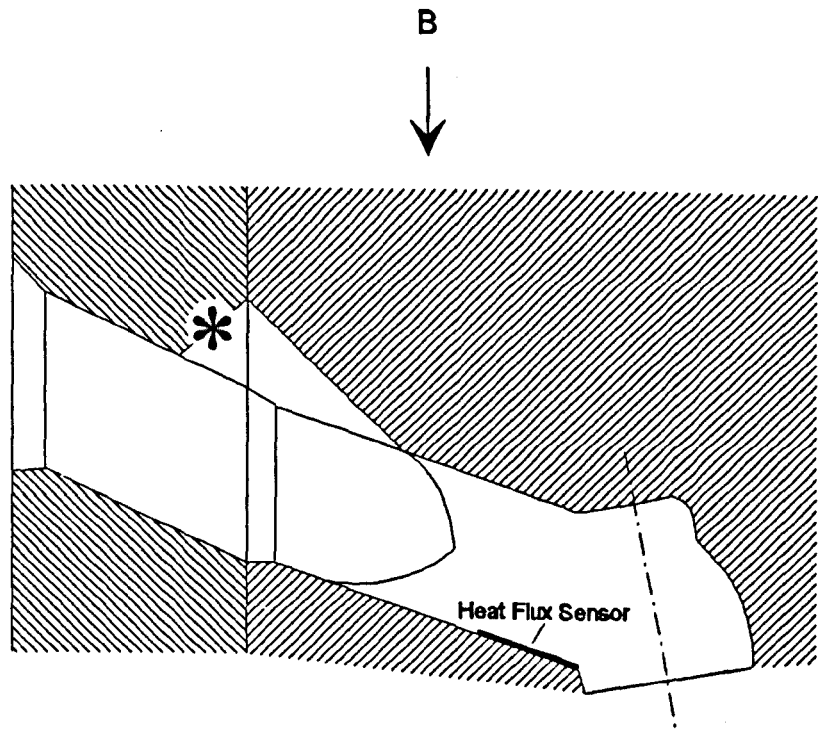

Figure 8.1 - Positioning of Heat Flux Sensor Used for Heat Transfer Measurements Analysed in Chapter 8

(Injector Tip Position - '*')

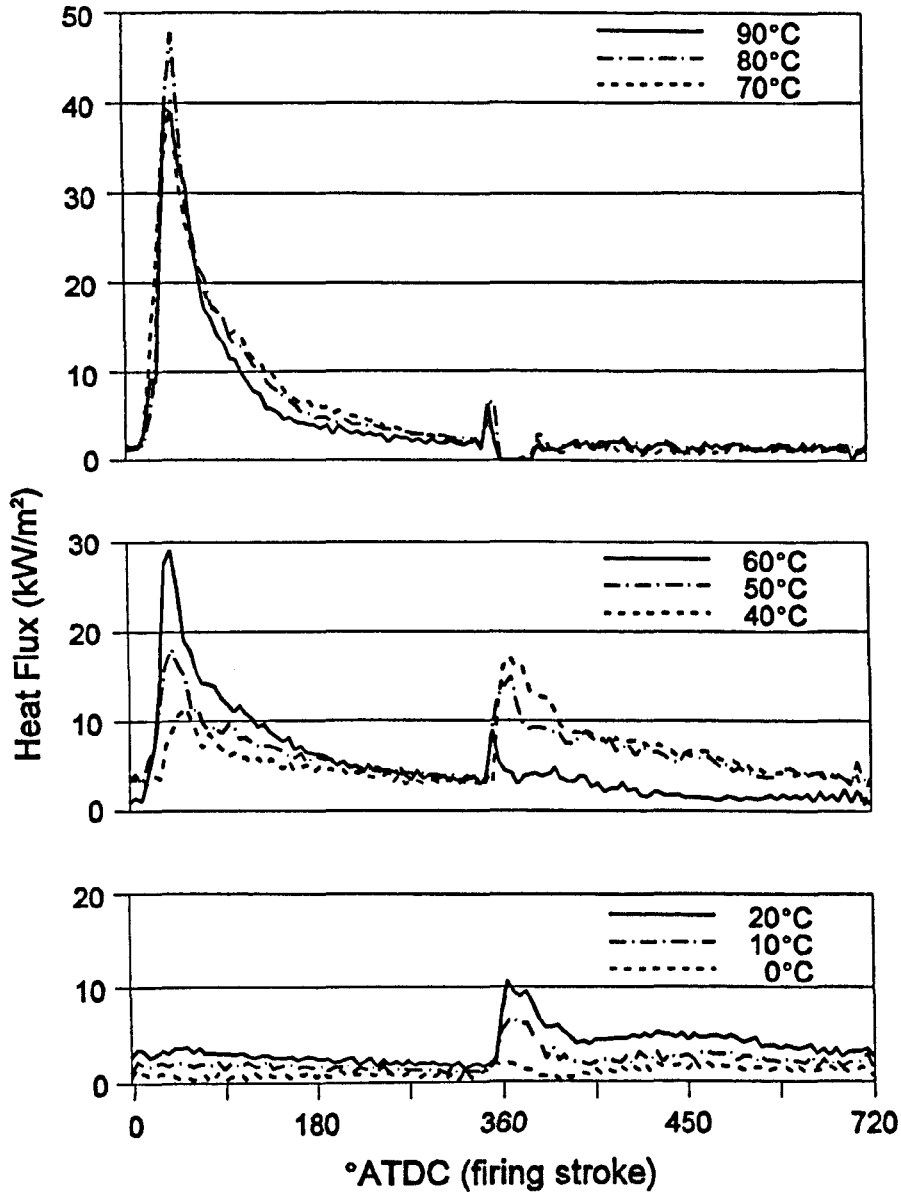

Figure 8.2 - Variation of Crank-Angle Resolved "Heat Fluxes to Fuel" with Coolant Temperature. Engine Operating at 1000 RPM, 0.53 bar MAP and Stoichiometric AFR, with EOI at 0°ATDC

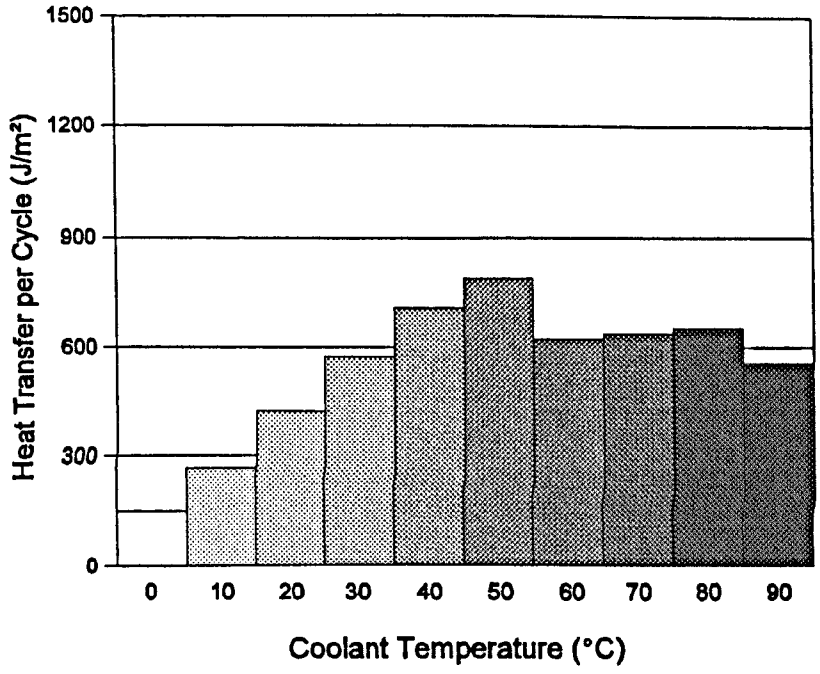

Figure 8.3 - Variation of Heat Transfer per Cycle with Coolant Temperature at 1000 RPM, 0.53 bar MAP, Stoichiometric AFR and with EOI at 0°ATDC

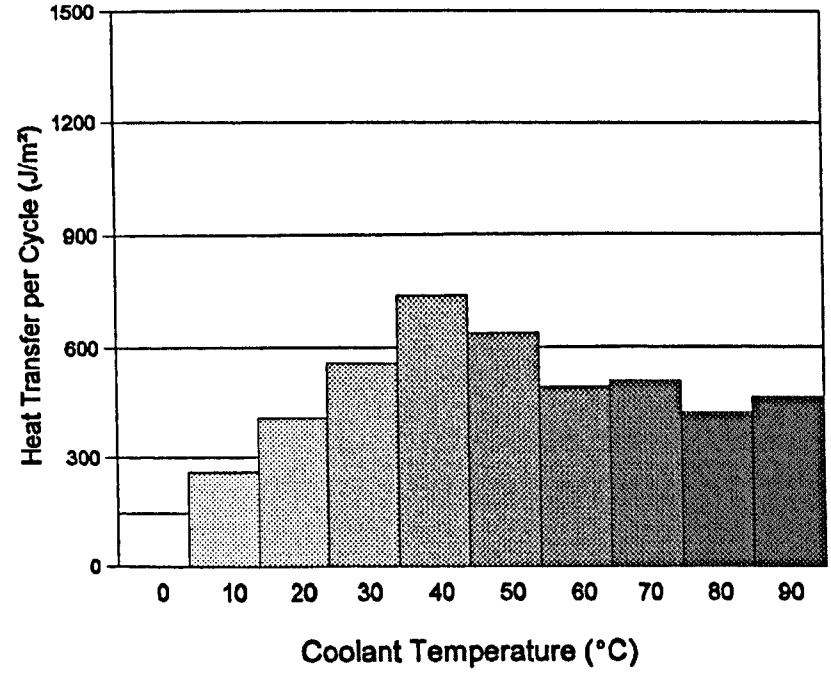

Figure 8.4 - Variation of Heat Transfer per Cycle with Coolant Temperature at 1000 RPM, 0.53 bar MAP, Stoichiometric AFR and with EOI at 270°ATDC

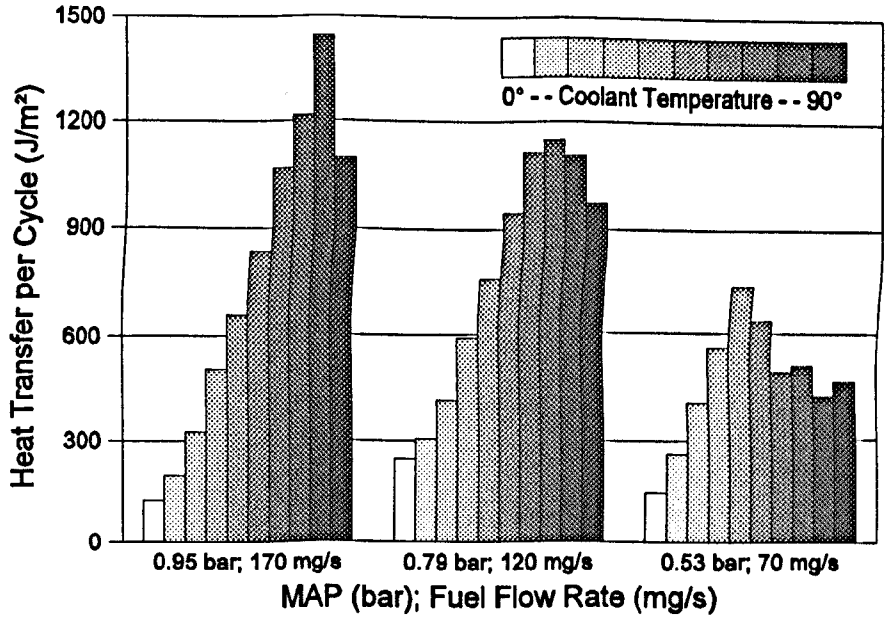

Figure 8.5 - Variation of Heat Transfer per Cycle with Coolant Temperature and MAP, at 1000 RPM with Stoichiometric AFR and EOI at 270°ATDC

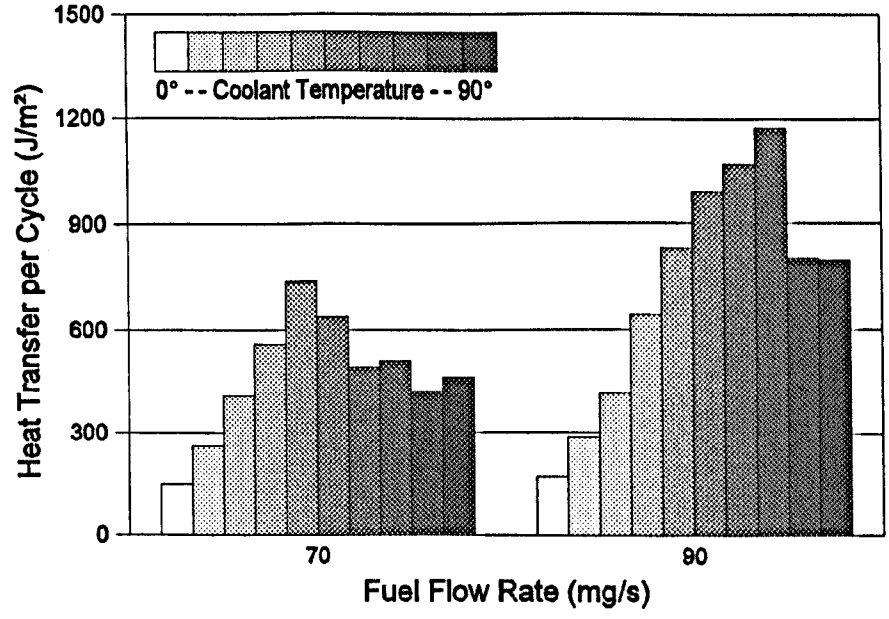

Figure 8.6 - Variation of Heat Transfer per Cycle with Coolant Temperature and Fuel Flow Rate, at 1000 RPM, 0.53 bar MAP and with EOI at 270°ATDC

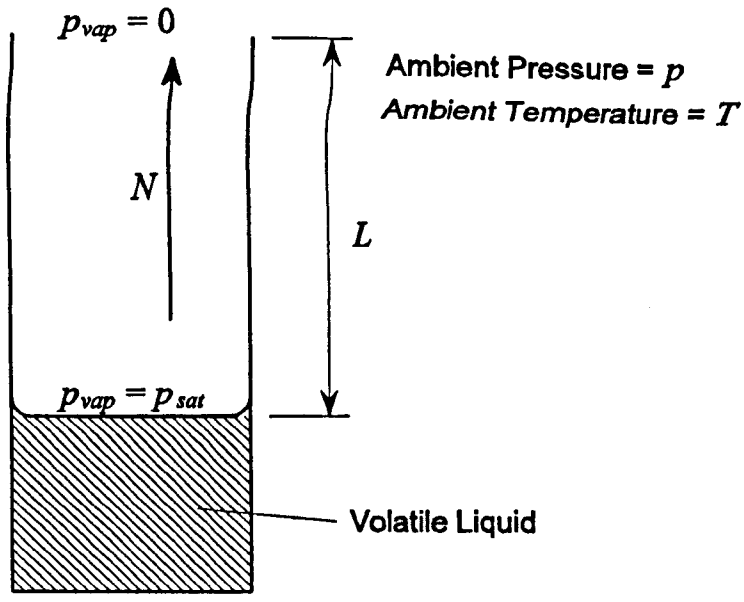

Figure 8.7 - Diagram of Stefan's Experiment **[8.2]**

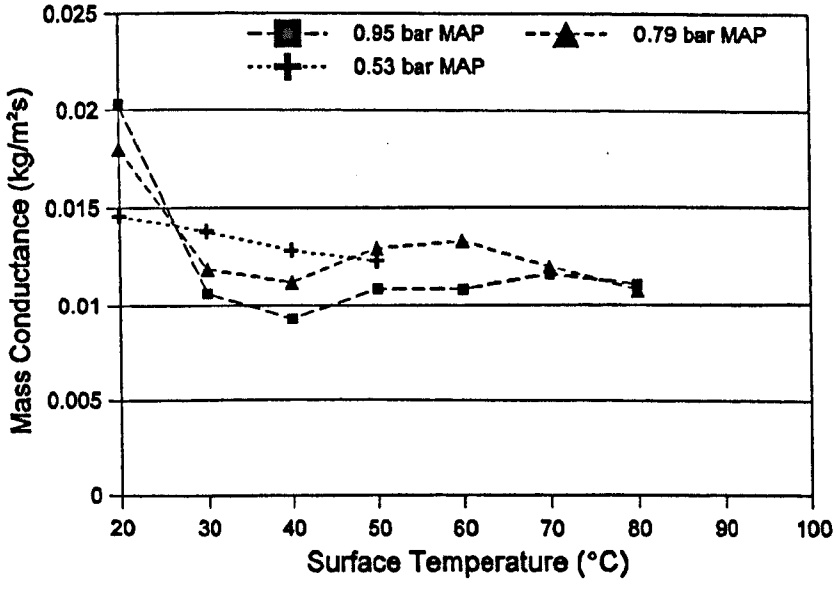

Figure 8.8 - Mass Conductance (g^*) Values Derived from Experimental Data for Warm-Ups at 1000 RPM and Stoichiometric AFR

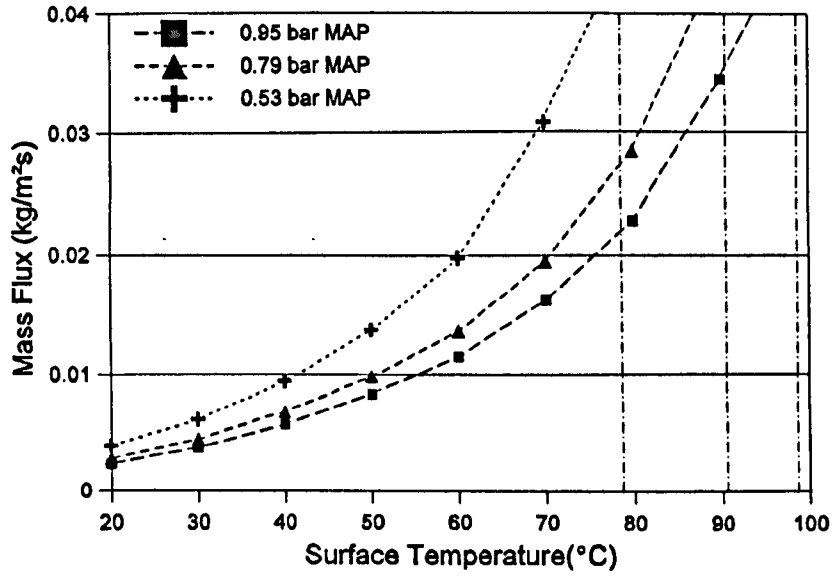

Figure 8.9 - Variation with Port Surface Temperature and MAP of Mass Flux Resulting from Convective Mass Transfer within Inlet Port with Engine Running at 1000 RPM

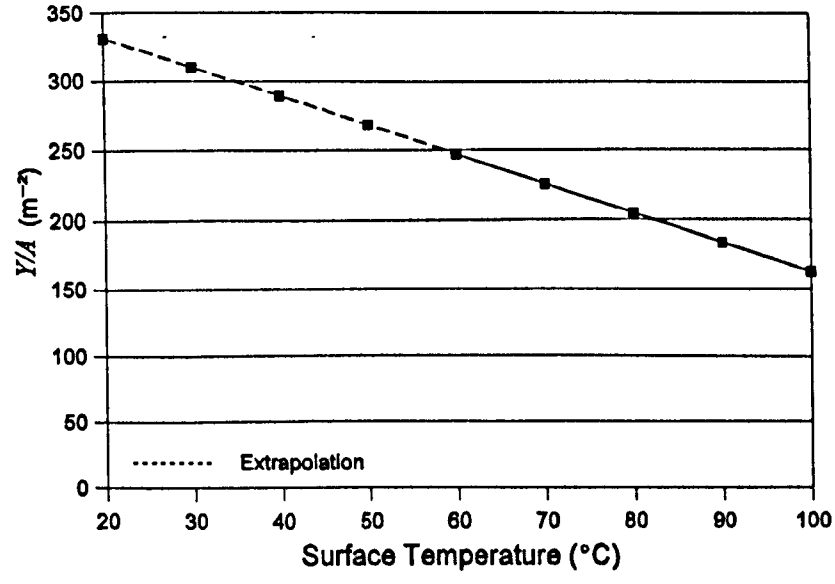

Figure 8.10 - Variation of Inferred Local Fuel Deposition Factor (*Y/A*) with Port Surface Temperature

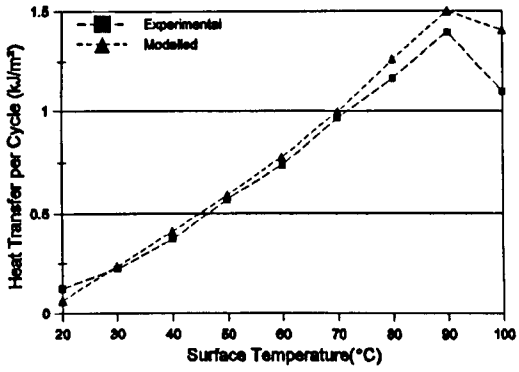

(a) 0.95 bar MAP,
170 mg/s Fuel Flow Rate

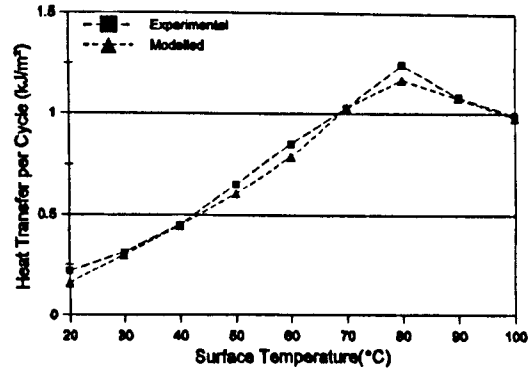

(b) 0.79 bar MAP,
120 mg/s Fuel Flow Rate

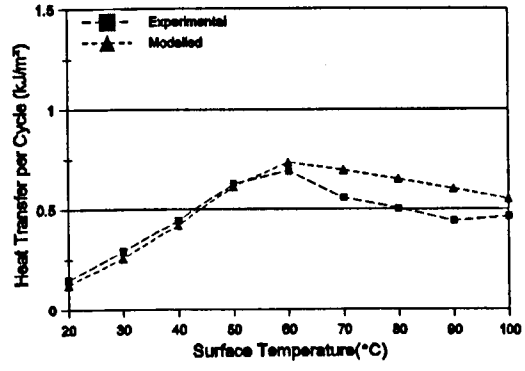

(c) 0.53 bar MAP,
70 mg/s Fuel Flow Rate

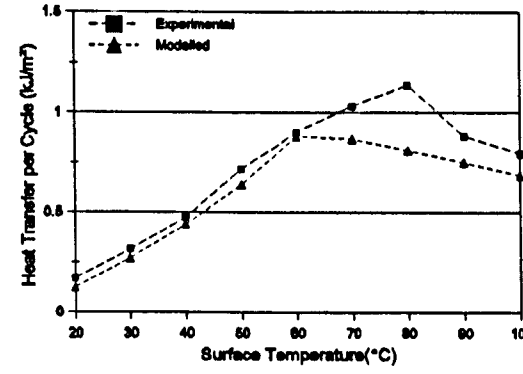

(d) 0.53 bar MAP,
90 mg/s Fuel Flow Rate

Figure 8.11 - Agreement Between Experimental and Modelled Heat Transfer Data for Warm-Up Tests Run at 1000 RPM with EOI at 270° ATDC

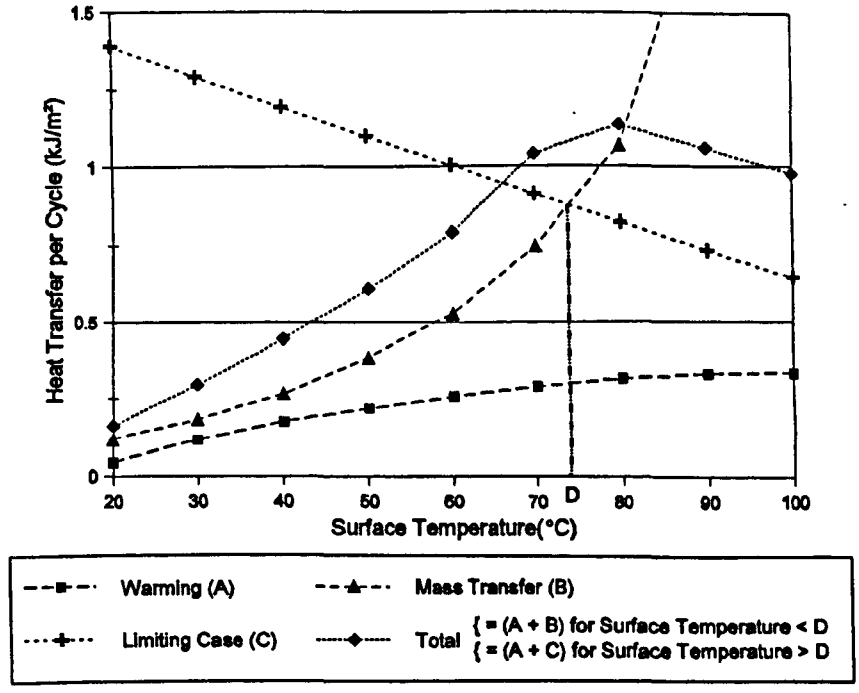

Figure 8.12 - Variation of Constituent Parts of Heat Transfer Model with Port Surface Temperature for Operating Conditions of: 1000 RPM, 0.79 bar MAP, Stoichiometric AFR and EOI at 270°ATDC

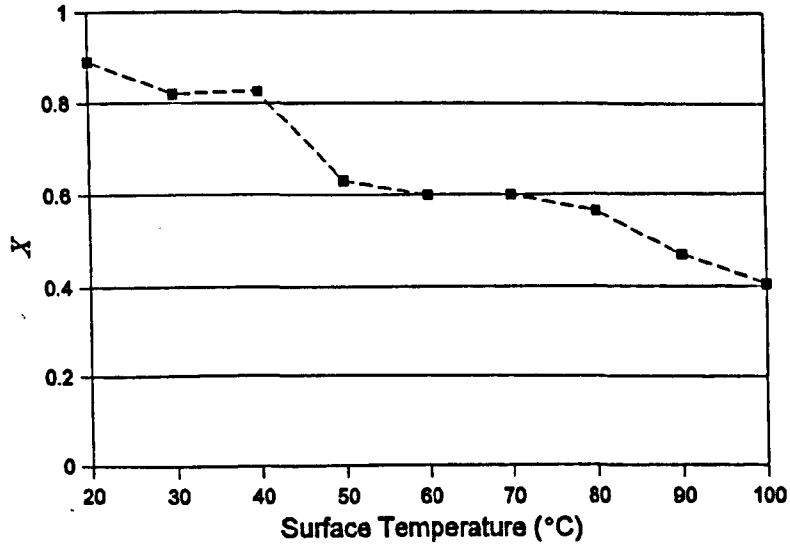

Figure 8.13 - Variation of Fuel Deposition Factor (X) with Port Surface Temperature, from Fuel Perturbation Tests Carried Out with Isooctane at 0.79 bar MAP, 1000 RPM and Stoichiometric Mean AFR

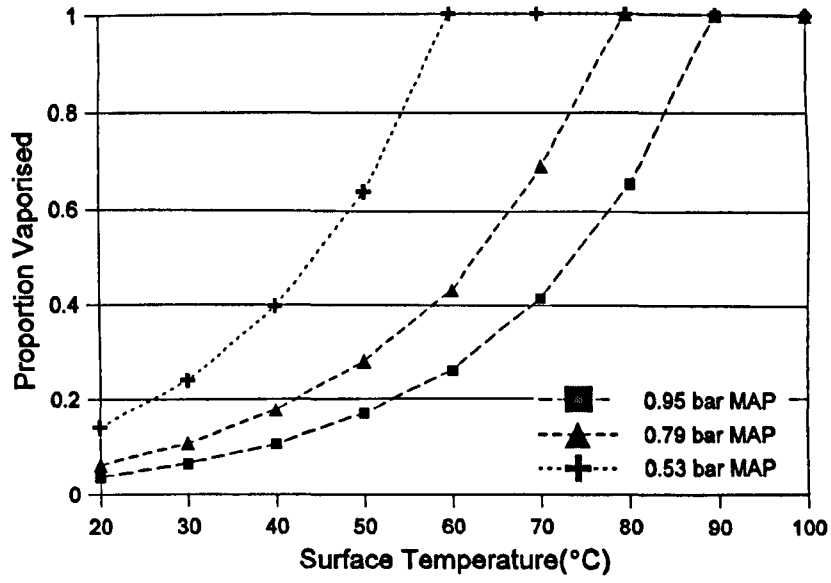

Figure 8.14 - Variation with Port Surface Temperature and MAP in Proportion of Isooctane Fuel Deposited on Heat Flux Sensor Indicated to be Vaporising at 1000 RPM and Stoichiometric AFR, with EOI at 270°ATDC

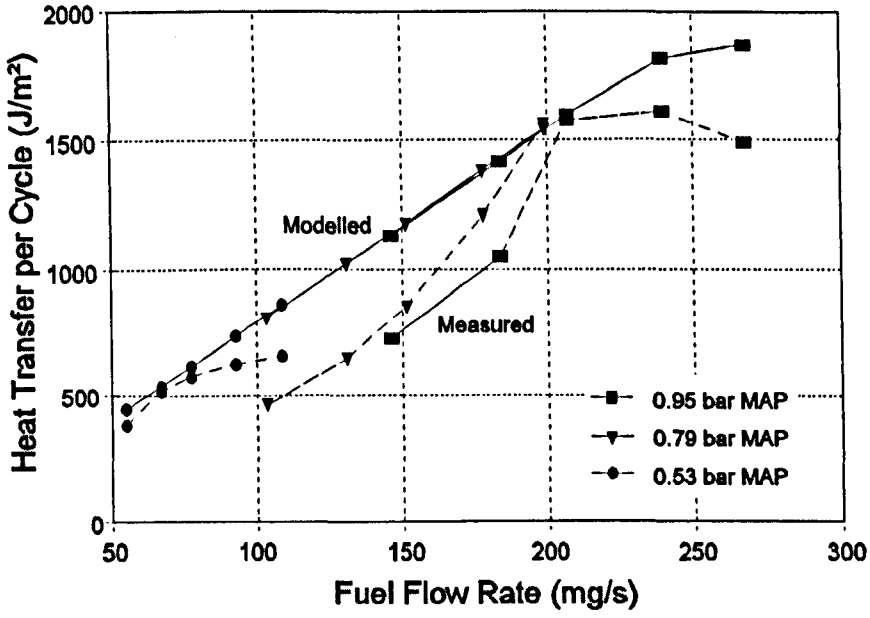

Figure 8.15 - Variation in Modelled and Measured Heat Transfer Rates with Fuel Flow Rate and MAP. Engine Fully-Warm and Running at 1000 RPM

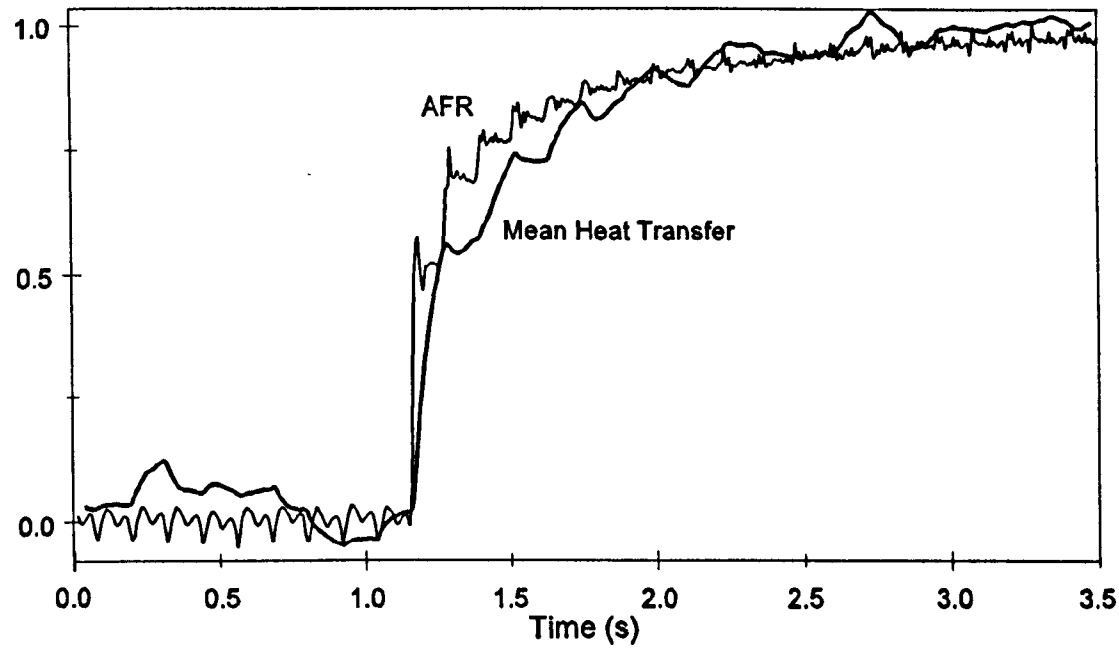

Figure 9.1 - Normalised Mean Heat Transfer and Inverted AFR Plots when Fuel Flow Rate is Step-Increased from 103 mg/s to 199 mg/s with a Fully-Warm Engine Running at 1000 RPM and 0.79 bar MAP on Isooctane Fuel

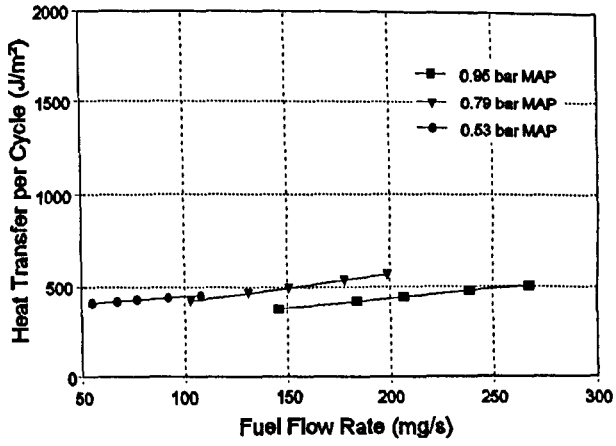

(a) Surface Temperature = 40°C

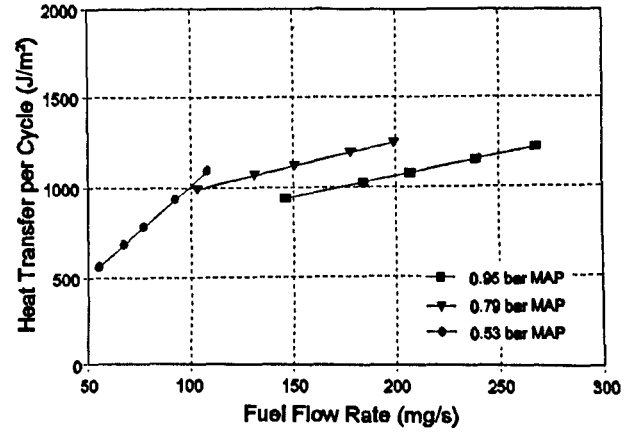

(b) Surface Temperature = 70°C

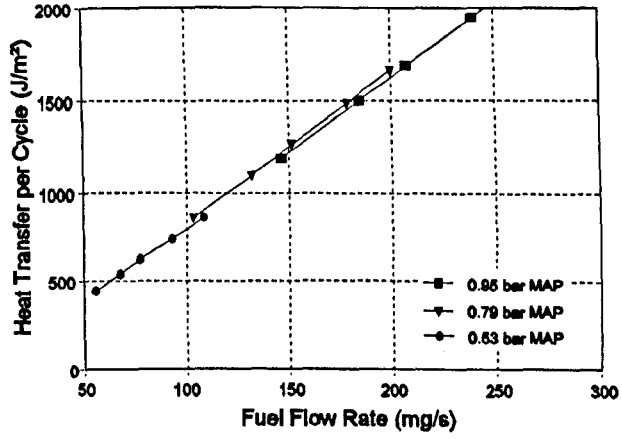

(c) Surface Temperature = 100°C

Figure 9.2 - Variation in Modelled Heat Transfer Rates with MAP, Fuel Flow Rate and Port Surface Temperature with the Engine Running at 1000 RPM on Isooctane Fuel